UCL Chemical Engineering Doctoral Thesis

Electrocatalyst Degradation in Polymer Electrolyte Membrane Water Electrolysers

James Alexander Dodwell

2022

A thesis submitted for the partial fulfilment of the requirements for the degree of Doctor of Philosophy at University College London

Electrochemical Innovation Lab
Department of Chemical Engineering
Torrington Place
London
WC1E 7JE

I, James Alexander Dodwell, confirm that the work presented in this thesis is my own.

Where information has been derived from other sources, I confirm that this has been indicated in the thesis.

Signature	Date

In memory of Ona and Michael Crowdy.

My Dear Grandparents, who were always proud

i. Acknowledgements

I would firstly like to express my sincere gratitude to Prof Dan Brett, Dr Gareth Hinds and Dr Rhodri Jervis. They provided everything I needed to complete this PhD; from giving me the opportunity and funding to study at UCL Engineering, to the provision of equipment and their technical expertise, to the endless discussions of electrochemistry and much more besides. The quality of supervision has been highly motivating and has made this thesis possible.

I also owe thanks to my friends and colleagues within and without the department, especially to those in the electrolyser team, Max and Jude, for both becoming involved in my research and vice versa. This PhD was a much more enjoyable and diverse experience because of them. Particular thanks must also go to Toby, for both enabling the practical side of my research and for always being keenly interested.

To my wife Sarah, who both moved down to London with me so I could study at UCL, and who has always been a motivating force in my life, I will always be thankful. To my family- my wife, my mother, father and brothers, who have always encouraged me to achieve, I am eternally grateful. This thesis is a reflection on their efforts.

ii. Abstract

Polymer electrolyte membrane water electrolysis (PEMWE) is predicted to become one of the backbone technologies of the future 'hydrogen economy', but for this to be realized several obstacles must be overcome. Importantly, an understanding of PEMWE system lifetime is incomplete as the various degradation routes have not been fully characterized or quantified. In this thesis several improvements to this understanding are presented. Firstly, time-based *in situ* open circuit voltage (OCV) data under a range of relevant ambient pressure conditions are presented. The impact of aqueous and gaseous environments has been elucidated, and it has been shown that potential change during OCV may proceed on either the anode, cathode or neither. These practical results have been enhanced with a basic model of OCV which shows that there is no universal OCV profile that can be applied to all PEMWE conditions.

The impact of cathode potential change during OCV on the degradation of platinum has also been established. By the coupling of a 3-electrode PEM electrolyser cell, and using a differential pulse voltammetry technique, Pt dissolution from the cell was detected when the cathode potential rose above 0.85 V versus the normal hydrogen electrode (NHE). This reached a maximum dissolution rate at the highest cathode potential of 1.02 V NHE, and gradually decayed over an approximately 100 h period. This was established during OCV both on Pt black (PtB) and Pt on carbon (Pt/C) electrocatalysts. It was demonstrated that, in the case of Pt/C, the dissolution phenomenon may impact the lifetime of the PEMWE system to less than 5 years. It has been clearly shown that OCV conditions cause degradation of the cathode electrocatalyst, and so must be considered when evaluating PEMWE lifetime.

iii. Impact Statement

In this thesis are three major findings that have wider implications for PEMWE, both academically and industrially. Firstly, it has been demonstrated that, during periods of OCV (non-operation), the degradation of electrocatalysts may occur. It has been shown that there is a wide window of OCV conditions that may cause degradation. As PEMWE systems must be efficient during operation, the majority of PEMWE studies detail the reaction mechanisms, degradation and lifetime during operation only. The results of this thesis indicate that periods of OCV are both richly scientifically interesting and highly relevant when considering system lifetimes. Although this thesis outlines the mechanisms underlying the electrode potential nature of OCV and some of the attributable degradation mechanisms, this work is not complete and merits further research. Industrially, there are numerous implications on how best to operate PEMWE systems during periods of OCV to mitigate degradation and to improve lifetime.

Secondly, the degradation of the Pt electrocatalyst has been both observed and quantified. Depending on the amount of catalyst used on the PEMWE electrodes, this mechanism may become pertinent in determining the eventual lifetime of the system. Here the results are highly interesting, as the loss of Pt represents not only a lifetime limiting factor but is also a route by which Pt can be lost from the PEMWE system itself. As Pt is a scarce resource, mechanisms to either prevent this loss or reclaim this dissolved Pt should be investigated.

Thirdly, a low-cost electrochemical method of determining very low Pt concentrations has been used to determine dissolution from an electrochemical device for the first time. This technique requires a fraction of the cost of other methods that quantify extremely low concentrations of Pt, and so is far more accessible to academic and industrial groups who may be interested in evaluating Pt loss from electrochemical systems but may not have access to more expensive techniques.

iv. Publications

Primary publications

J. Dodwell, M. Maier, J. Majasan, R. Jervis, L. Castanheira, P. Shearing, G. Hinds, L. Brett, Open-circuit dissolution of platinum from the cathode in polymer electrolyte membrane water electrolysers, J. Power Sources. 498 (2021) 229937.

Other publications

M.P. Browne, J. Dodwell, F. Novotny, S. Jaśkaniec, P.R. Shearing, V. Nicolosi, D.J.L. Brett, M. Pumera, Oxygen evolution catalysts under proton exchange membrane conditions in a conventional three electrode cell vs. electrolyser device: a comparison study and a 3D-printed electrolyser for academic labs , J. Mater. Chem. A. 9 (2021) 9113–9123.

M. Maier, R.E. Owen, M.T.M. Pham, J. Dodwell, J. Majasan, J.B. Robinson, G. Hinds, P.R. Shearing, D.J.L. Brett, Acoustic time-of-flight imaging of polymer electrolyte membrane water electrolysers to probe internal structure and flow characteristics, Int. J. Hydrogen Energy. (2021).

M. Maier, J. Dodwell, R. Ziesche, C. Tan, T. Heenan, J. Majasan, N. Kardjilov, H. Markötter, I. Manke, L. Castanheira, G. Hinds, P.R. Shearing, D.J.L. Brett, Mass transport in polymer electrolyte membrane water electrolyser liquid-gas diffusion layers: A combined neutron imaging and X-ray computed tomography study, J. Power Sources. 455 (2020).

M. Maier, Q. Meyer, J. Majasan, C. Tan, I. Dedigama, J. Robinson, J. Dodwell, Y. Wu, L. Castanheira, G. Hinds, P.R. Shearing, D.J.L. Brett, Operando flow regime diagnosis using acoustic emission in a polymer electrolyte membrane water electrolyser, J. Power Sources. 424 (2019) 138–149.

v. Table of Contents

i. Acknowledgements i
ii. Abstract ii
iii. Impact Statement iv
iv. Publications vi
v. Table of Contents vii
vi. List of Figures xi
vii. List of Tables xvii
viii. List of Important Equations xix
ix. List of Acronyms xxi
x. List of Scientific Terminology xxiii
1 Introduction 1
1.1 A Response to Climate Change 1
1.2 The Hydrogen Economy 9
1.3 Brown, Grey, Blue and Green 11
1.3.1 Brown, Grey, and Blue Hydrogen 11
1.3.2 Green Hydrogen 18
1.4 The Electrolysis of Water for Hydrogen Production 21
1.4.1 Alkaline Water Electrolysis 22
1.4.2 Solid Oxide Electrolysis 27
1.4.3 Polymer Electrolyte Membrane Water Electrolysis 30
1.4.4 The Future of Electrolysis 35
2 Theory of Water Electrolysis 37
2.1 The Thermodynamics of Water Electrolysis 37
2.1.1 Reversible Cell Voltage and Thermoneutral Voltage 37
2.1.2 Electrode Potentials 43
2.2 Kinetics of Water Electrolysis 49
2.3 Ohmic Resistance, Mass Transport and the IV Curve 56
3 Research Aims 59
4 State-of-the-Art 64
4.1 The Nature of PEM-Based Systems During Open Circuit Periods 64
4.1.1 O_2 and H_2 Permeation through Nafion 66

4.2 OER Electrocatalysts in PEMWE 74
4.3 HER Electrocatalysts in PEMWE 81
4.4 The Degradation of Electrocatalysts 88
4.5 Measurement of Electrocatalyst Dissolution by SFC-ICP-MS 94
4.6 Summary 102
5 Methodology 104
5.1 PEMWE Cell Construction 104
5.2 Balance of Plant Construction 106
5.3 CCM Fabrication 107
5.3.1 Catalyst Ink Formulation 107
5.3.2 CCM Fabrication by Decal Transfer 108
5.4 Overview of Electrochemical Methods Applied to PEMWE 109
5.4.1 Constant Potential Hold 109
5.4.2 IV Curves 110
5.4.3 Galvanostatic Electrochemical Impedance Spectroscopy (GEIS) 110
5.4.4 Cyclic Voltammetry (CV) 114
5.4.5 Open Circuit Voltage (OCV) 114
5.5 Voltammetric Techniques and ICP-MS 116
5.5.1 The Voltammetry of Pt 116
5.5.2 The Voltammetry of Ir and Ru 117
5.5.3 ICP-MS 119
5.5.4 The Treatment of Water Samples for Total Pt Loss Measurements 119
5.6 3-Electrode PEMWE Cell Development 120
5.6.1 3-Electrode PEMWE Cell Design 120
5.6.2 Validation of the New 3-Electrode PEMWE Cell 122
6 Chapter 1 - An Investigation of OCV Profiles Under a Range of PEMWE Cell Conditions 129
6.1 Chapter Introduction 129
6.2 Estimation of Reversible Potentials and the pH of Nafion in PEMWE 130
6.3 PEMWE OCV Profiles Under a Range of Conditions 133
6.3.1 The Impact of Dissolved Gases 136
6.3.2 The Influence of Water Flow 148
6.3.3 ‘Dry’ Cathodes, and the Impact of Electroosmotic Drag 151
6.4 Chapter 1 Conclusions 156
7 Chapter 2 - Mathematical Modelling of OCV 158
7.1 Chapter Introduction 158

7.2 Developing a Mathematical Model of OCV in PEMWE 158
7.2.1 Dissolved Gas Concentration and Diffusion Considerations 160
7.2.2 Electrochemical Considerations 166
7.3 Results and Discussion 174
7.3.1 Comparison of Model and Real OCVs 175
7.3.2 The Effect of Water Phase Length on the OCV Profile 181
7.3.3 The Effect of Temperature and Pressure 185
7.3.4 Limitations of the Mathematical OCV Model 187
7.4 Chapter 2 Conclusions 189
8 Chapter 3 - The Application of Voltammetry to Electrocatalyst Dissolution, and the Dissolution of PtB in PEMWE 191
8.1 Chapter Introduction 191
8.2 Voltammetry as a Method of Determining Electrocatalyst Dissolution 192
8.2.1 Voltammetry of Pt 192
8.2.2 Voltammetry of Ir and Ru 198
8.2.3 Testing against Standard Solutions and Comparison to ICP-MS 199
8.2.4 Interference Testing 203
8.3 The Dissolution of Pt from a PtB Cathode Electrocatalyst during OCV and Operation 206
8.3.1 Cell and Test Setup for PtB Dissolution 206
8.3.2 Dissolution of Pt from PtB during OCV and Operation at 1 A cm^{-2} 207
8.3.3 Effect of Pt Dissolution on Electrode Lifetime 213
8.3.4 PtB Surface Changes 224
8.3.5 Mechanisms of Pt Dissolution in PEMWE Cathodes 225
8.4 Chapter 3 Conclusions 227
9 Chapter 4 - The Dissolution of Pt/C in PEMWE 230
9.1 Chapter Introduction 230
9.2 The Dissolution of Pt from Pt/C during OCV 231
9.2.1 Cell and Test Setup 231
9.2.2 The Dissolution of Pt from Pt/C during OCV and Operation at 1 A cm^{-2} 232
9.3 Measurement of Total Pt Loss from Pt/C 239
9.3.1 Voltammetry of Samples Treated with Aqua Regia 240
9.3.2 Measurement of Dissolved Pt and Pt(0) from a PEMWE 241
9.3.3 The Mechanism of Pt(0) Loss 249
9.3.4 Estimation of Pt/C Lifetime Based on Total Pt Loss 250

9.4 Investigation of Pt Dissolution Signal during the OCV-Operation Transition 253
9.5 Chapter 4 Conclusions 260
10 Overall Conclusions 262
11 Further Work 265
12 Bibliography 267

vi. List of Figures

Figure 1. The change in annual average air temperature between 1980 and 2019. 2

Figure 2. The Keeling Curve. 4

Figure 3. The weighted average energy costs of renewable sources in comparison to fossil fuels. 6

Figure 4. UK electricity demand and the supply from wind, solar, nuclear and on-demand sources. 8

Figure 5. Illustration of the 'Hydrogen Economy' infrastructure proposed by J.O'M Bockris. 10

Figure 6. Coal Gasification (CG). 12

Figure 7. H2 production by steam methane reforming (SMR). 13

Figure 8. The levelised cost of brown, grey, blue and green hydrogen (LCOH). 15

Figure 9. The carbon footprint of historical and forecast H2 production. 17

Figure 10. The nameplate electrical capacity of water electrolysers installed worldwide 2000-2017. 20

Figure 11. Increase in water electrolysis capacity 2020-2023, covering all types of electrolysis 21

Figure 12. Typical setup of an AWE cell 23

Figure 13. The efficiency range and the current density operational range of AWE (AEL), PEMWE (PEMEL) and SOEC (SOEL). 25

Figure 14. ‘Zero-gap’ AWE 27

Figure 15. Typical setup of a solid oxide electrolyser cell 28

Figure 16. Typical setup of a PEMWE cell. 32

Figure 17. 2016 estimate of capital cost of electrolysis for the years 2020 and 2030 ... 34

Figure 18. Reversible voltage and thermoneutral voltages of water splitting reaction. 42

Figure 19. pH – potential (Pourbaix) diagram of water. 47

Figure 20. pH - potential (Pourbaix) diagrams of the thermodynamically stable states of a) Iron and b) Iridium. 49

Figure 21. Differing charge transfer coefficients on the outcome of the Butler-Volmer equation and the net reaction rate. 52

Figure 22. Application of the Butler-Volmer equation at high overpotential for HER. .. 53

Figure 23. Reaction coordinates of a catalysed HER. 55

Figure 24. The Volcano plot of HER. 55

Figure 25.The IV curve. 58

Figure 26. Breakdown of the 2010 capital cost of PEMWE components. 60

Figure 27. Gas diffusion in dry and hydrated Nafion membranes. 70

Figure 28. Volcano plot of oxide electrocatalysts for OER. 75

Figure 29. The rate of OER as a function of the potential. 79

Figure 30. Reported electrocatalyst loadings of OER and HER electrocatalysts in PEMWE. 82

Figure 31. Mechanisms of Pt degradation in PEMFC. 90

Figure 32. Scanning flow cell-inductively coupled plasma – mass spectrometry. 95

Figure 33. Dissolution of nanoparticle Pt/C in SFC-ICP-MS. 97

Figure 34. pH – potential (Pourbaix) diagram of Pt. 100

Figure 35. Schematic of 3-electrode cell used in this thesis. 104

Figure 36. The balance of plant supporting the PEMWE cell. 106

Figure 37. The CCM layout for hot pressing.....109
Figure 38. Randles equivalent circuit of the PEMWE cell.....111
Figure 39. AC current and the voltage response to a) high frequency b) medium frequency and c) low frequency. 112
Figure 40. Nyquist plot representative of the Randles equivalent circuit.....113
Figure 41. 3-electrode cell containing an in-line Luggin capillary connected to a reference electrode. 120
Figure 42. GEIS of 3-electrode PEMWE cell at 0.1 A cm-2 DC. 123
Figure 43. Cell EIS, fitting and the anode plus cathode fitting.....124
Figure 44. Rs values for the cell, anode and cathode. 126
Figure 45. IV curves of the cell, anode and cathode of the 3-electrode cells 128
Figure 46. Impact of dissolved gases on anode and cathode potential in a PEMWE single cell during OCV. 136
Figure 47. Estimation of the electrode potentials in PEMWE. 137
Figure 48. *in situ* cyclic voltammetry of a) IrOx anode at 3 mg cm-2 and b) Pt/C cathode. 140
Figure 49. Experimental electrode potentials in dissolved gas environments. 142
Figure 50. Variations in potential at the beginning of the OCV period at a) the anode and b) the cathode.....144
Figure 51. Impact of water flow on anode and cathode potential in the PEMWE cell during OCV. 148
Figure 52. Impact of gas bubbles on anode and cathode potential in the PEMWE cell during OCV 150
Figure 53. PEMWE systems with ‘dry’ cathode at OCV. 152

Figure 54. Impact of pre-OCV operation time on anode and cathode potential in the PEMWE cell during OCV with a fully wet anode. 153
Figure 55. Impact of pre-OCV operation time on anode and cathode potential in the PEMWE cell during OCV with a anode containing oxygen bubbles 154
Figure 56. The model PEMWE system used for the simulation of OCV 159
Figure 57. Experimentally derived values for the permeability of (a) hydrogen and (b) oxygen in hydrated Nafion over the PEMWE temperature range. 163
Figure 58. Example Evans (mixed-potential) diagrams of ORR and HOR occurring on an electrode. 169
Figure 59. The rate and direction of potential change of a capacitive mixed-potential electrode under different fluxes of hydrogen and oxygen 170
Figure 60. Comparison of real OCV data to the modelled OCV data with the closest conditions. 176
Figure 61. The OCV potential balance over the range of anode phase lengths (LO2), cathode phase lengths (LH2), temperatures and H2 pressures. 179
Figure 62. The potential of a) the anode and b) the cathode after 2 h at OCV under each OCV condition. 180
Figure 63. Example of the impact of variation of the phase length on the anode and cathode potentials during OCV. 183
Figure 64. The rate and direction of potential change of the anode and cathode. 184
Figure 65. OCV models at 3mm phase depth for the anode and cathode water phases. 186
Figure 66. OCV models at 0.1mm phase depth of anode and cathode 187

Figure 67. The reaction of formaldehyde and hydrazine to form a formaldehyde-hydrazone complex. 194
Figure 68a) Potential profile of DPV and LSV techniques with time. 195
Figure 69a) Typical Pt DPV profiles of the sample and sample with the 1st and 2nd standard additions. 197
Figure 70 Dissolved Pt concentration in PEMWE cathode water as a function of cathode potential, measured by ICP-MS and DPV. 201
Figure 71. Limit of detection tests of Pt standard solutions with DPV and ICP-MS 202
Figure 72. DPV profiles of Pt catalytic wave voltammetry with a) the addition of Ir and b) the addition of Ru. 204
Figure 73. Measurement of 1 ngL-1 Pt (IV) solution with various concentrations of Ir (III) and Ru (III). 205
Figure 74. Evolution of cathode potential, anode potential and cell voltage with time. 208
Figure 75. Cathode potential of OCV tests during the OCV period 208
Figure 76. Pt dissolution rate from the PEMWE PtB cathode. 209
Figure 77. Pt dissolution as a function of increasing cathode potential in a PEMWE. . 211
Figure 78. The Pt dissolution rate from the onset of operation 213
Figure 79. Method used to forecast dissolution through OCV and operation after the OCV period 216
Figure 80. Average Pt dissolution rate as a function of the duration of operation versus the duration of the OCV period. 221
Figure 81. Comparison of Pt dissolution rates for the cathode at OCV and under potential control. 223

Figure 82. Cyclic voltammetry of PtB cathode. 225

Figure 83. Evolution of cathode potential, anode potential and cell voltage with time. 233

Figure 84. Pt dissolution rate from the PEMWE Pt/C cathode. 234

Figure 85. Average Pt dissolution rate from Pt/C electrocatalyst as a function of the duration of operation versus the duration of the OCV period. 236

Figure 86. Cyclic voltammetry of Pt/C cathode. 238

Figure 87. Impact of the presence of nitrates in DPV 241

Figure 88. Dissolution rate of Pt from the PEMWE Pt/C cathode. 242

Figure 89. Measurement of total Pt lost from a PEMWE during period of OCV. 244

Figure 90. Measurement of dissolved Pt concentration and measurement of total Pt lost as a function of potential. 245

Figure 91. Comparison of the estimated Pt dissolution rate profiles 247

Figure 92. Measurements of Pt dissolution and total Pt loss during operation at 1A cm-2 and at the start of the OCV period 249

Figure 93. Average total Pt loss rate from Pt/C electrocatalyst as a function of the duration of operation versus the duration of the OCV period. 251

Figure 94. Cathode potential of the 1 A cm-2, 0.24 V and 0.92 V OCV transition tests. 255

Figure 95. Pt dissolution rates during OCV and after the transition from OCV 256

vii. List of Tables

Table 1. Electrochemical reactions relevant to PEMWE. 73

Table 2. Experimental parameters for the determination of dissolved Pt concentration by DPV. 117

Table 3. Experimental parameters for the determination of dissolved Ru(III) and Ir(III). 118

Table 4. Fitting results of the Randles equivalent circuits. 125

Table 5. Estimation of Erev (H+/ H2) and Erev (O2 / H2O) in PEMWE cell at 293 K and ambient pressure. 133

Table 6. The conditions of the OCV tests performed and their relation to real operation. 135

Table 7. Parameters used to fit the Butler-Volmer equation. 138

Table 8. Anode and cathode electrode capacitances measured by GEIS and CV..... 140

Table 9. Approximate time for electrode potentials to reach Erev, and the electrode potential at 2 h 141

Table 10. The solubility and diffusional parameters used in the OCV model..... 165

Table 11. Electrochemical parameters used for the development of the OCV model. 172

Table 12. Constants and variables used for the model of OCV 173

Table 13. Comparison of real and modelled OCV tests. 175

Table 14. Fitted values for Pt dissolution from PtB during OCV. 214

Table 15. Fitted values for Pt dissolution during operation after the OCV period. 215

Table 16. Pt dissolution amounts and estimations of the cathode electrode lifetimes at 3 mg cm-2 PtB. 218

Table 17. Fitted values for Pt dissolution from PtB during OCV. 235

Table 18.Pt dissolution amounts and estimations of the cathode electrode lifetimes at 0.5 mg cm-2 Pt on Pt/C. 237

Table 19. Fitting profiles for the Pt(II) and Pt(IV) dissolution profiles. 243

Table 20. Fitting profiles for the total Pt loss profiles.. 245

Table 21. Fitted values for total Pt loss from Pt/C cathode during OCV and operation. 252

Table 22. Fitting parameters of the exponential decay function.. 257

Table 23. Pt Dissolution rates at OCV. 258

Table 24. Integration results of total Pt dissolved during the current / potential hold periods. 259

viii. List of Important Equations

(1) Coal gasification reaction 12

(2) Water-gasification reaction 12

(3) Syngas reaction 13

(4) Water splitting reaction 21

(5) OER in AWE 24

(6) HER in AWE 24

(7) OER in SOEC 28

(8) HER in SOEC 28

(9) OER in PEMWE 31

(10) HER in PEMWE 31

(11) The Gibbs free energy 37

(13). Simplified Gibbs free energy 39

(15) Reversible potential from the Gibbs free energy 40

(17) The thermoneutral voltage 41

(19) The enthalpy of formation 43

(20) The cell voltage 44

(21) The Nernst equation 44

(23) The quotient of reaction 45

(24) The quotient of reaction of OER and ORR 45

(25) The quotient of reaction of HOR and HER 45

(36) Calculation of reaction overpotential 50

(37) Butler-Volmer equation for OER 50

(38) Butler-Volmer equation for ORR 50

(39) The combined OER and ORR Butler-Volmer equation 50

(40) The dissolution of Pt oxide reaction 98

(41) Capacitance from the constant phase element 114

(42) Henrys law of the solubility of gases 130

(43) The ideal gas law 131

(44) van't Hoff equation 131

(46) Change of potential as a function of capacitance 138

(48) Diffusivity of dissolved gases through water 162

(49) Diffusivity of dissolved gases through Nafion 162

(56) Pulse profile equation 214

(57) Exponential decay equation 215

ix. List of Acronyms

AC	Alternating Current
AEL	Alkaline Electrolysis (used in conjunction with AWE)
AEM	Anion-Exchange Membrane
AFM	Atomic Force Microscopy
AST	Accelerated Stress Test
AWE	Alkaline Water Electrolysis / Electrolyser
BoT	Beginning of Test
CCM	Catalyst Coated Membrane
CCS	Carbon Capture and Storage / Sequestration
CG	Coal Gasification
CPE	Constant Phase Element
CV	Cyclic Voltammetry
DC	Direct Current
DEMS	Differential Electrochemical Mass Spectrometry
DPV	Differential Pulse Voltammetry
ECSA	Electrochemically Active Surface Area
EDX	Energy Dispersive
EIS	Electrochemical Impedance Spectroscopy
EoT	End of Test
EU	European Union
GCE	Glassy Carbon Electrode
GHG	Greenhouse Gas
HER	Hydrogen Evolution Reaction
HHV	Higher Heating Value
HMDE	Hanging Mercury Drop Electrode
HOR	Hydrogen Oxidation Reaction
ICP-MS	Inductively Coupled Plasma – Mass Spectrometry
IEA	International Energy Agency
IL-TEM	Identical Location – Transmission Electron Microscopy
IRENA	International Renewable Energy Agency
LCOE	Levelised Cost of Electricity
LCOH	Levelised Cost of Hydrogen
LHV	Lower Heating Value
LSV	Linear Scanning Voltammetry
MEA	Membrane Electrode Assembly
MMO	Mixed Metal Oxide
MS	Mass Spectrometry
NHE	Normal Hydrogen Electrode
OCV	Open Circuit Voltage
OER	Oxygen Evolution Reaction
ORR	Oxygen Reduction Reaction

P.A.	Per Annum
PEEK	Polyether Ether Ketone
PEM	Polymer Electrolyte Membrane
PEMEL	Polymer Electrolyte Membrane Electrolysis (Used in conjunction with PEMWE)
PEMFC	Polymer Electrolyte Membrane Fuel Cell
PEMWE	Polymer Electrolyte Membrane Water Electrolyser
PGM	Precious Group Metal
RMS	Root Mean Squared
RPM	Revolutions per Minute
RRDE	Rotating Ring Disk Electrode
SFC	Scanning Flow Cell
SFC-ICP-MS	Scanning Flow Cell- Inductively Coupled Plasma – Mass Spectrometry
SMR	Steam Methane Reforming
SOEC	Solid Oxide Electrolysis
SOEL	Solid Oxide Electrolysis (used in conjunction with SOEC)
SPE	Solid Polymer Electrolyte
TEM	Transmission Electron Microscopy
UNFCCC	United Nations Framework Convention on Climate Change
XCT	X-ray Tomography
XRF	X-ray Fluorescence

x. List of Scientific Terminology

Symbols

[X]	Concentration of (X) (mol)
$\alpha_{O/R}$	Charge transfer coefficient
C_x	Concentration of (X) (mol)
c_p	Molar heat capacity (J K^{-1} mol^{-1})
CPE_{dl}	Constant phase element double layer capacitance ($S \cdot S^n$)
D	Diffusivity constant (cm^2 s^{-1})
ε	Molar permeation rate of gases (mol $cm^{-1}s^{-1}$)
E_{anode}	Anode reversible potential (V NHE)
$E_{cathode}$	Cathode reversible potential (V NHE)
E_{cell}	Cell reversible potential (V)
E_{corr}	Corrected electrode potential (V NHE)
E_{rev}	Reversible potential (V NHE)
E_{thermo}	Thermoneutral voltage (V)
F	Faraday constant (96485 A mol^{-1})
G	Gibbs free energy (KJ mol^{-1})
H_F	Enthalpy of formation (KJ mol^{-1})
H_{sol}	Enthalpy of solution (KJ mol^{-1})
i	Current density (A cm^{-2})
i_o	Exchange current density (A cm^{-2})
i_{total}	Total current density on electrode (A cm^{-2})
k	solubility constant (mol dm^{-3} atm^{-1})
l_x	Phase length of (X) (cm)
n	Number of electrons in reaction
pX	partial pressure of (X) (atm)
ρ	Porosity
R_s	Series resistance (Ω cm^{-2})
R_{mem}	Membrane resistance (Ω cm^{-2})
R_{ct}	Charge transfer resistance (Ω cm^{-2})
S	Entropy (J K^{-1})
τ	Tortuosity
U	Internal energy (KJ mol^{-1})
ϒ	Number of protons involved in reaction

Units

A cm^{-2}	Amps per square centimeter
atm	atmospheres
^oC	Degrees celcius
CO_2e	Equivalent carbon dioxide
Gt	Gigatonne
GW	Gigawatt
KWh	Kilowatt-hour
Mt	Megatonne
MW	Megawatt
MWh	Megawatt-hour
ppm	Parts-per-million

Less common molecules and acronyms

CNT	Carbon nanotube
CTAB	Cetrimonium bromide
C_xH_y	Hydrocarbon
IrO_x	Iridium oxide
$Ir_xRu_{1-x}O_x$	Iridium-ruthenium oxide
LSM	Lanthanum strontium manganite
Pt/C	Platinum on carbon
PtB	Platinum black
RuO_x	Ruthenium oxide
YSZ	Yttria-stabilized zirconia

1 Introduction

1.1 A Response to Climate Change

Over the past 40 years, global warming has become an accepted reality. The notion of climate change, which became scientific consensus in the 1980s, made worrying predictions for our future, if carbon dioxide (CO_2) emissions into our atmosphere were not significantly curtailed. Unfortunately, an effective global effort to reduce emissions was never made, and now we are living in that future. Global warming has transformed from an intangible threat to an issue that is apparent in our every day lives. Records for monthly high air temperatures are constantly being broken. The arctic ice coverage has been shrinking at a rate that, possibly by 2040, could mean it disappears entirely during the summer months [1]. Forest fires, which drive yet more CO_2 into the atmosphere, are becoming ever more numerous and extensive [2]. The global annual average air temperature increased by 0.7 ^oC between 1980 and 2019, with the severest warming generally occurring in the polar regions (Figure 1) [3]. It is now clear that, without significant action to reduce CO_2 emissions, the global atmospheric temperature could rise by as much as 5 ^oC by 2100 [4].

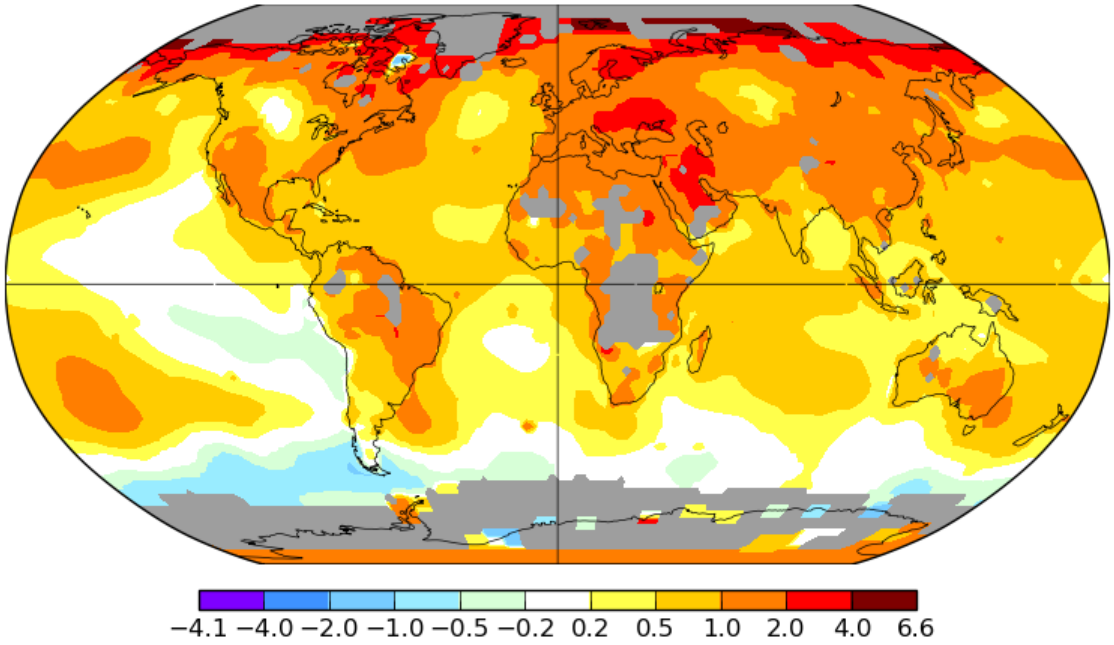

Figure 1. The change in annual average air temperature between 1980 and 2019. Average global temperature rise was 0.7°C in this period. Grey areas indicate missing data. Source NASA [3,5].

To combat runaway global warming, the 1990s heralded the first international agreements aimed at reducing greenhouse gas (GHG) emissions. In 1992, the United Nations Framework Convention on Climate Change (UNFCCC) was created with the overall aim to achieve the 'Stabilization of greenhouse gas concentrations in the atmosphere at a level that would prevent dangerous anthropogenic interference with the climate system' [6]. In 1997 this convention was put into action by the Kyoto Protocol, which was ratified by 192 parties [7]. Its aims were to incentivise nations to reduce GHG emissions by creating maximum permissible emission levels for several of the parties involved. Any emissions beyond this cap would have to be offset with the purchase of carbon credits, thus creating a form of trading which would incentivise renewables, carbon-reducing and carbon-capture schemes [8]. In 2015 these climate targets were enhanced with the addition of the Paris Agreement, which set out a

commitment for signatories to stabilise the global temperature rise to less than 2 ^{o}C, and ideally less than 1.5 ^{o}C, above pre-industrial levels [9]. However, whilst the Kyoto Protocol did bring about a real reduction of GHGs from a number of nations [10], it was and is still not a globally enforced accord. To avoid hindering economic growth amongst developing nations, it was decided, for those nations, not to impose emissions targets. This allowed developing countries to grow their economies on fossil fuels with the intention that they would transition to renewables once developed. This was one of the issues that prompted the United States to withdraw from the protocol, as it was believed that the terms would place GHG-unrestricted nations at an economic advantage to nations that had imposed restrictions. Of those countries, China and India, along with the United States, contributed 48.6 % of global emissions in 2017 [11].

A good summary of the Kyoto agreement was made by the climatologist Jerry Mahlman, who called it a 'Valid first step' but adding the qualification that '30 Kyoto's might do the job [to reduce GHG emissions]' [12]. Equal criticism has been weighted on the Paris Agreement, which is non-binding and now allows each country to set their own emissions targets. As member states are able to withdraw from this agreement, as the United States did in 2017, this puts considerably more pressure on the remaining states, making it less and less likely that the GHG reduction goals will ultimately be met [13].

A simple method of gauging the impact of these accords is to measure CO_2 concentration in the atmosphere. The Mauna Loa Atmospheric Observatory in Hawaii has constructed the longest running dataset, beginning in the 1958 International Geophysical Year and continuing to the present day [14]. The trendline from the data is known as the 'Keeling Curve', named after the founder of the measurement program

Charles Keeling, and plots an almost uninterrupted rise in atmospheric CO_2 concentration over the past 60 years (Figure 2).

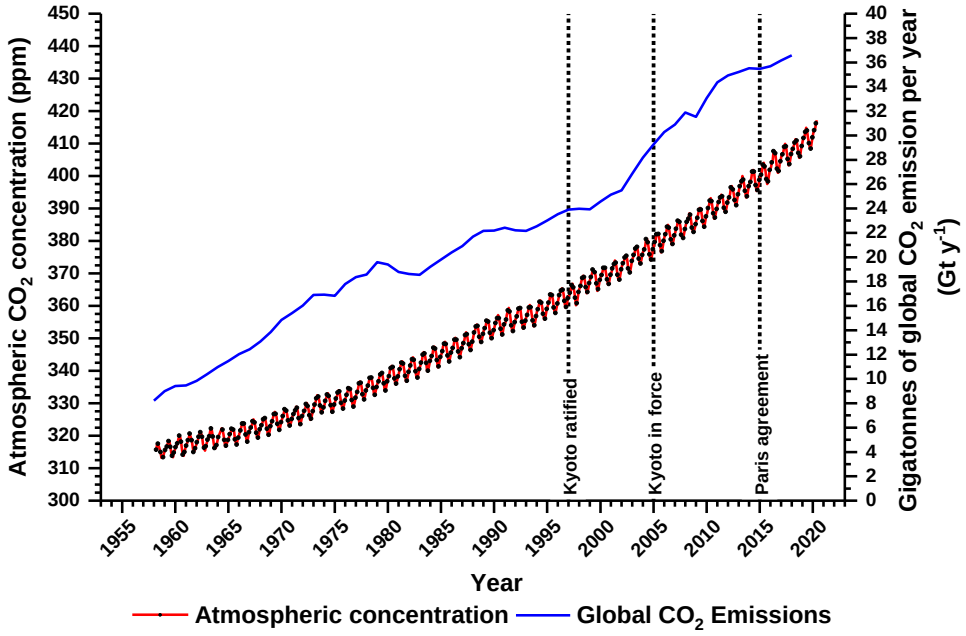

Figure 2. In red is the Keeling Curve, the monthly mean atmospheric CO_2 concentration measured at the Mauna Loa Atmospheric Observatory from 1958 to the present day. In blue is the annual global CO_2 emissions. Data source for Keeling Curve - Scripps CO_2 Program and [15]. Data source for CO_2 emissions - [16] with data published online at OurWorldInData.org. Retrieved from: 'https://ourworldindata.org/co2-emissions [Online Resource].

As of 2020, the atmospheric CO_2 concentration was still on an upward path, and so the need to address and reduce GHG emissions is becoming ever greater. It is now predicted by the UNFCCC that, to meet the goals of the Paris Agreement, GHG emissions must be cut by 7.6 % every year [17]. Instead of this however, the rate of annual CO_2 emissions has not yet reached its peak.

The challenge of controlling climate change is enormous in scale. Up until now, the efforts in reducing GHGs have made little effect on the global picture. However, there is

some cause for optimism that current and future efforts may have substantially more positive impact on the climate than past ones. Firstly, climate change is now apparent beyond all reasonable refute. The switch from fossil fuels to renewables is now done in the hope that it will remedy the climate problems of today, and not a problem that may be faced in the future. Secondly, fossil fuels are becoming an ever-rarer commodity. At current use rates, the known reserves of gas and oil are expected to run dry in around 50 years [18]. After this, it is imperative that other forms of energy are found, whether they be renewable or nuclear. The question that must be asked then is: if it must be done tomorrow, why not do it today? Thirdly, the cost of renewable energy is ever decreasing and becoming more and more cost-competitive against fossil fuels [19]. Between 2010 and 2019, the overall energy cost of photovoltaics has decreased by 82 %, with onshore and offshore wind at 39 % and 29 % respectively. Indeed, the agreed energy supply prices for the next 2 years show that, on average, the energy from photovoltaics and onshore wind will be sold more cheaply than the equivalent energy delivered by coal, oil, and natural gas (Figure 3). Renewables are now attractive from both an environmental and an economic standpoint, and this is proving to be a huge driver for change in the way that energy is sourced.

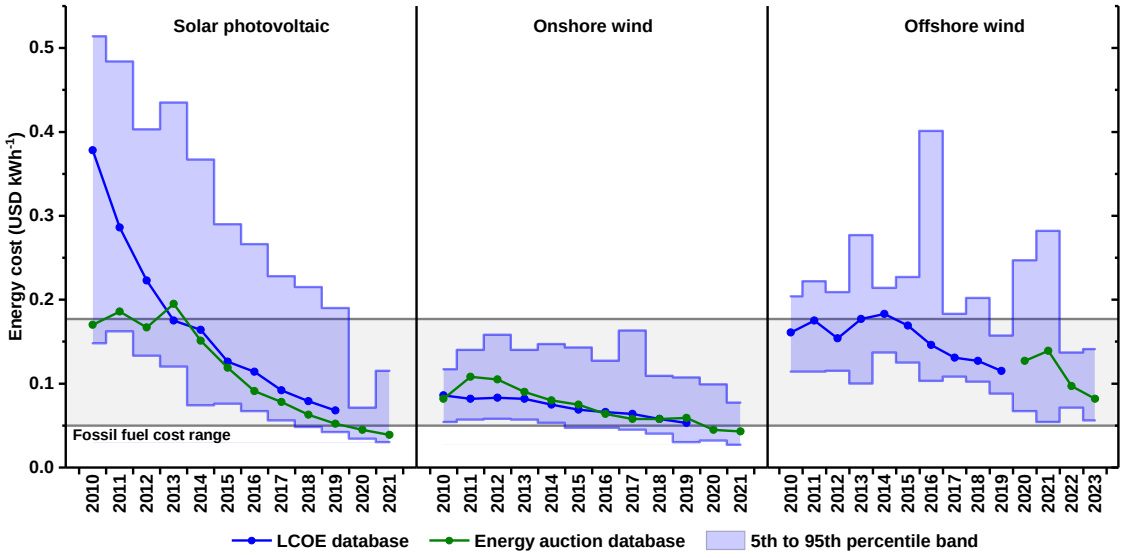

Figure 3. The weighted average energy costs of renewable sources in comparison to fossil fuels, shown by the Levelized Cost of Electricity (LCOE) and agreed energy supply prices (Energy Auction). The banding represents the 5th and 95th percentiles of the LCOE or auction prices, whichever is the smallest (5th percentile) or largest (95th percentile). Data source – the International Renewable Energy Agency (IRENA) [19].

In the UK, for example, the contribution of renewable electrical energy, as a function of the total amount supplied from all sources, rose from 6.1 % in 2010 to 44.6 % in 2020. This represents a difference in installed capacity of nearly 25 GW, of which the onshore and offshore wind supply is 6 GW and 8 GW respectively, with photovoltaics supplying roughly 5 GW [20]. This increased capacity is displacing fossil fuels, and nowadays it is very common for the electricity grid to have no input from any coal-fired power plants. This is a trend seen in many developed nations, and it is set to continue well into the future. At current rates, renewable energy in the UK may make up to 65 % of the energy market in 2030.

Although renewable energy is now cost-competitive and environmentally friendly, the current renewable sources can pose substantial challenges to the electricity grid. The

electrical output from solar and wind is dependent on the weather, the time of day and the season. Their power output is therefore as variable as the weather and just as unpredictable. The stacked graph in Figure 4 shows UK electricity supply and demand over the period of a week, with the contributions of solar, wind, nuclear power, and the on-demand power sources (gas turbines and import / export principally). Electrical power demand normally follows a daily double-peak profile, where demand is higher in the mornings and evenings, and dropping during the workday and night. In the case of solar, whilst the power peaks are somewhat of a match for overall demand, the peak height itself is highly variable and is generally not at maximum output during the times of highest demand. In the case of Figure 4 (and more generally also), wind energy does not match demand. Unlike solar, which has daily cycles, wind's daily output cannot be predicted beyond weather forecasts and long-term general trends. The combination of solar and wind energy therefore creates a highly variable and unpredictable power output, hence the need for on-demand sources to balance the grid.

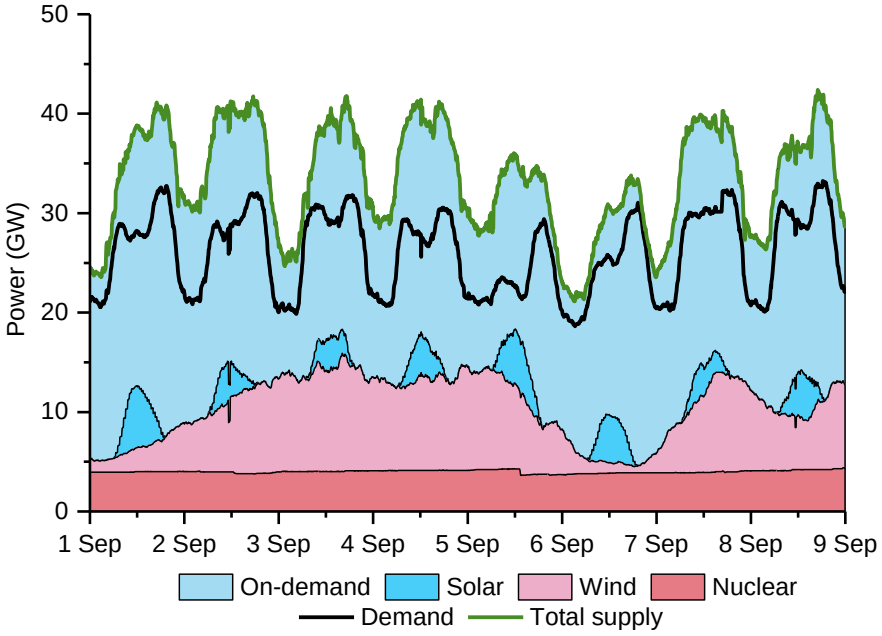

Figure 4. UK electricity demand and the supply from wind, solar, nuclear, and on-demand sources (gas turbine and import/export) covering the period 1st-9th September 2020. Data are stacked. Data source – GB Gridwatch (https://www.gridwatch.templar.co.uk/).

Increased use of wind and solar energy will lead to an increase in grid unpredictability, and so the capacity of grid balancing must increase in turn. Balancing is therefore an increasingly important element of the renewable electricity grid, and for true sustainability, balancing cannot be performed by fossil fuel sources. Energy storage systems are needed to provide this balancing function. The best example of this is pumped-storage hydroelectricity, where electricity is produced by releasing water from an uphill reservoir to spin turbines connected to electricity generators. The exact reverse is also the case when there is excess electricity in the grid, as the turbines can be powered to pump water uphill and store the excess electrical energy as gravitational potential energy. This creates a high-efficiency and high-capacity energy storage method that can respond very rapidly to spikes in supply or demand. Along with hydroelectricity, a burgeoning range of storage methods now exist, such as mechanical

energy storage in flywheels, thermal methods such as molten-salt storage, and electrochemical methods such as hydrogen and batteries. Hydrogen and batteries are of particular interest as their technology can be applied beyond grid storage. Importantly they are potential environmentally friendly solutions for the other sector that still relies entirely on fossil fuels, transportation. In 2016, transportation was the most polluting sector (9.1 Gt CO_2e p.a.[1] globally) after electricity and heat generation (15 Gt CO_2e p.a. globally) [21], and so the transition away from fossil fuels here is equally essential to combat climate change.

1.2 The Hydrogen Economy

The 'hydrogen economy', although still existing largely in concept only, articulates the potential of H_2 as an alternative to fossil fuels in heating and transportation. This concept was first properly developed by J.O'M Bockris in the 1970s [22,23], and describes an economy where sustainable energy is used to produce H_2. The H_2 is distributed through pipelines as natural gas currently is, and is used in applications that fossil fuels currently supply (Figure 5). H_2 contains no carbon within the molecule, and so when combusted the product is only water and energy. This is of course in contrast to hydrocarbons, which do contain carbon, and so additionally release CO_2 on combustion. By using H_2 as

[1] CO_2e is *equivalent*-CO_2. It is used to express the output off all types of GHG emissions equivalent to their potency as greenhouse gases relative to CO_2. For example, methane is 84 times more potent that CO_2 as a greenhouse gas, so 1 tonne of methane release is equivalent to 84 tonnes of CO_2.

the carrier of chemical potential energy as opposed to hydrocarbons, energy can be provided carbon-free, thus being environmentally friendly. The ultimate manifestation of the hydrogen economy is a society that uses H_2 for heating, for transportation, for off-grid electricity generation, and as a feedstock for chemical synthesis.

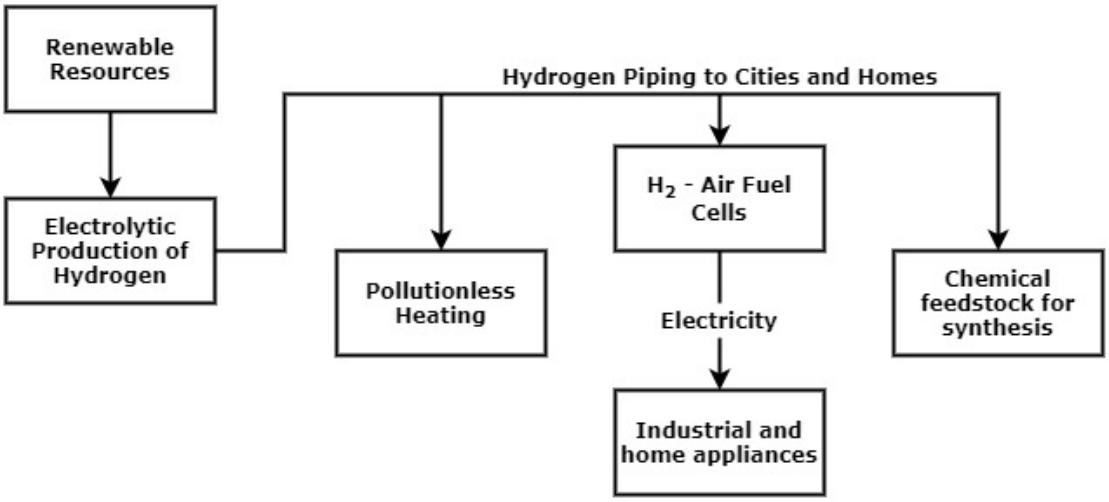

Figure 5. Illustration of the 'Hydrogen Economy' infrastructure proposed by J.O'M Bockris.

One of the inherent drawbacks of the hydrogen economy concept is that H_2 does not exist in any useable quantity in the earth's crust or atmosphere. H_2 gas is highly permeable, and due to its low molecular weight, it has the tendency to rise in the atmosphere. Over long periods of time this has caused any trapped H_2 to permeate through the earth's crust, into the atmosphere, leading to it eventually being lost into space. H_2 must therefore be synthesised from hydrogen-rich feedstocks, this typically being hydrocarbons or water.

1.3 Brown, Grey, Blue and Green

Even without the existence of the hydrogen economy there is a global need for H_2 in a range of applications. According to a 2019 report by the International Energy Agency (IEA) the four predominant industries consuming H_2 are oil refining (33 % of total H_2 production), ammonia production (27 %), methanol production (11 %) and steel production (3 %) [24]. These extremely large industries require a total annual H_2 production of approximately 70 Mt (megatonnes). In the same report it was stated that 98 % of this H_2 is 'brown' or 'grey', meaning that is produced from fossil fuels in a way that releases CO_2 into the atmosphere. Only 2 % of the H_2 produced was 'blue' or 'green', meaning that it is made in a way that does not result in CO_2 release into the atmosphere. Therefore, H_2 production is currently a net contributor to atmospheric CO_2, and hence the H_2 production industry must move towards blue and green hydrogen to become carbon free and sustainable.

1.3.1 Brown, Grey, and Blue Hydrogen

The distinction between brown, grey and blue H_2 depends on the initial feedstock for the production process, and on whether any CO_2 is released into the atmosphere during production. Fundamentally, all production methods that are classed under one of these colours use hydrocarbon-based feedstock, and all produce CO_2 during the process.

Brown H_2 is produced by the reaction of coal with oxygen (O_2) and steam in a process known as Coal Gasification (CG). In typical coal-to-H_2 plants there are two main reactions involved in the overall process. Firstly, syngas (a mixture of carbon monoxide (CO) and H_2) is produced by the partial oxidation of coal, reacting with steam and O_2, resulting in H_2 and CO (Equation (1). After this, the water-gas shift reaction takes place to produce

further H_2 from the reaction of the CO with water (Equation (2). CO_2 is the product of these reactions, but as coal has numerous impurities, several purification steps are required to produce pure H_2 and CO_2 streams.

$$3C + O_2 + H_2O \rightarrow H_2 + 3CO \quad (1)$$

$$CO + H_2O \rightarrow CO_2 + H_2 \quad (2)$$

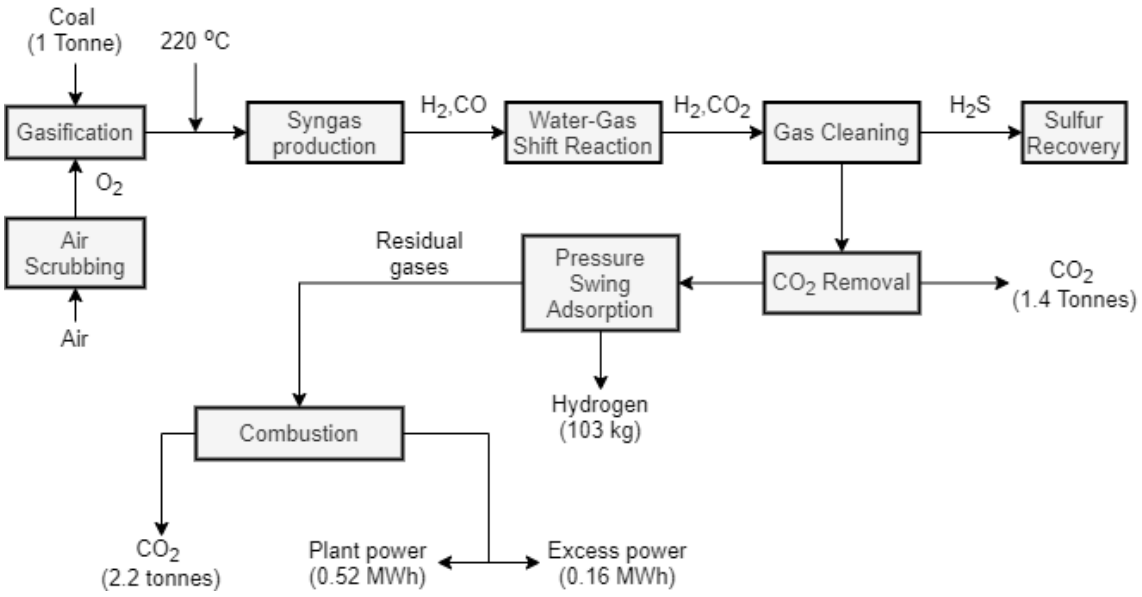

Figure 6. Coal Gasification (CG), the process of producing H_2 from coal and water. All values of production, waste and excess energy produced are based on the input of 1 tonne of coal into the process, although the ratio between the numbers is representative of an industrial CG plant. Figure reproduced from [25].

As the syngas production and water-gas shift reactions do not consume all the feedstock, after the removal of the CO_2 and H_2 the residual gases are typically used in power generation. This provides enough power for the gasification process and provides some excess power that is fed into the electricity grid. The cost of H_2 from CG is therefore largely dependent on the cost of the feedstock and capital cost of the plant, and can be

reduced further by the sale of electricity. In 2006, CG accounted for 19 % of total H_2 production globally [25].

Steam methane reforming (SMR) is the prime example of a grey H_2 process and is the most widespread and the cheapest process currently available. SMR uses hydrocarbon oils and natural gas as the feedstock, and proceeds with the reaction of the hydrocarbons with superheated steam producing syngas (Equation (3).The syngas then undergoes the water-gas shift reaction (Equation (2) to produce further H_2.

$$C_xH_y + xH_2O \rightarrow xCO + (x + 0.5y)H_2 \quad (3)$$

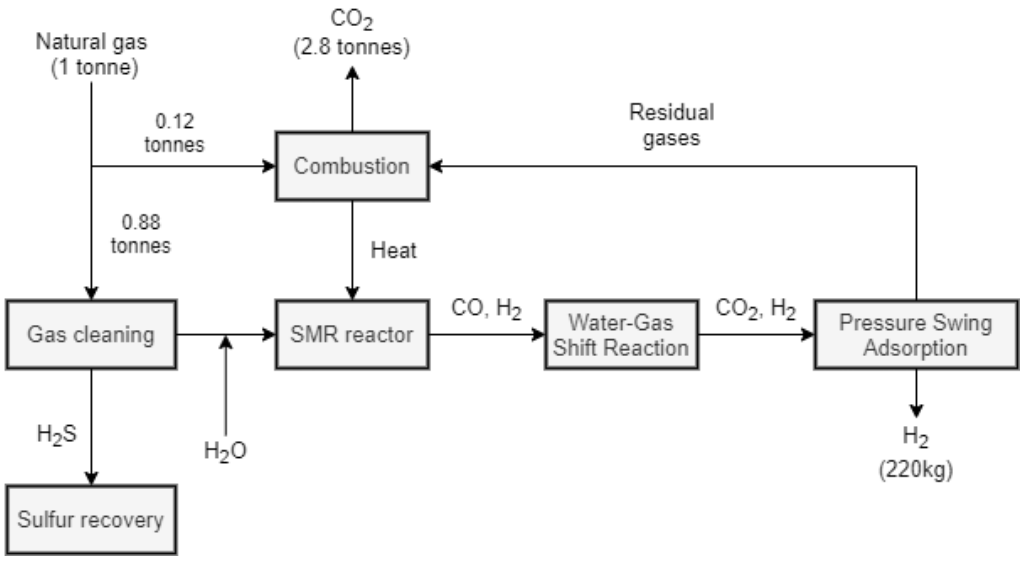

Figure 7. H_2 production by steam methane reforming (SMR). Values are based on the input of one tonne of natural gas, although the ratio between the numbers are representative of an industrial scale SMR. Data reproduced from [26].

Unlike CG, SMR is an endothermic process overall and so requires a continuous input of energy. This typically comes from the burning of the feedstock, and so reduces the amount of H_2 that can be extracted per unit of the hydrocarbons put into the process. Nevertheless, the higher purity (relative to CG) and low cost of the feedstock means that SMR is the dominant process in the H_2 production market. In 2004, SMR was reported to have produced 80 - 85 % of the world's H_2 [27].

The emission of CO_2 by CG and SMR preclude their use in the hydrogen economy. H_2 is only environmentally benign if the whole production and use cycle releases no CO_2 into the atmosphere; and whilst there may be some justification for relocating the source of CO_2 release (for example, taking CO_2 emissions away from the car exhaust to improve urban air quality), the overall process is still environmentally damaging. However, the concentrated CO_2 stream that is created by CG and SMR means that CO_2 capture and storage (CCS) is possible. Thus, H_2 produced by CG or SMR coupled to CCS is free from atmospheric CO_2 emissions. H_2 made by these means is termed 'blue hydrogen'. As blue hydrogen largely uses existing processes and infrastructure, it is a less disruptive technology and currently has the benefits of being cheaper than green hydrogen, whilst being only marginally costlier than grey or brown hydrogen (Figure 8).

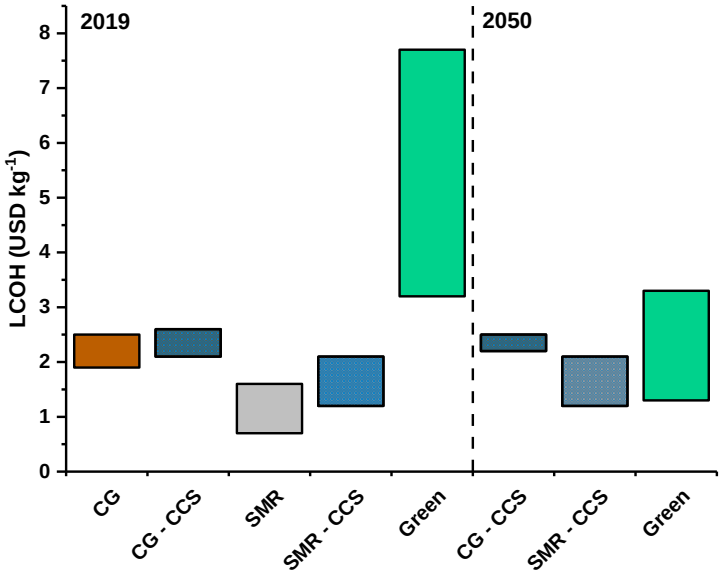

Figure 8. The levelized cost [2] of brown, grey, blue and green hydrogen (LCOH) in 2019 and the expected LCOH in 2050. Data source – International Energy Agency (IEA)[28].

Blue hydrogen may therefore have a role in the hydrogen economy, especially if the use of fossil fuels persists; however, it does have several drawbacks that green hydrogen methods are not encumbered by. Firstly, blue hydrogen still draws from the depleting reserve of fossil fuels, and so it is intrinsically linked to the volatility of fossil fuel prices. These would be expected to rise as fossil fuels become harder to attain, and blue hydrogen may become more expensive as a result. Although the switch from fossil fuels to biomass in SMR is possible [24], the current low cost of fossil fuels means that there would be no resultant reductions in the cost of blue hydrogen [29]. SMR using biomass is also not as technologically mature as conventional SMR, and many green hydrogen methods already supersede it in terms of perceived maturity [30]. As is highlighted in

[2] The 'levelised cost' is the sum of all the costs of the plant over its expected lifetime divided by the sum of the output. In the case of Figure 8, the output metric is the weight of hydrogen.

Figure 8, there is relatively little scope for cost savings to be made in CG-CCS or SMR-CCS by 2050.

Secondly, whilst CG and SMR are well-established technologies, CCS is still an upcoming process and does not currently exist at the necessary scales to sequester all the CO_2 produced from H_2 production. This can be seen in Figure 9, which also shows that the current rate of annual increase in CCS capacity (approximately 8 %) will not match the forecast growth rate of H_2 demand. For blue hydrogen to be realised, the rate of CCS capacity increase must increase by 20% annually until 2050. This calculation assumes that all CCS capacity will be dedicated to H_2 production; however, CCS capacity must be shared with coal, oil, and gas power plants until they are phased out by renewables. A blue hydrogen economy is therefore beset by two major uncertainties: uncertainty of the supply of fossil fuels and uncertainty around the storage of CO_2.

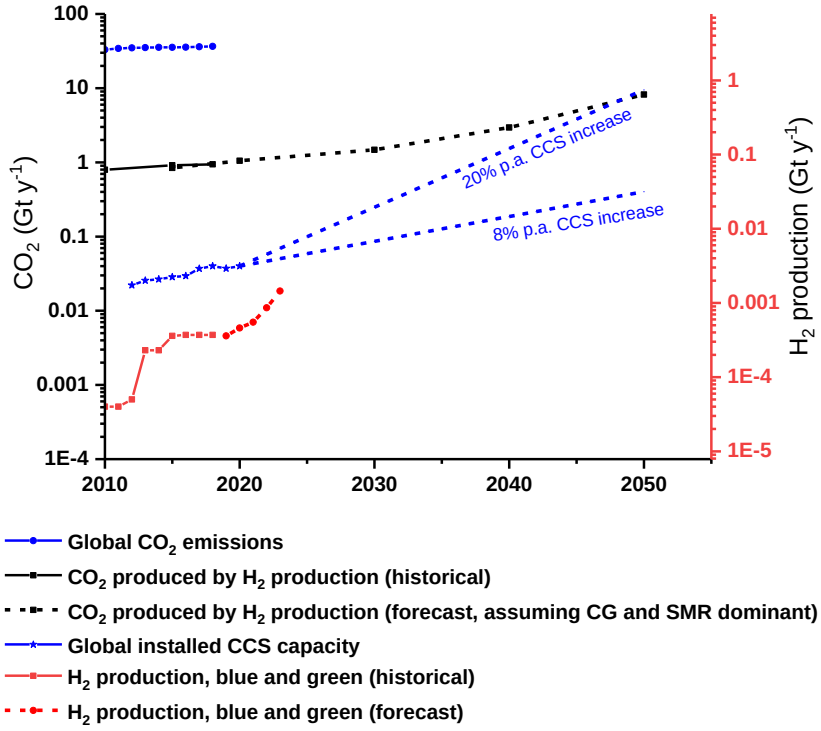

Figure 9. The carbon footprint of historical and forecast H_2 production. The CO_2 output is calculated as 12.73x the mass of H_2 produced, as derived from Figure 7. Included are the global annual CO_2 emissions from all sources, the annual capacity of CCS, and the annual production of low-carbon H_2 (blue and green). The y-axes are scaled by a factor of 12.73 for ease of comparison. Data source for CO_2 emissions [16] with data published online at OurWorldInData.org. Retrieved from: 'https://ourworldindata.org/co2-emissions [Online Resource]. Data source for CO_2 produced by H_2 production, historical and forecast, calculated from [31]. Data source for global installed CCS capacity [32].

The historical and forecast increase in low-carbon H_2 production, as shown by the red plot in Figure 9, shows that the anticipated rate of growth in low carbon H_2 is greater than the growth rate of CCS capacity. Between 2025-2030 the rate of growth of low carbon H_2 production will become limited by CCS capacity if blue hydrogen is used exclusively. For these reasons, blue hydrogen may only be a short- to medium- term solution to decarbonisation [30]. It may be possible to produce H_2 at scale using existing

infrastructure, thus hurrying the onset of the hydrogen economy, but in the long-term, it will not keep up with the pace of anticipated demand.

1.3.2 Green Hydrogen

Green hydrogen is distinct from brown, grey or blue hydrogen in that it does not rely on fossil fuels at the point of H_2 production. Green hydrogen is produced almost entirely by water electrolysers; these are systems which apply a voltage between two plates submerged in water, causing the water to split into its constituent parts, O_2 and H_2. Water and electricity are the feedstock for this reaction. The reaction itself releases no CO_2; however, for the produced H_2 to be classed as truly green, the electricity must be drawn from renewable resources like solar or wind [3]. Water electrolysers, powered by renewables, splitting water into H_2 and O_2 with no CO_2 emissions, with the downstream H_2 combustion producing no CO_2, are the ultimate vision of the hydrogen economy [22,23]. Electrolysers are currently the only method of green hydrogen production that are technologically mature enough to be used at scale [30]. Other methods, such as biomass gasification with CCS [33], photocatalysis [34] and anaerobic digestion [35] are methods under development, however they are not yet mature enough for

[3] If electricity is drawn from the grid, the type of hydrogen would be an as-yet undefined colour. This does highlight that the 'colour' of hydrogen for a given process simply exists to categorize the methods and doesn't necessarily equate to one process being greener than the other. Although no new methods of hydrogen production have been discovered in the last decades, the types of feedstocks, both chemical and electrical, are now extremely varied. It has therefore been increasingly common practice to give a new colour to a particular method, such as 'turquoise' for methane pyrolysis, or 'pink' for electrolysis coupled to nuclear. These are only a few examples, and about nine generally accepted colours are categorized now. In the authors opinion, the simplicity and purpose of the colouring convention (to categorise environmental impact) has been lost because of the variety of colours. Green is certainly better than the environment than grey (because of the well engrained connection between the colour green and environmentalism), but is turquoise better than pink?

commercialization [36]. However, as the green hydrogen economy is still very small in comparison to the scale required of it, there may well still be a future place for these upcoming methods. The scale required of these green technologies is such that it is unlikely that one method will ever become predominant. Electrolysis does appear to be on track to become the dominant green hydrogen method though, as evidenced by both the last decade of rollout (Figure 10) and the pipeline of new electrolyser installations (Figure 11). There is international recognition of the importance of water electrolysers, and in the European Union (EU) alone there is now a roadmap to install 40 GW of electrolyser capacity by 2030 [37].

Unfortunately, electrolysis is currently a more expensive method of producing H_2 than CG or SMR, with or without CCS (Figure 8), and there are two reasons for this. First is the capital cost of electrolysers, which are typically in the range of 1000 – 2300 € $kW^{-1}_{electrical}$. Electrolysers are typically 60 - 82 % efficient in converting the electrical energy into H_2 (thermal energy) [38], and so the capital cost in terms of thermal energy is approximately 1220 – 3800 € $kW^{-1}_{thermal}$ at the extremes. SMR, in contrast, has been reported to cost 333 € $kW^{-1}_{thermal}$, and up to 380 € $kW^{-1}_{thermal}$ with CCS [39]. The upfront costs of electrolysis are therefore substantially higher than those of grey or blue hydrogen production. Predictions of the capital cost of electrolysis for the year 2030 are in the of range of 500 – 1000 € $kW^{-1}_{electrical}$, and so bring electrolysis closer to SMR. The high capital cost can however be addressed with long operational lifetimes, and commercial electrolysers are predicted to have lifetimes in excess of 60,000 h by 2030 [38].

The second cause of high green hydrogen prices relates to the use of renewable electricity sources. Historically, wind and solar electricity were not cost-competitive when compared to fossil fuel electricity, so the operating cost of electrolysers were always high. This is no longer the case, and onshore wind and solar electricity are now beginning to outcompete fossil fuel electricity (Figure 3). The prices of these resources are still on downward trajectories, and so the price of green hydrogen is expected to reduce further. The culmination of the reducing feedstock costs, reducing capital costs and long system lifetimes means that green hydrogen is becoming cost competitive. It has been estimated by the European Commission that green hydrogen will become cost-competitive with grey, in areas where the electricity supply is cheap, as soon as 2030 [40].

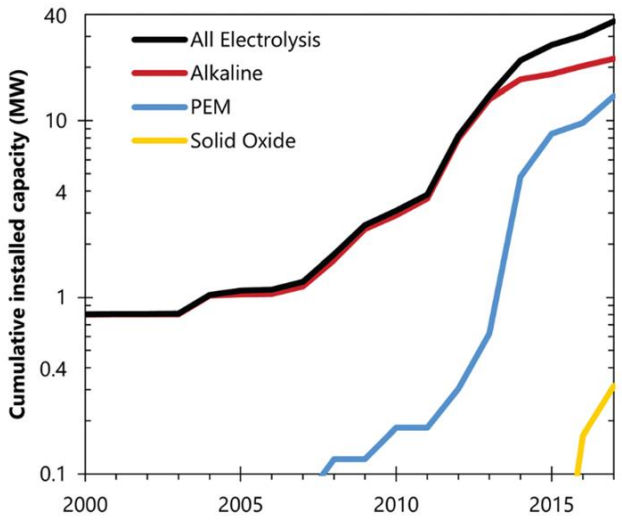

Figure 10. The nameplate electrical capacity of water electrolysers installed worldwide 2000-2017. Note this figure is electrical capacity and not the H_2 production capacity. Graph sourced from [41].

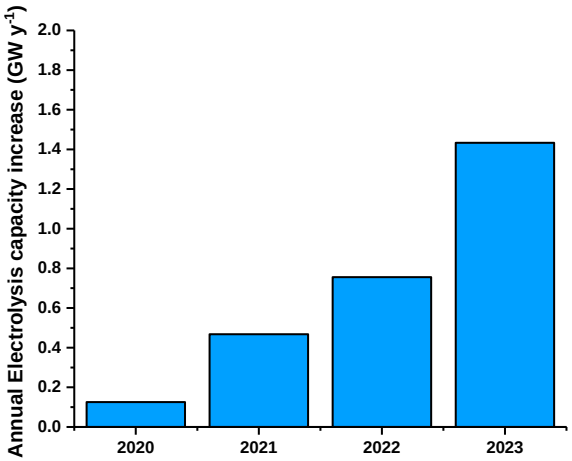

Figure 11. Increase in water electrolysis capacity 2020-2023, covering all types of electrolysis. Note this figure is electrical capacity and not the H_2 production capacity. Data source – IEA [28].

1.4 The Electrolysis of Water for Hydrogen Production

Water electrolysis is one of the oldest known electrochemical reactions. Troostwijk and Deimain first observed the splitting of water into O_2 and H_2 in 1789, a date which predates even the invention of the Volta Pile and the advent of electrochemistry as a separately identified scientific discipline [42]. Troostwijk and Deiman observed that the discharging of electricity between two gold electrodes in water produced gas at each electrode [43]. In 1800, Nicholson and Carlisle deduced that the product gases in this reaction came from the decomposition of water (Equation (4).

$$\mathrm{H_2O} \rightarrow \frac{1}{2}\mathrm{O_{2(g)}} + \mathrm{H_{2(g)}} \quad (4)$$

This reaction is the basis of all water electrolyser technologies, and the observations on the gold electrodes are fundamentally the same regardless of the specific electrolysis technique. On one electrode (the anode) O_2 is produced, and on the other electrode (the cathode) H_2 is produced. The volumetric ratio of H_2 to O_2 is 2:1, reflecting the molecular structure of water. Practically, there are several distinct routes to which this overall water splitting reaction can be achieved. Within the field of electrolysis there are three methods that, as of 2020, are promising candidates for commercialization: alkaline water electrolysis (AWE), polymer electrolyte membrane water electrolysis (PEMWE) and solid oxide electrolysis (SOEC).

1.4.1 Alkaline Water Electrolysis

AWE was the first electrolysis technique to find industrial use, with the first recorded application being in the 19th century to produce H_2 feedstock for ammonia synthesis. The defining feature of AWE is the use of a caustic electrolyte, typically sodium or potassium hydroxide, to allow for ionic transport between the electrodes. Due to its history of use, AWE is regarded as the most technologically mature electrolysis process. AWE is known to exhibit long lifetimes (>90,000 h) with performance in the range of 0.2 - 0.4 A cm^{-2} [44]. The primary benefit of AWE is that it is made using relatively inexpensive materials such as iron, nickel, and cobalt, which is possible due to an electrochemical environment that is less corrosive relative to PEMWE. AWE systems are currently the most widespread type of electrolyser, with approximately 20 MW of capacity installed by 2017 (Figure 10). A typical AWE electrolyser cell design is given in Figure 12.

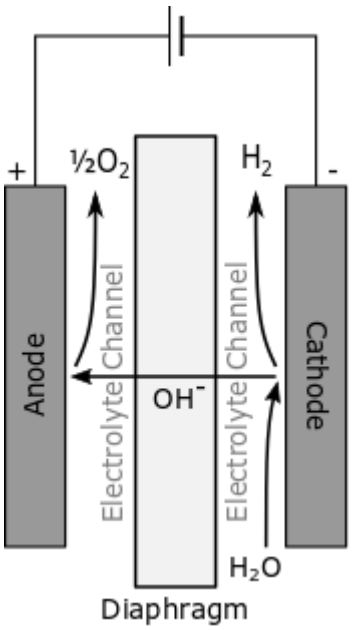

Figure 12. Typical setup of an AWE cell

In AWE systems, the electrodes are separated both by flow channels and a semi permeable diaphragm. The flow channels allow for the movement of electrolyte and water across the electrodes whilst also removing the product gases from the cell. The diaphragm is typically a material made of chemically treated asbestos [45], or more recently, Zirfon® [46]. Electrolyte permeates into these materials to allow ionic transport, but do not readily allow the permeation of gas. One of the essential functions of any electrolyser is the complete separation of the product gases, both for gas quality reasons and for safety, so stopping cross permeation of gases is essential. As the diaphragm is not entirely gas permeable, it is necessary to operate conventional AWE systems with no pressure differential between the anode and cathode. Ensuring this is one of the major considerations of AWE systems [47].

In electrolysis, the water splitting reaction, shown in Equation (4, is the product of two distinct electrochemical half-reactions, with one half reaction occurring at each electrode. In AWE the half-reactions are as follows:

Anode $$2\mathrm{OH}^- \rightarrow \frac{1}{2}\mathrm{O}_2 + \mathrm{H}_2\mathrm{O} + 2\mathrm{e}^- \quad (5)$$

Cathode $$2\mathrm{H}_2\mathrm{O} + 2\mathrm{e}^- \rightarrow \mathrm{H}_2 + 2\mathrm{OH}^- \quad (6)$$

The reaction therefore follows with the formation of the hydroxide intermediate, which migrates from the cathode through the electrolyte and diaphragm, to the anode. In AWE it is common to use catalysts on the electrodes to improve the kinetics and efficiency of the reaction. Precious metal catalysts, such as iridium oxide (IrO_x) and platinum (Pt), are considered to be the highest performance catalysts for the AWE half reactions shown in equations (5 and (6 [48], however they are not widely used due to their high costs. Therefore typical AWE catalysts, such as high surface area Ni or Co oxides, are used for the oxygen evolution reaction (OER) at the anode, and Ni for the hydrogen evolution reaction (HER) at the cathode [49].

A comparison of AWE with PEMWE and SOEC shows that, for the same area of cell, AWE is generally the poorest performance electrolysis method (Figure 13). When operating at equivalent efficiencies, the specific H_2 production is between a quarter and half that of PEMWE [50]. This poorer efficiency is due to the cell having (1) higher ohmic losses than PEMWE due to the relatively longer pathway that the hydroxide ions have to migrate, and (2) mass transport effects caused by the blockage of catalytic sites by the gas bubbles [50]. Finally, the caustic electrolyte used in AWE has the potential to react with atmospheric CO_2 to form insoluble carbonates, both reducing the conductivity of the electrolyte and leading to possible blockages of components of the cell or supporting equipment [51]. There is a major benefit to using a liquid electrolyte however, which is

that it is easily replaced if it becomes contaminated. This is in comparison to the use of a solid electrolyte, where contamination becomes a much more substantial issue, often requiring the replacement and reconditioning of the electrolyser cell.

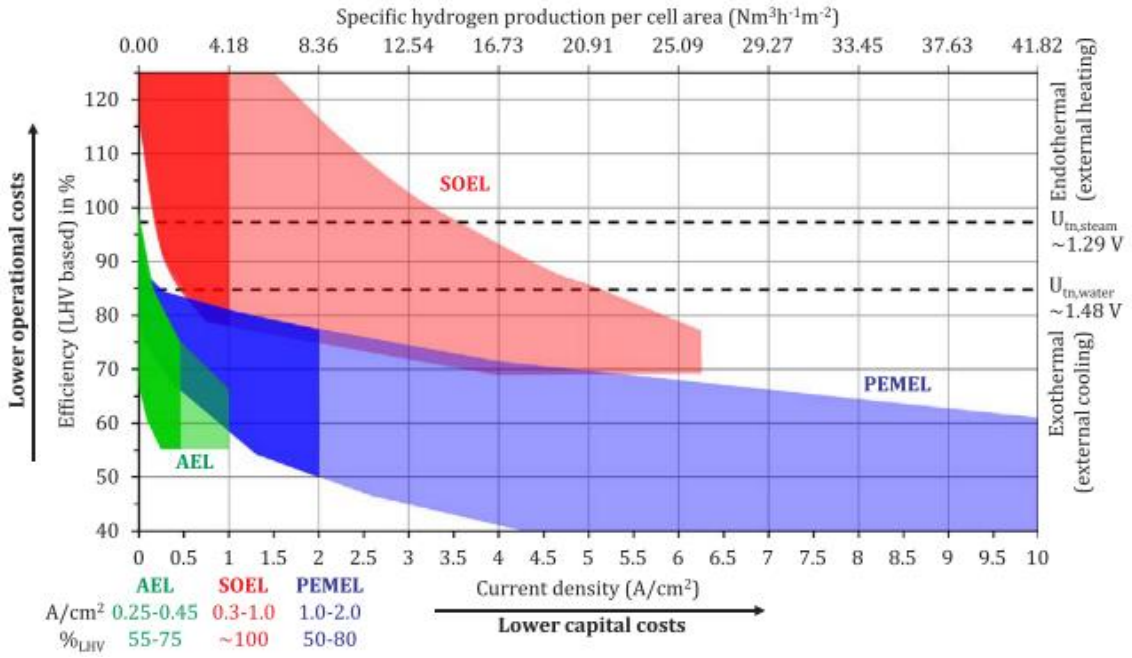

Figure 13. The efficiency range and the current density operational range of AWE (AEL), PEMWE (PEMEL) and SOEC (SOEL). Higher current density range results in a higher amount of H_2 produced per unit area of electrolysis. A lower efficiency comes from a higher voltage, showing that an increasing amount of power goes into heating. Graph from [52].

AWE is still a technology with scope for improvement, and there have been some recent advances in the field that address some of its limitations. One of the most promising recent improvements has come with the invention of 'zero-gap' AWE, a method which uses thin membranes in replacement of the diaphragm, and porous electrodes in replacement of solid electrodes [53,54]. The use of porous electrodes and the membrane allows for the space between the electrodes to be narrowed, as the product gases can diffuse through the electrode and into the channels outside of the electrochemical area, rather than being contained by the solid electrodes. The distance

between electrodes is therefore reduced from approximately 2 mm in conventional AWE to 0.5 mm in zero-gap AWE [54]. This reduces the path length for ionic transport and thus reduces ohmic losses. With reduced gap between the electrodes, the membrane must be more gas impermeable than the conventional diaphragm, however. This can be made possible with the use of an anion exchange membrane (AEM), a solid polymer containing cations that are bound to the polymer. This makes the membrane conductive to the hydroxide ions but impermeable to gas. 'Zero-gap' AWE has achieved improved performance over conventional AWE, with reports of voltages of 1.85 V (80 % efficiency based on higher heating value (HHV) or 66 % efficiency based on lower heating value (LHV)[4]) at 2 A cm^{-2}, operating in the performance range of PEMWE [55]. Additionally, it has been shown that zero-gap AWE systems may operate with reduced electrolyte concentrations with adequate performance [56], and even in pure water alone, relying on the AEM alone to achieve the ionic contact between the electrodes, albeit with substantially reduced performance [57]. Whilst a highly promising innovation, zero-gap AWE is not fully technologically mature, as numerous uncertainties remain over the long-term stability of the AEM. Lab-scale tests have shown that they may be operated for several hundreds of hours only [57], still well short of the lifetimes required of commercial AWE systems. Finding a stable AEM formulation has therefore become on the of primary focuses in AWE research in recent years, both for alkaline electrolysis and alkaline fuel cells [56,58].

[4] The distinction between the LHV and HHV in the context of water electrolysis is the difference between calculating the efficiency from the reversible cell voltage (LHV) or the thermoneutral voltage (HHV). These terms are clarified in Section 2.1.1.

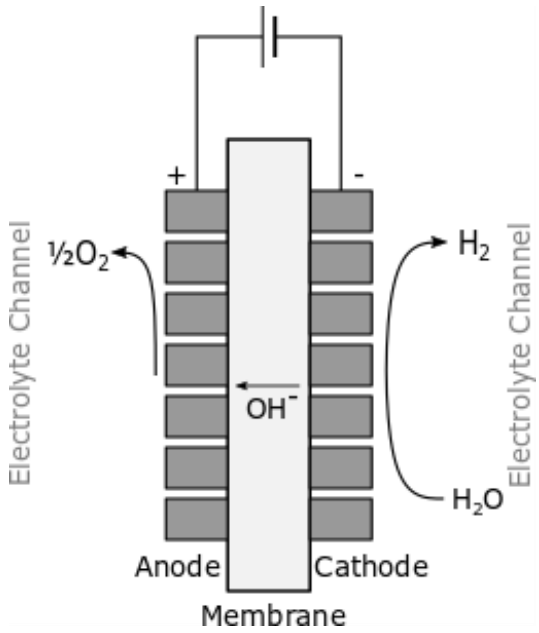

Figure 14. 'Zero-gap' AWE, with the anion exchange membrane sandwiched between porous electrodes.

1.4.2 Solid Oxide Electrolysis

Of the three electrolysis methods discussed, solid oxide electrolysis (SOEC) is the least commercially adopted electrolysis technique and is still largely a subject of research and development. SOEC is distinct from AWE and PEMWE in that it operates at temperatures typically well above the boiling point of water, normally 500 – 1000 ^{o}C, and so the reaction follows with the electrolysis of steam as opposed to liquid water [59,60].

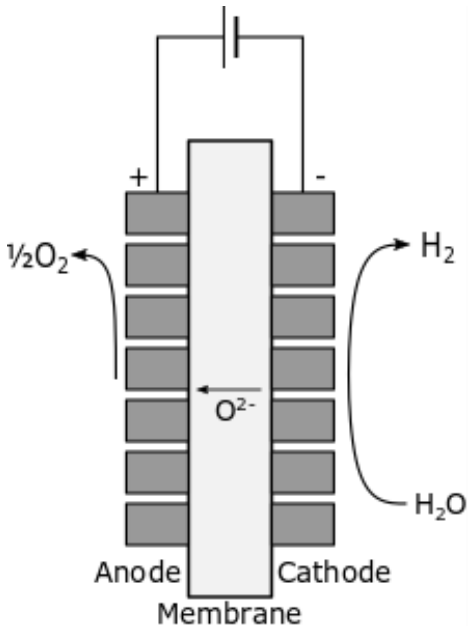

Figure 15. Typical setup of a solid oxide electrolyser cell

The high temperature of operation necessitates the use of ceramics, and so the typical construction of a SOEC is a lanthanum strontium manganite (LSM) supported on yttria-stabilized zirconia (YSZ) anode, a YSZ electrolyte membrane and a YSZ-supported Ni cathode [61–63]. The electrolysis reaction in SOEC proceeds with the reduction of water at the cathode, producing H_2 and the double-negatively charged O^{2-} ion. The O^{2-} migrates through the YSZ membrane and is oxidized at the anode producing O_2.

Anode $$O^{2-} \rightarrow \frac{1}{2}O_2 + 2e^- \quad (7)$$

Cathode $$2H_2O + 2e^- \rightarrow H_2 + O^{2-} \quad (8)$$

The main benefit of SOEC is that, at the elevated temperatures at which it operates, the water electrolysis reaction becomes much more efficient than at low temperature. SOEC systems can operate at high specific H_2 production rates above 100 % HHV efficiency

(Figure 13), effectively meaning that the electrolyser can cool during operation [5]. The major benefit of SOEC may therefore come with its ability to utilise excess heat from industrial processes to produce cheap green hydrogen. Additionally, the high temperature of operation makes SOEC a more versatile system than PEMWE or AWE, as SOEC can perform other reduction reactions besides the reduction of water. Notably, it has been shown that SOEC is able to reduce CO_2 in a co-electrolysis reaction with water, producing CO and H_2, both useful feedstocks for the formulation of synthetic fuels [64,65].

SOEC is not a fully mature technology however, and to date there has only been limited commercial rollout in comparison to the other electrolysis methods (Figure 10). Literature sources place the lifetime of SOEC systems currently in the hundreds [66,67] to thousands of hours [68,69], and so SOEC may still not be economical due to their short lifetimes. The high degradation rates have been attributed to numerous phenomena, such as the inactivation of the anode by the intercalation of chromium from the stainless steel supporting materials [66], and the delamination of the anode from the electrolyte due to the internal O_2 pressures acting at the anode - electrolyte interface [70]. Grain and void formations within the YSZ electrolyte have also been identified and shown to increase the ohmic resistances over several thousands of hours operation [68]. The cathode can also undergo degradation under high partial pressures of steam. The Ni catalyst reacts with the steam to form volatile Ni (II) hydroxide, leading to its reduction and redeposition at the cathode, forming a high density (less porous)

[5] An explanation for this is given in the Section 2.1.

cathode electrode with reduced electrochemically active surface area (ECSA) [71]. Finally, the thermal cycling of the cell from ambient to operational temperatures is known to induce stress fracturing of the SOEC materials [72].

1.4.3 Polymer Electrolyte Membrane Water Electrolysis

AWE remained the unchallenged electrolysis method until the 1950s, when Grubb and Neidrach from General Electric developed polymer electrolyte membrane water electrolysis (PEMWE) [73]. PEMWE differs from AWE in the key aspect that the reaction occurs in a solid acid as opposed to a caustic solution, and the half reactions occurring at the electrodes produce migrating protons instead of hydroxide ions. The essential difference therefore is that PEMWE is an acidic system whereas AWE is alkaline. State-of-the-art PEMWE systems are noted for having superior specific H_2 output than AWE (Figure 13) with reported lifetimes in excess of 20,000 h [44]. The response time is another important factor for electrolysers due to their potential for use in grid balancing [74], and PEMWE is generally regarded as being the most suitable application for this process. Response time can be categorized in three manners – the response time for an electrolyser to come to its nominal performance from a shut-down state, the response time to a variation in load, and finally the response time for the change in load to cause a stabilized change in the hydrogen output. In the case of response time for an electrolyser to come from a fully shut down state to fully operational, this is usually a few minutes for PEMWE [52,75,76]. For AWE however, this can be up to an hour if starting from cold [52]. In this case, the faster response time for PEMWE comes from the fact that it is capable of more rapid self-heating. From cold, a PEMWE can operate at higher current density than AWE, with the effect of this being that PEMWE can be

more exothermic than AWE at low temperature. The result is a greater self-heating rate up to the nominal operational temperatures and so has a faster response time. The second and third response times to consider are the responses to power fluctuations when operational. For PEMWE this response time is typically 50 ms, whereas for AWE this can be up to 2 s [52]. The cause of this is the double layer capacitance that exists in all electrochemical systems, and with power fluctuations this double layer capacitance charges or discharges. This prevents immediate change in potential with a change in current density, and so there is a delay between the current changing and the hydrogen production rate changing also. The response time is therefore affected by both the capacitance of the system and the current density. As PEMWE operates at higher current density and has a generally lower double layer capacitance than AWE the response times are typically shorter in PEMWE than AWE [52,75,76].

The half reactions that occur in PEMWE are as follows:

Anode $$\mathrm{H_2O} \rightarrow \frac{1}{2}\mathrm{O_2} + 2\mathrm{H^+} + 2\mathrm{e^-} \quad (9)$$

Cathode $$2\mathrm{H^+} + 2\mathrm{e^-} \rightarrow \mathrm{H_2} \quad (10)$$

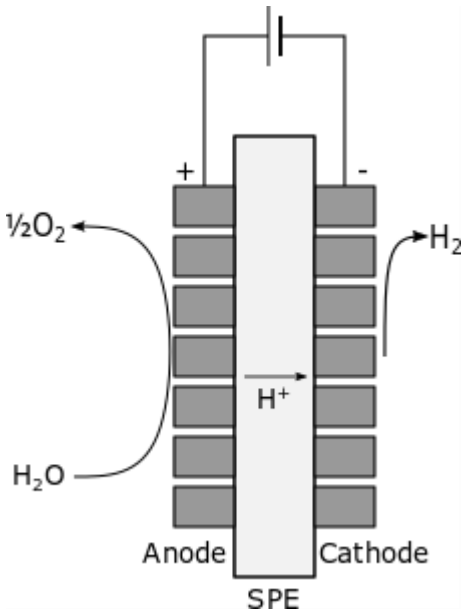

Figure 16. Typical setup of a PEMWE cell containing an iridium oxide or iridium-ruthenium oxide anode catalyst, Nafion® SPE and Pt based cathode catalyst.

The electrolysis reaction in the case of PEMWE proceeds with the oxidation of water at the anode, releasing O_2, protons and electrons. The protons then migrate through the solid polymer electrolyte (SPE) and reduce at the cathode, forming H_2 (Figure 16). As in AWE and SOEC, catalysts are used to improve the kinetics of the reaction. The state-of-the-art materials used in PEMWE include IrO_x and iridium-ruthenium ($IrRuO_x$) mixed metal oxides (MMOs) [77,78]. At the cathode, PtB or Pt/C are used [79]. The SPE is a branched fluoropolymer containing an anionic backbone, typically Nafion® or, less commonly, Aquivion® [80]. One of the major drawbacks of PEMWE in comparison to AWE is its highly acidic nature caused by the SPE. This creates a highly corrosive environment that necessitates the use of corrosion resistant materials, usually titanium substrates coated with Pt. This in turn drives up the cost of the system, and so PEMWE systems are more expensive than AWE per unit area. This however is offset by the substantially higher current density that can be achieved with PEMWE (Figure 13), and

so a comparison of the capital cost per kW of electrolysis puts the costs in a more comparable perspective (Figure 17).

Although the errors in estimations of capital cost in Figure 17 are rather wide, there are some clear general trends. Firstly, SOEC is estimated to be the most expensive electrolysis method in 2020 and 2030, likely owing to the uncertainty of material use and its specific H_2 production rate. Uncertainty is reflected in the range of capital cost estimates also, with the lower percentile estimates coming close to the range of AWE and PEMWE. Secondly, AWE is the most cost-effective method currently, and has lower capital cost estimates in all categories. The difference in values is not major however, and advances in the performance and efficiency of PEMWE systems may bring it close to AWE. In the study in which these values were obtained, the experts also were polled in a prediction of which electrolysis method would be the most suitable in 2020 and 2030 (within the case study postulated by the report, a 10 MW electrolyser delivering intermittently into the gas grid at 20 - 30 bar). In 2020, AWE came top of this poll, followed by PEMWE. In 2030 however, PEMWE was clearly regarded as being the most suitable, with SOEC following. The view that AWE has a diminishing role may reflect the view that conventional AWE has reached the zenith of its performance, whereas the performance of PEMWE and SOEC is still improving.

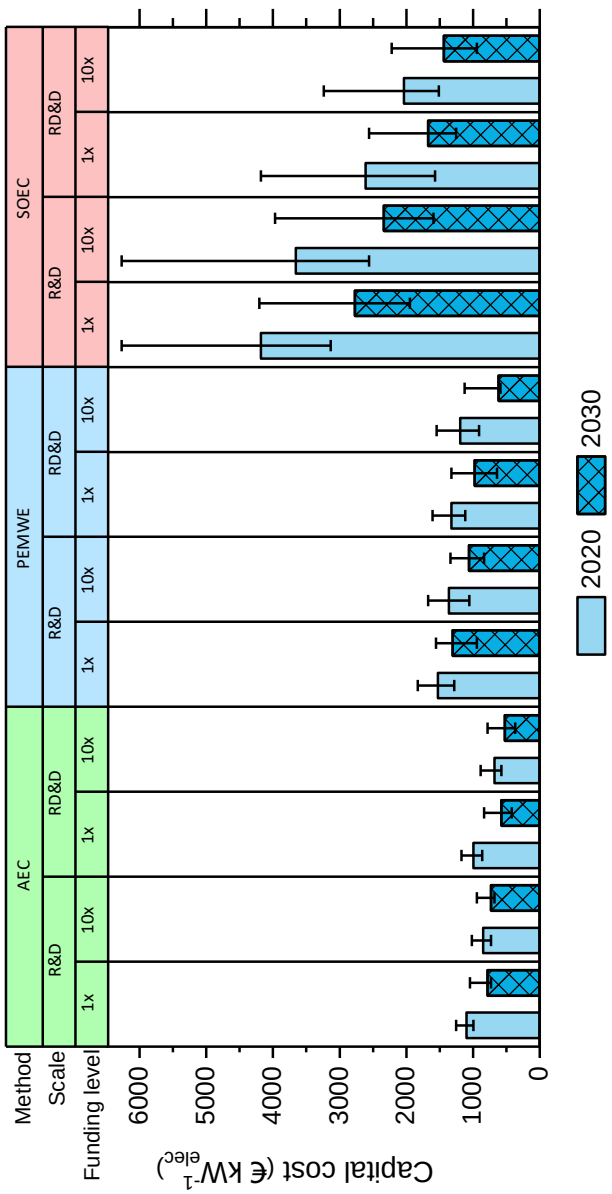

Figure 17. 2016 estimate of capital cost (capex) in euros per kW of electrolysis for the years 2020 and 2030 for AWE, PEMWE and SOEC. This estimates several possible scenarios in which capex may be affected. First is capex scenario with the level of R&D funding received, 1x and 10x 2016 level. Also estimated are the scenarios where the capital costs are reduced by the economies of scale-up. R&D is capex with only small-scale rollout whereas RD&D (research, development and deployment) has the benefits of scale. Presented are the mean values of several expert estimations, with the lower and upper error bars representing a mean of the 10th and 90th percentiles. Values from [38] and adjusted for inflation to 2020 values by multiplying by a factor of 1.054.

1.4.4 The Future of Electrolysis

In the 2020s and moving into 2030s, PEMWE and AWE are going to both be widely used for grid balancing and for vehicle refuelling. The likelihood is that the global PEMWE capacity may reach that of AWE, or even overtake it. Whilst PEMWE capital cost may remain greater than AWE per unit area, the performance of PEMWE can still be improved upon. In conventional AWE, however, there doesn't seem to be scope for substantial further improvements to its performance. If the hydrogen economy is to be fully realised, it seems highly likely that both AWE and PEMWE will have roles. The difference in AWE and PEMWE system cost and performance is predicted to be small, and the potential scale of the hydrogen economy (and the urgency for it) is so large that it will likely mean that large volume manufacturing of both will be needed. The fact that AWE and PEMWE draw from differing stocks of raw materials would also be a strength for a hydrogen economy using both methods. A limitation in supply of Pt, for example, would affect PEMWE and PEM fuel cell (PEMFC) production; however, it would not affect AWE, and so rollout of electrolysis would continue with a greater emphasis on AWE production. Likewise, if Ni or Co were to become scarcer, then PEMWE would be able to take up a larger role. The availability of Ir in PEMWE is a well-recognized concern that may also limit PEMWE rollout at very large scales, and it is predicted to become a bottleneck that must be remedied by (1) doubling the mining production of iridium, (2) reducing the amount of iridium used in the electrolyser by fivefold and (3) recovering and recycling up to 90% of the catalyst. Without these implemented the maximum installation rate of PEMWE systems was calculated at approximately 2 GW p.a. With full implantation of the remediations, the production capacity of PEMWE system can be up to 8 GW p.a.

With further development, and the solving of the aforementioned stability issues, SOEC may come to play an increasingly important role in the hydrogen economy also, especially in areas where cheap renewable electricity and waste heat may be harnessed together. This, however, is reliant on solutions to the aforementioned issues being found. Zero-gap AWE, along with some other electrolysis methods that have not been mentioned in detail (bipolar membrane water electrolysis [81], proton conducting solid oxide electrolysis [82] and biological electrolysis [83] for example) are still in active research and development and are presently not close to commercialization. As such, it is not possible to make a reasonable estimation about their role in the hydrogen economy as the key parameters such as lifetime, performance and capital cost are not known.

To meet the Paris Agreement, the 2020s and 2030s are the decades where the unrelenting rise in atmospheric CO_2 concentration (as seen Figure 2) must be stopped. This gives up to 20 years for the green technologies such as electrolysis, fuel cells and batteries, to transition from their current niche market to use on a global scale. The long development times of new green technologies may preclude their adoption in this early part of the transition. Those that are now mature or maturing are therefore almost certain to see at least some use on very large scales. This means that PEMWE, AWE, PEMFC and battery technologies will find widespread use.

2 Theory of Water Electrolysis

2.1 The Thermodynamics of Water Electrolysis

2.1.1 Reversible Cell Voltage and Thermoneutral Voltage

Electrochemical water splitting is fundamentally constrained by the laws of thermodynamics. In theory, a reaction, such as that between H_2 and O_2, will radiate the same quantity of energy regardless of the method of the reaction. On combustion, the energy is released as heat, whereas in an electrochemical cell with the same overall reaction, the energy is released primarily as electrical power. The maximum useable energy that is released from a reaction is called the Gibbs free energy. The Gibbs free energy is expressed in equation 11a with the Gibbs free energy under standard conditions given in equation 11.

$$\Delta G = \Delta G^{o} + RT \ln Q \tag{11a}$$

$$\Delta G^{0} = \Delta U^{0} + P^{0}\Delta V - T\Delta S^{0} \tag{12}$$

Where ΔG is the Gibbs free energy, R is the universal gas constant and Q is the quotient of the reaction (shown in Equation 23). ΔG^0 is the change in Gibbs free energy at standard conditions. In essence, Equation 11 is an expression of how, for any given reaction, the Gibbs free energy changes based on the balance of the reactants and products present in the chemical system. These equations express the maximum work that can be performed on by a thermodynamic system at constant pressure and temperature. This value is highly significant as it informs on whether a given reaction

will happen spontaneously or not. If $\Delta G > 0$ the reaction will not occur spontaneously and will require an input of energy, whereas a reaction with $\Delta G < 0$ will be spontaneous. At $\Delta G = 0$ the system will exist in thermal or electrochemical equilibrium. In this case the value of Q becomes the value of the equilibrium constant K, which is used in Equation 21.

ΔU^0 is the change in the internal energy at standard conditions. This is the intrinsic energy of the system, relating to bond strengths and random movements, rotations, and intermolecular interactions.

The $P^0\Delta V$ component is pressure at standard conditions (P^0) and the change in volume (ΔV). This component expresses the work done on the surroundings in terms of volume expansion or contraction. In the case of the $H_2 - O_2$ reaction, the change in volume is negative, from 2 moles of H_2 gas and 1 mole of O_2 to 2 moles of liquid water or water vapour. This equation assumes that there is no pressure change during the reaction, and so all the energy goes into volume change.

The $T\Delta S$ components is temperature (T) and the change in entropy (ΔS). This component expresses the energy provided by or released into the surroundings because of the change in the entropy of the system. Naturally, all things tend towards a state of high entropy (disorder), and any reaction which causes an increase in entropy (solid to liquid to gas, or a reaction which results in a greater number of molecules being produced) receives energy as a result. Conversely, if a reaction causes a reduction in entropy there is an energy penalty on the reaction.

When calculating the energy changes of a reaction, it has become practice to simplify Equation(12, as the values of ΔU^0 and $P^0\Delta V$ are specific only to the energy changes caused by the chemical reaction. They are typically summed in the following equation:

$$\Delta H_F^0 = \Delta U^0 + P^0\Delta V \quad (13)$$

ΔH_F^0 is the enthalpy of formation of a reaction. $P\Delta V$ in the case of water splitting is a minor consideration, requiring approximately -3.72 KJ mol^{-1} of work under standard conditions. For simplification therefore, ΔU^0 and ΔH_F^0 can be approximated to be the same value. Substituting Equation (13 into (12 gives the familiar Gibbs free energy equation:

$$\Delta G^0 = \Delta H_F^0 - T\Delta S^0 \quad (14)$$

In the case of water splitting, the standard enthalpy of formation is 285.83 KJ mol^{-1} [84]. This value is given per mole of water. As the reaction proceeds with the formation of one and a half gaseous molecules from one molecule of water, the entropy of the system increases. ΔS^0 of water splitting is 163.34 J K^{-1} mol^{-1}, so $T\Delta S^0$ is 48.68 KJ mol^{-1} at standard temperature.

$$\begin{aligned}\Delta G^0 &= 285.83\ \text{KJ mol}^{-1} - 48.68\ \text{KJ mol}^{-1} \\ &= 237.18\ \text{KJ mol}^{-1}\end{aligned} \quad (15)$$

ΔG^0 of water splitting is positive, so it therefore requires an input of energy to initiate the reaction. This of course applies equally well for an electrochemical reaction; an electrolyser will have to provide the equivalent amount of electrical energy to initiate the water splitting reaction, and the expression of this energy is voltage. The definition of voltage (or potential difference) is 'The work done per unit charge to move the charge between two points in an electric field'. In the case of an electrochemical cell, the two points can be considered the two electrodes, and so the voltage is directly correlated to the energy. Voltage is correlated to energy in the following equation:

$$E^0_{rev} = -\frac{\Delta G^0}{nF} \tag{16}$$

Where n is the number of electrons participating in the reaction, and F is the Faraday constant (96485 C mol^{-1}). Using ΔG^0 in this equation provides the absolute minimum voltage required to initiate this reaction under standard conditions. This is referred to as the reversible voltage (E_{rev}). As can be seen from Equations 9 and 10, per H_2O molecule it is a 2-electron reaction.

$$E^0_{rev} = -\frac{237180\ \text{J mol}^{-1}}{2 \times 96485\ \text{C mol}^{-1}} = -1.23\ \text{V} \tag{17}$$

-1.23 V represents the reversible voltage at room temperature. The negative value represents that this reaction is non-spontaneous and requires an input of energy for the reaction to proceed. In typical electrolyser convention, however, the voltages are generally expressed as positive. This is the voltage at which the products and reactants

will exist in equilibrium and is the absolute minimum voltage that a net electrolysis reaction will take place under standard conditions. As TΔS is positive, the reaction may proceed with an additional gain of energy from the surroundings, i.e. the system cools. This will occur until the cell voltage reaches the voltage of ΔH_F, defined in the same manner as E^0_{rev}:

$$E^0_{thermo} = \frac{\Delta H^0_F}{nF} \tag{18}$$

$$E^0_{thermo} = \frac{285830\ J\ mol^{-1}}{2 \times 96485\ C\ mol^{-1}} = 1.48\ V \tag{19}$$

E^0_{thermo} is the thermoneutral voltage and is the voltage at which there is no heat gained or lost from the system; the TΔS contribution is balanced by the cell's emission of heat due to the increase in the various resistances within the cell. At voltages greater than the thermoneutral voltage, therefore, the electrolysis reaction proceeds with the emission of heat into the surroundings.

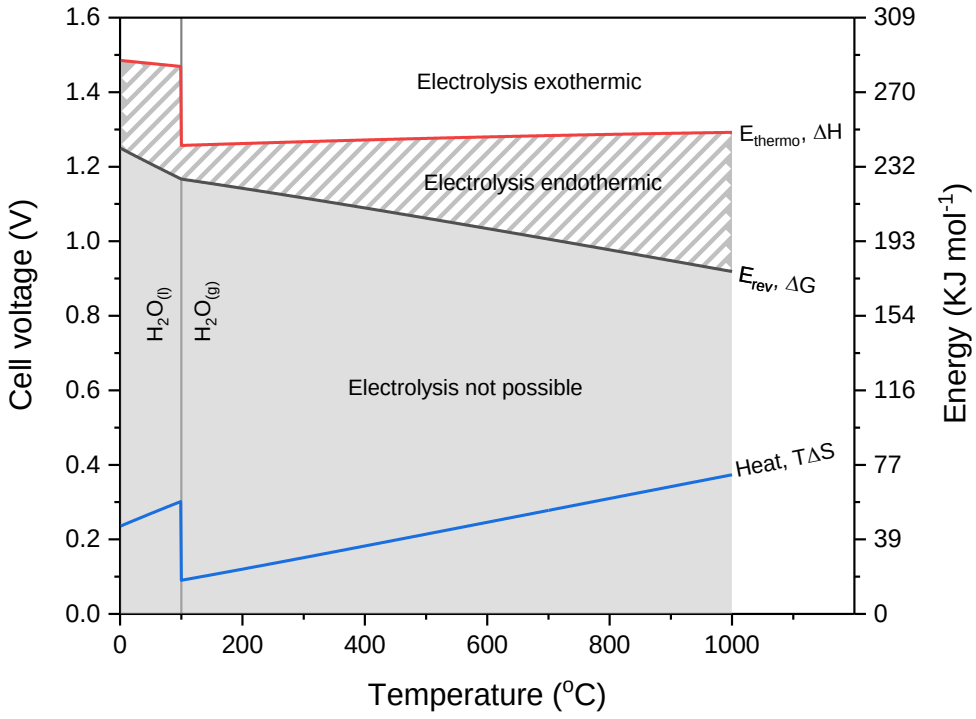

Figure 18. Reversible voltage and thermoneutral voltages of the water splitting reaction as a function of temperature.

Numerous elements of this thermodynamic system have a temperature dependency, as shown in Figure 18. Firstly, the water liquid - gas phase transition has an impact both upon the overall enthalpy of the reaction and its entropy. The enthalpy of formation decreases at this point, as the water splitting reaction does not also have to overcome the intermolecular forces of water in the reaction. In equal measure, the TΔS decreases due to the greater entropy of steam compared to water. With increasing temperature in the steam phase, the ΔS of reaction also slightly increases. This means that TΔS increasingly contributes to the overall reaction with temperature. As enthalpy also has a slight dependence on temperature, ΔH_F (E_{thermo}) increases slightly with temperature. This may be approximated using Kirchoff's law:

$$H_{F,T} = H_F^0 = c_p(T - T_0) \quad (20)$$

Where $H_{F,T}$ is the enthalpy of formation of the molecule at the temperature, and c_p is the specific heat capacity. To approximate the ΔH_F of the reaction, this must be calculated for all reactants and products. The result of the increase in $T\Delta S$ and ΔH_F is that the ΔG^0 (E_{rev}) of reaction decreases with temperature. This is where the effect of water splitting at high temperatures (SOEC) compared to low temperatures (PEMWE and AWE) is apparent. PEMWE and AWE operate in a temperature range where the kinetics of reaction at E_{thermo} are still poor. These cells therefore must be increased beyond E_{thermo} to get adequate reaction rates. Because of this, these cells are exothermic during operation. In high temperature electrolysis (SOEC) however, these systems can often get adequate reaction rates below E_{thermo} and so may be endothermic in operation. Considering this, the efficiency of an electrolyser may be calculated in two different ways: The voltage over E_{rev} (also called lower heating value or LHV) or over E_{thermo} (higher heating value or HHV). In low temperature electrolysis it is common practice to calculate efficiency in reference to E_{thermo}, as above this all energy supplied to the electrolyser is done so with electrical energy, not thermal energy. In SOEC, where a greater difference between E_{rev} and E_{thermo} exists, and as systems usually operate under E_{thermo}, efficiency is more often calculated from the voltage over E_{rev}.

2.1.2 Electrode Potentials

The overall reaction discussed so far explains the electrolysis reaction occurring as a whole. As already mentioned, in electrochemistry a reaction proceeds with two

separate half-reactions, an oxidation reaction and a reduction reaction, occurring on the anode and cathode respectively. The half-reactions have their own reversible potentials, and the overall reversible voltage is a sum of both. The half-reactions that occur for water electrolysis under standard conditions are the same as that for PEMWE:

$$E_{cell} = E^0_{anode} - E^0_{cathode} \quad (21)$$

Anode $H_2O \rightarrow \frac{1}{2}O_2 + 2H^+ + 2e^-$ $E^0(O_2 / H_2O) = 1.23$ V (9)

Cathode $2H^+ + 2e^- \rightarrow H_2$ $E^0(H^+ / H_2) = 0.00$ V (10)

Overall $H_2O \rightarrow \frac{1}{2}O_{2(g)} + H_{2(g)}$ $E_{cell} = 1.23$V (4)

These electrode potentials are the values given under standard conditions. The reaction in Equation (10 is the reaction that occurs on the normal hydrogen electrode (NHE), and so it is 0.00 V by definition. In PEMWE the conditions of water splitting are close to that of the NHE (although the exact conditions are not known). Electrolysers do not operate under standard conditions however; they vary both in temperature and the reactant and product concentration. As such, there can be a significant deviation from the standard potentials under standard conditions, especially when the cells are operated in high pH environments (as is the case in AWE). The half-cell potential at each electrode can be calculated by the Nernst equation:

$$E_{rev} = E^0_{rev} - \frac{RT}{nF}\ln Q \quad (22)$$

Where E^0_{rev} is the half-cell potential under standard conditions, and Q is the quotient of the reaction. (23 describes any given reaction, and the corresponding reaction quotient is given in Equation (24.

$$aA + bB \leftrightarrow cC + dD \tag{23}$$

$$Q = \frac{[C]^c[D]^d}{[A]^a[B]^b} \tag{24}$$

The reactants and products are calculated based on their concentration in solution or their partial pressure. For the anode half-reaction in Equation (9 the quotient of the reaction is as follows:

$$Q_{(O_2/H_2O)} = \frac{[H_2O]}{[H^+]^2\ pO_2} \tag{25}$$

Assuming standard conditions of unity pressure and a concentration of water of 1 mol, the quotient for the reaction becomes a factor of the proton concentration alone, and this can be fed back into the Nernst equation.

$$Q_{(O_2/H_2O)} = [H^+]^2 \tag{26}$$

$$E_{rev\ (O_2/H_2O)} = E^0_{rev(O_2/H_2O)} + \frac{RT}{nF} \times \ln [H^+]^2 \tag{27}$$

This equation can then be rearranged to calculate the half-reaction potential as a factor of pH.

$$E_{rev(O_2/H_2O)} = E^0_{rev(O_2/H_2O)} + \frac{\gamma}{n} \times \frac{RT}{F} \times 2.303 \times \log [H^+] \quad (28)$$

In this equation, the number of protons involved in the reaction is replaced with γ. Assuming the reaction occurs under standard temperature (298.15 K), Equation (28 can be written as follows:

$$E_{rev(O_2/H_2O)} = E^0_{rev(O_2/H_2O)} - \frac{\gamma}{n} \times 0.059137 \times pH \quad (29)$$

The same deduction can be applied for the cathode half reaction (Equation (10).

$$Q_{(H^+/H_2)} = \frac{pH_2}{[H^+]^2} \quad (30)$$

$$Q_{(H^+/H_2)} = [H^+]^2 \quad (31)$$

$$E_{rev(H^+/H_2)} = E^0_{rev(H^+/H_2)} - \frac{RT}{nF} \times \ln [H^+]^2 \quad (32)$$

$$E_{rev(H^+/H_2)} = E^0_{rev(H^+/H_2)} - \frac{\gamma}{n} \times \frac{RT}{F} \times 2.303 \times \log [H^+] \quad (33)$$

$$E_{rev(H^+/H_2)} = E^0_{rev(H^+/H_2)} - \frac{\gamma}{n} \times 0.059137 \times pH \quad (34)$$

Using Equations (29 and (34, the reversible potentials of the OER at the anode and HER at the cathode can be calculated over the pH range. This produces the pH – potential (Pourbaix) diagram of water (Figure 19).

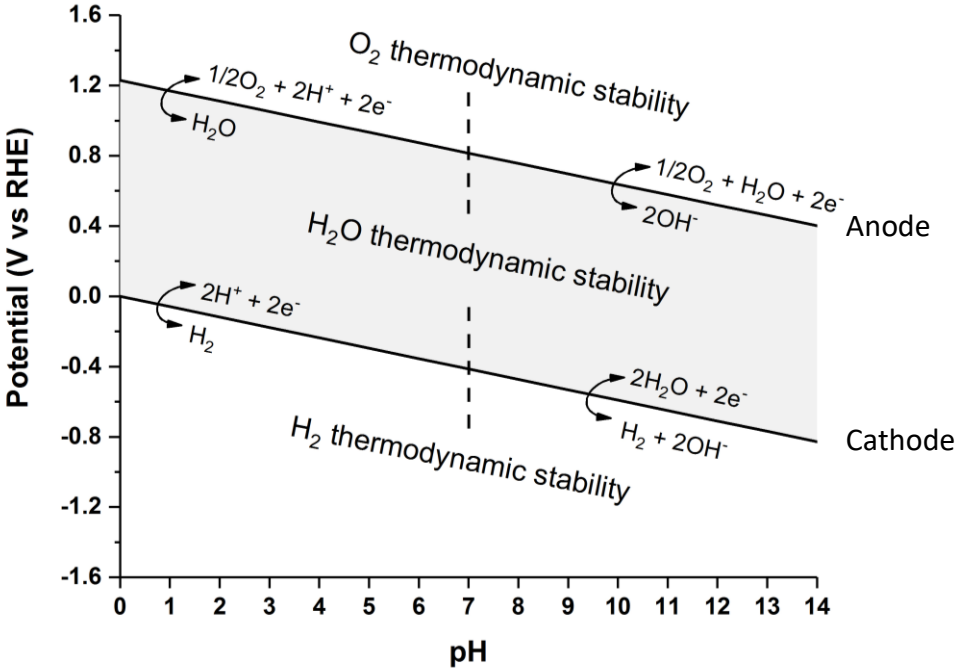

Figure 19. pH – potential (Pourbaix) diagram of water- The thermodynamically stable states of the water system over the range of pH and potential.

This graph expresses the thermodynamically stable species at any given pH and potential. The descending shaded band is the region in which water is thermodynamically stable, and above and below this are the thermodynamically stable species for O_2 and H_2 respectively. In acidic environments, the water splitting reaction proceeds with proton transport, whereas in alkaline media the reaction proceeds with the transport of hydroxide ions. In alkaline media (and in AWE correspondingly), whilst the potential difference remains unchanged, the reversible potentials for both OER and HER are substantially lower than in acidic media (PEMWE).

Anode $\quad 2\mathrm{OH}^- \rightarrow \frac{1}{2}\mathrm{O}_2 + \mathrm{H}_2\mathrm{O} + 2\mathrm{e}^-$ $\quad E_{rev}\,(O_2 / OH^-) = 0.40\ V$ (35)

Cathode $2H_2O + 2e^- \rightarrow H_2 + 2OH^-$ $E_{cathode}$ (H_2O / H_2) = -0.83V (36)

Overall $H_2O \rightarrow \frac{1}{2}O_{2(g)} + H_{2(g)}$ E_{cell} = 1.23V (4)

As already mentioned, E_{rev} represents the thermodynamic minimum potential at which the reaction can occur, but for higher reaction rates the electrode potentials must be more than this; greater than E_{rev} at the anode, and less than the E_{rev} at the cathode. In PEMWE, this places the anode electrode in a highly corrosive environment, as it is both at high potential and low pH. There are very few materials that are not susceptible to corrosion in this environment (Figure 20) [85]. Precious metals such as Pt and Ir undergo oxidation in this region; however, their oxidized species are not water soluble in this range, and form a thin surface oxide which is still conductive or semi-conductive [86,87]. The need for precious metals is one of the major disadvantages of PEMWE. In contrast, AWE does not have the same requirement for precious metals, as the reversible potential for OER is substantially lower whilst also being at high pH. This is a substantially less corrosive region, and so a wider range of materials may be used in AWE systems. Importantly, precious metals typically do not have to be used.

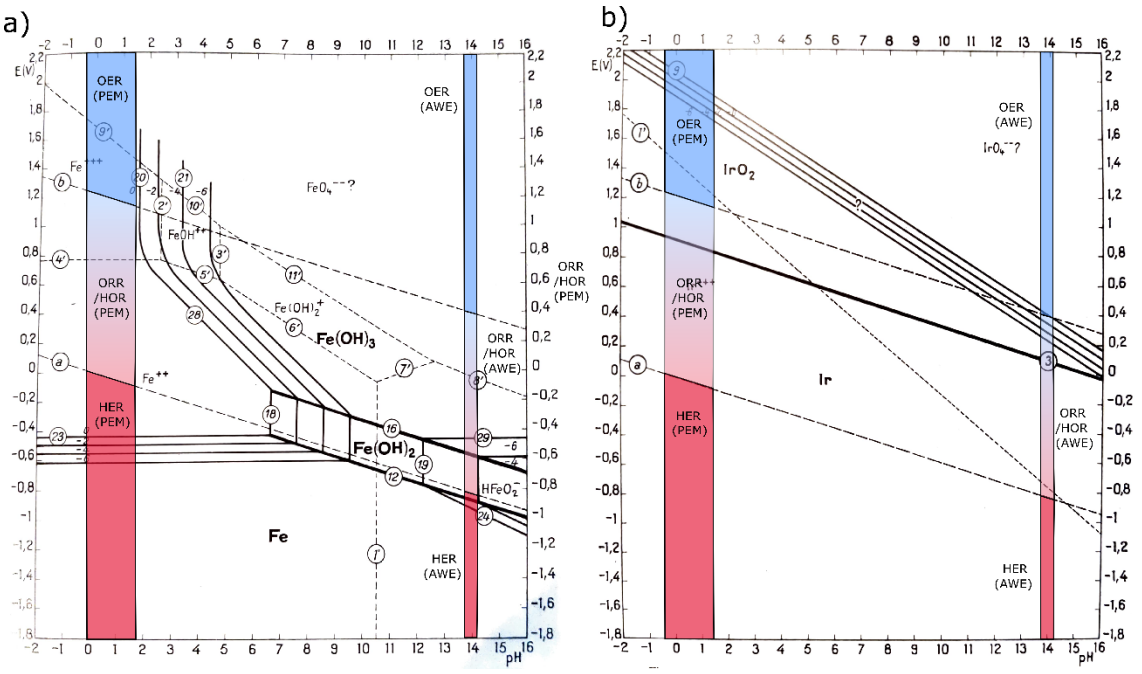

Figure 20. pH - potential (Pourbaix) diagrams of the thermodynamically stable states of a) Iron and b) Iridium. Included in this figure are approximations of the potential-pH range of electrodes during OER, HER, ORR and HOR. Pourbaix diagrams reprinted from [85].

2.2 Kinetics of Water Electrolysis

As is the case in all chemical reactions, in electrolysis there is both a thermodynamic element and a kinetic element. The thermodynamics of the reaction are unchanging; at a specific temperature, pH, and pressure there will always be the same E_{rev}. However, the kinetics of the reaction can vary greatly. With higher kinetics, more H_2 is produced per specific area per unit time, meaning that it can be made more cost-effective and with a smaller footprint. In electrolysis, the kinetics of the overall reaction can be altered in a substantial number of ways, predominantly using catalysts to facilitate the reaction.

In electrochemistry, the rate of a reaction is governed by the potential at which the reaction is occurring. Taking OER in PEMWE under standard conditions as an example, if the electrode has a potential below E_{rev} (O_2 / H_2O) no net reaction can occur, so there

is a zero rate of reaction. When the electrode is over E_{rev} (O_2 / H_2O) however, the rate of reaction becomes a factor of how far above E_{rev} (O_2 / H_2O) the electrode potential is.

$$\eta = E - E_{rev(O_2/H_2O)} \tag{37}$$

η is the electrode overpotential in this equation and E is the electrode potential. The rate of reaction rises exponentially with overpotential, and can be calculated using the Tafel equations (Equations 37 and 38) and Butler-Volmer equation (Equation (40). E_{rev} (O_2 / H_2O) is, by definition, the potential at which the oxidation reaction (OER) and reduction reaction (ORR) occurs in equal quantities on the electrode. When calculating the kinetics of the reaction, the reverse reaction must therefore also be considered. At high overpotentials, the rate of reaction is almost entirely dominated by OER (the forwards reaction). At low overpotentials however, the rate of reaction is dependent also on the rate of the reverse reaction occurring. At potentials below 1.23 V, the backwards reaction (ORR) is the dominant mechanism in the reaction, which increases with a decreasing potential. This relationship is expressed as follows:

OER $$i_a = i_o \exp\left(\frac{\alpha_0 nF}{RT}\eta\right) \tag{38}$$

ORR $$i_c = i_o \exp\left(\frac{\alpha_r nF}{RT}\eta\right) \tag{39}$$

Combined $$i = i_a - i_c = i_o \exp\left(\frac{\alpha_o nF}{RT}\eta\right) - \exp\left(\frac{\alpha_r nF}{RT}\eta\right) \tag{40}$$

In these equations are two important new parameters: the charge transfer coefficients, α_o and α_r, and the exchange current density, i_o. For electrolysis, the charge transfer coefficient is a measure of the efficiency of the catalyst in facilitating the reaction. It is a dimensionless quantity between 0 and 1. In single electron-reactions, this value is an expression of the reaction symmetry, essentially a measure of whether the transition state of a molecule during a reaction is more reactant-like or more product-like. It usually has a value between 0.3 - 0.7 in these cases [88]. In multi-electron processes, such as OER and HER, the reaction proceeds with not a single electron step but several steps in progression, resulting in one or several reaction intermediates. The activity coefficient then becomes an expression of multiple factors of the reaction, such as the number of steps involved, the number of electrons transferred before and during the rate determining step, and the reaction stoichiometry [89]. As is shown in Figure 21, the complete Butler-Volmer equation (Equation (40) is essential in determining reaction rate at low overpotential due to the high rate of the reverse reaction occurring. At high overpotential however, the reverse reaction becomes negligible, and so can be approximated using Equations (38 or (39 only.

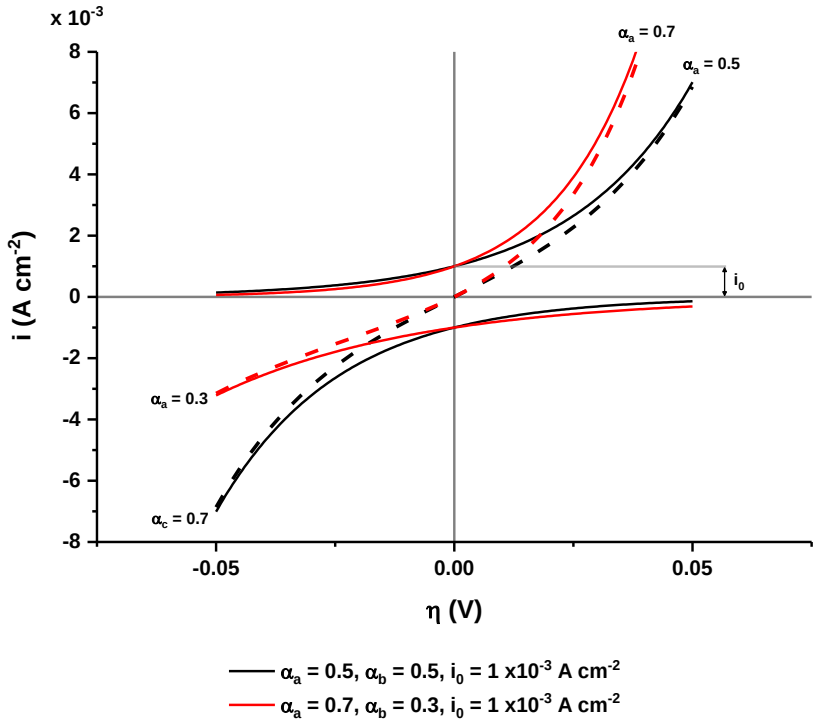

Figure 21. Differing charge transfer coefficients on the outcome of the Butler-Volmer equation and the net reaction rate (dotted line). Exchange current density is the current of the oxidising or reducing reaction at zero overpotential, the voltage at which the oxidising and reducing reaction rate is equal.

The exchange current density, i_o, is a measure of the rate of reaction occurring in the oxidising and reducing direction when the system is in equilibrium. i.e. there is no net reaction taking place. The potential at which this occurs is the reversible potential of the reaction. The value of the exchange current density is dependent both on the reaction occurring and the on the nature of the electrode itself, and as a result can vary widely. For example, HER on a polycrystalline Pt electrode has an exchange current density measured at 10^{-3} A cm^{-2} under standard conditions, whereas HER on Hg under the same conditions is in the region of 10^{-12} [90,91]. The impact of i_o on the rate of HER is shown in Figure 22. As can be seen, although the charge transfer coefficients are similar, Hg is a far poorer catalyst for HER relative to Pt due to the extremely low exchange current

density. To obtain the same reaction rate on Hg as on Pt, the electrode would have to be at an overpotential over 500 mV lower than Pt.

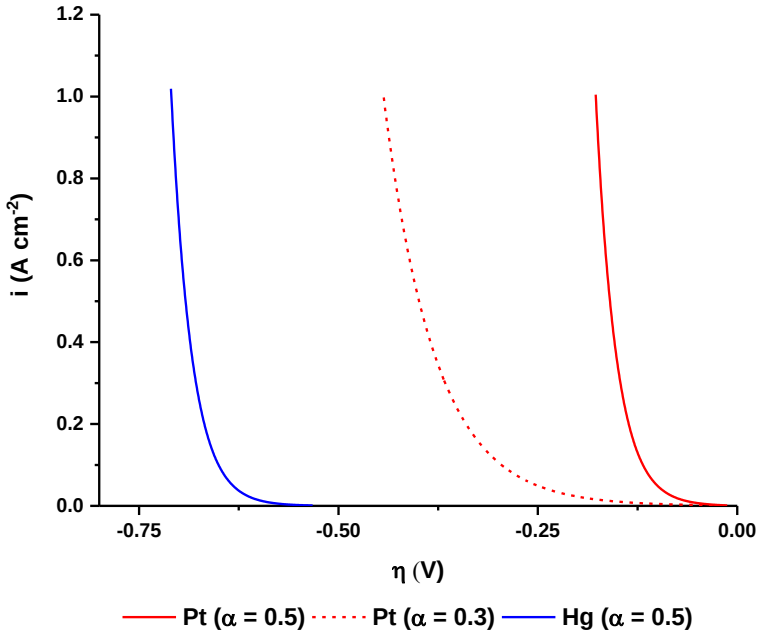

Figure 22. Application of the Butler-Volmer equation at high overpotential for HER, using experimentally derived values for i_0 of 1 x 10^{-3} A cm^{-2} and 1 x 10^{-12} A cm^{-2} for Pt and Hg respectively. Charge transfer coefficients at 0.5 are experimentally derived [90,92]. Pt α = 0.3 is not experimentally derived but is illustrative to show the impact of α at high overpotential.

The choice of catalyst is therefore very important in determining the performance of the electrolyser, because if the overpotential at a fixed current density can be reduced, H_2 can be produced more cost-effectively. Catalytic materials are therefore one of the most widely researched aspects of fuel cell and electrolyser systems.

As previously mentioned, a catalyst improves the reaction rate by breaking the overall reaction into several individual steps. Taking HER as an example again, the overall reaction to produce H_2 involves reduction with two electrons. As it is widely regarded

that any electron transfer reaction proceeds with the reaction of a single electron at a time, it can be deduced that HER proceeds in 2 separate electron-transfer reactions, with the formation of an intermediate species [88]. For HER, the intermediate species is a hydrogen atom adsorbed onto the metal surface (M-H bond). The essential function of this intermediate is that the ΔH_F of M-H formation is neither too high that the adsorption reaction suffers from slow kinetics, nor too low that the subsequent desorption to H_2 reaction has a resulting high ΔH_F and suffers from slow kinetics itself. The ideal ΔH_F for HER balances the reaction kinetics of adsorption and desorption, and therefore has a ΔH_F in between the two values (Figure 23). This is often demonstrated with the use of 'Volcano plots' (Figure 24), which measure a kinetic parameter of the reaction against the ΔH^0_F of the intermediate of a range of potential catalysts. The ascending slope of the Volcano plot demonstrates catalysts with low M-H ΔH_F of formation, so that desorption is the kinetically hindered step (Figure 23c), whereas the descending slope demonstrates catalysts with high ΔH_F where the adsorption step is kinetically hindered (Figure 23a). At the top of the volcano, therefore, are the catalysts that are best suited for the reaction in question, as they best balance the adsorption and desorption reaction (Figure 23b).

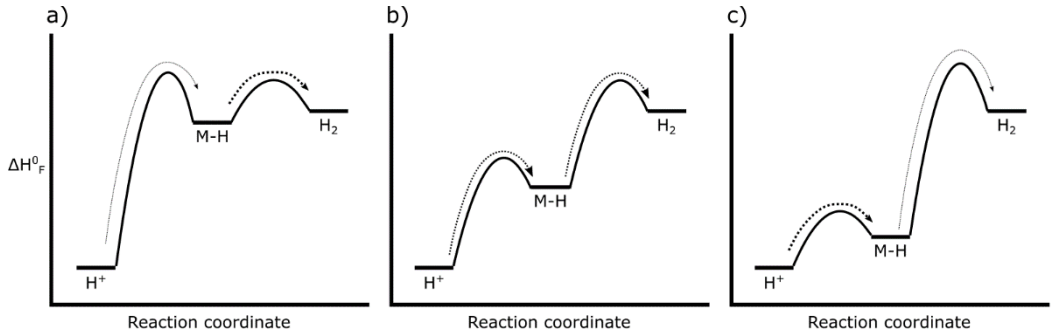

M-H formation	Slow	Medium	Fast
H_2 formation	Fast	Medium	Slow
Overall rate	Slow	Medium	Slow

Figure 23. Reaction coordinates of a catalysed HER with a) high ΔH_F of M-H formation so that M-H formation is kinetically hindered, b) medium ΔH_F so that the adsorption-desorption reactions are both less kinetically hindered and c) a low ΔH_F of M-H formation so that M-H desorption to H_2 becomes kinetically hindered.

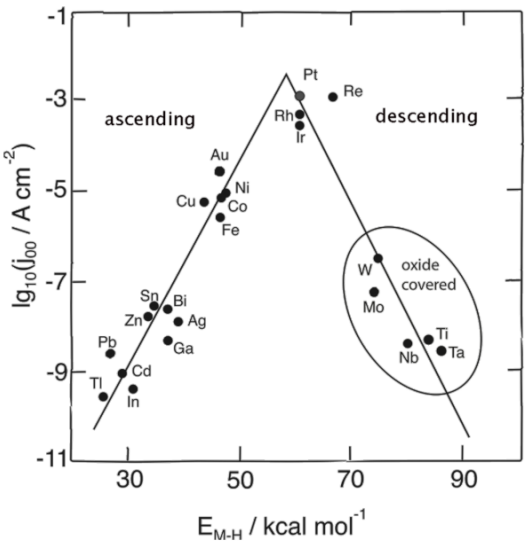

Figure 24. Volcano plot of E_{M-H} (ΔH_F) bond strength of several metals against the exchange current density. Graph taken from [93] with data from [94].

HER is a reaction that proceeds with the formation of only one intermediate species [93]; however many reactions, including OER, proceed with the formation of multiple intermediate species [95]. In these cases, the volcano plots normally focus on the rate determining step in the reaction.

2.3 Ohmic Resistance, Mass Transport and the IV Curve

One of the major contributors to efficiency loss in electrolysers are the ohmic resistances that are present in the cell. These resistances are, by definition, constant, and so at higher reaction rate they cause greater efficiency losses due to increased overpotential. The major contributor to this ohmic overpotential in an electrolyser is resistance due to the transport of ions through the electrolyte [96]. Lesser sources of ohmic resistances arise from electrical resistances in the catalysts, the electrical contacts between phases of the electrolyser, and from the wiring of the cell. Electrolysers typically operate in the current density range where ohmic resistances are a major consideration, and so reducing ohmic overpotential can substantially improve the efficiency of an electrolyser. The most common method to reduce ohmic overpotential in PEMWE is to use thinner membranes [97].

A final phenomenon that can affect the performance of the electrolyser relates to the migration rate of reactant to the electrodes. This is called ‘mass transport overpotential’, and manifests as a resistance that increases with current density. This places an upper limit on the current density that can be achieved through the electrolyser, which is known as the ‘limiting current density’ [98]. Although a phenomenon which is the subject of much more consideration in PEM fuel cells [99,100], mass transport in electrolysers is still a concern. In PEMWE, the anode electrode is a common concern for

mass transport, as by design it has to effectively uptake water whilst releasing oxygen easily [101]. An imbalance in this causes the mass transport overpotential to rise, and this is a magnified effect at high current density where more oxygen is produced [102]. There is therefore a substantial amount of research dedicated to designing electrodes that are effective in managing the transport of water and gas. In AWE, mass transport overpotentials can arise both from the gas production and from the transport of the hydroxide ion through the electrolyte [103]. Mass transport in electrolysers is not a well-characterised phenomenon, as it is highly dependent on the construction of the electrolyser cell and its operation. Factors such as the temperature, pressure, porosity of the supporting layers, and hydrophilicity can all have an impact upon mass transport [104].

The thermodynamic, kinetic, ohmic and mass transport overpotentials of the electrolyser all contribute to the overall cell voltage during operation. When scanned over a current density range, this gives rise to the IV curve (Figure 25), which is the most commonly used method of comparing the performance of electrolysers. This is analogous to Figure 13, as the reduced efficiency is the result of higher voltage.

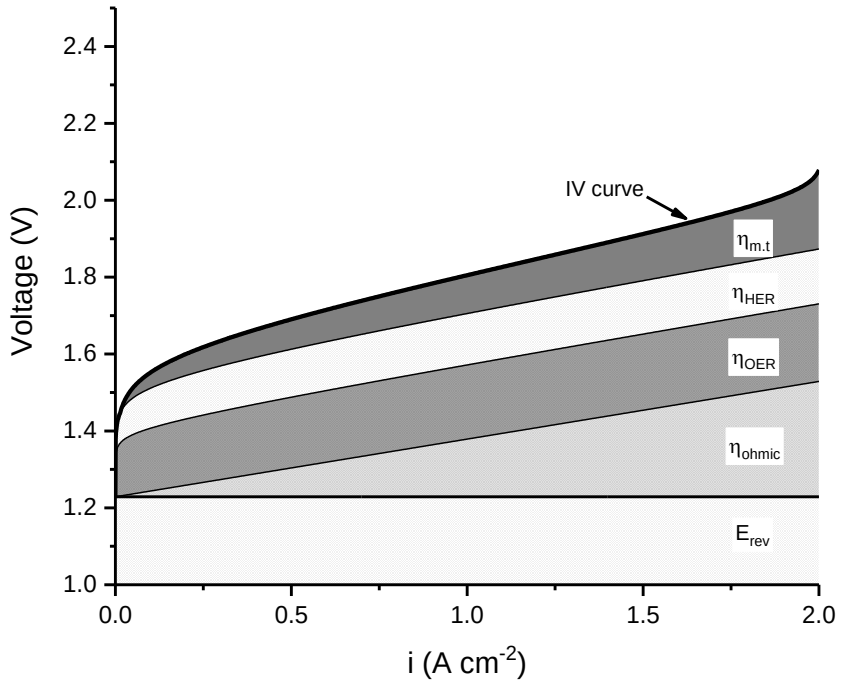

Figure 25. The potential contributions of the reversible cell voltage (E_{rev}), the ohmic overpotential (η_{ohmic}), the OER and HER overpotentials (η_{OER} and η_{HER}) and mass transport overpotential ($\eta_{m.t}$) to the overall performance of an electrolyser cell. Note, this graph is a demonstration only and is not a reference for true PEMWE operation.

3 Research Aims

To improve the cost-competitiveness of green hydrogen against grey or blue (Figure 8), several cost reductions need to be made across the sector. In a 2020 study by IRENA, two major improvements that were needed were highlighted [105]. Firstly, the cost of renewable electricity must further reduce, from the approximately 0.053 USD kWh^{-1} (Figure 3) to 0.020 USD kWh^{-1}. Secondly, the capital cost of electrolyser systems must be reduced, ideally by 80 %. Matters such as further improving electrolyser efficiency and lifetime were also stated here as lesser cost reducing factors. The projected cost reductions in green hydrogen are highly ambitious. Currently, green hydrogen costs approximately 6 USD kg^{-1} [106], but the projections for cost by 2030 are substantially less than this, at 1.3 – 2.9 USD kg^{-1} [107] [6]. The EU target for the cost of green hydrogen is less than 2 € kg^{-1} [108]. For this to be realised, the cost of electrolyser systems must decrease substantially.

A widely disseminated 2010 study, published by K. Ayers et al of the former Proton Energy Systems (now a subsidiary of Nel ASA), gives one cost breakdown of a medium-scale, 13 kg H_2 day^{-1} PEMWE system, wherein the contributing costs of the system components are given as a ratio of the overall cost (Figure 26) [109].

[6] Converted from EUR to USD with exchange rate of 1.19 USD to 1 EUR (09.03.2021).

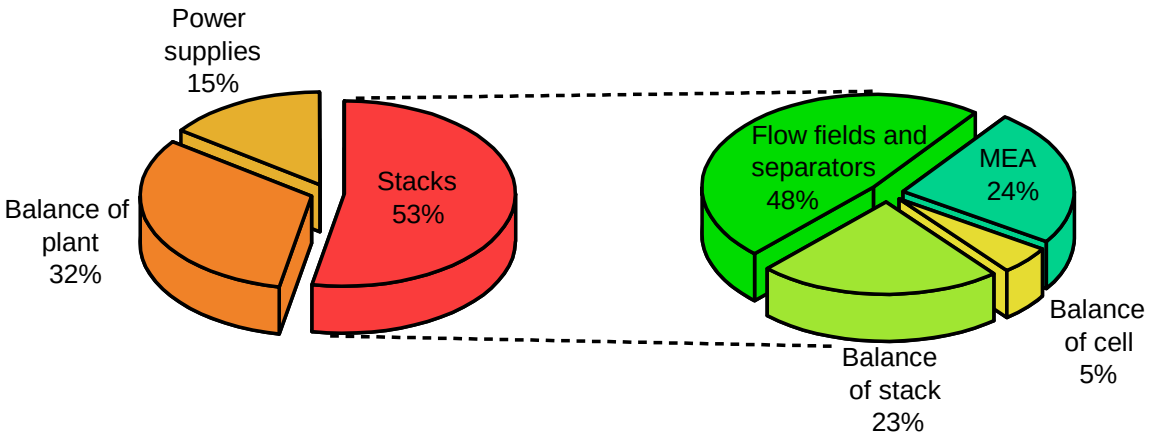

Figure 26. Breakdown of the 2010 capital cost of PEMWE components. Reprinted from [109].

As stated in the report, this represents the cost ratio at commercial levels of manufacture of the stack[7] components, i.e. with the cost reductions associated with high-volume manufacturing. However, the overall cost does not factor in the economies-of-scale cost reductions in the balance of plant and power supplies, because complete electrolyser systems are not currently produced at extremely high volume. Stacks are produced at large-scale, however. Multiple stacks are used per electrolyser system, and multiple hundreds of components are used per stack. The study has stated that, at higher manufacturing rates, the cost of the balance of plant will decrease, and so the overall cost ratio will become even more weighted towards the stack in the future. It should be stated here that this represents a cost breakdown in 2010, and this ratio is likely to have changed somewhat since. Within the PEMWE stack, the flow fields and separators constitute almost half of the stack cost, followed by the membrane

[7] A 'stack' is an array of electrolyser cells connected in series

electrode assembly (MEA)[8] at 24 %. Whilst not stated in the study, it is widely known that the widespread use of precious metals (PGM) in PEMWE is one of the major cost drivers of PEMWE systems [44], and so by reducing their use, the system cost can be substantially reduced. As mentioned in section 1.4.3s, PGMs have dual functions in the PEMWE system, both offering the best OER and HER catalytic performance, and offering corrosion protection against the highly corrosive conditions of low pH, high potential and the presence of fluorides [110,111]. The major research field in PEMWE is therefore dedicated to reducing or replacing PGMs, using several approaches that will be discussed section 4.

Cost reductions in PEMWE cannot come with losses in the performance or lifetime, however, and so any developmental materials are benchmarked in an electrochemical setup to test efficiency against the status-quo. The tests in literature typically take the form of glassware tests (for example, rotating disk electrodes, which will be referred to as 'in-vitro' in this thesis), particularly for new types of catalyst materials [112]. Analysis also often takes place in small-scale PEMWE cells (in-situ) to analyse performance under real PEMWE conditions [78,80,113]. Both approaches often use constant operation tests

[8] The MEA used in this case is the component of the electrolyser consisting of the membrane and two electrodes (Figure 16). In PEMFC, the MEA usually consists of a gas diffusion layer (GDL) made of carbon fibres also. In PEMWE, carbon cloths are non-essential components of the electrolyser, as the flow fields and separators can fulfil this gas diffusion purpose. In this case, the MEA can also be named the 'catalyst coated membrane' (CCM), and these two acronyms are sometimes used interchangeably in PEMWE literature. The author believes that the K. Ayers study here utilises a CCM design, and the cost of gas diffusion layers is contained in the flow field and separators ratio.

over the course of several hours to several thousands of hours (both constant voltage and constant current tests are widespread) as the ultimate tool for analysing performance and durability. This is of course prudent, as the PEMWE materials must perform well and durably under operation. This approach is not a holistic one, however, as it naturally can only characterise degradation - related phenomenon occurring because of operation. As it is anticipated that one of the purposes of electrolysers will be for electrical grid balancing of highly variable renewable energy (Figure 4), an electrolyser will never operate continuously in this role [76]. Highly intermittent or variable operation, wherein the electrolyser will be subject to numerous start-stops or current fluctuations, is the inevitable result of the grid balancing function [52,114–117]. This itself is not a new observation, and, although it is less commonly seen, characterization of the PEMWE components under variable operational conditions is seen in literature [118,119]. The conditions of the PEMWE system during periods of non-operation is not comprehensively understood though, and this represents a gap in the knowledge that is only starting to become addressed with recent research. The limit of current understanding of PEMWE during non-operational periods will be discussed in section 4 also.

In this thesis, the overall aim was to address some of aforementioned limits of understanding pertaining to PEMWE, with particular emphasis on developing a better understanding of the conditions of PEMWE during periods when the cell is non-operational (when it is at ‘open circuit’, or ‘OCV’). Furthermore, this thesis has aimed to improve the understanding of how these conditions affect the OER and HER electrocatalysts.

In Chapter 1 the conditions in the 3-Electrode PEMWE cell during OCV, the condition expected of an electrolyser during periods of non-operation is reported.

In Chapter 2, the findings of OCV conditions were developed into a mathematical model of PEMWE at OCV. This allowed for a wide range of OCV conditions to be investigated. This work overcame the limitations of the 3-electrode cell design with regards to differential pressure operation and temperature range.

In Chapter 3, the application of a voltammetric technique to quantify electrocatalyst degradation by dissolution is reported. The voltammetry method determined was compared to inductively coupled plasma – mass spectrometry (ICP-MS) in terms of limits of detection, and, using this technique, the dissolution of Pt from the cathode during OCV and operational periods was observed and quantified.

Finally, in Chapter 4, the voltammetry method was used to determine the dissolution of a Pt/C electrocatalyst during OCV and operational periods.

4 State-of-the-Art

4.1 The Nature of PEM-Based Systems During Open Circuit Periods

Whilst there is relatively little dedicated research on the electrochemical conditions of PEMWE systems during periods of open circuit, in PEMFC this region has been more intensively studied. This is because in PEMFC, the voltage of OCV is typically below the sum of the theoretical reversible cell potentials. During operation therefore, the PEMFC only operates at voltages below this value, and this has a negative impact on the systems overall performance [120]. A study by Zhang et al [121] gave a PEMFC cell OCV of 1.042 V at 3 atmospheres of H_2, a voltage drop from the reversible voltage that was attributed to (1) the high rate of crossover of H_2 from the anode to the cathode[9] and (2) the continuous oxidation and passivation of the Pt ORR electrocatalyst under an O_2 atmosphere. Pt oxidation was here stated to occur at electrode potentials greater than 0.88 V NHE. They furthermore found that the kinetics of both mechanisms increased with temperature, thus dropping OCV further. Jung et al [122] performed a computational analysis to understand OCV, instead taking into account the effects of carbon support oxidation in addition to H_2 crossover. They determined that the major driver altering OCV was H_2 crossover, and only a minor contribution came from the oxidation of carbon.

[9] In PEMFC, the anode performs the hydrogen oxidation reaction (HOR), as opposed to PEMWE anode that performs OER. The PEMFC anode therefore is in a H_2 atmosphere whereas the PEMWE anode is in an O_2 / water atmosphere.

In PEMWE, the conditions of OCV are not comprehensively understood, and there are currently only a few works that consider it in detail. Brightman et al [123] first reported on OCV conditions in a 3-electrode PEMWE cell, which allowed for the electrode potentials to be discerned from the overall cell voltage. In this work it was shown that the cathode potential is highly dynamic during OCV periods, rising from a potential close to E_{rev} (H^+ / H_2) to approximately 1 V NHE over the course of approximately 1 hour. The anode potential remained close to the E_{rev} (O_2 / H_2O). This was reported to be caused by the crossover of oxygen from the anode, through the membrane, and into the cathode. H_2 crossover was not considered here because the anode potential remained high throughout the OCV test. Through the analysis of degradation of the Pt HER electrocatalyst (degradation mechanisms are covered separately later), a report by Rakousky et al [124] determined similar OCV conditions.

Whilst using a conventional electrolyser cell, Weiß et al [119] stated contrary findings to the above, postulating that the voltage decay they observed during OCV was the result of H_2 crossover through the membrane, reducing the potential of the anode electrode. These two results are in contrast, and so investigation into the cause of this difference was warranted, thus forming part of this thesis. The major differences between these studies are that Brightman et al and Rakousky et al operated with a constantly wet cathode (with water being actively supplied to the cathode) and operating with no differential pressure at 60 ^oC. Weiß et al operated with a 'dry' cathode at 80 ^oC, with 9 bar of differential pressure at the cathode. Both operation modes are considered representative of commercial PEMWE systems. 60 ^oC and 80 ^oC are typical operating temperatures [44]. Supporting the case of Weiß et al, 'dry' cathode operation is the

commercial norm [113,125–127]. Supporting the case of the 'wet' cathode, however, although it is less common in PEMWE [128,129], during operation the cathode of 'dry' cathode systems does become wet as a consequence of electroosmotic drag (EOD) [130,131]. To the best knowledge of the author, information on the H_2 pressure at the cathode in commercial systems during OCV is not publicly available, and so can only be speculated upon. For reasons of safety, it may be common practice to reduce the H_2 pressure when the PEMWE is non-operational in order to decrease the rate of H_2 permeation through the membrane, thus preventing the formation of an explosive atmosphere at the anode [132,133]. Alternatively, high pressure may be maintained to allow for faster response times, and to avoid mechanical degradation of PEMWE components caused by pressure swings [134,135]. Irrespective of this, it is likely that the two distinct modes of operation during OCV may well induce different electrochemical environments on the electrodes, which in turn will affect their potential responses in different ways. Clearly here, the crucial determiner of the electrode potentials during OCV are the rates of permeation of H_2 and O_2 through the Nafion membrane.

4.1.1 O_2 and H_2 Permeation through Nafion

Gas permeation through the SPE is a well-characterized phenomenon. There are several reasons for this, in addition to the reasons aforementioned. H_2 permeation in both PEMWE and PEMFC represents a parasitic process, i.e. it reduces the Faradaic efficiency of the system, as the permeated H_2 cannot be collected or reacted in an electrochemically useful manner. H_2 crossover becomes a greater concern with the decrease in thickness of the membrane, and this is particularly concerning for PEMFC, where membranes thinner than 25 µm are typically used [136]. This was demonstrated

by Yuan et al [137] on Nafion membranes of various thicknesses, wherein it was determined that thinner membranes exhibit higher initial gas permeability, a shorter lifetime, and increased gas permeability once degraded. They attributed this to the formation of pinholes and the thinning of the membrane. Thicker membranes exhibited both reduced crossover and more stable performance, which indicated that the crossover mechanism itself was one of the causes of degradation (though thicker membranes have increased ohmic resistance). Inaba et al [138] expanded upon this work to determine the underlying causes of this degradation. The test they performed involved holding the PEMFC with a 30 µm membrane continuously at OCV, rather than operation, for 60 days. H_2 crossover rate was periodically determined by linear sweep voltammetry (LSV), and with this, they measured a rise in crossover rate over time. This was correlated to membrane thinning by measurement of increasing fluoride concentrations in the effluent water at the anode and cathode, indicative of degradation of the fluorinated polymer. They ascribed the underlying cause of this reaction not to be the crossover of H_2 however, but O_2 crossover instead causing the formation of peroxides at the anode. These peroxides may breakdown to peroxyl radicals, which may then degrade the membrane by attacking the backbone of the fluorinated polymer membrane [135].

The anode in PEMFC creates ideal conditions for peroxide formation, being both at low potential due to the H_2 atmosphere and containing a Pt/C catalyst. Indeed, experiments on peroxide formation with rotating ring disk electrodes (RRDEs) have shown that, at between 0 - 0.1 V NHE, the amount of oxygen reducing to peroxide in comparison to the amount reducing to water is substantial, at between 20 – 60 %, with higher rates of peroxide formation observed at lower Pt loadings [139–141]. The cause of this ratio

increase at lower potentials is because oxygen reduction to peroxide is a two-electron reaction, whereas reduction to water is a four-electron reaction. Water formation is still the dominant mechanism because water formation may occur below 1.229 V NHE, with peroxide formation only occurring below 0.695 V NHE [142].

Peroxide-induced membrane thinning is an anticipated degradation mechanism in PEMWE also. In fact, with the lower potential of the cathode (performing HER) compared to the PEMFC anode, the rate of peroxide formation would, in theory, be anticipated to be higher. During HER however, the high kinetics of H_2 formation suppress peroxide formation [143]. At low current density, a greater proportion of the current participates in peroxide formation, and so operation may therefore be associated with increased membrane degradation. Although not directly correlated to peroxide attack, Grigoriev et al [144] performed an intermittent cycling test on a catalyst coated membrane (CCM), performing a series of current cycles for up to 5500 h. The cell was deliberately of sub-optimal design (utilizing a Pt anode catalyst as opposed to IrO_x) to accelerate degradation. Over the course of the test, the Nafion 115 membrane reduced from 140 µm to 35 µm. Analysis by energy dispersive x-ray (EDX) of the membrane after the test recognized several cationic species present, notably potassium, calcium, and silicon, likely originating from the feed water. It was postulated here that these cationic contaminants might have caused the high rate of membrane thinning observed. Interestingly, the presence of ionic impurities significantly catalyses the breakdown of peroxide to peroxyl radicals, particularly dissolved transition group metals such Fe^{2+}, Fe^{3+}, Ti^{3+}, Co^{2+} and Cu^{+} [111]. This is a known concern when developing non-PGM based catalysts also, and so non-PGM catalysts in PEMFC and PEMWE must be resilient to dissolution [145].

Stucki et al [146] reported on a post-mortem analysis of the CCM of a 400 cm^2 PEMWE cell, wherein the thinning of the Nafion 117 membrane over 5 years of operation was found to be substantial. It was stated here that membrane thinning was the lifetime limiting factor of the PEMWE system. Although the exact role of peroxide was not determined, it was assumed it was the major driver of membrane thinning, and the authors stated that membranes with improved stability are required.

Multiple studies have shown that the crossover of H_2 and O_2 through Nafion is also dependent on the hydration of the Nafion membrane itself. Higher permeation rates are generally associated with higher hydration, which there means that PEMWE systems are expected to have higher crossover rates than PEMFC under analogous conditions. Schalenbach et al [147,148] determined that the rate of crossover of hydrated Nafion was between 5 – 10 times greater in comparison to dry Nafion between 30 – 80 ^oC. It was also found that, within the differential pressure range used in the report (1 – 5 bar), crossover solely follows the principles of Fickian diffusion.

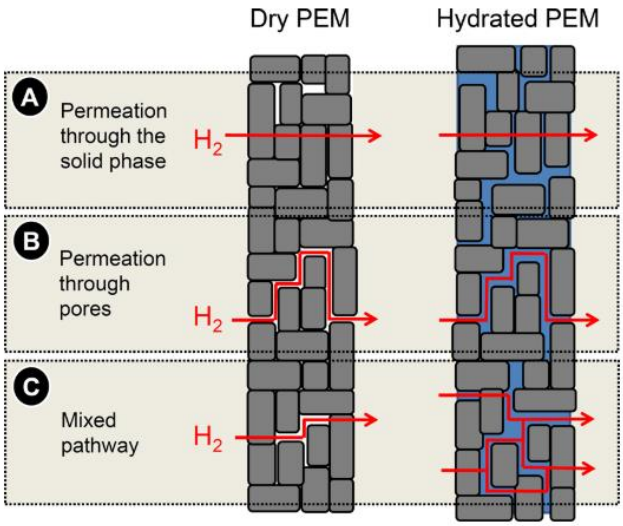

Figure 27. Possible pathways for gas diffusion in dry and hydrated Nafion membranes. Reprinted from [147].

The greater gas crossover rate through hydrated Nafion has been explained to be due to the uptake of water into the membrane. As the Nafion polymer consists of a hydrophobic fluorinated backbone with a hydrophilic sulfonic acid sidechain, the Nafion polymer clusters into domains of hydrophobic and hydrophilic regions [149]. The result is a network of hydrophilic pores that may uptake water and thus swell proportionally to the amount of hydration [150,151]. In terms of gas crossover, the swollen pores allow for a greater rate of gas permeation (Figure 27b), as O_2 and H_2 can dissolve and permeate through the water-containing channels now within in the Nafion membrane [152]. This, in addition to gas diffusion through the hydrophobic state (Figure 27), is thought to be the cause of greater crossover when hydrated. Water uptake itself is found to be a function of both the sulfonic acid group concentration in the membrane and on the temperature, and so OCV at elevated temperature may be expected to show greater crossover rates also [131].

In conclusion, although a systematic study on PEMWE OCV conditions has not been performed, a large body of information exists around the underlying principles surrounding gas crossover through water and hydrated Nafion. The potentials of the anode and cathode are therefore expected to be a function of three main factors.

Firstly, the electrode potentials will be a function of the pure gas partial pressures (whether the electrode exists in a gaseous environment or environment with water and dissolved gas) and the reversible potential of ORR and HOR. This is expected to dictate the electrode potentials only before any gas has permeated through the Nafion. As calculated by the Nernst Equation, E_{rev} is relatively insensitive to changes in the partial pressure of these gases when pure. For example, an order of magnitude decrease in partial pressure of O_2 (pO_2) would theoretically decrease E_{rev} (O_2 / H_2O) by 14.8 mV, while an order of magnitude decrease in partial pressure of H_2 (pH_2) results in a 29.6 mV increase in E_{rev} (H^+/H_2). The difference in reversible potential for ORR with dissolved O_2 compared to gaseous O_2 at the same atmospheric pressure is only approximately 22 mV. This in itself clearly cannot account for the change in potentials observed by Brightman et al [123] and Weiß et al [119].

Secondly, the potential will be affected by the rate of gas crossover. This is expected to be the major effect driving potential change in PEMWE at OCV. A theoretical estimation, or practical demonstration, of the effect of mixed O_2 / H_2 gas compositions on the electrode potential in a PEMWE has not yet been published. In PEMFCs however, H_2 crossover is known to decrease the cathode potential even at very low crossover rates. In a theoretical study by Vilekar et al [153] it was calculated that a H_2 crossover flux of

5 nM cm^{-2} s^{-1} in an ambient pressure oxygen atmosphere was sufficient to lower the electrode potential by ≈160 mV.

Thirdly, OCV is known to be affected by other electrochemical reactions asides from ORR and HOR. The primary reactions that occur within the potential range of PEMWE OCV are given in Table 1. Some of the expected electrochemical reactions in the 0 – 1.23 V range pertain to forms of IrO_x reduction, forms of Pt oxidation or the oxidation of the carbon support for the Pt catalyst. The specific impact that the above reactions have on the OCV of PEMWE has not been demonstrated, however. This list is non-exhaustive, and there are numerous complexities that exist around electrocatalyst degradation. This matter is covered in more detail later in this section.

Table 1. Electrochemical reactions relevant to PEMWEs within the electrode potential range of the anode and cathode during OCV. Shown are the theoretical reversible electrode potentials and the potentials at which these reactions have been observed experimentally.

Reaction		E^0_{rev} (NHE)	Catalyst	Practical reaction potentials (NHE)	Ref
1)	$2H_2O \rightarrow O_2 + 4H^+ + 4e^-$	1.23 V	IrO_x	1.48 V at 0.5 mA cm^{-2}	[154]
			Pt	1.77 V at 0.5 mA cm^{-2}	[155]
2)	$O_2 + 4H^+ + 4e^- \rightarrow 2H_2O$	1.23 V	IrO_x / Ti	0.5 V at 0.5 mA cm^{-2}	[156]
			Pt	0.85 V at 0.5 mA cm^{-2}	[157]
3)	$2H^+ + 2e^- \rightarrow H_2$	0.000 V	IrO_x	-0.007 V at 0.5 mA cm^{-2}	[158]
			Pt	-0.007 V at 0.5 mA cm^{-2} †	[90,159]
4)	$H_2 \rightarrow 2H^+ + 2e^-$	0.000 V	IrO_x	-	-
			Pt	0.007 V at 0.5 mA cm^{-2} †	[90,159]
5)	$Ir_2O_3 + H_2O \leftrightarrow IrO_2 + 2H^+ + 2e^-$	0.926 – 0.950 V	IrO_x	-	[160,161]
6)	$Ir + 2H_2O \leftrightarrow IrO_2 + 4H^+ + 4e^-$	0.926 V	IrO_x	-	[160]
7)	$Pt \leftrightarrow Pt^{2+} + 2e^-$	1.19 V	Pt	0.85 V	[162,163]
8)	$Pt + H_2O \leftrightarrow PtO + 2H^+ + 2e^-$	0.88 V	Pt		[153]
9)	$Pt + H_2O \leftrightarrow Pt(OH)_2 + 2H^+ + 2e^-$	0.98 V	Pt		[153]
10)	$Pt(OH)_2 \leftrightarrow PtO_2 + 2H^+ + 2e^-$	1.11 V	Pt		[153]
11)	$H_2O_2 \leftrightarrow O_2 + 2H^+ + 2e^-$	0.695 V	Pt / IrO_x		[142,153]
12)	$C + 2H_2O \leftrightarrow CO_2 + 4H^+ + 4e^-$	0.207 V	Pt	0.6 - 1 V	[153,164–166]

† The overpotentials were here calculated from the Nernst equation with charge transfer coefficients of α = 0.5 and exchange current density of i_0 = 1 x 10^{-3} A cm^{-2}, as stated in the references.

4.2 OER Electrocatalysts in PEMWE

PEMWE electrocatalysts, particularly those under OER, must operate under conditions significantly more severe than that experienced in AWE or PEMFC. There are two reasons for this. Firstly, the use of a sulfonic acid-based solid polymer electrolyte (SPE) results in a low pH environment for PEMWE and PEMFC. The exact pH of a hydrated SPE has not been fully established, but three separate studies using different determination techniques have produced an approximate pH range. Using a methylene blue dye, Seger at al [167] determined that the proton activity of Nafion was equivalent to 1.2 M H_2SO_4 (pH ≈ -0.08). In two electrochemical-based studies, Umeda et al [168] estimated the pH of Nafion at 0.8, and Brightman et al [169] at 1.4. Secondly, during operation, the OER electrocatalyst is subject to potentials well in excess of 1.7 V NHE [123,170]. Low pH and high potential environments create a highly corrosive atmosphere in which very few materials have thermodynamic stability (Figure 20) [171]. This explains why PGMs are widely used in PEMWE, as these materials are typically the most corrosion-resistant elements known. It is important to state however, that whilst understanding the thermodynamic stability of an element is important, it does not necessarily indicate how rapidly it will degrade under PEMWE conditions as the kinetics of corrosion need to be considered as well.

Pt catalysts, usually Pt/C, are the state-of-the-art for catalysing HER, HOR and ORR; however, it typically exhibits poor reaction kinetics for OER in PEMWE [144]. Instead, IrO_x is typically used for OER in PEMWE, exhibiting both good reaction kinetics and corrosion resistance at typical OER potentials. The use of Ir is, however, not ideal for several reasons. Firstly, Ir is a highly expensive material, contributing towards a large

proportion of the cost of the MEA (Figure 26) [127]. Secondly, the scarcity of Ir creates challenges for the scale-up of PEMWE. According to Babic et al [172], approximately only 4 tonnes of Ir is mined annually, usually as a by-product of Pt mining. This naturally makes Ir a material very susceptible to supply – demand issues, and the increasing demand for Ir in the past several years has driven up the cost of the raw material. IrO_x, despite being the most stable OER catalyst, still suffers from relatively poor reaction kinetics in comparison to the best performing catalyst, ruthenium oxide (RuO_x), which has been experimentally demonstrated to be a superior catalyst (Figure 28) whilst also being a cheaper material [155,173].

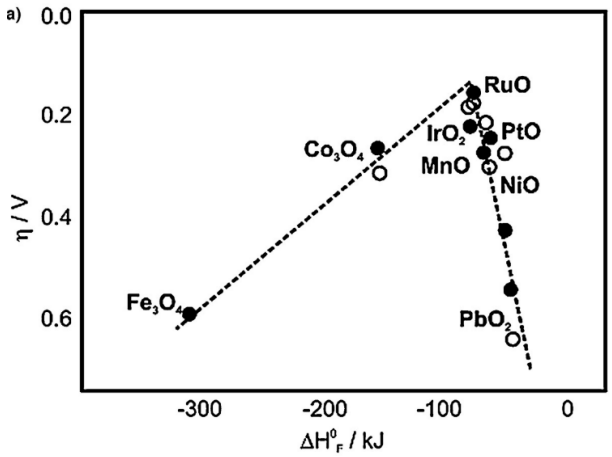

Figure 28. Volcano plot of oxide electrocatalysts for OER. Reprinted from [174].

However, the major downside of RuO_x is its susceptibility to corrosion, and during OER it is known to corrode proportionally to the rate of OER to a significant degree (Figure 29) [175]. A solution to both the issue of poor IrO_x kinetics and the stability issues of RuO_x is to incorporate both Ir and Ru in a mixed metal oxide (MMO) in a range of Ir : Ru ratios. According to Saveleva et al [176], in these Ir – Ru MMOs, the OER takes place

preferentially on the Ru, and the purpose of Ir instead becomes one of stabilizing the Ru oxidation states during OER. Specifically, Ir was hypothesised to prevent both the formation of irreversible oxidation states of hydrous Ru (IV) oxide or RuO_3. RuO_4, which is thought to be the reaction intermediate, is also stabilized by Ir, which helps to prevent its dissolution [177].

A range of Ir – Ru MMO molar ratios have been tested at OER conditions to establish both performance and lifetime. Reksten et al [178] tested MMOs *in vitro* over the full ratio, from IrO_x to RuO_x, and observed that a roughly linear relationship between Ru ratio and performance at 1.5 V NHE existed. The rate of OER on RuO_x here was an order of magnitude higher than pure IrO_x. Furthermore, it was shown that, at current densities more practical for PEMWE, MMOs with high Ru ratios again performed best. The improved performance of high Ru ratio in these MMOs has been demonstrated in subsequent publications, both *in vitro* and *in situ*. Audichon et al [179] tested MMOs in a PEMWE cell, and found that the relationship between Ru ratio and performance was not necessarily linear however, as they determined that, whilst high Ru ratios had the best performance, equal ratios were found to have worse performance than either RuO_x or IrO_x alone. A report by Mamaca et al [173] agrees with these findings also, determining that high Ru ratio Ir – Ru MMOs had good performance in a PEMWE cell (100 mV lower overpotential than IrO_x at 1 A cm^{-2}).

Less well established than electrochemical performance is the true effect that Ir has on stabilizing Ru in the MMO. Recent evidence from long-term studies of Ir – Ru OER performance has shown that, whilst in comparison to pure RuO_x they are significantly more stable, Ir – Ru MMOs still suffer a high degree of Ru corrosion. This was evidenced

in a report by Kasian et al [180], who coupled an electrochemical cell to inductively coupled plasma – mass spectrometry (ICP-MS) to detect dissolved Ir and Ru during OER. They saw that the rates of Ru dissolution were consistently higher than Ir, and determined that the performance of Ir – Ru MMOs approached that of pure IrO_x with the loss of just the surface Ru. Despite the corrosion, it was argued that the use of Ir – Ru MMOs is still justified as Ru reduces the cost of the overall catalyst by reducing the amount of Ir where it is not needed i.e. within the bulk of the catalyst rather than the surface. This method of electrochemical leaching has itself been the focus of investigation, as it has been shown that the removal of Ru from an electrochemically prepared $Ir_{0.7}Ru_{0.3}O_2$ species creates extremely active OER electrocatalysts [181]. It has been shown that, in comparison to electrochemically prepared IrO_x, the $Ir_{0.7}Ru_{0.3}O_x$ with the Ru leached from the surface had a 13-fold reaction rate improvement *in vitro*. This was attributed to the presence of highly active amorphous IrO_x and hydroxide surfaces with low coordination. These catalysts were further tested in a PEMWE cell for 400 h at 1 A cm^{-2}, showing performance superior to a more conventionally produced $Ir_{0.7}Ru_{0.3}O_2$ and with no loss in performance over time.

Although generally much lower in magnitude, even pure IrO_x catalysts have been demonstrated to undergo dissolution in proportion to the rate of OER [175,180]. A separate study by Kasian et al [182] investigated the dissolution of Ir from thermally prepared and electrochemically oxidized IrO_x, finding that the rate of dissolution from electrochemically oxidized Ir was several times greater during OER. This was attributed to the presence of soluble hydrous Ir oxide species ($Ir^{III}OOH$), which was found to have improved reaction kinetics over IrO_x but at the expense of increased susceptibility to dissolution. This finding was determined by the isotopic labelling of the IrO_x catalysts

with O^{18}. By ICP-MS analysis, the authors determined that O^{18} was present in the product oxygen from the electrochemically oxidized IrO_x only, lending credence to the presence of the soluble species. As a side note, the structural differences between thermally prepared and electrochemically oxidized catalysts are that the thermally prepared catalyst generally has greater crystallinity, forming a rutile structure with oxygen atoms present throughout the material (bulk oxide). Electrochemically oxidized IrO_x catalysts generally are more amorphous than rutile IrO_x, and as electrochemical oxidation of IrO_x is a near-surface effect, these catalysts are not bulk oxides.

The findings of Kasian et al offer a good explanation for the observations by Cherevko et al [163, 175], who showed the improved performance of metallic Ir and Ru over IrO_2 and RuO_2 for OER. Metallic species are assumed to undergo surface oxidation before the onset of OER, thereby making them analogous to the electrochemically oxidized Ir. The performance and dissolution rate of the various catalysts in this study were correlated, in the order of Ru > Ir > RuO_x > IrO_x. Dissolution of the metal catalyst versus the thermally oxidized species was measured by ICP-MS and found to be approximately 3 orders of magnitude greater (Figure 29).

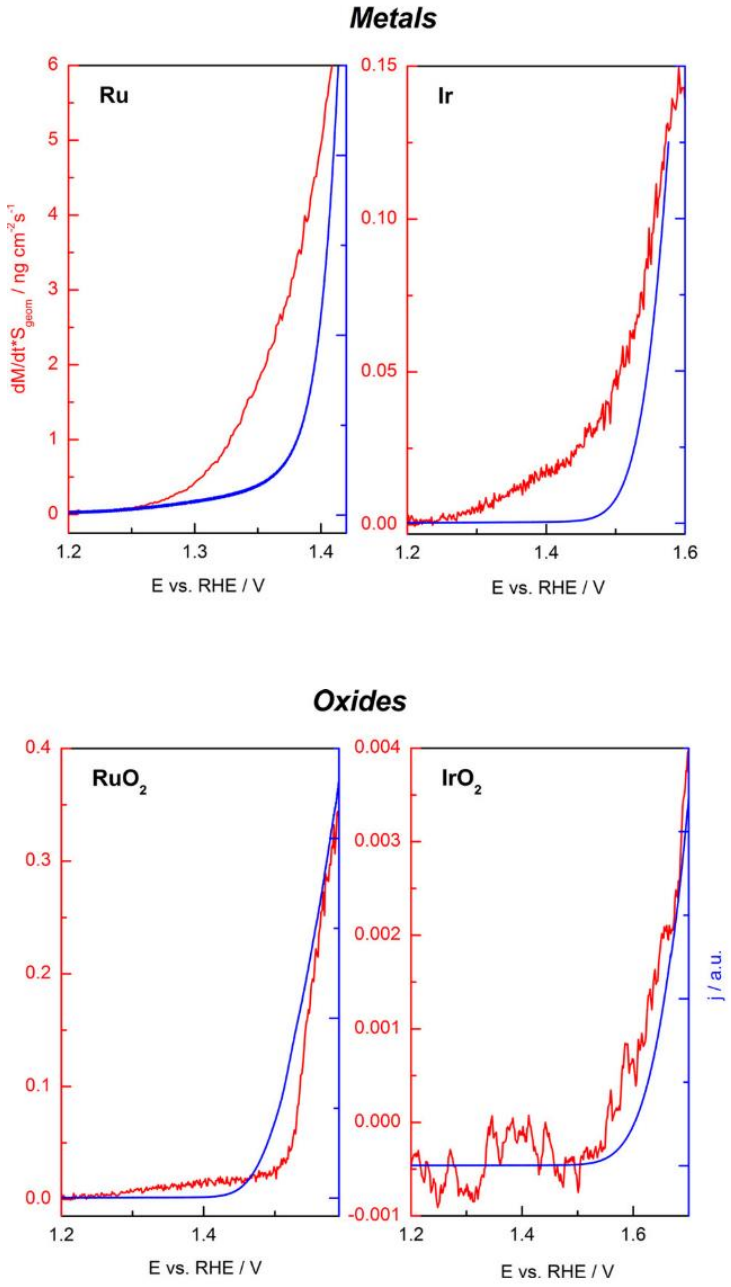

Figure 29. The rate of OER as a function of the potential of Ir, Ru, IrO_2 and RuO_2 compared to the respective rates of dissolution. Measurements performed *in vitro* in 0.1M H_2SO_4. Reprinted from [175].

Aside from Ir and Ir – Ru MMOs, another theme in OER electrocatalyst research is to incorporate materials other than Ru into OER electrocatalysts, either as part of MMOs in binary or ternary mixtures with Ir, or as a supporting material. MMOs of Ir, Sn and Nb have been shown in several studies to be promising electrocatalysts. For one example,

with molar ratio of $Ir_{0.4}Sn_{0.3}Nb_{0.3}O_2$, comparable electrochemical performance to pure IrO_2 was demonstrated and durability shown over approximately 1 day [183]. The doping of these MMOs with fluorine has also been investigated as a means of increasing the electronic conductivity of the electrocatalysts [184–186], an issue that tends to hinder electrocatalysts with low Ir ratios. A final promising approach for reducing the amount of Ir used in PEMWE is to grow Ir electrocatalysts onto a supporting material. Notably, studies have successfully tested Ir supported on TiO_2. TiO_2 is typically regarded as being non- or semi-conductive, but can be made conductive, and highly electrochemically active, at a weight ratio of 60 % Ir / TiO_2 [187]. In a set of studies by Rozain et al [188,189], an investigation was made into the impact of performance on a range of catalyst loadings, both with pure IrO_x and Ir deposited onto titanium. In these works, it was firstly determined that the loading of pure IrO_x affected the performance in PEMWE up to approximately 0.7 mg cm^{-2}, after which there was no performance gain from using a higher loading. Secondly, they tested Ir supported on TiO_2 at a range of loadings. Interestingly, whilst pure IrO_x was found to improve in performance with higher loadings, this trend was reversed in the case of IrO_2 - Ti. This was explained to be due to a difference in the mechanism affecting performance. In pure IrO_x, lower loadings increased the ohmic resistance through increased contact resistance, whereas IrO_x – Ti suffered from diffusional limitations with higher loadings. In an operational test of 1000 h, IrO_x – Ti at 0.12 mg cm^{-2} of IrO_x was found to initially perform similarly to pure IrO_x at 0.32 mg cm^{-2}, whilst also showing a reduced degradation rate over time. IrO_x – Ti is therefore a highly promising catalyst that may substantially reduce the reliance of PEMWE on Ir. Note that the typical loadings for anode catalysts in PEMWE are in excess of 1 mg cm^{-2} (Figure 30) [44].

Overall, the state-of-the-art in OER electrocatalysts in PEMWE remains IrO_x or Ir – Ru MMOs with high Ir ratios. In fact, to the best knowledge of the author, Ir – Ru MMOs and supported IrO_x are the only catalyst developments over bulk IrO_2 that have been tested for substantial durations at scales approaching commercial applicability [80,179,181,190]. Most research efforts are focused around reducing the loading of the known effective OER catalysts rather than attempting to discover new types. Some of the most important works in the field of OER electrocatalysis in PEMWE are therefore focused on investigating the relationship between IrO_x loading and performance [188,189]. A further factor that hinders research into novel OER electrocatalysts is that the exact OER mechanism has not been fully elucidated. Although multiple studies are beginning to uncover the mechanism [191], there is no firm consensus and so multiple possible reaction pathways exist [95,192].

4.3 HER Electrocatalysts in PEMWE

The major differentiator between OER and HER electrocatalysts is that, during operation in PEMWE, they exist in conditions substantially more reducing than their OER counterparts (Figure 20). For this reason, there is a much larger range of materials that can withstand the cathode environment (Figure 24). Although, as good reaction kinetics are of course still necessary, Pt is the predominant HER electrocatalyst.

As the reaction kinetics typically dictate the amount of catalyst required for good performance, and as the kinetics of HER in PEMWE are far greater than OER, the amount of catalyst used for HER is usually 3 – 5 times less with respect to PGM (Figure 30). With less catalyst used initially there is therefore less of a cost saving to be made by the replacement of Pt with non-PGM alternatives. A majority of electrocatalyst research in

PEMWE is therefore focused on the OER electrocatalyst, which is considered to be a larger contributor to the PEMWE capital cost. There is hence a less substantial body of research dedicated specifically to the HER catalyst, with regards to both the development of new materials and the development of a better understanding of their nature and degradation.

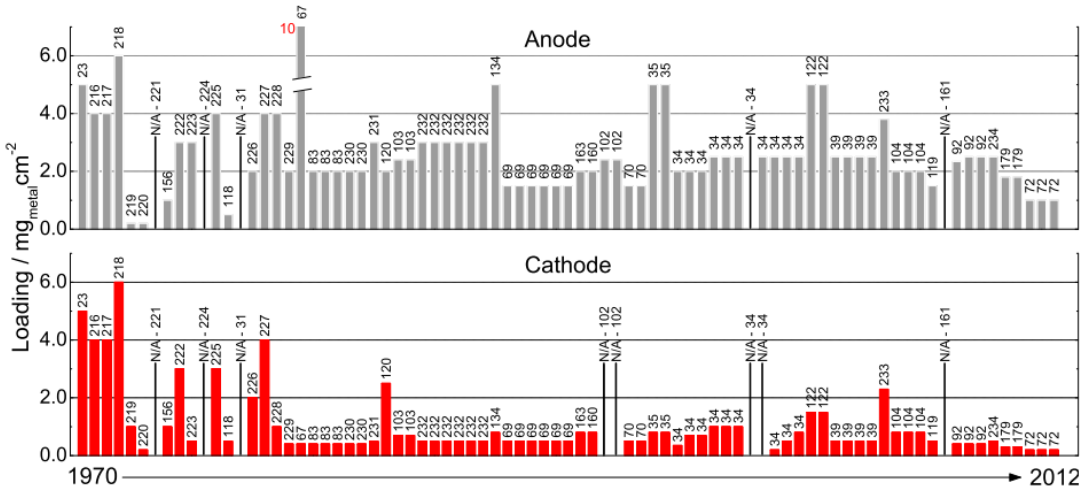

Figure 30. Reported electrocatalyst loadings of OER and HER electrocatalysts in PEMWE. Reprinted from [44].

McCrory et al [193] reported a substantial body of work, which benchmarked a range of HER electrocatalysts in acidic media for solar water splitting devices (Solar aided PEMWE). In this work, a range of electrocatalysts were deposited on glassy carbon electrodes and all tested in an identical manner, with the material used primarily being alloys of Co, Mo and Ni. An observation of the HER overpotential at a fixed current density of 10 mA cm^{-2}, as well as 2-hour durability tests and potential cycling, showed that a Ni-Mo alloy electrocatalyst had initial overpotentials of -45 mV at 10 mA cm^{-2}, similar to Pt at -40 mV. A 30,000 potential cycle test from -0.1 – 0.1 V NHE did reveal a

drop in overpotential from -45 mV to -400 mV however, although this finding has a limited impact as potential cycling on Pt was not also performed. These catalysts have recently been further investigated for performance in the cathode of a PEMWE system by Kim et al [194]. In this work, Ni-Mo electrocatalysts were deposited on carbon paper and placed at the cathode. IrO_x was loaded at 0.1 mg cm^{-2} at the anode, which was also deposited onto carbon paper. Separating these two layers was a Nafion 212 membrane (50 µm thickness, typically thinner than a normal PEMWE membrane, which are more commonly 150 µm), thus forming the MEA. The performance of this system was analysed between 60 – 90 ^oC at 1 A cm^{-2}, with cell voltages recorded between 1.9 – 2 V. A loss in performance of over 36 h was noted, however. At 90 ^oC, with the cell held at 2 V, the PEMWE cell saw a loss of the floating current density from 1.85 A cm^{-2} to 1.7 A cm^{-2}. Whilst in the paper this was regarded as an acceptable loss of performance, an accurate extrapolation of this data to the several thousands of hours required for PEMWE lifetime is not possible, and so the claim of acceptable stability cannot be substantiated. Furthermore, the MEA design was unusual for PEMWE, i.e. with a very thin membrane and a low loading of IrO_x. Carbon paper is also a poor material choice to use at the anode as carbon is susceptible to corrosion at high potential (Table 1) [171]. This choice of MEA therefore makes this report less of an investigation into the performance of Ni-Mo electrocatalysts and more of a test of the MEA design. As the low loading of Ir would be expected to impart generally poorer electrolysis performance, and as the carbon support would be expected to corrode at the anode at an appreciable rate, the performance loss here cannot solely be attributed to a loss of Ni-Mo activity. Ni-Mo may therefore still be an effective HER electrocatalyst, and further research into the performance in PEMWE is still of interest. Highlighted here is also the need for more

commonality in PEMWE testing conditions, both in terms of the MEA used, the supporting hardware, and the testing regimes.

Mo-containing HER electrocatalysts in a range of formulations are also receiving interest as possible low-cost replacements to Pt. Kim et al [112] have reported on the optimization of Cu_xMo_{1-x} catalysts for HER, where x = 0.93 – 1, and have demonstrated the performance both *in vitro* and *in situ*. The performance of Mo-containing catalysts was found to have a several times greater HER activity than pure Cu, and they stated that, as a cost-per-mass activity, Cu_xMo_{1-x} catalysts are 2.2 - 10.8 greater than Pt. Performance in a PEMWE was found to give a cell voltage of 2.0 V at 0.7 A cm^{-2} [10]. Through multiple cyclic voltammetry (CV) sweeps *in vitro* they did, however, show that the catalyst performance suffers considerably through potential transients, with a three-fold reduction in reaction rate when held at a fixed voltage.

Very high HER performance was reported by Han et al [195], who fabricated a core-shell catalyst of a Mo-Co core and MoO_x shell. The shell was formed by the simultaneous electrochemical etching of Co from the surface and the oxidation of the remaining Mo. By doing this, they produced a catalyst of extremely high ECSA that could overcome the issue of poor HER kinetics on Mo. Performance against a Pt foil was measured and showed that Pt had approximately 2.5 times the activity of the optimal MoO_x – MoCo formulation. They furthermore demonstrated *in vitro* the stability in HER performance over 30 h.

[10] For reference, state-of-the-art PEMWE performance with Pt/C HER catalyst would be approximately 1.6 V at 0.7 A cm^{-2}, although this performance can depend numerous other factors, such as the cell used, the temperature and the porous transport layers.

Molybdenum sulfides (MoS) are a further variant of Mo-based catalysts that have been found to have interesting HER kinetics [196–199]. Poor reaction kinetics are again overcome by the production of extremely high surface area materials, being formed either by the production of monolayer MoS catalysts, by deposition onto carbon nanotubes (CNTs) or onto carbon blacks. Like the aforementioned studies, typical performance analysis follows a series of *in vitro* studies followed by testing in a PEMWE cell. These materials have been demonstrated to have stable performance up to 24 h.

As a summary, the general trend for non-PGM HER materials is that there is a well-established compromise of performance compared to Pt. This has been demonstrated both *in vitro*, where the catalyst generally has lower exchange current densities and higher Tafel slopes (a practical manifestation of the charge transfer coefficient), and in PEMWE where the performance is normally either about 200 mV greater than Pt at a constant current density, or approximately half the current density at the same overpotential. This loss of performance has been justified, as these reports state that non-PGM materials represent cost savings compared to Pt. Whilst this may be the case as a weight-per-weight comparison, the effect that the non-PGM catalyst will have on the PEMWE cell as a whole cannot be ignored. As has been mentioned in the introduction, the high performance of the PEMWE system is what defines it above AWE. A reduced performance of the HER electrocatalysts will require a larger PEMWE system as a whole to produce the same quantity of H_2. Therefore, this will mean that more of the other materials will be required. As the Pt HER electrocatalyst and the MEA does not represent the largest cost within the PEMWE stack (Figure 26), then any cost reductions in the HER electrocatalyst may well be countered by the higher cost of the OER electrocatalyst, Nafion and separator materials needed. Although to the best knowledge

of the author a techno-economic analysis of this has never been done, it is likely that the benefits of non-PGM materials may only be realised if there is an order of magnitude cost increase in Pt. A drop-in replacement for the HER electrocatalyst may therefore currently only be suitable if both the performance and durability match that of Pt.

Palladium (Pd) has been found to be a potential HER electrocatalyst for PEMWE. Although still considered a PGM, and currently of a similar cost to Pt, the reliance of PEMFC and PEMWE on Pt makes these technologies highly dependent on the supply and demand of Pt. This does ultimately create uncertainty over Pt supply, especially with the greater rollout of PEMFC and PEMWE. Pd has proved to be a catalyst with similar performance to Pt, as reported by Ramakrishna et al [200]. In this study, Pd was deposited on nitrogen doped carbon nanotubes (N-CNTs) and was tested both *in vitro* and in a PEMWE system. Using comparable mass loadings to Pt, Pd/N-CNTs were shown to have a high ECSA and similar performances to Pt in the PEMWE system. Cell voltages were recorded at 1.8 V for Pt/C and 1.85 V for Pd/N-CNT at 1 A cm^{-2} with loadings of 0.7 mg cm^{-2} of catalyst. In addition, the Pd/N-CNT was tested for up to 50 h at 1 A cm^{-2} with no loss of performance noted. This report highlights the potential for Pd as a replacement catalyst for HER, although again this cannot be used as proof of long-term stability as a 50 hour test is not representative of long-term performance.

Asides from Pd and other non-PGM materials, other approaches to reducing costs of the HER electrocatalyst are similar to that of OER electrocatalysts: reducing the amount of electrocatalyst used by mixing with other metals or by creating core-shell catalysts containing a Pt shell and a low-cost core material [201,202]. Most of the research in this field is, however, non-PEMWE specific. Pt is widely used in PEMFC systems as both the

ORR and HOR electrocatalyst, and reduction of the loadings here is very important for cost-savings [203]. As HER produces a more reducing environment than ORR or HOR, the catalysts used in PEMFC may therefore be used in HER provided that the materials used are also resistant to hydride formation [204]. PEWME-specific data on such electrocatalysts is not currently available in the literature, however.

Research on extremely low loadings of Pt HER electrocatalyst is a final field worth highlighting. The electrodeposition of Pt plating solutions onto carbon paper has proved an effective method of creating HER electrocatalysts, the high surface area necessary being provided by the fibrous carbon paper. A report by Kim et al [79] gives a method of electroplating Pt onto carbon paper at a very high deposition underpotential, working under the theory that at very low potentials the high concentration of H_2 adsorbed onto the Pt surface passivates the Pt, rendering it less conductive than the carbon support. This creates the preference for Pt to electroplate onto the carbon support rather than the recently formed Pt. In theory this creates a Pt monolayer on the carbon paper. Furthermore, by performing potential pulses this layer was roughened, further increasing the Pt ECSA. A range of electrocatalysts created by this method were compared with Pt/C dispersed on carbon paper, and in a PEMWE these catalysts were shown to have similar performance despite having a loading of 0.021 mg cm^{-2}, compared to 0.4 mg cm^{-2} of the conventional material. The mass activity of the electrodeposited Pt was therefore 19 times greater than conventional Pt/C. This work is highly promising, and, if long-term performance could be demonstrated, this catalyst could ultimately make the cost of the HER electrocatalyst and the cathode negligible.

4.4 The Degradation of Electrocatalysts

As already addressed, the harsh nature of PEMWE imparts significant stresses on the electrocatalysts. From the work of Brightman et al [123] and Weiß et al [119], we can estimate the potential range in which the OER and HER electrocatalysts may exist. In PEMWE, OER electrocatalysts may be anywhere from 0.0 – 2.0 V NHE, and HER electrocatalysts may be anywhere from -0.3 – 1.03 V NHE. Degradation also does not necessarily have to be electrochemical in nature, and these phenomena will also be covered.

It is worth highlighting here that, unlike PEMFC, PEMWE-based ASTs are not particularly advanced in literature or industry. Fuel cell systems regularly undergo a standard AST (IEC 62282-3-300), which is a test program that stresses a fuel cell under a number of conditions representative of real operating conditions. In PEMWE, no standard AST currently exists, which can largely be attributed to a generally poorer understanding of the exact degradation mechanisms that do occur in electrolysers.

The research into degradation mechanisms of electrocatalysts in PEMWE systems can be very briefly summarised. OER electrocatalyst degradation has already been discussed in relation to IrO_x and Ir – Ru MMOs, and the degradation of HER electrocatalysts in a PEMWE environment has, to date, only been studied by Brightman [123]. Through a series of potential cycles on the cathode from an operational potential of 0.1 – 1.0 V NHE, it was shown in this report that the ECSA of the Pt/C cathode reduced by approximately 30 %. This was attributed to electrochemical Ostwald ripening. With the lack of substantial further information about electrocatalyst degradation in a PEMWE environment, the two major sources of useful information come from analysis

of PEMFC electrocatalyst degradation, and more recently from studies coupling electrochemical cells coupled to ICP-MS.

In PEMFC, Pt/C is the most widely used electrocatalyst, and hence there is a good depth of information about this. Both the catalyst and the potential range experienced means that degradation mechanisms may be common across both PEMWE and PEMFC. There are also a range of physicals condition that are similar across both PEMWE and PEMFC that are known to cause degradation. For example, PEMFC's can undergo a process known as 'flooding', whereby the anode (the electrode that oxidises the hydrogen) can become submerged in the water that is produced by the reaction [272]. The net effect of both the blockage of hydrogen at the anode and the migration of oxygen through the membrane causes the potential of the anode to rise, eventually creating conditions favourable for corrosion of carbon supporting the Pt catalyst. The result of this is the irreversible loss of performance across the flooded part of the cathode. Start-up / shut-down of the PEMFC is another circumstance which may impart similar degradation mechanisms. When a fuel-cell is non-operational for an extended period, due to the permeation of air through the membrane, there is the tendency for air to accumulate at the anode and displace hydrogen. This causes a degradation during start-up as the anode is forced into oxidising a reactant. Under usual circumstances HOR occurs; however, with the displacement of hydrogen this is not possible, and so the potential of the anode rises up to the potential in which carbon support oxidation occurs instead, thereby degrading the catalyst and reducing the performance of the fuel cell [273].

A summary of the major Pt degradation mechanisms was given in a report by Shao – Horn et al [205] (Figure 31).

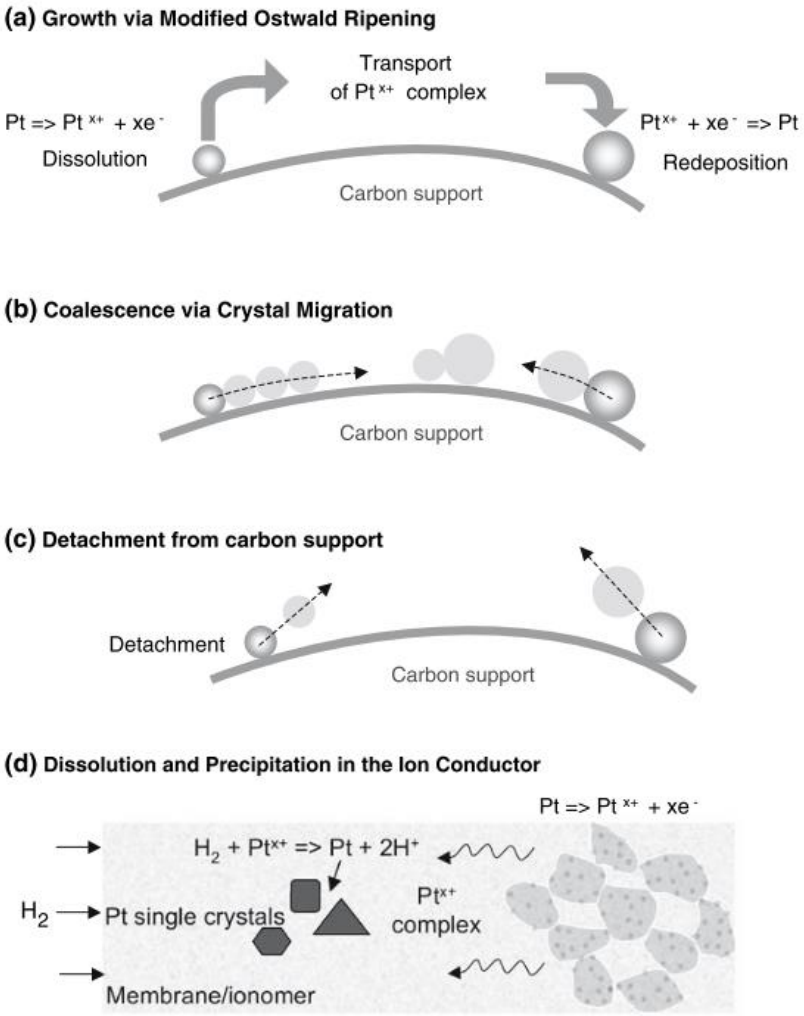

Figure 31. Mechanisms of Pt degradation in PEMFC. Reprinted from [205]

Electrochemical Ostwald Ripening (a) is the mechanism by which, at high potentials, smaller Pt particles have the tendency to dissolve first and to redeposit on larger Pt particles. The cause of this has been explained by Parthasarathy and Virkar [206], and relates to the fact that the higher surface area to volume ratio of smaller particles, and the higher instability of surface atoms compared to the bulk, reduces the potential at which oxidation reactions may occur, and so makes smaller particles more susceptible to dissolution. In the context of Pt particles, this means that dissolution of the smaller particles occurs at a lower potential than larger particles, and so dissolution and redeposition onto larger particles occurs. Parthasarathy and Virkar characterised the

rate at which Ostwald ripening occurs, finding that the average particle size grew from 1 nm to 13 nm over the course of 7 days in a solution of $PtCl_4^-$. Sharma et al [207] performed an accelerated stress test (AST) on Pt/C consisting of potential cycling between 0.4 – 1.6 V NHE. They investigated the contribution of three degradation mechanisms to the overall degradation: particle coalescence and / or Ostwald ripening (Figure 31a, b), dissolution and / or detachment of the Pt from the carbon support (Figure 31c, d), and the loss of electronic conductivity to the catalyst. Using a combination of CV to measure ECSA, transmission electron microscopy (TEM) to measure particle size, and x-ray fluorescence (XRF) to measure Pt mass loss, the various degradation mechanisms were elucidated. They determined that Ostwald ripening imparted the largest loss of ECSA up to around 500 cycles, during which time the Pt nanoparticles coarsened from an average diameter of 2.6 nm to 3.3 nm. After this period, they determined that dissolution or detachment and electronic conductivity loss contributed increasingly to the overall ECSA loss. Over 1600 cycles approximately 50 % of the catalyst ECSA was lost.

The coalescence degradation mechanism, whereby the Pt particles migrate and merge, rather than dissolve and redeposit, is also considered a major degradation mechanism in Pt/C. Due to the similarity in the result of the process (larger particles), Ostwald ripening and coalescence are difficult to differentiate. The most effective tool to observe coalescence is with the use identical location TEM (IL-TEM), as it allows the same nanoparticle to be observed before and after a test. Zana et al [208] performed this on a Pt/C catalyst that had undergone different potential cycling regimes. Through ECSA loss analysis of these regimes, they concluded that Ostwald ripening and coalescence occur concurrently, and that coalescence is likely to contribute a greater amount of ECSA

loss overall than Ostwald ripening. They also determined that, under normal automotive loads (0.6 - 1 V NHE) there was little detachment from the carbon support observed, but this became more substantial with potential cycles up to 1.5 V NHE. Coalescence was also attributed to be the dominant particle growth mechanism by Siroma et al [209], who used a combination of scanning electron microscopy (SEM) and atomic force microscopy (AFM) to analyse Pt particle growth on a glassy carbon electrode (GCE) in an oxygen gas rich electrolyte. Here they determined that Ostwald ripening was not a substantial mechanism overall, although they did explain that this may be due to their test conditions (potentiostatic control), and that ripening may be more likely in a PEMFC electrode where there may be a greater distribution of potentials across the electrode. They finally observed that, under a N_2 purged electrolyte, particle growth and degradation was mitigated, indicating that O_2 plays a role in degradation, although this was not further defined.

The detachment of Pt from the carbon support (Figure 31d) is thought to occur due to the corrosion of carbon. The reversible potential for carbon corrosion is 0.207 V NHE (Table 1, reaction 12), which means that, as all PEMFC and PEMWE electrodes may exist at this potential and above, there is at times a thermodynamic preference for carbon corrosion. As the reaction kinetics for carbon corrosion are very poor however, under normal operation regimes in PEMWE and PEMFC, carbon corrosion is generally not regarded as a major degradation mechanism. Research has shown that certain PEMFC operational regimes can enhance the degradation of the carbon support and release the catalyst, however. Castanheira et al [210] investigated the degradation of Pt/C in a similar manner to Zana et al [208]. Under a series of PEMFC accelerated stress tests (ASTs), they used a combination of CV, Raman spectroscopy, TEM and differential

electrochemical mass spectrometry (DEMS) to determine, similarly to Zana et al, that, within the range of 0.6 – 1 V NHE, the corrosion of the carbon support was not a significant contributor to the overall electrocatalyst degradation. They instead found that degradation proceeds predominantly by Ostwald ripening and / or particle agglomeration. Conversely, with potential cycling of the electrode in the 1 – 1.5 V NHE region, carbon corrosion was evident both by the appearance of C=O Raman bands, and by the detection of CO_2 by DEMS. A high loss of ECSA was also determined here, adding weight to the argument that carbon corrosion was breaking the electronic pathway to the Pt nanoparticles. Within the DEMS profile a further observation was noted with respect to carbon corrosion, with the detection of CO_2 formation at approximately 0.65 V NHE. This was attributed to carbon corrosion catalysed by Pt. This phenomenon was initially investigated by Roen et al [211], who, using mass spectrometry (MS), measured the concentration of CO_2 against potential on MEAs with 0 % (carbon black only), 10 % and 30 % Pt/C. Like Castanheira et al, they measured a CO_2 peak at approximately 0.65 V NHE, the intensity of which was related to the percentage weight of Pt on the carbon. No peak was present with 0 % Pt, thus proving that catalytic effect that Pt has on carbon oxidation.

The final Pt degradation mechanism highlighted by Shao – Horn et al is the dissolution of Pt to Pt^{2+} (Figure 31d). The dissolution of the Pt catalyst has been found to occur at 0.85 V NHE [162], and in PEMFC these dissolved species have the tendency to migrate into the membrane, either by diffusion or by electronic flux. Within the membrane, Pt^{2+} becomes reduced again by the H_2 that permeates from the anode. The result of this process are detectable bands of Pt and even Pt particles that have grown inside the membrane [212]. There are some distinctions between PEMWE and PEMFC that may

impact this dissolution mechanism, however. Pt dissolution in PEMFC occurs at the cathode (the O_2 reducing side), the electrode at high potential. In PEMWE the high potential electrode (the anode) is not typically Pt due to the poor reaction kinetics of Pt for OER; Pt instead is used at the cathode. The cathode during operation is highly reducing, and only becomes oxidising during OCV [123]. Finally, in PEMFC, Pt^{2+} migrates into the membrane; however, in PEMWE Pt^{2+} may additionally dissolve into the electrolyte, either at the anode or cathode. A significant proportion of Pt^{2+} may preferentially migrate into the electrolyte rather than the membrane. Pt dissolution in PEMWE systems thus far, however, has not been investigated, and this was one of the subjects of study in this thesis.

4.5 Measurement of Electrocatalyst Dissolution by SFC-ICP-MS

Although dissolution of the electrocatalysts in PEMWE *in situ* is not yet known, a field of research that has gained a substantial amount of attention recently regards the dissolution of PGMs in electrochemical systems, and the findings made in which are highly relevant to PEMWE, particularly during periods of OCV. This field of research concerns the use of a scanning flow cell (SFC), a specialized type of electrochemical cell that has both a flowing electrolyte and a translatable working electrode. This cell allows for local electrochemical measurements over a wide working electrode, or it can be used to perform electrochemical measurements on distinct materials with a high throughput, as is visualised in Figure 32. Additionally, the electrolyte is flowed through the cell, and so any corrosion products are carried with the flowing electrolyte. The contents of the electrolyte can then be analysed by inductively coupled plasma – mass spectrometry (ICP-MS) [213]. This complete system (SFC-ICP-MS) has become a highly useful tool in

dissolution analysis over the last decade, as it is able to discern, with extremely high sensitivity, dissolution arising from particular electrochemical processes such as surface oxidation or reduction [214]. SFC-ICP-MS has now been widely used on PGM and non-PGM materials in both the potential range of fuel cells and electrolysers [198,215,216].

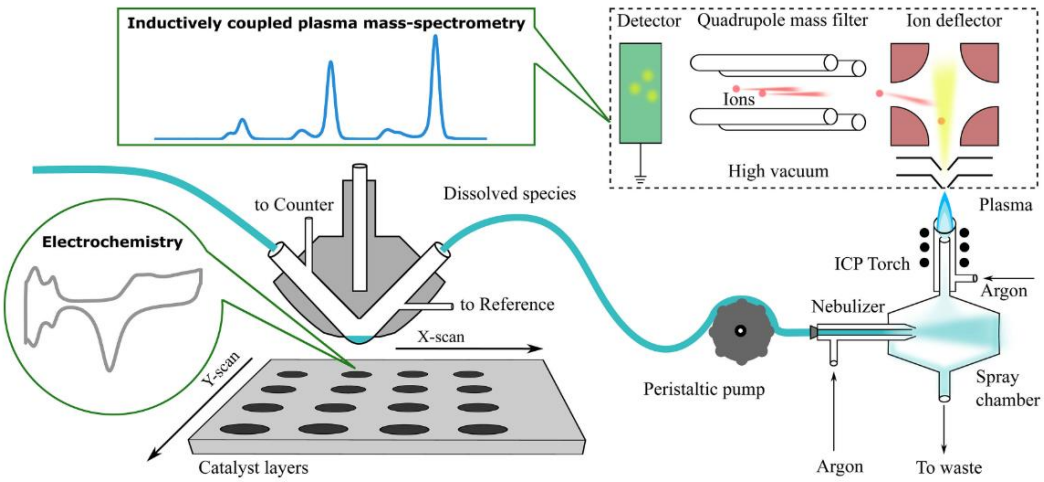

Figure 32. Setup of scanning flow cell-inductively coupled plasma – mass spectrometry (SFC-ICP-MS). Reprinted from [214]. The Scanning flow cell (SFC) is an electrochemical cell that contains a moveable working electrode on a plate (grey table). The table can move hence a number of working electrodes can be tested in a short time. Electrolyte is flowed through the cell, and this is connected to an ICP-MS, which nebulizes the electrolyte and ionizes the elements contained within it. These ions then pass into a quadrupole mass spectrometer in which they are detected.

As one of the first examples of the applicability of SFC-ICP-MS to PEMWE, a study by Göhl et al [217] used this technique to analyse the dissolution of a non-PGM electrocatalyst, tungsten carbide (WC), under potential ranges relevant to both PEMWE and PEMFC. Through analysis of the dissolution response to both constant potential / current operation and anodic and cathodic potential sweeps, they

determined that WC was both highly stable and an acceptable catalyst in the HER region; however, it suffered from high rates of dissolution at 0.8 V NHE and above, making it an unsuitable material for both ORR and OER. At an OER overpotential especially, they observed an extremely high rate of dissolution. This work is a very good demonstration of the power of this tool, as the enhanced knowledge gained by directly measuring degradation because of electrochemical phenomenon means that novel electrocatalyst materials may be rapidly screened. This paper also showed a test regime, one of testing electrocatalyst materials under both constant potential and under potential swings, that is now a common theme in much of the other SFC-ICP-MS literature.

For PEMWE, the dissolution of PGMs is of course of greatest importance. SFC-ICP-MS has been performed now on a range of PGMs, including Pt both in crystalline form and nanoparticles, and IrO_x and Ir – RuO_x MMOs [180,218]. One of the earliest reports using SFC-ICP-MS was provided by Topalov et al [219], who investigated the dissolution of a polycrystalline Pt electrode under potential control. In this work they made the interesting finding that, when it occurred under potential control, dissolution of Pt was not a continuous process but a transient one, only occurring during redox changes on the Pt. This therefore occurred during Pt oxidation, during Pt oxide reduction, or during OER. This process was also observed on nanoparticle Pt/C by Pavlišič et al [220], where they produced a very good example of the behaviour described (Figure 33).

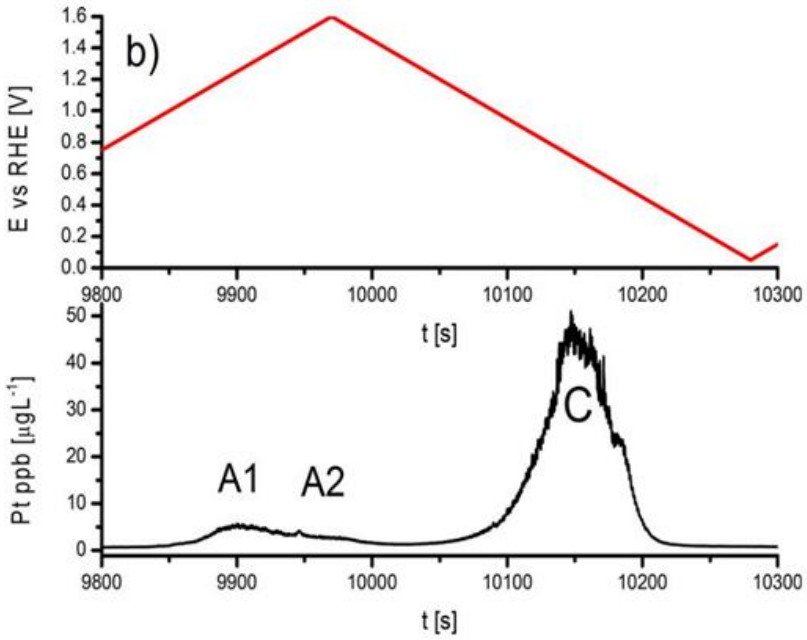

Figure 33. The transient dissolution of nanoparticle Pt/C (black) as a function of the electrode potential (red). Denoted as A1 is the dissolution peak produced because of Pt oxidation, A2 is the dissolution caused by the onset of OER, and the large peak denoted C is the dissolution mechanism observed as a result of the reduction of the Pt oxide. Reprinted from [220].

This complex profile, whereby dissolution by reduction is extremely high compared to that by oxidation, is a general observation with other PGMs also [215]. One explanation for this effect was given in a separate study by Topalov et al [221]. They here stated that the Pt dissolution mechanism (Table 1. Reaction 7) couples with Pt oxide formation and place-exchange to create this transient phenomenon. Briefly, place exchange is the mechanism by which sub-surface Pt oxides are formed. During oxidation, oxygen species adsorb on the surface of the Pt (they associate on the Pt surface without initially chemically reacting). Chemisorption follows this (Pt-O bond formation). Whether a sub-surface oxide is formed depends on the concentration of the surface oxides, as initially the enthalpy of surface oxidation is higher than the enthalpy of sub-surface oxidation. As the concentration of surface oxides build up however, and the electrostatic

repulsion between the negatively charged oxygen atoms increases, then the enthalpy of surface oxide formation decreases and eventually becomes less than the enthalpy of sub-surface formation, and so a sub-surface oxide forms. The process by which this happens is a redox reaction between the sub-surface and surface Pt; sub-surface Pt becomes oxidized and the surface Pt is reduced. The surface Pt may then undergo another oxidation to form an oxide surface, or it may undergo dissolution, direct electrochemical dissolution or chemical dissolution (Equation(41) (as Pt place-exchange leaves Pt at the electrode surface, even though it is chemically bonded to a sub-surface oxide group, it may additionally undergo chemical dissolution). The passivated layer suppresses this reaction, however; and as long as place-exchange is not occurring, the rate of this chemical dissolution process will diminish along with electrochemical dissolution. For this reason, the transient nature of oxidative dissolution was explained, as the surface concentration of adsorbed species will only increase with increasing potential, and at a steady potential it will reach an equilibrium and so place-exchange and the associated dissolution will stop occurring. Thus, only with increase in potential will this dissolution mechanism occur.

$$\mathrm{PtO} + 2\mathrm{H}^{+} \rightarrow \mathrm{Pt}^{2+} + \mathrm{H_2O} \qquad (41)$$

During oxide reduction, the surface Pt is reduced and is thus able to be dissolved; however, the potential of the electrode also allows for the redeposition of the dissolved Pt. A cycle forms whereby Pt is becoming dissolved but is also being redeposited. The dissolution reaction also exposes sub-surface oxides that, in addition to electrochemical dissolution, can then undergo direct chemical dissolution also. Chemical oxidation

(Reaction 7.1) is promoted by higher acidity, and higher scan rates promote redeposition over dissolution as deposition is a reduction process. Both relationships are trends observed throughout the SFC-ICP-MS literature.

Cherevko et al [215] have demonstrated a similar effect on Ir, Rh, Pt, and Au, but expanded upon this work with a deeper investigation of dissolution during OER at increasing overpotentials. At OER they demonstrated that there was a continuous dissolution process occurring, although for Ir, Pt and Pd the rate of this was never greater than the Pt – oxide dissolution transient, and there was no, or only a very limited, relationship between current density and the dissolution rate. Dissolution during OER here was stated to occur only due to further surface oxidation and the oxide surface restructuring, and as a result it was largely transient at the potentials tested, a phenomenon consistent with other works by the same author [222]. In the case of Ru and Au however, dissolution rate increased sharply with increased current density and remained high. The difference between these results can be explained by the process in which the materials oxidize. Pt and Ir, when oxidising in acidic conditions, tend to passivate (Figure 20b, Figure 34) [85]. In the same pH - potential range for Au and Ru however, oxidation to a water-soluble species is expected (corrosion).

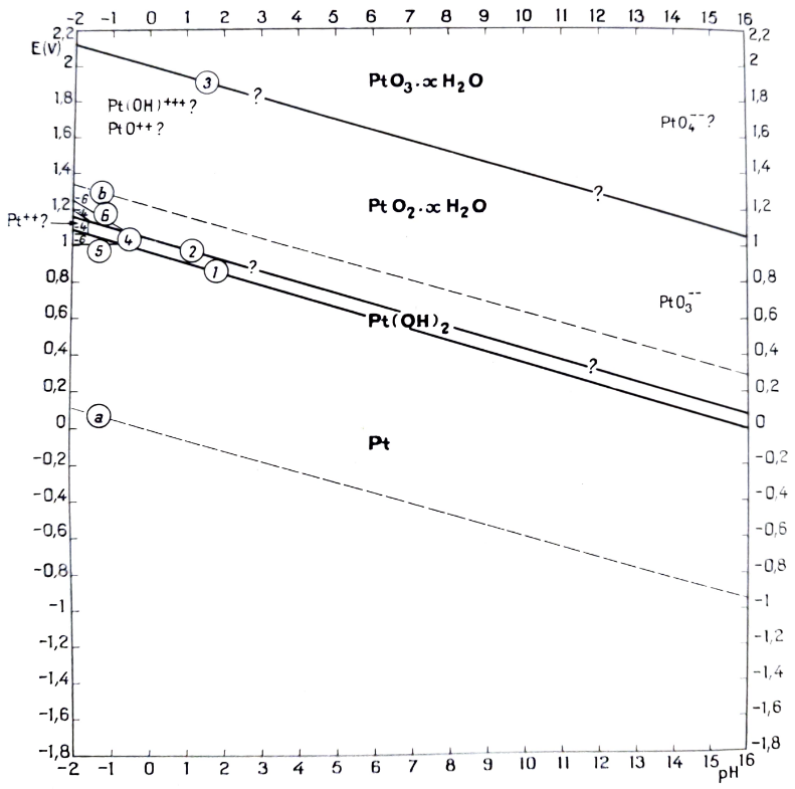

Figure 34. pH – potential (Pourbaix) diagram of the thermodynamically stable states of Pt in aqueous non-coordinating electrolyte. Reprinted from [85].

SFC-ICP-MS potential cycling studies have also been performed on a Pt electrode in solutions with the presence of chloride ions by Geiger et al [223]. This was an experiment aimed at investigating the effect of chloride impurities on the rates and types of dissolution occurring, as groups such as Cl^- can coordinate to Pt to form soluble complexes, thus enabling dissolution. This work is of relevance to PEMWE as chlorides are known contaminants in the feedwater, with the expectation that Cl^- would alter the redox potentials for dissolution and possibly alter the oxidation processes. The results were, however, contrary to this hypothesis. At the low Cl^- concentrations used, the passivation of Pt upon oxidation was still the dominant mechanism, although Cl^- did affect the dissolution profiles observed. During the oxidative and reductive sweep, in comparison to analogous Cl^- free tests, there was a marked increase in the transient

dissolution amount at the highest concentration of Cl^- (1000 μM) at potentials greater than 1.5 V NHE. This was taken as evidence of Cl^- attack of the Pt surface oxide. It was determined that, although the Pt oxidation mechanisms overall are the same in Cl^--containing and Cl^--free electrolyte, the presence of Cl^- does initially hinder the formation of the Pt-oxide passivated layer by the reaction of the surface with Cl^- ions. This occurs from as low as 0.76 V NHE as opposed to 0.85 V NHE for Pt dissolution and oxidation. Furthermore, the formed $[PtCl_4]^{2-}$ species was suggested to have a higher deposition overpotential, thereby also influencing the dissolution profile during the reductive sweep.

Finally, SFC-ICP-MS has been used to gather more information pertaining to the OER mechanism itself. As already mentioned, the OER mechanism, whilst numerous models have been proposed, has not been definitively elucidated. The application of SFC-ICP-MS to IrO_x during the OER process itself has been highly interesting, and this technique has made several demonstrations that have been useful in uncovering the mechanism occurring. Firstly, it has been demonstrated, through the use of isotopically labelled oxygen (O^{18}) on the IrO_x, that the OER mechanism itself involves the release and reformation of surface oxides, and that this exchange of surface bound oxygen atoms occurs much more rapidly with hydrous surface oxides [224]. Additionally, it has been demonstrated that OER and dissolution may be intrinsically linked, indicating that a common intermediate of OER (possibly Ir^{3+} or Ir^{6+}) may be responsible for both the OER mechanism itself and the dissolution [225,226]. This, in conjunction with the general activity – stability trends observed with the Ir – RuO_x MMOs, raises the interesting possibility that there is a fundamental inverse correlation between the rate of activity of an OER electrocatalyst and its lifetime.

4.6 Summary

This review of the literature contains what the author believes to be the majority of literature in the fields of PEMWE performance and OCV, the state-of-the-art in PEMWE electrocatalysts, and the literature surrounding electrocatalyst dissolution in its various guises. In contrast to PEMFC, PEMWE is not an intensively studied field. This is true also for electrolysis in general when compared to their fuel cell counterparts. In some cases, the findings in PEMFC literature are directly relevant to PEMWE. For example, HER and HOR in PEM have a high similarity in terms of mechanism and potential range. Therefore, the electrocatalysts used in these cases are identical. OER and ORR are not the same, however. Different catalysts are required, and the high potential at OER means that only a very narrow range of materials are suitable (PGMs), thus presenting a narrow scope for cost or performance improvements. As one of the major concerns over PEMWE remains its high cost, one of the most important fields of work that may directly drive down costs are investigations into using reduced amounts of PGMs.

Although the general consensus is that the lifetime limiting factor in PEMWE is the thinning of the SPE, understanding and quantifying the degradation of the electrocatalysts is very important. Firstly, PEMWE performance ultimately depends on the long-term efficacy of the electrocatalysts. Efficacy will change if the electrocatalyst degrades over time to a less efficacious material, such as Ru leaching from Ir – Ru MMOs leaving behind IrO_x only, or the oxidation of the IrO_x supporting material to a non-conductive oxide. Secondly, catalyst loadings in PEMWE are continuously being fine-tuned so that valuable PGMs are not wasted within the electrocatalyst bulk. The most active catalyst is one in which every electrocatalyst atom contributes to the ECSA.

Whilst approaches to make this kind of catalyst make cost savings, it does make the PEMWE more susceptible to electrocatalyst degradation, as less extra electrocatalyst material becomes available as redundancy. Therefore, by using less, the 'tipping point' at which degradation begins to impact performance is brought closer, and so electrocatalyst degradation may begin to hinder the PEMWE performance sooner than has been previously observed. For this reason, the reduction in electrocatalyst loading must come with an improved understanding of how, and to what extent, degradation occurs in PEMWE. The SFC-ICP-MS literature is highly useful for this, as it aids in the understanding about how degradation, in particular dissolution, manifests. It cannot, however, be extrapolated with any real accuracy to make a prediction about how long the electrocatalyst will last in a real PEWME system at real loadings. To date, an attempt to quantify electrocatalyst degradation by dissolution has not been made in PEMWE, and this represents a gap in the knowledge that was the subject of study in this thesis.

5 Methodology

5.1 PEMWE Cell Construction

The 3-electrode PEMWE cell developed in this study (Figure 35) was an adaptation of that used by Brightman et al [123] (Figure 41).

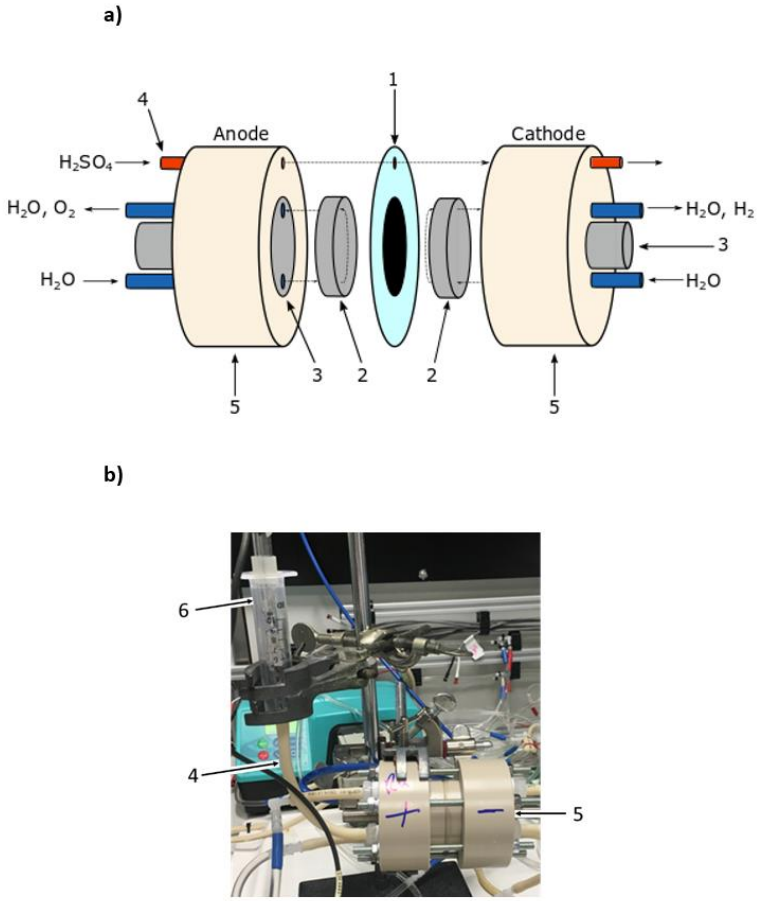

Figure 35. Schematic of 3-electrode cell (a) and the cell setup (b) used in this thesis. The cell design consists of CCM with a Nafion peripheral area acting as a gasket (1), PGM-coated titanium gas diffusion layers (2), gold-coated titanium pistons (3), Luggin capillary (4) in ionic contact with the Hg / $HgSO_4$ reference electrode in a reservoir of 0.5 M H_2SO_4 (6). The cell is contained within polyether ether ketone (PEEK) cell halves (5) and compressed with threaded rods.

The PEMWE cell design in Figure 35 has a 5 cm^2 circular active area, consisting of a CCM (1), a sintered titanium gas diffusion layer (GDL, Merelex Corporation TI-M-01-FM.2MMT, thickness 2 mm, average pore size 100 µm), a diamond titanium mesh (Goodfellow – TI008720) (2), and pneumatically actuated titanium pistons (3). Both (2) and (3) were coated with 1 µm of PGM (TEER coatings). The PGM coating used varied depending on the test. For the OCV tests a Pt coating was used so that the test was most representative of commercial PEMWE. For testing of Pt dissolution an Au coating was used.

To facilitate electrode potential measurements, ionic contact to the Nafion membrane in the CCM was made through a hole bored through the cell halves 1 mm from the edge of the current collector (4), the membrane around the sealing edge was pierced at the hole and filled with 0.5 M H_2SO_4. One end of the hole in the completed cell was connected to a reservoir containing a Hg / $HgSO_4$ reference electrode, and the other was closed off after H_2SO_4 had drained through it. Upon operation, the pistons were pneumatically driven with 150 N cm^{-2} pressure to bring the GDL and CCM into intimate contact.

In order to ensure that any drift in the reference electrode did not impact the OCV results, the Hg / $HgSO_4$ reference electrode was regularly tested against two other Hg / $HgSO_4$ reference electrodes and a saturated calomel electrode. Throughout all testing regimes, the potential of the reference electrode did not drift by greater than 5 mV. Additionally, the reference electrode was regularly topped up with 0.5 M H_2SO_4 to avoid potential change caused by contaminants.

5.2 Balance of Plant Construction

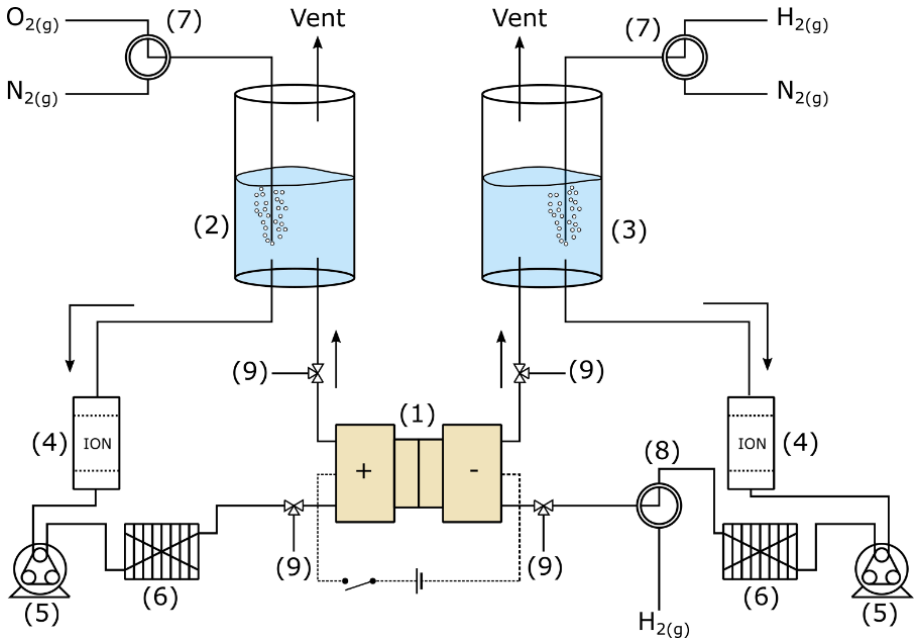

Figure 36. The balance of plant supporting the PEMWE cell.

Figure 36 gives the PEMWE cell balance of plant used in this thesis. (1) is the PEMWE cell. (2) and (3) are the 4.5 L anode and cathode water / gas separation towers respectively, both maintained with 4 L of H_2O before each test. (4) Are the mixed-bed ion exchange resin columns. (5) are the peristaltic pumps, set at a flow rate of 5 mL cm^{-2} min^{-1}. (6) are the heat exchangers set so that the inlet temperature of the water into the cell is 60 ^oC. (7) are the three-way valves to allow the gas purging of the reservoirs. (8) is a 3-way valve to allow $H_{2(g)}$ flow through the cathode. (9) are the sample valves to allow water samples to be taken at the inlet and outlet of the anode and cathode.

5.3 CCM Fabrication

The CCMs used in this study were produced in-house. The CCM production method chosen was a multi-step process that is provided in detail below. In brief, it consists of the formulation of catalyst inks, the spraying of the inks onto a Teflon - based substrate, the decal transfer of the layer onto the Nafion membrane, and the acid washing of the CCM to ion-exchange out any impurities in the Nafion or electrocatalyst layers. In this study IrO_2 – PtB CCMs and IrO_2 – Pt/C CCMs were produced, both using Nafion 117 membranes (175 µm thickness).

5.3.1 Catalyst Ink Formulation

There are three ink recipes that were used in this thesis: a IrO_2 ink, a PtB ink and a Pt/C ink. All inks contained a certain amount of Nafion ionomer to act as a binder to the membrane. Both PtB and IrO_2 inks were made following the same recipe; 1 g of PtB (Sigma maintained at 60 $^{\circ}$C Aldrich 520780, 25-34 $m^2 g^{-1}$) or IrO_x (Alfa Aesar 43396) was mixed with 1 mL deionised water (18.2 MΩ cm) and 0.01 g polyacrylic acid solution (Sigma-Aldrich 52395, 35 wt % in water). The slurry was then stirred until the catalyst was fully wetted. To this, 5 g of Nafion dispersion was added (D521, 5 wt % Nafion dispersion in 45 % water) and mixed so that a ratio by mass of 4:1 catalyst: Nafion solids was achieved. This mass ratio was chosen as it has approximately similar volumetric ratios to the more standard Pt/C: Nafion ratios, which are more commonly around 2:1 [227]. After further mixing, 4 mL more deionised water was added, followed by 5 mL isopropyl alcohol (IPA, Sigma Aldrich W292907). The ink was then dispersed in an ultrasonic bath for a minimum of 30 minutes prior to spraying.

The major difference between the IrO_2 / PtB recipe and Pt/C recipe was the weight ratio of catalyst: Nafion. 1g of Pt on carbon (Pt/C) (Alfa Aesar 42204, 70 m^2g^{-1}) was mixed with 5 mL deionized water and stirred until the catalyst was fully wetted. To this, 10 g of Nafion dispersion was added and mixed so that a ratio by mass of 2:1 Pt/C: Nafion solids was achieved. After further mixing, 5 mL isopropyl alcohol was added. The ink was then dispersed in an ultrasonic bath for a minimum of 30 minutes prior to spraying.

5.3.2 CCM Fabrication by Decal Transfer

Catalyst inks were hand sprayed using a Spraycraft SP30KC spray gun onto pre-weighed 5 mil glass reinforced Teflon sheets on a hot plate set at 90 ^oC. A 5 cm^2 circular mask was placed over the Teflon sheet in order to produce a defined spray geometry. Periodically during spraying, the substrate was weighed on a 4-point analytical balance to give an accurate measure of the mass gain and hence the catalyst loading. With the appropriate catalyst loadings, the sprayed catalyst layers were sandwiched onto 16 cm^2 Nafion® 117 membrane (Fuel Cell Store 591239), with two more Teflon substrates backing each catalyst-sprayed Teflon sheet, and finally backed by a pressure distributing felt. Decal transfer here was chosen as the process to produce the CCMs as it was the easiest method by which the catalyst loading onto the CCM could be measured. As Nafion is a highly hydrophilic material, the direct spraying of the catalyst onto the membrane makes it difficult to measure mass as the Nafion uptakes the water from the spray inks. This uptake is greater than the weight of the catalyst, and so the membrane requires careful drying before it can be weighed. As PTFE is hydrophobic and therefore does not uptake water itself, it is significantly easier to weigh the mass of the catalyst layer once sprayed.

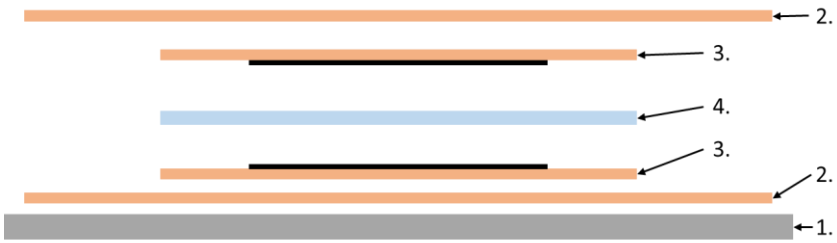

Figure 37. The CCM - Teflon layout for hot pressing. (1) The pressure distributing felt. (2) The Teflon sheets. (3) The Teflon sheets with the catalyst layers. (4) Nafion® 117 membrane.

This sandwich was placed into a Bungard hot press preset at 140 °C. 6 bar pressure was applied for 5 minutes, after which the sandwich was removed from the press and left to cool. The Teflon layers were peeled off from the Nafion, leaving the catalyst layers laminated on the Nafion membrane, thus producing the CCM. The CCMs were then soaked in 125 mL of 0.5 M H_2SO_4 for a minimum of 1 day prior to use.

5.4 Overview of Electrochemical Methods Applied to PEMWE

All electrochemical tests on the PEMWE cell were performed using a Gamry Interface 5000 potentiostat.

5.4.1 Constant Potential Hold

The constant potential hold test was performed in section 8.2 to provide water samples for analysis by voltammetry and ICP-MS. In this test, the cathode of the PEMWE was controlled, and was held at a series of potentials ranging from -0.07 V NHE (operation at approximately 1 A cm^{-2}) to 1 V NHE. The cathode was stepped up in the positive direction and was held at each potential for 1 minute whilst the water samples from the cathode were taken. In this test, the cell was maintained at 60 °C by a heater / chiller

(Huber Unichiller 010 Olé), with an active water flow through both the anode and cathode at 5 mL cm^{-2} min^{-1}.

5.4.2 IV Curves

IV curves in this thesis were performed under current control. The cell temperature was maintained at 60 ^{o}C with a 5 mL cm^{-2} min^{-1} flow of water at both the anode and cathode. The cell was pre-conditioned before the IV curve with an operational period of 30 minutes at 1 A cm^{-2} (limited to a maximum cell voltage of 2 V). To produce the IV curve, the cell was held at a stepwise series of current densities ranging from 1 A cm^{-2} to 0.01 A cm^{-2}. Each current density was held for 1 minute, and the cell voltage was measured as an average of the final 10 seconds of data at each step.

5.4.3 Galvanostatic Electrochemical Impedance Spectroscopy (GEIS)

Electrochemical impedance is a technique by which an electrochemical cell may be analysed by its response to variations in current or voltage. Galvanostatic impedance measures the voltage response of the cell to a variation in the input current. The way in which an electrochemical cell responds to changes in current is dependent on the electrochemical parameters of the cell itself, crucially in regards to the resistance of the electrolyte to ion migration, the resistance associated with the electrochemical reaction itself, and the capacitance of the electrochemical double layer. These parameters can be expressed as an electrical circuit (the Randles equivalent circuit). Shown in Figure 38. Shown in Figure 38a is the Randles equivalent circuit used in this study to express the whole PEMWE cell.

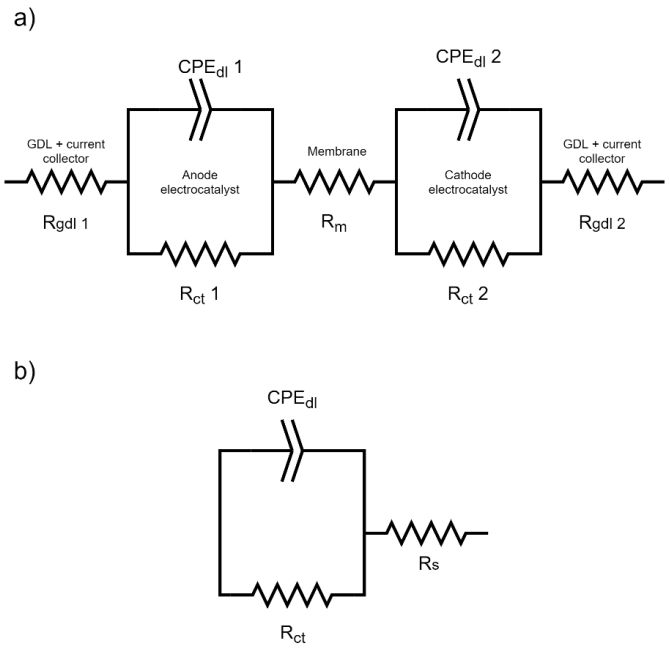

Figure 38. Randles equivalent circuits of a) the PEMWE cell b) the anode or cathode separately. Constant phase elements (CPEs) are here used in replacement of capacitor elements as the EIS measurements in PEMWE have been shown to deviate from ideal capacitive behaviour [228].

The principle of GEIS is that the voltage response to AC current does not always follow ohms law in capacitive systems. As capacitors charge their voltage increases, and as such they introduce an increasing resistance in the circuit. At very high current frequencies (Figure 39a), the capacitor charges and discharges rapidly enough that there is no appreciable difference in the overall resistance of the circuit. Current passes through the capacitor with zero resistance. As such, the current does not pass through the charge transfer elements (R_{ct}) in the Randles equivalent circuit; the only resistance present is that of the membrane resistance (R_m). The voltage signal is therefore correlated to current by ohms law at this frequency. Here, the AC voltage signal is in-phase with the current signal. At lower AC frequencies (Figure 39b), as the capacitive element begins to be charged, it begins to impart an increasing resistance on the cell. The result of this is that the AC voltage signal falls out of phase with the current. At very low frequencies

(Figure 39c) the AC frequency is low enough that the capacitor fully charges. The current therefore passes through the R_{ct} and R_m elements only. As these are resistance elements the current and voltage oscillations becomes in phase with each other again.

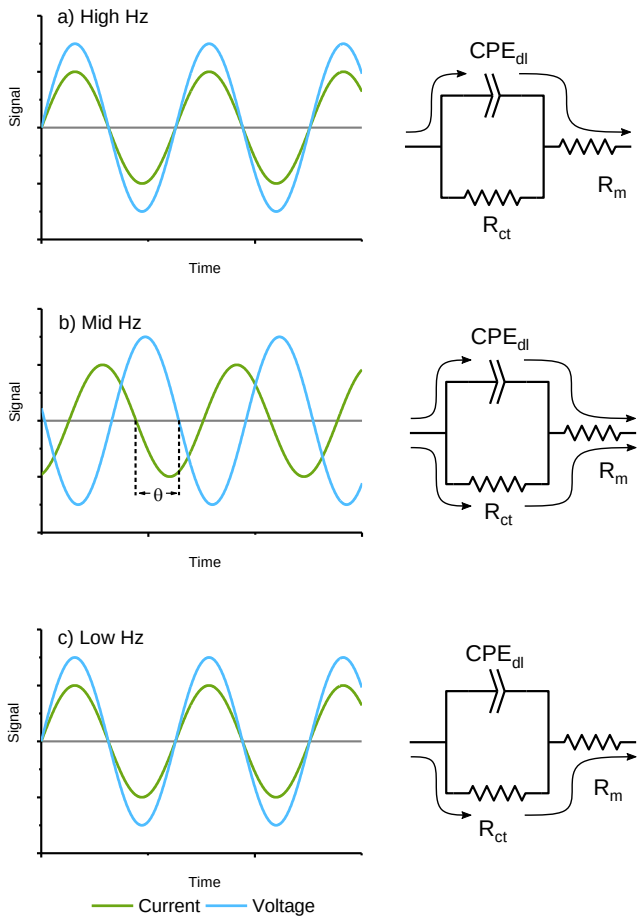

Figure 39. AC current and the voltage response to a) high frequency b) medium frequency and c) low frequency. The corresponding current paths in the Randles equivalent circuit are also shown.

Over a range of AC frequencies therefore, the phase difference between the current and voltage signal progresses from being in phase, to out of phase, to in phase again. There are therefore two elements of the overall impedance signal, a real resistance element (z_{real}) and a phase difference that is measured in degrees. This therefore provides polar

coordinates that are converted to Cartesian coordinates to provide the imaginary resistance element (z_{imag}). Figure 40 is a representative Nyquist plot for the PEMWE Randles equivalent circuit (Figure 38b) and graphs the real versus imaginary resistances over the frequency range (blue line). In this graph form, the voltage signal is in phase with the current at the points that the x-axis is crossed. These values correlate to R_m and R_{ct}. The capacitance is calculated from the maximum value of z_{imag}.

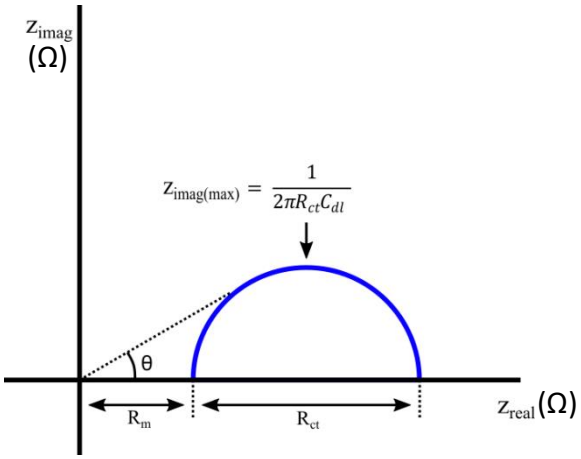

Figure 40. Nyquist plot representative of the Randles equivalent circuit in Figure 38b.

The reality of electrochemical devices is that they cannot be properly described by a single capacitive element in the Randles equivalent circuit. This is because electrodes have surface roughness, may non-uniformly distribute reaction across the electrode, and may be of non-uniform thickness. In replacement of a pure capacitor in the Randles equivalent circuit is a constant phase element (CPE). The CPE element includes an 'α' factor (unrelated to charge transfer coefficient), a dimensionless expression of the deviation of the impedance signal from an ideal capacitor, where α = 1 is an ideal capacitor and α = 0 is a pure resistor with no capacitance. The overall capacitance may

be estimated from the CPE values by the use of Equation (42, as provided in a report by B. Chang [229].

$$C = \frac{(Y_0 R_{ct})^{(1/\alpha)}}{R_{ct}} \sin\left(\frac{\alpha\pi}{2}\right) \quad (42)$$

The parameters of GEIS used in this study are as follows. The DC current density was ranged from 0.01 to 1 A cm^{-2}, with the root mean squared (rms) amplitude of the AC signal being 10 % of the DC signal. The AC frequency was varied from 50 kHz to 100 mHz with 10 frequencies tested per frequency decade. Before each GEIS measurement, the PEMWE cell was pre-conditioned at the respective DC current density for 1 minute.

5.4.4 Cyclic Voltammetry (CV)

Cyclic voltammetry was performed on both the anode and cathode in the PEMWE cell. The potential range for the CV measurements were between 0.05 and 1.2 V NHE with a scan rate of 20 mV s^{-1}. For the anode CV, the anode inlet water was N_2 purged, and the cathode was purged with H_2 gas. For the cathode CV, the cathode inlet water was N_2 purged, and the anode water was air purged. The water flow was maintained at 5 mL cm^{-2} min^{-1} and the cell temperature maintained at 60 ^oC throughout the test. Prior to the CV's reported, each electrode underwent three CV profiles beforehand.

5.4.5 Open Circuit Voltage (OCV)

The OCV tests consisted of (1) operation at 1 A cm^{-2} for a defined time, and (2) the OCV period. There are several distinct OCV states that have been tested in this thesis. Note that the numbers that follow reference the components of the balance of plant, as shown in Figure 36. Testing of different dissolved gas compositions ($O_{2(dis)}$ / $N_{2(dis)}$ / $H_{2(dis)}$)

was achieved by adjusting the 3-way valves (7) so that different gases were bubbled into the reservoirs through the fritted glass bubbler. The flow rate of gas was in excess of 500 mL min^{-1}. To ensure the complete gas saturation of the water in the reservoirs, the gas was bubbled for at least 1 h prior to the OCV period of the test starting.

In flowing water tests, the peristaltic pumps (5) were continuously operated both during pre-OCV operation and during the OCV period. In tests with no flowing water during OCV there were two separate approaches that were made. Firstly, in tests with no flow and dissolved gas only, the pumps were operated for 10 s after the start of the OCV period to attempt to remove gas bubbles from the cell halves. Secondly, in tests with no flow and gas present ($O_{2(g)}$, $N_{2(g)}$ or $H_{2(g)}$), the pumps were stopped 10 s before the start of the OCV period to accumulate gas in the cell halves.

In the tests with 'dry' cathodes, the cathode peristaltic pump was turned off during operation and OCV. Finally, in test 7 where the cathode was actively dried by an input of hydrogen gas into the cathode, the cathode pump was turned off and the 3-way valve (8) was switched to allow this. Hydrogen was pumped through the cathode 60 s before the onset of OCV and for the whole duration of OCV. In the OCV tests studying Pt dissolution, the PEMWE cell has a continuous flow of water but with no gases bubbled into the reservoir.

In OCV measurement of the electrolyser, it is important to note that, whilst it is in theory assumed that there is no current movement between the working electrode and reference electrode, in practice the potentiostat always has a small amount of current transfer between the two electrodes. This is typically in the range of nA to pA. Based on diffusion estimations later in this thesis, it can be assumed that the current that transfers

between the electrodes is negligible and will not affect the potential of the electrodes in any measurable manner.

5.5 Voltammetric Techniques and ICP-MS

5.5.1 The Voltammetry of Pt

The voltammetric analysis of Pt by differential pulse voltammetry (DPV) was performed on a VA 797 Computrace (Metrohm UK). The electrochemical cell consisted of a hanging mercury drop electrode (HMDE) as working electrode, Ag/AgCl reference electrode and a GCE as counter electrode. For note, a HMDE device creates a working electrode by creating a very small drop of mercury at the end of a capillary. This creates a spherical micro-electrode that both facilitates the diffusion of ions and also creates an extremely regular surface. Mercury is also a very poor HER catalyst, and hence electrochemistry in water is possible well below the typical potential at which HER occurs. Electrochemistry below -0.5 V NHE is regular with HMDE. The supporting electrolyte consisted of 0.7 M H_2SO_4 (Sigma Aldrich 339741), 6.7 mM formaldehyde (Sigma Aldrich 252549) and 3 mM hydrazine sulfate (Sigma Aldrich 455865). 1.5 mL of supporting electrolyte was pipetted into the electrochemical cell with 9 mL deionized water (18.2 MΩ cm) and 1 mL of sample. The hydrazine reduces any Pt(IV) species to Pt(II), and the reaction of hydrazine and formaldehyde forms formaldehyde hydrazone, which can complex Pt(II) to form a positively charged Pt(II) - hydrazone complex. The voltammetric technique for the determination of Pt concentration comprises pre-concentration of the Pt complex by adsorption on the surface of the HMDE, followed by DPV in the HER region. The experimental parameters for the test are given in Table 2. For quantification of dissolved Pt concentration, the method of standard additions was used; two DPV sweeps were

taken at the initial concentration, followed by two sweeps with one standard addition of 10 µL of 1 µg L^{-1} Pt solution, followed by a further two sweeps with a final addition of the same concentration and volume. From this the initial concentration was calculated from a line of best fit. Representative DPV sweeps and the line of best fit can be found in Figure 69.

Table 2. Experimental parameters for the determination of dissolved Pt concentration by DPV. The effect of the terms on the DPV profile is given in Figure 68.

Parameter	Pt(II)
Pre-concentration step	
Stirring rate, r	600 rpm
Pre-concentration potential	-0.6 V (Ag/AgCl | 3 M KCl)
Pre-concentration duration	120 s
Equilibration duration	10 s
DPV sweep	
Start potential	-0.6 V (Ag/AgCl | 3 M KCl)
End potential	-1.1 V (Ag/AgCl | 3 M KCl)
Potential step	0.006 V
Step time (t_1 and t_2)	0.3 s
Sweep rate (v)	0.02 V s^{-1}
Pulse amplitude (A)	0.05 V
Characteristic catalytic wave potential	-0.88 V (Ag/AgCl | 3 M KCl)

5.5.2 The Voltammetry of Ir and Ru

Voltammetry of Ir and Ru was performed on the VA 797 Computrace. The electrochemical cell was different depending on the element under analysis, although the same solution is used throughout. For the detection of Ru, a HMDE is used; and for

Ir, a GCE is used as working electrode. Both cell configurations use an Ag/AgCl/KCl_{sat} reference electrode and Pt wire counter electrode. For Ru(III), the initial supporting electrolyte consists of a 1 mol L^{-1} acetate buffer at pH 4.9 (made by mixing 81 mL of 1 mol L^{-1} ethanoic acid with 50mL 1 mol L^{-1} NaOH. To this solution, $NaBrO_3$ was added to achieve a concentration of 0.154 mol L^{-1} in the electrolyte. 5mL of sample solution was mixed with 5 mL of the supporting electrolyte in the electrochemical cell. Before analysis the solution was deaerated with N_2, followed by a pre-concentration step at a potential of 0.150 V Ag/AgCl/KCl_{sat} for 300 s. After this, DPV was applied to the electrode, with the characteristic potential of Ru reduction was stated by C. Locatelli [230] to occur at - 0.23 V Ag/AgCl/KCl_{sat} .

For the detection of Ir(III) the HMDE was swapped out for a GCE, and 1 mL of cetrimonium bromide (CTAB) and 1 mL of KCl is added. The electrode undergoes a pre-concentration step again followed by another DPV sweep. The characteristic potential of Ir-reduction is around 0.55 V (Ag/AgCl/KCl_{sat}).

Table 3. Experimental parameters for the determination of dissolved Ru(III) and Ir(III).

Parameter	Ru(III)	Ir(III)
Pre-concentration step		
Stirring rate, r	600 rpm	600 rpm
Pre-concentration potential	0.15 V (Ag/AgCl/KCl_{sat})	0.8 V (Ag/AgCl/KCl_{sat})
Pre-concentration duration	300 s	240 s
Equilibration duration	10 s	10 s
DPV sweep		
Start potential	0.2 V (Ag/AgCl/KCl_{sat})	0.75 V (Ag/AgCl/KCl_{sat})
End potential	-0.5 V (Ag/AgCl/KCl_{sat}))	0.3 V (Ag/AgCl/KCl_{sat})
Potential step	0.05 V	0.05 V
Step time (t_1 and t_2)	0.1 s	0.1 s
Sweep rate (v)	0.1 V s^{-1}	0.1 V s^{-1}
Pulse amplitude (A)	0.05 V	0.05 V
Characteristic catalytic wave potential	– 0.23 V (Ag/AgCl/KCl_{sat})	0.55 (Ag/AgCl/KCl_{sat})

5.5.3 ICP-MS

The quantification of Pt concentrations by ICP-MS was performed using a Varian 820-MS. The samples were conditioned to 1% HNO_3 to stabilise any elements in solution. Pt standard solutions (19078 Sigma Aldrich – Diluted to test concentrations with 0.1 mol L^{-1} HCl) in the range of 0.2 – 20 ng L^{-1} were used to produce the calibration curve. The Pt concentrations from the PEMWE that were tested in the ICP-MS were compared against this calibration curve to give the concentrations.

5.5.4 The Treatment of Water Samples for Total Pt Loss Measurements

The preparation of the samples for total Pt measurements by voltammetry was performed in the following procedure. 5 mL of water sample was pipetted into a glass vial preweighed on a 4 decimal point balance. The vial was then placed in an oven preset at 99 ^oC and containing a desiccant. Once dried, the vial was removed from the oven and was left to cool. Once cooled, 1.6 mL of 37 % HCl was pipetted into the vial followed by 0.4 mL of 65 % HNO_3. The vial was then weighed. The vial was then shaken until thoroughly mixed and was then placed in a 100^oC heated sand bath under a fume hood. The sample was then left overnight. The vials were then weighed so that the mass loss due to gas evolution could be factored. 1 mL of the solution was then pipetted into a separate vial containing 4 mL of type 1 water. The solutions were then left in a fridge until analysis.

5.6 3-Electrode PEMWE Cell Development

5.6.1 3-Electrode PEMWE Cell Design

The 3-electrode PEMWE cell developed in this thesis was an adaptation of that used by Brightman et al [123]. In the Brightman cell, a Nafion Luggin capillary was used as a salt bridge, connecting the reference electrode to the surface of the electrocatalyst under test by passing through a hole bored in the cell half, current collector and GDL (Figure 41).

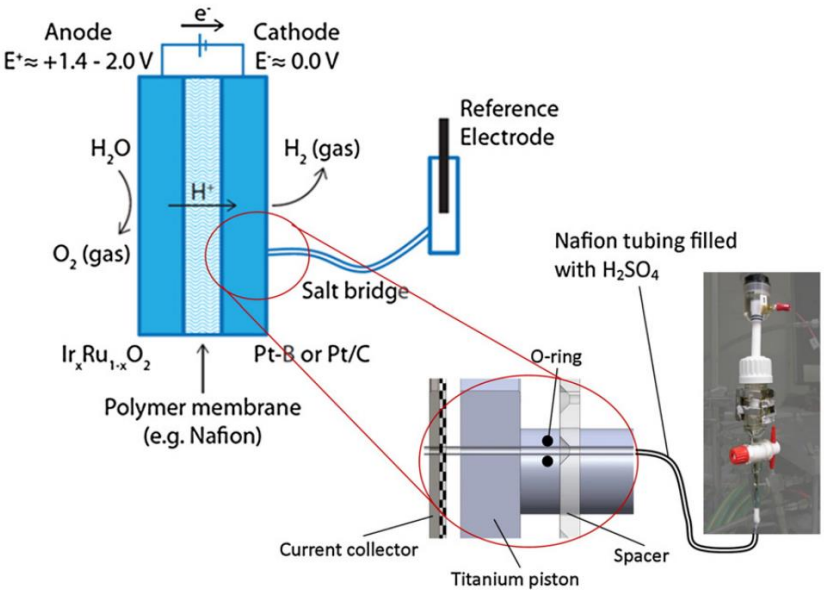

Figure 41. 3-electrode cell containing an in-line Luggin capillary connected to a reference electrode. Reprinted from [123].

As the author was aware of certain limitations regarding the long-term mechanical stability of this 3-electrode design, and as the aim of this thesis was to perform tests over the course of several days, a new and simpler 3-electrode PEMWE cell design was developed. The final cell design used in this thesis is described in detail in section 5.1.

The Brightman cell, and the cell used in this thesis, had similar design principles and componentry, and the only major difference was the positioning of the Luggin capillary. The Luggin capillary was instead located on the sealing edge of the cell and was designed to use the exposed Nafion on the CCM that forms the watertight seal as an extension of the salt bridge to link the reference electrode with the electrocatalysts. This design worked under two assumptions: Firstly, that the Nafion within the sealing edge remained hydrated and highly ion conductive. Secondly, it was assumed that the performance of the cell at the edge of the electrode was the same as that at the centre of the cell. Herein lies a possible weakness worth highlighting with this cell design however; which is that there is some evidence in PEMWE literature that, during operation, the current is non-homogeneous across the active area with greater currents experienced around the edges of the cell [231]. The exact reasons for this are unclear; however, some studies have shown that both the dynamics of the bubble behaviour and water stoichiometry can affect the homogeneity of performance [232,233]. Differences in the uniformity of the thickness of the GDL and current collector can also have a profound impact upon current distribution [234]. It may therefore have been expected that, during operation, the overpotentials measured may have been of the edge rather than the whole cell. The existence of this possible 'edge effect', whilst important to operation, was unimportant during OCV, as there is no net current during this period. As much of this thesis regards *in situ* phenomenon during OCV periods, this 'edge effect' was overlooked.

5.6.2 Validation of the New 3-Electrode PEMWE Cell

The new 3-electrode PEMWE cell design necessitated a set of validation tests to ensure performance, and to test whether the off-centre positioning of the Luggin capillary contributed any iR drop in the measurement. Determining iR drop is common practice in electrochemistry, and it is equally important with *in situ* devices with 3-electrode cells [235–237]. In this study, iR drop was determined using the approach adopted by Offer et al [238] - performing galvanostatic electrochemical impedance spectroscopy (GEIS) over a range of current densities. In this study, the change in the determined series resistance (R_s) over current density (which should be constant with respect to current density) was attributed to the iR drop.

By consideration of the Randles equivalent circuit for a PEMWE cell (Figure 38a), R_s is a combination of both the membrane series resistance (R_{mem}) and, to a lesser extent, the series resistance of the GDLs and current collectors (R_{gdl} 1 and R_{gdl} 2). From EIS alone these resistance values cannot be distinguished from one another, and the R_s value is the sum of these. There were three R_s values produced when GEIS on the 3-electrode PEMWE cell was performed: R_s of the whole PEMWE cell (measured between the working electrode and counter electrode), R_s of the anode (between the working electrode and reference electrode) and R_s of the cathode (between the reference electrode and counter electrode). With negligible iR drop, $R_{s/anode} + R_{s/cathode}$ should have been equal to $R_{s/cell}$ and should have been constant with current density. The values for $R_{s/anode}$ and $R_{s/cathode}$ predominantly denote what contribution of the R_{mem} was taken by each electrode coupling and does not relate to individual electrode performance.

GEIS measurements were taken at current densities increasing from 0.01 A cm^{-2} to 1 A cm^{-2} DC. The CCM in this test was an IrO_x anode at 3 mg cm^{-2} and Pt/C cathode at 0.5 mg cm^{-2}. Representative Nyquist plots for the cell, anode and cathode EIS at 0.1 A cm^{-2} DC are given in Figure 42. The EIS curves of the anode and cathode were fitted to the Randles equivalent circuit shown in Figure 38b, with the results of the fittings overlaid as dotted lines in Figure 42. Fittings were performed using the Levenberg-Marquardt method up to 1000 iterations. R_s was calculated at each current density in this manner, although it may additionally be determined as the leftmost point at which the EIS plot crosses the x-axis.

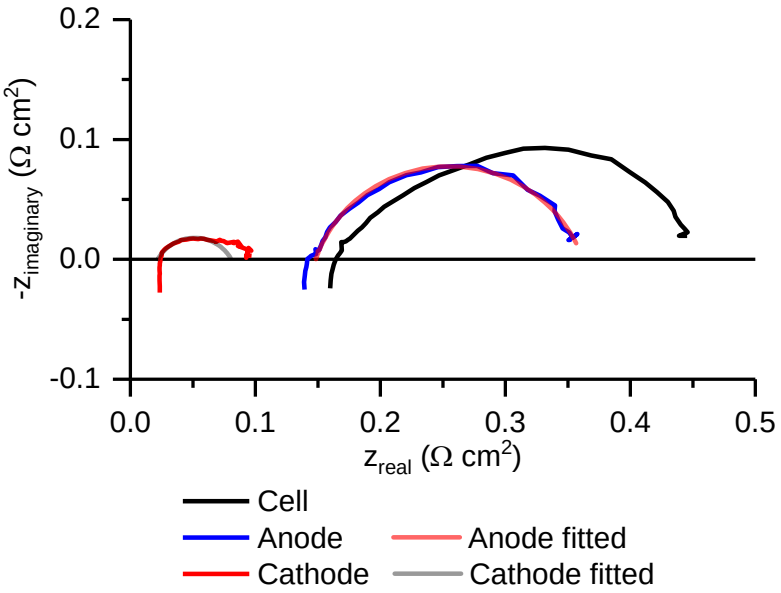

Figure 42. GEIS of 3-electrode PEMWE cell at 0.1 A cm^{-2} DC. Shown in black is the measured cell GEIS. The measured anode shown in blue and the measured cathode shown in red. The best fit of the anode and cathode impedances are shown in pink and grey respectively.

The full cell EIS was fitted to the Randles equivalent circuit in Figure 38a, with the results of this fitting shown in Figure 43. In addition to this, as the parameters for the anode

and cathode have been fitted, and the Randles equivalent circuit is a series combination of the anode and cathode equivalent circuits, the expected EIS curve from this combination is also given. The results of the fittings are given in Table 4. As can be seen, the anode plus cathode fit is a relatively good match for the cell EIS, with only slight differences in the measured CPE and charge transfer resistances. The cause of this difference may again be due to 'edge' effects – The anode and cathode may have slightly improved performance at the edge and so have reduced charge transfer resistances compared to the centre. This would mean that the cell EIS, which may be considered a measurement of the entire cell, would have slightly poorer performance than the anode plus the cathode EIS, which may have given the performance in the area close to the Luggin capillary only.

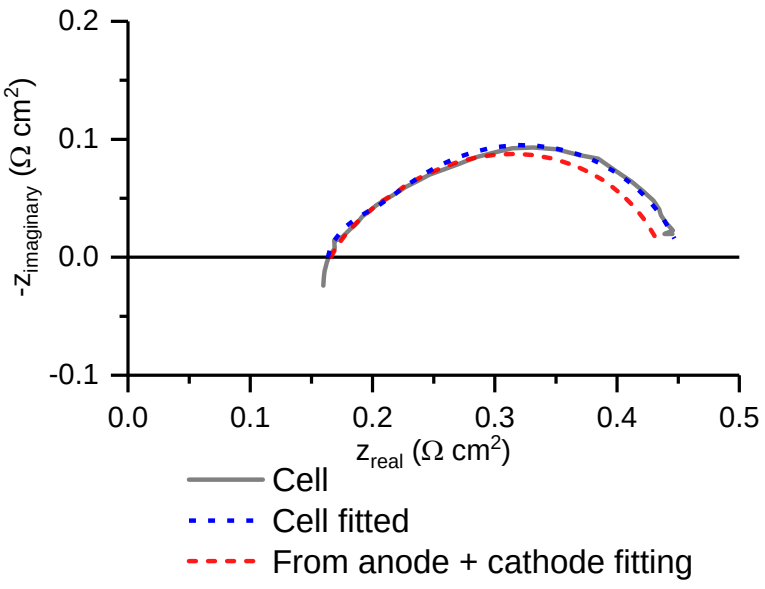

Figure 43. GEIS measurement of the cell shown in grey. The fitted Randles equivalent circuits based on the 2-electrode (cell) is shown in blue, with the fitted anode plus cathode Randles equivalent circuits given in red.

Table 4. Fitting results of the Randles equivalent circuits in Figure 38 to the EIS curves in Figure 42.

Fitting	*Parameter*	*Value*
Anode	$R_{s/Anode}$	0.149 ± 0.002 Ω cm^2
	$R_{ct/Anode}$	0.214 ± 0.006 Ω cm^2
	$CPE_{dl/Anode}$	0.464 ± 0.034 $S*S^{-\alpha}$ cm^{-2}
		α = 0.801 ± 0.022
Cathode	$R_{s/Cathode}$	0.022 ± 0.001 Ω cm^2
	$R_{ct/Cathode}$	0.059 ± 0.003 Ω cm^2
	$CPE_{dl/Cathode}$	0.553 ± 0.081 $S*S^{-\alpha}$ cm^{-2}
		α = 0.699 ± 0.028
Cell (Cell from anode + cathode)	R_s	0.163 ± 0.002 Ω cm^2
		(0.171 ± 0.002 Ω cm^2)
	$R_{ct/Anode}$	0.253 ± 0.029 Ω cm^2
		(0.214 ± 0.006 Ω cm^2)
	$CPE_{dl/Anode}$	0.388 ± 0.046 $S*S^{-\alpha}$ cm^{-2}
		α = 0.807 ± 0.064
		(0.464 ± 0.034 $S*S^{-\alpha}$ cm^{-2})
		(α = 0.801 ± 0.022)
	$R_{ct/Cathode}$	0.036 ± 0.024 Ω cm^2
		(0.059 ± 0.003 Ω cm^2)
	$CPE_{dl/Cathode}$	0.114 ± 0.138 $S*S^{-\alpha}$ cm^{-2}
		α = 0.807 ± 0.064
		(0.553 ± 0.081 $S*S^{-\alpha}$ cm^{-2})
		(α = 0.699 ± 0.028)

As a side note, one of the interesting benefits of the 3-electrode cell in this case is that it has a greater capability of resolving the $R_{ct/Cathode}$ and $CPE_{dl/Cathode}$ than the cell EIS alone. As the charge transfer resistance of HER is generally much lower than OER, its lesser contribution to the cell EIS signal means that it becomes more obscured by the OER signal, and so cannot be accurately determined. For instance, the standard error from fitting of $R_{ct/Cathode}$ is approximately 67 %, whereas from the 3-electrode measurement this error is 5 %.

The fitting procedure used above was performed on the GEIS curves over a range of current densities, with the R_s values given in Figure 44. Included here is the difference

between the anode plus cathode R_s minus the cell R_s. As can be seen here, $R_{s/Anode}$ and $R_{s/Cathode}$ varies only slightly with current density. If iR drop was present it would typically manifest as a rise in R_s rather than as a drop, which is particularly evident with $R_{s/Anode}$. Additionally, the difference in series resistance between $R_{s/Anode}$ + $R_{s/Cathode}$ and $R_{s/cell}$ changes with current density, but this is a negligible effect and is indeed negative also. At 1 A cm^{-2} this would equate to a difference of -3 mV overall. The most likely explanation for the reduction in R_s with current density is the increased heating of the membrane due to the higher voltage of operation (reaction is more strongly exothermic). This data does not exclude iR drop, but it does show that the influence of iR drop in this cell setup is negligible, and therefore does not need to be considered.

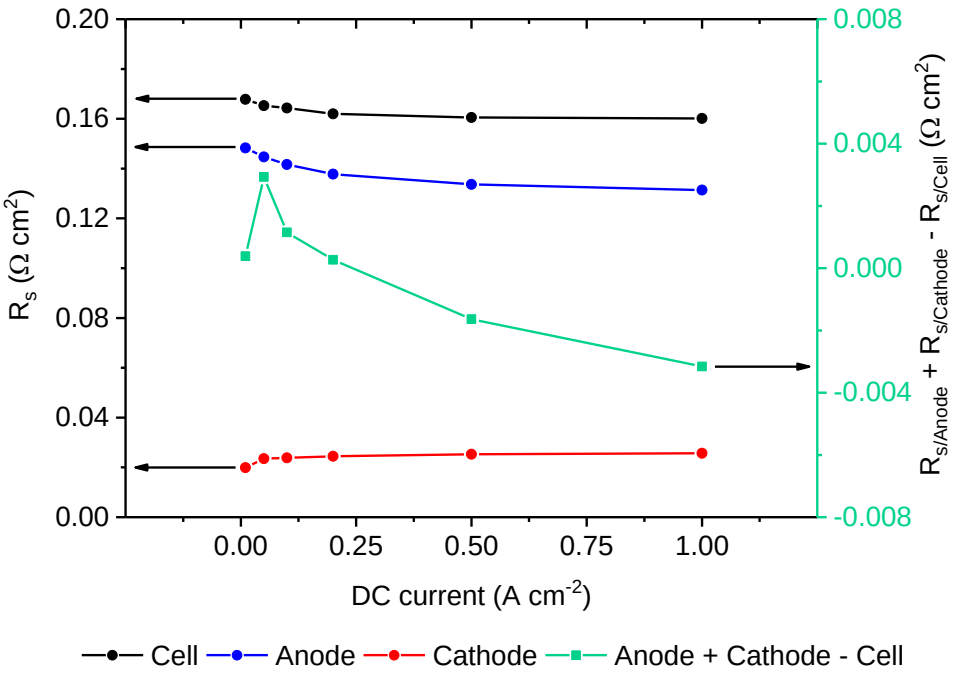

Figure 44. R_s values for the cell (black), anode (blue) and cathode (red) over a range of current densities, and the difference between the anode plus cathode series resistances minus the cell resistance (green).

Of relevance later in this thesis is the capacitance of the anode and cathode electrode. From the GEIS measurements in Table 4, a capacitance of 0.249 ± 0.032 F cm^{-2} was calculated for the anode and 0.113 ± 0.034 F cm^{-2} for the cathode.

As a final validation test of the new 3-electrode cell, the performance was analysed through IV curves and compared to the Brightman design in Figure 41. In each of these IV curves the CCM was of the same design (Nafion 117 CCM with 3 mg cm^{-2} IrO_2 and 0.5 mg cm^{-2} Pt/C). The IV curves are given in Figure 45. As can be seen, there is comparable performance of the new 3-electrode cell to the Brightman design, with a cell overpotential approximately 30 mV greater at 1 A cm^{-2}, equivalent to 11% poorer efficiency from E_{thermo}. This difference is relatively small and is still within the expected performance range of PEMWE cells of similar construction [78,96], and so the design was deemed suitable for use.

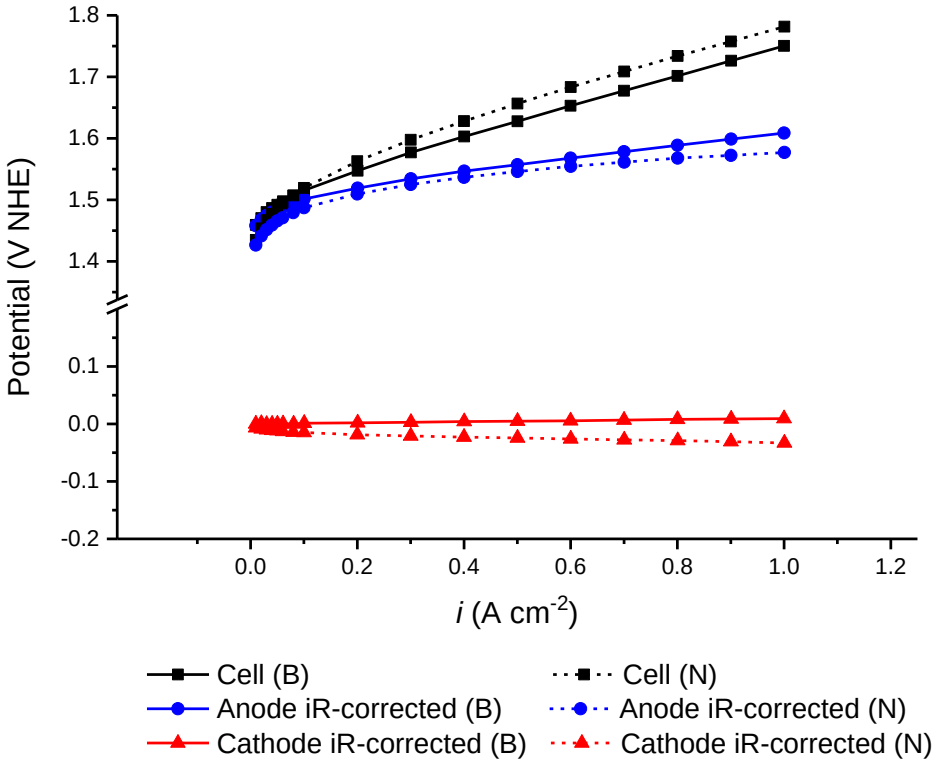

Figure 45. IV curves of the cell, anode and cathode of the Brightman 3-electrode design (B) and the new 3-electrode design used in this study (N). The anode and cathode IV curves in this figure have been iR-corrected.

6 Chapter 1 - An Investigation of OCV Profiles Under a Range of PEMWE Cell Conditions

6.1 Chapter Introduction

In this chapter, OCV profiles under a range of different conditions that may be expected in PEMWE systems has been investigated. This was performed to bridge the gap of knowledge, and to draw more insights into the possible cause of the difference in OCV profiles present in literature [119,123]. Due to pressure limitations of the cell used, all the tests in this report have been performed under ambient pressure. They have furthermore been performed at 20 ^{o}C in order to mitigate any effect that cooling may have on the electrode potentials during the OCV period. This report covers several conditions that may be expected of the electrolyser. Importantly, the effect of the wet vs dry cathode has been investigated. Additionally, we have looked at the importance of electroosmotic drag (EOD) of water collecting at the cathode under different PEMWE orientations, and we have observed the effect that water with differing dissolved gases has upon the electrode potentials.

The PEMWE cell in this chapter used Nafion 117 membrane, an IrO_x anode at 3 mg cm^{-2}, Pt/C cathode at 0.5 mg cm^{-2} of catalyst, and Pt coated GDL components. The conditions of the balance of plant can be found in section 5.2.

6.2 Estimation of Reversible Potentials and the pH of Nafion in PEMWE

To define E_{rev} (H^+/ H_2) and E_{rev} (O_2 / H_2O) in PEMWE systems, the crucial elements of the Nernst equation in regard to product and reactant concentration have to be approximated. The Nernst equation and reaction quotients (Q) for ORR and HOR are as follows:

$$E = E^0 + \frac{RT}{nF}\ln Q \tag{22}$$

$$Q_{(O_2/H_2O)} = [H^+]^4 pO_2 \tag{25}$$

$$Q_{(H^+/H_2)} = \frac{[H^+]^2}{pH_2} \tag{30}$$

The partial pressure (pO_2 or pH_2) of the reactants will vary depending on whether the electrode is in gas or dissolved gas. If gas, the partial pressure may be assumed to be unity, as in this test the PEMWE cell was operated at ambient pressures and the product gas streams in PEMWE are typically very pure. The partial pressure of dissolved gas may be approximated using Henrys law of the solubility of gases, shown in Equation (43.

$$C = k\, p_{gas} \tag{43}$$

In this equation, C is the concentration of the dissolved molecule, k is the solubility constant and p_{gas} is the partial pressure of the molecule in the gas phase. Concentration

can be converted to partial pressure of the dissolved molecule by applying the ideal gas law (Equation (44).

$$p_{(dis)} = \frac{k\, p_{gas} RT}{101.325} \tag{44}$$

k may be calculated for non-standard conditions using the van't Hoff equation (Equation (45).

$$k = k^0 \exp\left[\frac{-\Delta H_{sol}}{R}\left(\frac{1}{T}-\frac{1}{T_0}\right)\right] \tag{45}$$

k_0 is the solubility constant under standard conditions, and $\Delta_{sol}H$ is the enthalpy of dissolution. The enthalpy of solubility of oxygen in water can be considered constant at -12.06 KJ mol^{-1} under the small temperature range in which PEMWE systems operate. However, for hydrogen, the enthalpy changes to a greater extent over a low temperature range, and can be approximated with the following expression:

$$\Delta H_{sol} = 0.140T - 45.97 \tag{46}$$

In this work all the tests were undertaken at 293 K. The equilibrium concentrations expected at 1 atm therefore are O_2 at 1.41 mM (pO_2 3.4 x 10^{-2} atm) and H_2 at 0.81mM (1.94 x 10^{-2} atm). As this is only an estimation, the true dissolved gas

concentration may have differed from this. The impact that an inaccuracy in the dissolved gas concentration may have is limited however, as it has already been mentioned that the Nernst Equation is relatively insensitive to minor changes in reactant or product concentration. An important assumption here is made that the surface concentration of the reactant and product species on the electrode matches that of the bulk solution concentration. This assumption therefore does not consider the impact that potential or other species in the solvent may have on the surface concentration.

A final necessary value for calculating E_{rev} (H^+/ H_2) and E_{rev} (O_2 / H_2O) was the pH of Nafion. For this, two separate approaches were taken. Firstly, the reversible potentials based on the literature pH range estimate of Nafion (-0.08 – 1.4) were calculated, the results of which are given in Table 5. Secondly, using the results of OCV test 2 (Table 6 and Figure 46) an independent estimation of Nafion pH was made. OCV test 2 was ideal for establishing the pH, as the pH_2 was approximated to be 1.94×10^{-2} atm, the Nafion was fully hydrated (water is present at both anode and cathode electrode), and the anode was deaerated, thereby removing the influence of oxygen crossover. The average cathode potential measured in the final hour during this test was -15.01 mV ± 0.79 . This provided a pH estimation of Nafion in PEMWE at $1.11^{+0.02}_{-0.01}$. As the exact pH_2 has only been theoretically determined however, there may be some inaccuracy in this pH estimation. It is therefore sensible to estimate the pH based on a reduced pH_2 as well. Due to the length of time that the cathode reservoir had H_2 bubbling through it by the end of this OCV test (3 h) it may be assumed that the pH_2 of $H_{2(dis)}$, if not at complete equilibrium, would be at least close to. A lower limit of pH_2 may realistically be above half the theoretical equilibrium value (0.97×10^{-3} atm), which places the pH of Nafion at

$1.26^{+0.02}_{-0.01}$. Both these pH values are within the ranges estimated by the aforementioned literature sources. E_{rev} (H^+/ H_2) and E_{rev} (O_2 / H_2O) of this PEMWE system, operating at 293 K and ambient pressures can therefore be estimated with reasonable precision (Table 5). In the OCV profiles that follow in this report, E_{rev} (H^+/ H_2) and E_{rev} (O_2 / H_2O) are represented by bands that show the range in where E_{rev} is expected to be.

Table 5. Estimation of E_{rev} (H^+/ H_2) and E_{rev} (O_2 / H_2O) in PEMWE cell at 293 K and ambient pressure under dissolved and gaseous conditions. Based on the literature values of Nafion and the estimation of Nafion pH based on the cathode potential of OCV test 2.

	$\mathbf{E_{rev(O_2/H_2O)}}$ **(V NHE)**		$\mathbf{E_{rev(H^+/H_2)}}$ **(V NHE)**	
Nafion pH	$O_{2(g)}$	$O_{2(dis)}$	$H_{2(g)}$	$H_{2(dis)}$
-0.08 (lit)	1.234	1.212	0.005	0.054
1.11 (this)	1.165	1.143	-0.065	-0.015
1.26 (this)	1.156	1.134	-0.073	-0.024
1.40 (lit)	1.148	1.126	-0.081	-0.032

6.3 PEMWE OCV Profiles Under a Range of Conditions

During OCV, a PEMWE electrode may experience a range of local environmental conditions. Of primary importance is whether the electrode is in a 'dry (i.e. thin water film) environment or fully immersed in bulk water. Other factors, such as whether there is an active water flow during OCV, will also modify the concentration of the dissolved gases in the cell over time, and so will also impact the OCV. To determine the effect of these varying conditions, a range of OCV tests were performed (Table 6). The tests were divided broadly into four separate analyses. First were a set of tests to determine the

importance of dissolved gases in the cell halves. This encompasses tests 1 to 3 in Table 6. In these tests the cell had an active flow of water in both anode and cathode compartment with different dissolved gas compositions. The second set of tests determined the impact of flowing water vs. non flowing water in the cell during OCV. This encompasses Tests 1, 4 and 5. Thirdly, the effect of 'dry' oxygen and hydrogen at the anode and cathode respectively were analysed, involving tests 5, 6 and 7. Finally, OCV profiles were analysed with a cell run with the cathode wetted only with water transported from the anode by electroosmotic drag. The cells were operated for various lengths of time before the OCV period to collect different amounts of water at the cathode. This was performed with both aerated water supplied to the anode (Tests 8, 9 and 10) and with oxygen bubbles at the anode (Tests 11, 12 and 13).

Table 6. The conditions of the OCV tests performed and their relation to real operation. A selection of the tests were measured repeatedly in order to verify the repeatability of the measurements. These were tests 2, 3 and 5. The measurements were found to be qualitatively repeatable. Repeats for other OCV profiles were not taken.

Test	Pre-OCV operation duration (s)	Anode at OCV	Cathode at OCV	Relevance to commercial PEMWE systems
1	1000	$O_{2(dis)}$	$H_{2(dis)}$	Active supply of water to both sides
		Flowing	Flowing	
2	1000	N_2 degassed	$H_{2(dis)}$	None
		Flowing	Flowing	
3	1000	$O_{2(dis)}$	$N_{2(dis)}$	None
		Flowing	Flowing	
4	1000	$O_{2(dis)}$	$H_{2(dis)}$	Active supply of water to anode with water filled cathode or pump not running at cathode
		Flowing	Not flowing	
5	1000	$O_{2(dis)}$	$H_{2(dis)}$	No pumps active with water filled cathode and anode
		Not flowing	Not flowing	
6	1000	$O_{2(g)}$	$H_{2(dis)}$	Anode containing bubbles of O_2 gas with a water filled cathode
		Not flowing	Not flowing	
7	1000	$O_{2(g)}$	$H_{2(g)}$	Anode containing bubbles of O_2 gas with a 'dry' cathode
		Not flowing	Not flowing	
8	10	$O_{2(dis)}$	$H_{2(g)}$ + EOD H_2O	No pumps active with EOD water collecting at the cathode
		Not flowing	Not flowing	
9	100	$O_{2(dis)}$	$H_{2(g)}$ + EOD H_2O	
		Not flowing	Not flowing	
10	1000	$O_{2(dis)}$	$H_{2(g)}$ + EOD H_2O	
		Not flowing	Not flowing	
11	10	$O_{2(g)}$+ $O_{2(dis)}$	$H_{2(g)}$ + EOD H_2O	No pumps active with EOD water collecting at the cathode. Anode contains bubbles of trapped O_2 gas
		Not flowing	Not flowing	
12	100	$O_{2(g)}$+ $O_{2(dis)}$	$H_{2(g)}$ + EOD H_2O	

		Not flowing	Not flowing	
13	1000	$O_{2(g)}$+ $O_{2(dis)}$	$H_{2(g)}$ + EOD H_2O	
		Not flowing	Not flowing	

6.3.1 The Impact of Dissolved Gases

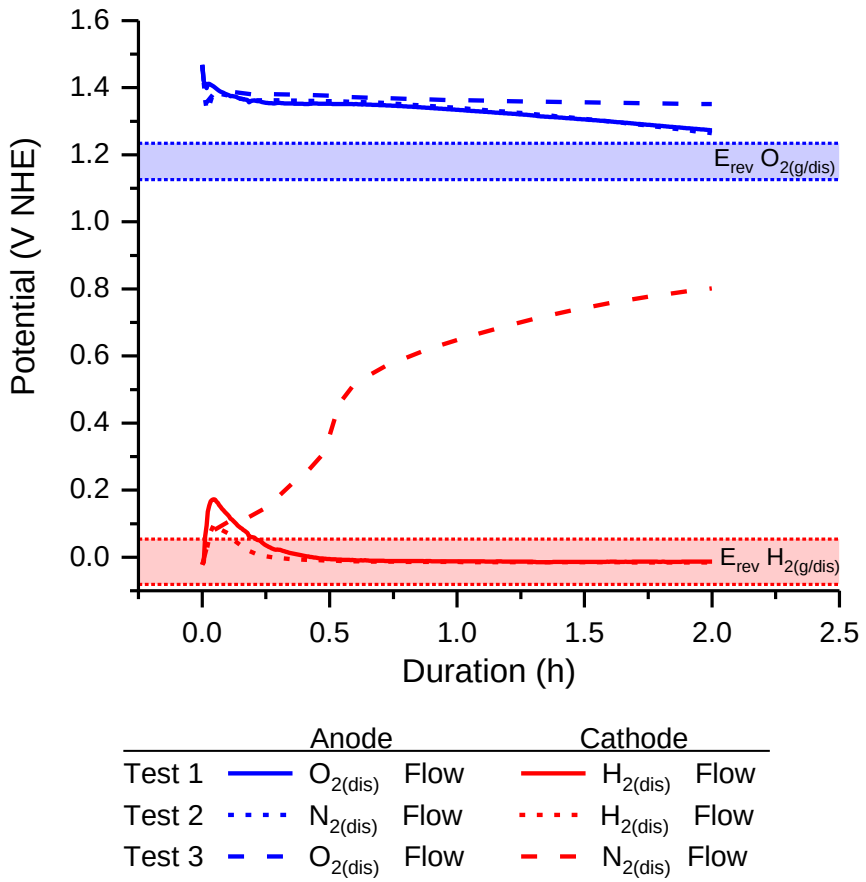

Figure 46. Impact of dissolved gases on anode and cathode potential in a PEMWE single cell during OCV with water flowing in both anode and cathode compartments. Included as a guide for the eye are the ranges in which E_{rev} (O_2 / H_2O) and E_{rev} (H_2 / H^+) would be expected in a PEMWE system at 293 K and ambient pressure conditions.

In the first series of tests, water purged with different gases was flowed continuously at the anode and the cathode (Figure 46). There are several features of these plots that are noteworthy. The potential of the anode remains greater than E_{rev} (O_2 / H_2O) throughout

the duration of the OCV period, despite an initial sharp drop in the potential. This high potential may be explained by the fact that, even though IrO_x is one of the most effective OER catalysts, it still has relatively poor kinetics (compared to HER), typically requiring > 250 mV overpotential to obtain practical reaction rates (Table 1, Reaction 1) [239]. With the potential of the anode electrode only 150 - 200mV above E_{rev} (O_2 / H_2O), the rate of OER would become negligible, and thus the potential would remain high. The decay in potential by this method has been modelled in Figure 47.

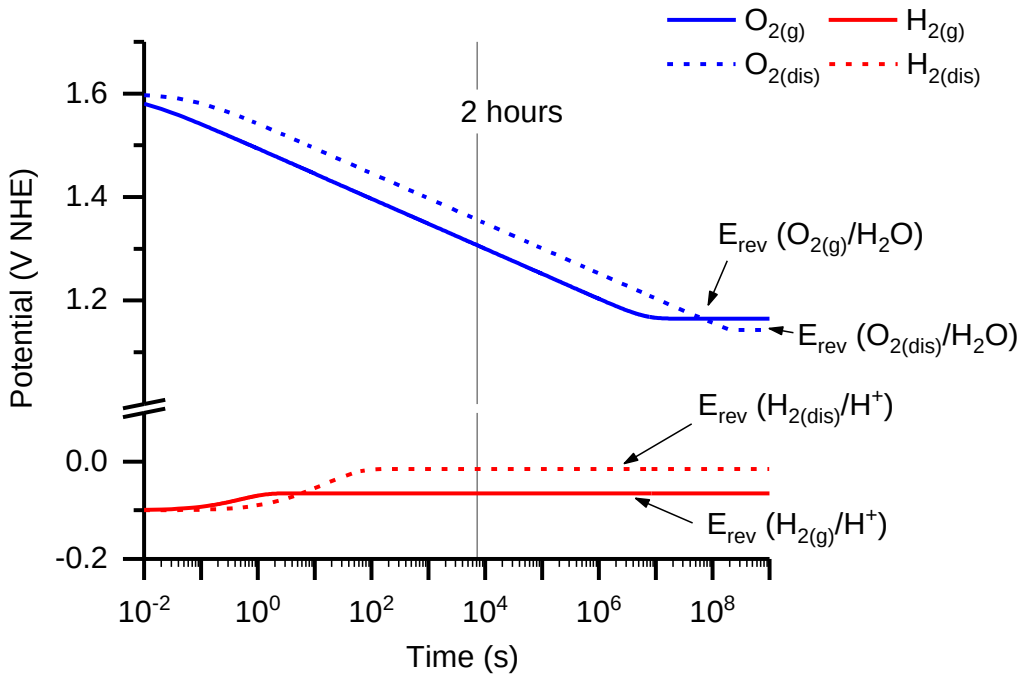

Figure 47. Estimation of the electrode potentials in PEMWE, assuming only OER at the anode (blue) and HER at the cathode (red). Due to the higher capacitance of the anode, the higher initial overpotential and worse OER kinetics, the time taken for the anode to decay to O_2/ H_2O reversible potential is 6 orders of magnitude greater than HER. Potential decay in dissolved gas is greater than pure gas due to the lower exchange current density, which is proportional to the difference in partial gas pressure. The parameters for the Butler - Volmer equation used in this modelling are given in Table 7.

Table 7. Parameters used to fit the Butler-Volmer equation that provides the potential decay profiles in Figure 47.

Parameter	Anode	ref	Cathode	ref
E_{rev} (V NHE)	1.165 (g) 1.143 (dis)	this at pH = 0.598 (Table 2)	-0.065 (g) -0.015 (dis)	this at pH = 1.11 (Table 2)
i_o (A cm^{-2})	1 x 10^{-9}	[240]	1 x 10^{-3}	
α_a	0.3	[192]	0.5	
α_c	0.3		0.5	
z	4		2	
T (K)	293		293	
C (F cm^{-2})	0.292		0.0433	
p_{gas} (atm)	1 (gas) 3.40 x 10^{-2} (dis)		1 (gas) 1.94 x 10^{-2} (dis)	
p_{gas}^{0} (atm)	1		1	

In addition to the Butler-Volmer equation, one of the important elements of this decay profile, and for the OCV in general, regards the capacitance of the anode and cathode. The capacitance governs the rate at which the electrode potential changes, as shown in Equation (47.

$$dV = \frac{i\,dt}{C} \tag{47}$$

Determining the capacitance of the electrodes was therefore essential in producing this decay profile. The anode and cathode capacitances were calculated by GEIS in section 5.6.2. In addition to this also, the capacitances of the electrodes were also determined by CV (Figure 48). The double layer capacitance here was determined by measuring the

current density in a region of the CV plot in which there is no electrochemical reaction occurring, and so any current is simply going to into the charging of the double layer. For Pt/C, the double layer capacitance may be measured from the region of lowest current in between the hydrogen adsorption peaks (H_{upd}) and the Pt oxidation peak. For IrO_x however, the peaks corresponding to the surface oxidation are typically broad and ill-defined [161,188,241], and so an estimation of capacitance by this means may be less accurate. For both CV plots however, 0.4 V NHE is a region in which there seems to be no electrochemical reaction occurring. Capacitance can be calculated by rearranging Equation (47, producing Equation 47 below.

$$C = \frac{i_{oxid} - i_{red}}{2v} \tag{48}$$

Where i_{oxid} and i_{red} are the currents of the oxidative and reductive sweeps respectively, and v is the scan rate of the CV. The capacitances measured by both CV and GEIS are given in Table 8.

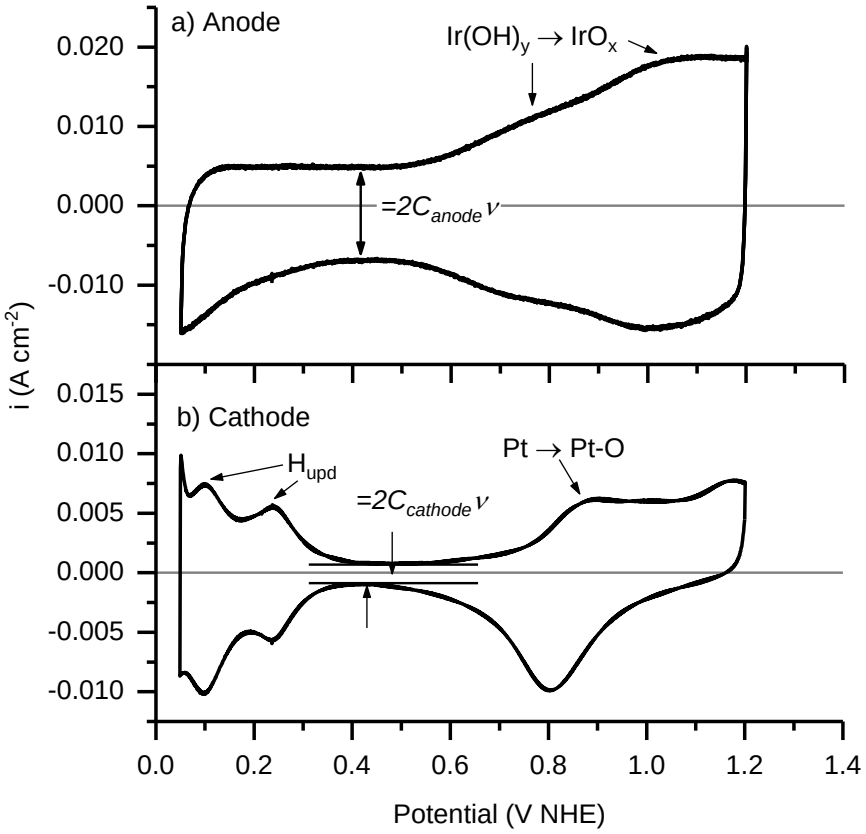

Figure 48. *in situ* cyclic voltammetry of a) IrO_x anode at 3 mg cm^{-2} and b) Pt/C cathode at 0.5 mg cm^{-2}. Scan rate (v) = 0.02 V s^{-1} for both. Current values for calculation of the electrode capacitance (C) were calculated from the points indicated by the arrows.

Table 8. Anode and cathode electrode capacitances measured by GEIS and CV

	C_{Anode} (F cm^{-2})	**$C_{Cathode}$ (F cm^{-2})**
GEIS	0.249 ± 0.032	0.113 ± 0.034
CV	0.292	0.043

There is a significant difference between the capacitance results obtained by GEIS and CV, and this is much more substantial for the cathode. The difference between C_{Anode} may be explained by either a poor fitting of the EIS curve, an incomplete Randles

equivalent circuit, or the possibility of a redox reaction occurring at the point at which the currents for the double layer capacitance were measured. For the cathode however, it is almost certain that $C_{Cathode}$ as measured by GEIS is inaccurate, as the CV of Pt is well characterized and double layer capacitance is often measured here [242]. For this work therefore, the capacitances measured by CV have been used for both anode and cathode.

The time taken for the potential to reach E_{rev} (O_2 / H_2O) and E_{rev} (H_2 / H^+) is dependent on whether the electrode is in a 'dry' or fully immersed environment, as this affects both E_{rev} (Table 5) and the exchange current density. At OCV, following operation at potentials of 1.6 V NHE at the anode and -0.1 V NHE at the cathode, the predicted times taken for the individual electrode potentials to decay to reversible potentials (assuming OER / ORR only at the anode and HER / HOR only at the cathode) are given in Table 9. These values are compared against Test 3 for the anode and Test 2 for the cathode so that potential change by gas crossover from the counter compartment may be ignored.

Table 9. Approximate time for electrode potentials to reach E_{rev}, and the electrode potential at 2 h

Electrode	Time range to reach E_{rev} (h)	Estimated potential at 2 (V NHE)	Actual potential at 2 h (V NHE)
Anode$_{(g)}$	x 10^3	1.307	1.322
Anode$_{(dis)}$	x 10^4	1.356	
Cathode$_{(g)}$	x10^{-3}	0.035 (= E_{rev} ($H_{2(g)}$ / H^+)	-0.015
Cathode$_{(dis)}$	x 10^{-1}	-0.015 (= E_{rev} ($H_{2(dis)}$ / H^+)	

In the fully immersed / dissolved gas condition that the electrodes are expected to be in, the anode potential modelling is in qualitative agreement with the experimental

result at 2 h (see Figure 49 also). The modelled potential decay is highly sensitive to slight variations in the charge transfer coefficient and exchange current density, and as these have not been well defined *in situ*, these predictions should be taken as indicative only. The extremely rapid kinetics of HER bring the cathode potential to E_{rev} (H^+/ H_2) within 100 s, which is in agreement with the cathode potentials observed at the beginning of the OCV periods of all the tests performed.

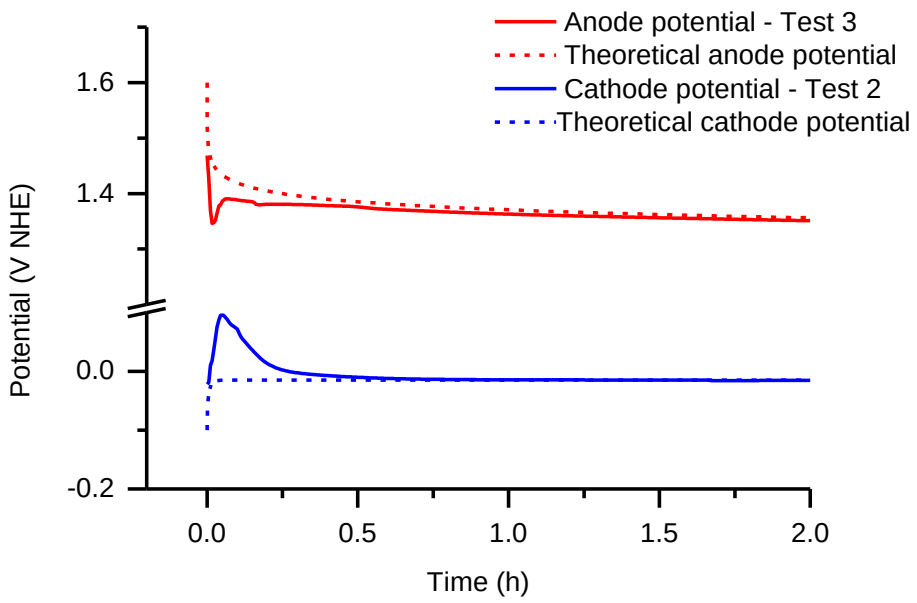

Figure 49. Experimental electrode potentials in dissolved gas environments (solid lines) measured against the modelled OCV profile in dissolved gas conditions (dotted lines). Test 3 anode data and test 2 cathode data are shown here, as no long-term crossover from the counter half of the cell is expected in these tests.

The mechanism of potential decay to E_{rev} (O_2 / H_2O) may explain the maintenance of the high anode potential over time in Test 3. However, the decay in potential in Tests 1 and 2 are greater than that in Test 3 after approximately 45 minutes at OCV. This is evidence of the crossover of H_2, which decreases the anode potential via the HOR, with the rate of voltage decay proportional to the hydrogen crossover rate.

During the first 200 s at the anode, and during the first 1000 s at the cathode, the electrode potentials are highly dynamic (Figure 50). At the anode, there is an initial decrease in potential followed by an increase, and at the cathode there is a gain followed by a steady decrease in potential. This is not the case for Test 1 at the anode however, where the profile only matches anode potential of Tests 2 and 3 during the first 20 s. After this, the potential remains higher than Tests 2 and 3 until approximately 200 s. This lack of an initial potential decay in Test 1 indicates that HOR or H_2 crossover is not occurring here. No suitable explanation for this can be found other than a possible instrumental error in the reference electrode.

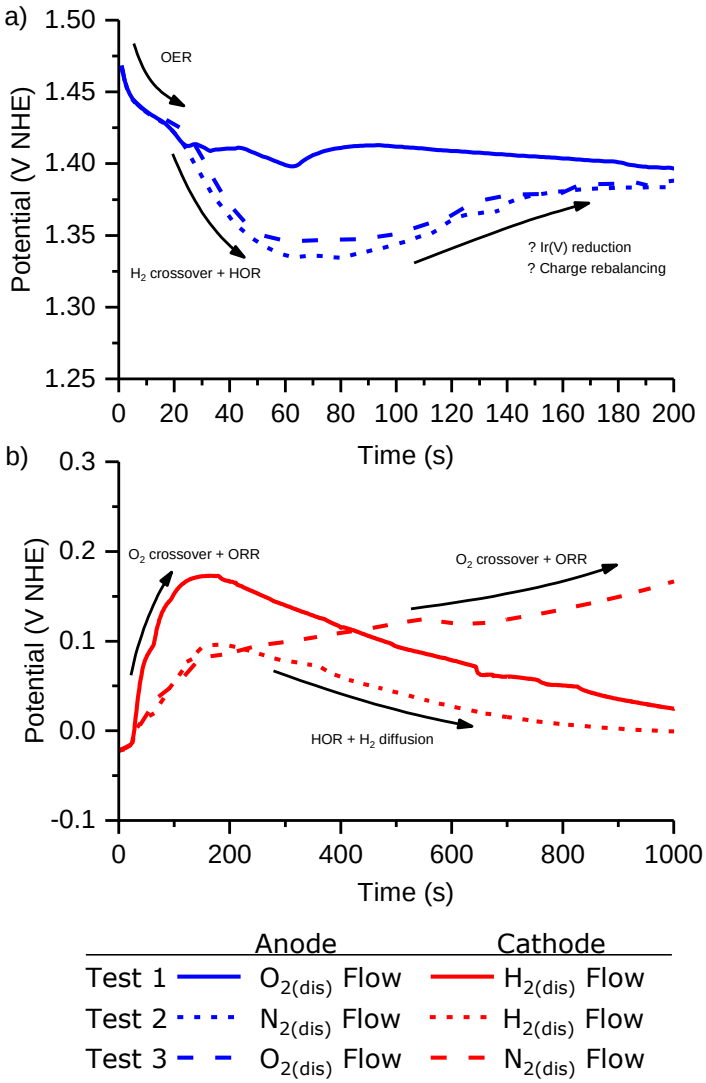

Figure 50. Variations in potential at the beginning of the OCV period at a) the anode (blue) and b) the cathode (red)

In the case of the anode, the initial 200 s of the OCV period shows three regions of interest. First is the region during the first 20 s, where the potential is seen to decay exponentially. In this region the potential decays only via OER through the capacitance effect described above. After this, there is a ≈ 100 mV drop in potential that is likely to have been caused by the crossover of H_2. This is clearly only a transient effect, and therefore indicates that the origins of this H_2 is distinct from that which causes the gradual reduction in the anode potential of Tests 1 and 2 over longer periods of time.

The origin of this H_2 is therefore attributed to bubbles trapped within the cathode electrode, GDL, or from within the membrane itself. Over longer periods of time the OCV will become determined by the rates of dissolved gas diffusion from the water flowing through the PEMWE cell.

No definitive explanation for the anode potential rise after the reduction by HOR can be given, however. The potential is well above the predicted E_{rev} (O_2 / H_2O), and so ORR cannot be the mechanism that raises the potential in this case. It may be possible that there is a net reduction of Ir occurring however, notably from the Ir(V) to Ir(IV) state. Ir(V) is known to be an oxidation state present during OER, and is an essential component of the OER mechanism [191,243]. However, Ir(III) has also been demonstrated to be present during OER, which may oxidize during OCV and therefore decrease the potential. As the exact mechanism of OER, and the structure of the Ir transition states, are not yet fully understood, then what is suggested here is conjectural [244,245]. An alternative explanation for this rise in potential may be that H_2 crossover does not occur evenly across the entire CCM area. Due to the positioning of the reference electrode it may be the case that the potential change is occurring in the region closest to the Luggin capillary, which may possibly have higher rates of H_2 crossover than other areas of the electrode. The potential shift may therefore be a signature of the charge rebalancing across the electrode. The non-uniform crossover across the CCM may also serve as an explanation for the comparatively lower impact of H_2 crossover on the anode potential in as shown Test 1.

The behaviour of the cathode potential during the first 1000 s of the OCV period is simpler to explain. There is an initial high crossover rate of oxygen, again caused by

oxygen gas trapped within the anode GDL, anode catalyst layer or membrane, which raises the potential of the cathode by ORR. In the case of Tests 1 and 2, the rate of potential increase is hindered by the H_2 that is already present at the cathode. For the potential of the cathode to decrease overall, the reaction rate of HOR must be at least twice that of ORR (2-electron reaction versus 4-electron reaction). The influence of the reaction kinetics on the rate of reaction may be ignored here, as the overpotential for ORR is extremely high, and the kinetics of HOR are fast enough that a small overpotential for HOR results in a high rate of reaction. Therefore, the potential in this case will be determined by the relative concentrations of the dissolved gases. This will in turn be affected by the diffusion rates of O_2 through Nafion and H_2 through the GDL, and the equilibrium concentrations in the Nafion and the GDL [102,147,148,246]. As the cathode potential in Tests 1 and 2 remains at E_{rev} (H^+/ H_2), the permeation rate of H_2 (the molar rate of diffusion, calculated by multiplication of the diffusion rate and equilibrium concentration) to the electrode must be at least twice that of O_2 permeation. Long-term diffusion of H_2 to the cathode in Test 3 is not possible however, as the water flowing through the cathode compartment is N_2 purged, and so the cathode potential in this test continues to rise. There is a difference in magnitude of the initial cathode potential change between Tests 1 and 2 also, indicating that there is a difference in the amount of O_2 crossover. This may be caused by either an increased dissolved O_2 concentration of Test 1, or by slightly different amounts of trapped oxygen in the anode GDL between the tests.

Gas crossover clearly affects the cathode potential to a greater extent than the anode potential. During the initial OCV period, shown in Figure 50, the average magnitude of the maximum potential change at the anode is 83 mV, whilst at the cathode it is 150 mV.

A measurement of the exact crossover flux in this study has not been performed; however it would be expected that, for a given flux, the cathode potential would be expected to undergo greater change than the anode potential. There are two reasons for this. Firstly, HOR is a 2-electron reaction, whereas ORR is a 4-electron reaction. Secondly, for the CCM used in these tests, the double layer capacitance (C_{dl}) of the anode and cathode were measured by CV (Figure 48), and the anode was found to have a substantially higher C_{dl} than the cathode, at 0.292 F cm^{-2} compared to 0.043 F cm^{-2}. It follows that, for a given electrochemical reaction occurring, the anode will undergo less potential change than the cathode. It can be calculated therefore, that for equivalent molar crossover flux of 1 nmol cm^{-2} s^{-1}, under HOR the anode potential would decrease by 0.66 mV s^{-1} whereas the cathode potential under ORR would increase by 8.91 mV s^{-1}. This is consistent with the general observation throughout this testing regime, that when the potential of the cathode changes it generally does so rapidly, whereas the anode potential tends to change more slowly. In the Weiß et al paper [119], both the anode and cathode loadings were lower than those used in this report, 1.75 mg cm^{-2} and 0.2 mg cm^{-2} for IrOx / Ti and Pt/C respectively, compared to 3 mg cm^{-2} and 0.5 mg cm^{-2} in the current study. Under similar dynamic conditions therefore, the rate of electrode potential change would be expected to be greater with lower loadings.

6.3.2 The Influence of Water Flow

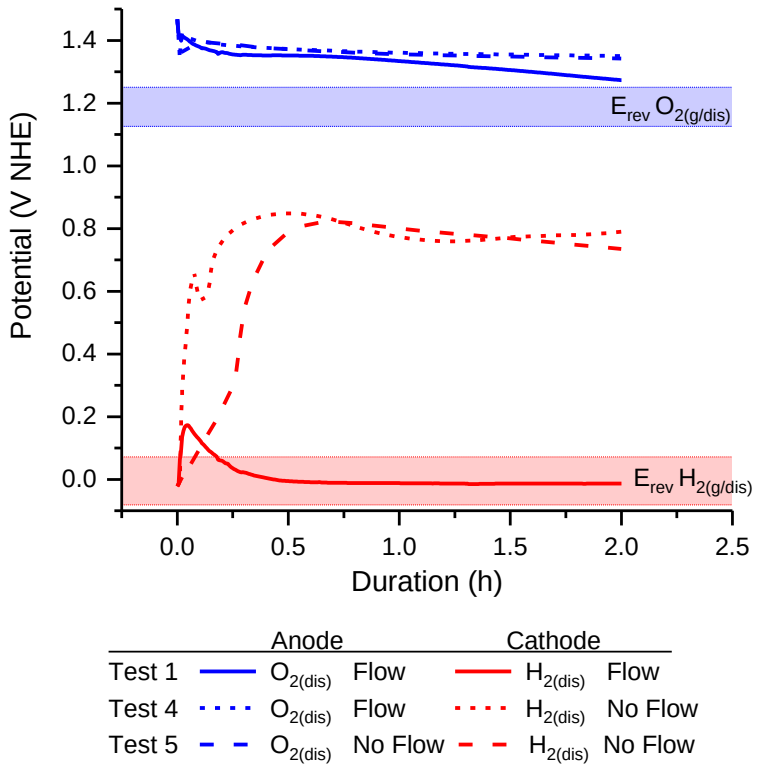

Figure 51. Impact of water flow on anode and cathode potential in the PEMWE cell during OCV. Shown in blue are the anode potentials of each test and shown in red are the cathode potentials. The light red and light blue bands represent the regions in which the potentials of the cathode (red) and anode (blue) may be expected if there was no crossover of gas from the counter electrode.

The presence of dissolved gases in water that is actively flowed through the PEMWE cell has shown to have an impact upon the potential profiles in Figure 46. Over the timescale of hours, transport of dissolved gases has been shown to be the major factor determining the individual electrode potentials, and therefore the OCV of the cell. In commercial systems, no water flow during OCV (or the flow of water only at the anode) is a highly likely scenario, as operation of pumps during shutdown simply wastes energy. With no water flow there will be three major effects in comparison to the active flow.

Firstly, the dissolved gas concentration is not maintained and so will decrease via reaction on the electrodes. Secondly, dissolved gas concentration at the electrodes becomes a factor of Fickian diffusion only. Thirdly, any gas bubbles present will not be removed by convection and will become trapped in the cell halves. Figure 51 shows the evolution of anode and cathode potentials during OCV in various flow configurations. In contrast to Test 1 (flow at both electrodes), rapid changes in the cathode potential without a substantial change in the anode potential are observed in Tests 4 and 5 (where flow is maintained at only one electrode). In these cases, it is clear that the combination of lower capacitance, the likely lower dissolved gas concentration, and the 4-electron ORR result in a very sharp change in cathode potential with no major shift in anode potential. The cathode potential in Tests 4 and 5 reaches a similar steady value around 0.8 V, placing it within the range expected of the Pt oxidation reactions (Table 1, reactions 7, 8, 9). The variation in the rate of potential change may be evidence that the continuous flow of water at the anode allows for a greater rate of O_2 crossover. This may indicate that there is some active transport of water through the sinter due to water flow. Alternatively, this may be due to slight differences in the conditions of the cell at the start of the OCV period. The sensitivity of the cathode potential to slight variations in concentration is evidenced by the transient interruption in the potential increase during the first 10 minutes of the OCV period.

The same initial dynamic behaviour in the anodes of Tests 4 and 5 (as was seen in as that in Tests 2 and 3) is evident at the anode again. However, over the longer term there is no drop in potential (as is seen in Test 1), indicating that there is a negligible rate of H_2 crossover. To explain this, it must be considered that the cathode electrode is also one of the barriers through which H_2 must permeate in order to reach the anode. With the

high cathode potential there is a high kinetic preference for the H_2 permeating through the cathode electrode to undergo HOR, which would decrease the concentration that ultimately crosses over to the anode. This raises the interesting possibility that a high enough rate of O_2 crossover may actually stop H_2 crossover, and the same logic may be applied in the reverse case.

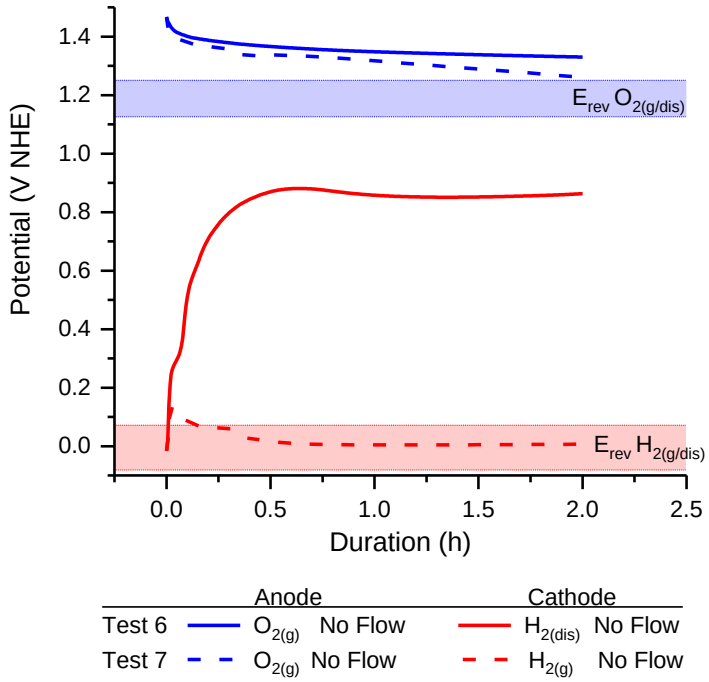

Figure 52. Impact of gas bubbles on anode and cathode potential in the PEMWE cell during OCV. The light red and light blue bands represent the regions in which the potentials of the cathode (red) and anode (blue) may be expected if there was no crossover of gas from the counter electrode.

As several of the previous tests have exhibited artefacts that could be ascribed to the presence of gas bubbles, an individual analysis on the impact of gas bubbles was undertaken. The results in the presence of gas bubbles, i.e. with no active flow of water just before and during the OCV period, is given in Figure 52. Test 8 in Figure 54 is also a suitable addition to this test set, but will be discussed separately in more detail in the

proceeding section. In Figure 52 it is shown that the presence of gas bubbles at the anode and / or the cathode provides results that are now expected: When the H_2 concentration at the cathode is high, the potential remains low (after the initial transient increase in potential). With a lower H_2 concentration at the cathode, as in Test 7, O_2 crossover dominates, thus forcing the cathode to oxidizing potentials and protecting the anode from HOR.

6.3.3 'Dry' Cathodes, and the Impact of Electroosmotic Drag

The most common mode of commercial PEMWE operation is with no active flow of water through the cathode. These systems therefore operate with a 'dry' cathode, which becomes wetted only due to electroosmotic drag (EOD) of water. The EOD coefficient is a measure of the number of water molecules transported through the membrane per proton, and although it has not been precisely determined, it is found to be a function of temperature, current density and membrane thickness [130,247]. Based on values and equations provided in the references, the EOD coefficient for PEMWE is estimated to be in the range of 1.86 – 6 [130,131,248–250]. The rate of EOD at 1 A cm^{-2} is therefore 0.35 – 1.12 µL cm^{-2} s^{-1}. The balance of plant of PEMWE systems is designed with EOD water in mind, and is usually separated from the H_2 gas inside pressure vessels which also act as water/gas separations units [126]. The H_2 gas produced at the cathode forces the water out of the stack during operation, but complete removal of water may not occur within the stack, especially in areas of the cathodes that are far removed from the cathode outlet. We investigated here the effect that different quantities of water at the cathode had on the anode and cathode potentials. Unlike the previous tests, the duration of operation pre-OCV was varied so that different quantities of EOD water were

collected at the cathode. This test was performed with both an anode containing dissolved O_2 only (Figure 53a) and containing dissolved O_2 and O_2 bubbles (Figure 53b). In each test the cell was operated for 10s, 100 s and 1000 s, respectively in order to accumulate different volumes of water at the cathode.

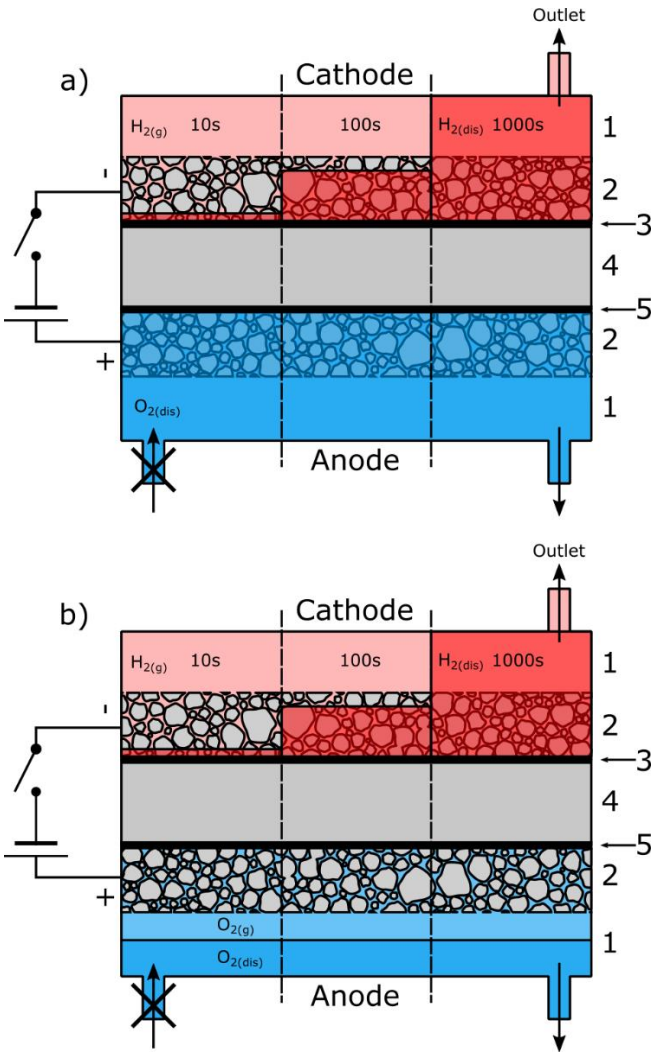

Figure 53. PEMWE systems with 'dry' cathode at OCV, with the amount of water collected at the cathode being a function of the length of time the cell was operated pre-OCV period. Water collected at the cathode during operation is here shown in dark red – the water collects over time and it gets deeper the longer it runs. Likewise, dark blue at the anode represents water at the anode. Shown in a) with dissolved oxygen at the anode and b) dissolved oxygen and oxygen gas bubbles. The cell consists of (1) water flow channel (2) GDL (3) cathode electrode (4) Nafion 117 membrane (5) anode electrode. At 1000 s, the

maximum pre-OCV operation duration, water was observed to be leaving the cathode compartment, and so it was assumed here that the maximum amount of EOD water had been collected in the cathode.

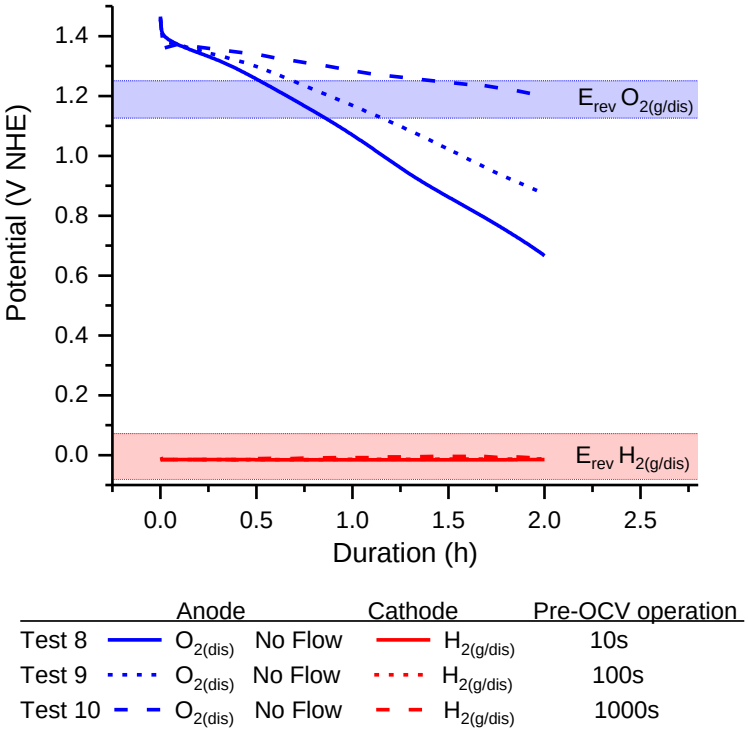

Figure 54. Impact of pre-OCV operation time on anode and cathode potential in the PEMWE cell during OCV with 'dry' cathode containing different volumes of water due to EOD, and anode containing dissolved oxygen. The light red and light blue bands represent the regions in which the potentials of the cathode (red) and anode (blue) may be expected if there was no crossover of gas from the counter electrode.

In the tests in Figure 54, the potential change occurred almost entirely on the anode. In none of the tests did the cathode potential change to the extent observed in Tests 4, 5 and 6. The lack of any dynamic behaviour at the onset of OCV indicates that the high concentration of hydrogen at the cathode electrode, either as gas bubbles or dissolved gas, completely overcomes the effect of any O_2 crossover. Worth noting here is the anode potential in Test 8, which reached values at which the reduction of IrO_x may occur (the reduction of IrO_x has been shown to coincide with Ir dissolution [225]). As the rate

of decrease of anode potential in Test 8 is relatively constant however, any Ir reduction reaction that occurs may only proceed at a rate that is much lower than that of the HOR.

The rate of potential drop observed at the anode is clearly dependent on the amount of water collected at the cathode. With a greater amount of water collected at the cathode the potential drop is lower. This shows that the rate of crossover may be dependent on the total distance that dissolved gas must travel to the electrode, and is not just a factor of the membrane thickness alone. A greater volume of water means that there is a greater distance between the gas / water interface and the electrode, and so the diffusion rate between these two points is slower as a result.

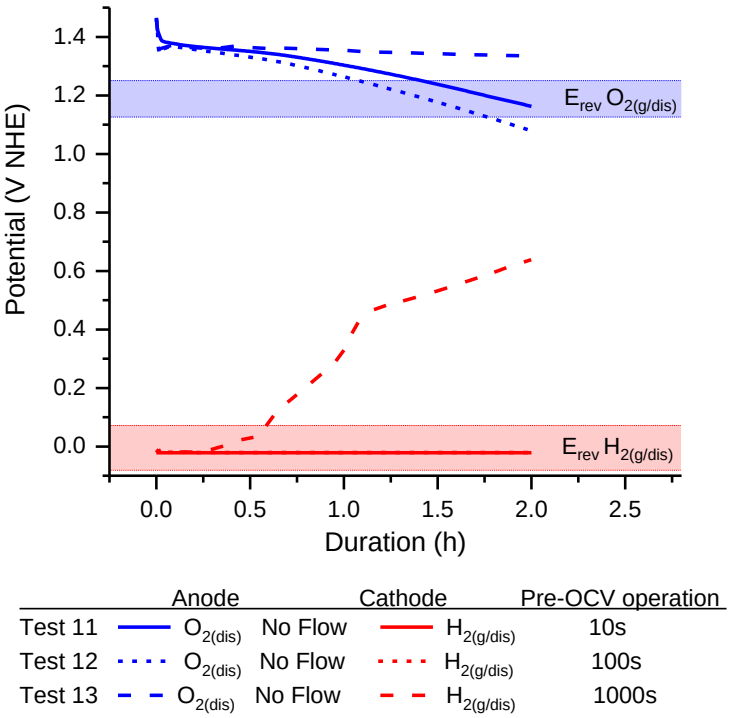

Figure 55. Impact of pre-OCV operation time on anode and cathode potential in the PEMWE cell during OCV with 'dry' cathode containing different volumes of water due to EOD, and anode containing dissolved oxygen and oxygen gas bubbles. The light red and light blue bands represent the regions in which the

potentials of the cathode (red) and anode (blue) may be expected if there was no crossover of gas from the counter electrode.

Finally, the effect of oxygen gas bubbles present at the anode electrode was investigated (Figure 55). In these cases, the anode undergoes less potential change in comparison to the tests in Figure 54, which can be ascribed to a higher concentration of O_2 present at the anode electrode. At these potentials, it is again unlikely that ORR is occurring to prevent the decrease in potential, so the more likely explanation is that the rate of hydrogen permeation is different in Tests 11 and 12. It would be expected that the potential decay rate in Test 11 would be greater than that in Test 12; however, this is not the case and may be an artefact. The cathode potential remains low except for in Test 13, which has 1000 s of pre-OCV operation. Here, the potential can be seen to gradually increase over 2 h. The rate of change of this in comparison to Tests 4, 5 and 6 is much lower however, and is an indication that, despite EOD water constituting the majority of the volume of the cell, there is enough H_2 trapped in the form of gas bubbles in the cathode to prevent the cathode potential from rising rapidly. In this test the rate of hydrogen crossover is negligible, and so the anode potential remains relatively unaffected. Overall, in these tests the anode is the electrode which undergoes the most potential change. These tests were performed under ambient conditions, and so represent the lower extreme of dissolved hydrogen concentration or hydrogen partial pressure. Even so, hydrogen crossover is the dominant crossover mechanism, with only the conditions of Test 13 providing an increase in cathode potential. With similar tests performed at higher differential pressures of hydrogen, it would be expected that the crossover rate of H_2 would increase, the cathode potential change would be reduced, and the anode potential would decrease to a greater extent.

6.4 Chapter 1 Conclusions

The major result of this chapter is to show that there is no universal OCV profile that may be ascribed to a PEMWE system during shutdown periods. This has significant implications for the implementation of operational strategies to mitigate degradation and in the design of accelerated stress tests for catalyst stability. Primarily, it has been shown that the cathode potential remains relatively constant and close to E_{rev} throughout the OCV tests, and the anode has either been shown to remain close to E_{rev} or decay slowly over time to reducing potentials. However, exceptions to this have been shown, whereby the cathode potential undergoes the majority of potential change and becomes oxidising. It therefore seems that the conditions of the electrodes are sensitive enough to cross permeation of gas that both the anode and cathode potential may change during OCV. The presence of bulk water at one electrode makes that electrode more susceptible to potential change, especially if the other electrode is under a 'dry' environment. In contrast, electrodes under 'dry' conditions are not observed to undergo significant potential change. If a continuous flow of water is present at both anode and cathode, the potentials of both electrodes change only very slowly. These results indicate that continuous flow of water through both electrode compartments, or the drying of both electrodes, may serve as a mechanism by which PEMWE electrodes may be protected from electrochemical degradation during OCV.

Another influencing factor on the response during OCV is the electrode capacitance, which can limit the change in potential due to an electrochemical reaction. It might therefore be expected that, with future reductions in PEMWE catalyst loading, electrode

potentials that cause electrocatalyst degradation would be reached more rapidly during OCV.

From this chapter, the overall conclusions can be made that the major influencing factors that affect electrode potentials during OCV are:

- The reaction kinetics of OER, ORR, HER and HOR.
- The gas concentration at the anode or cathode
- The rate of O_2 and H_2 crossover
- The capacitance of the electrodes

This work is further expanded upon in Chapter 2.

7 Chapter 2 - Mathematical Modelling of OCV

7.1 Chapter Introduction

In Chapter 1 it was demonstrated that the electrode potential profiles during OCV are highly affected by the conditions within the PEMWE cell. Whilst most of the OCV conditions tested showed a greater rate of anode potential change compared to the cathode, there were also OCV regimes in which the reverse was the case. This was especially true when O_2 bubbles were present close to the anode electrode and H_2 gas was far removed from the cathode electrode by water. This finding, that the potential change may occur on either electrode, is important. As potential change may ultimately result in degradation, both electrodes are therefore susceptible to the degradation mechanisms discussed in section 4.4, and this therefore warranted a more detailed investigation. Chapter 1 was not a comprehensive analysis of PEMWE OCV, however. For reasons already mentioned, only OCVs at ambient temperature and pressure were performed. It may be expected that both these are influencing factors of OCV, especially with regards to gas crossover rate and the reaction kinetics. In this chapter, a one-dimensional mathematic model of OCV in a PEMWE is reported. In this model, a wide range of differential pressures, temperatures and electrode-gas distances were able to be modelled.

7.2 Developing a Mathematical Model of OCV in PEMWE

The major findings made in Chapter 1 have here been expanded upon and developed into a mathematical model of OCV. This model allows investigations into the temperature and pressure effects that were not covered in Chapter 1. Using both first

principles and experimentally derived data, this is both a model of electrochemistry and of the migration of dissolved gas. Crucially, this work is an adaptation on mixed-potential theory that has been used in literature to understand voltage drop at OCV in PEM fuel cells [153].

As it has been experimentally determined that gas crossover through Nafion is governed by Fickian diffusion [147,148,251], this OCV model was based around the Fickian diffusion of O_2 and H_2 through water and the Nafion membrane. The PEMWE OCV model developed therefore considers that there are three major phases within the PEMWE cell: The water within the anode compartment ($\varphi_{H2O/A}$), the Nafion membrane (φ_{Nafion}) and the water within the cathode compartment ($\varphi_{H2O/C}$). In between the phases are the anode and cathode electrode ($A_{electrode}$ and $C_{electrode}$) (Figure 56).

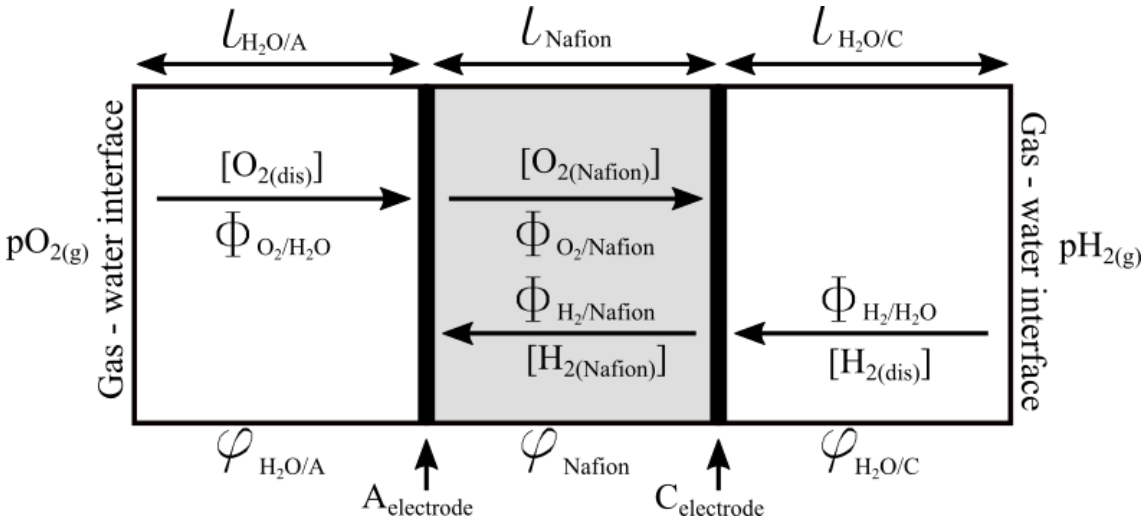

Figure 56. The model PEMWE system used for the simulation of OCV. The shaded area here represents the nafion membrane, with the electrodes represented as black lines. The non-shaded boxes here represent the wate phase which exists between the electrode and the oxygen or hydrogen.

7.2.1 Dissolved Gas Concentration and Diffusion Considerations

Within each phase in the PEMWE model there are two separate values for the concentration of $O_{2(dis)}$ and $H_{2(dis)}$ (this has not been shown in Figure 56 for the sake of clarity), the concentration at the beginning of the phase and the concentration at the end of the phase. From this, the difference in concentration, and therefore the molar diffusion flux of the dissolved gases (Φ) was calculated. For calculating this, the gas concentration in water has to be determined. At the gas – water interface, the concentration of $O_{2(dis)}$ and $H_{2(dis)}$ was approximated to be equal to the saturation concentration of the gas in water. This was achieved by application of Henrys' Law, as detailed in Chapter 1 (Section 6.2). The Henrys constant, k, has a temperature dependency that is calculated by the van't Hoff equation (Equation (45) and the expression of the variation of the enthalpy of dissolution for hydrogen (Equation (46). The enthalpy of oxygen dissolution within the PEMWE temperature range tested (20 – 80^{o}C) was assumed to be constant. Within the gas pressure range in PEMWE (1-20 bara) there is a direct correlation between the gas partial pressure and the saturation dissolved gas concentration [252], and so the Henrys law equation could be directly applied.

The molar diffusion flux of dissolved gases through the water and the Nafion membrane ultimately determine the rate at which the electrodes may undergo ORR or HOR, and so are the major factors in how the potential of the electrodes will change with time. For ORR to occur on the anode, the oxygen gas must diffuse through the water of length $l_{H2O/A}$. For HOR to occur on the anode, the H_2 gas must diffuse through the water of length $l_{H2O/C}$ plus the membrane length of l_{Nafion}. The converse is the case for the cathode. For determining molar diffusion flux of the dissolved gas through the water plus Nafion

phase, the calculation was made regarding each phase separately. This was done for two reasons. Firstly, one of the governing parameters for molar diffusion flux, the coefficient of diffusion (D), is different for each phase. Secondly, the concentration of dissolved gas before and after the electrodes may be different depending on the potential of the electrode the gas passes through. To take O_2 diffusion and ORR on the anode as an example, if the potential of the anode is at E_{rev} (O_2 / H_2O), then the concentration of the gas at the end of the water phase and the beginning of the Nafion phase will be the same. If the potential is slightly lower than E_{rev} (O_2 / H_2O) then the concentration of gas at the start of Nafion phase will be lower than the end of the gas phase proportional to rate at which ORR occurs. If the anode is substantially lower than E_{rev} (O_2 / H_2O) then it was assumed that the dissolved gas was completely reacted, and so there was no molar diffusion flux through the Nafion.

The molar diffusion flux of dissolved gas through water is additionally complicated by the GDL material in the PEMWE cell, as it both occupies volume, thus displacing water and the dissolved gas, and also makes the path length for dissolved gas diffusion through the water phase longer. The concentration of dissolved gas in the water phase is therefore a factor of the porosity (ρ) of the GDL, and the rate of diffusion is inversely correlated to the tortuosity (or 'tau' factor (τ)) of the GDL. The GDL material used in this study was identical to that reported by Maier et al [102], who, by the use of x-ray computed tomography (XCT), provided a GDL ρ of 28.7 % and τ of 3.3. With these values, the molar diffusion flux for each phase was calculated. Molar diffusion flux (Φ) for the water phases was calculated by Equation(49, and the molar diffusion flux for the Nafion phases was calculated by Equation (50.

$$\Phi_{H_2O/dis} = -D_{H_2O/dis} \frac{(C_{\varphi H_2O/start} - C_{\varphi H_2O/end})}{\tau\, l_{\varphi/H_2O}} \quad (49)$$

$$\Phi_{Nafion\ /\ dis} = -D_{Nafion/dis} \frac{(C_{\varphi Nafion/start} - C_{\varphi/Nafion/end})}{l_{\varphi/Nafion}} \quad (50)$$

Where D is the coefficient of diffusion and C_φ is the concentration of the dissolved gas in the respective phase. Both D and the coefficient of solubility, k, are experimentally derived parameters. Whilst the solubility and diffusion data of dissolved gases in water is well-established, there is less precise information pertaining to these values in hydrated Nafion. For the water phase, the solubility of dissolved gas has already been outlined in this report in Chapter 1 and has been directly used in this OCV model. The values for the diffusion coefficients of dissolved gas in water were taken from a report by Houghton and Wise [152]. There are two major sources of information from which the data of dissolved gases in Nafion were derived. Firstly is a review by Ito et al [246], in which all the known solubility, diffusivity and permeability data for O_2 and H_2 in Nafion (as of 2011) were collated. Secondly is a report by Schalenbach et al [147]. These sources represent the best data sets on dissolved gases in Nafion, but even so, the data sets here with regards to O_2 and H_2 are incomplete. For instance, values for the diffusivity and solubility of H_2 in Nafion have not been determined, but the permeability (which is the solubility multiplied by the diffusivity) has been. Although the permeability, diffusivity, and solubility values for O_2 in Nafion have been derived however, they are still imprecise (Figure 57). As the most important metric for this model of OCV is the permeability, then a simplification of the OCV system was able to be made so that the unknown solubility values in Nafion could be overlooked. As permeability is the multiplication of the

diffusivity and solubility, and as the permeability values have been derived (Figure 57), then the precise values for the solubility of the dissolved gases in Nafion becomes unimportant. It may become any arbitrary value therefore, and in this OCV model it was chosen to be the value for the solubility of the dissolved gas in water.

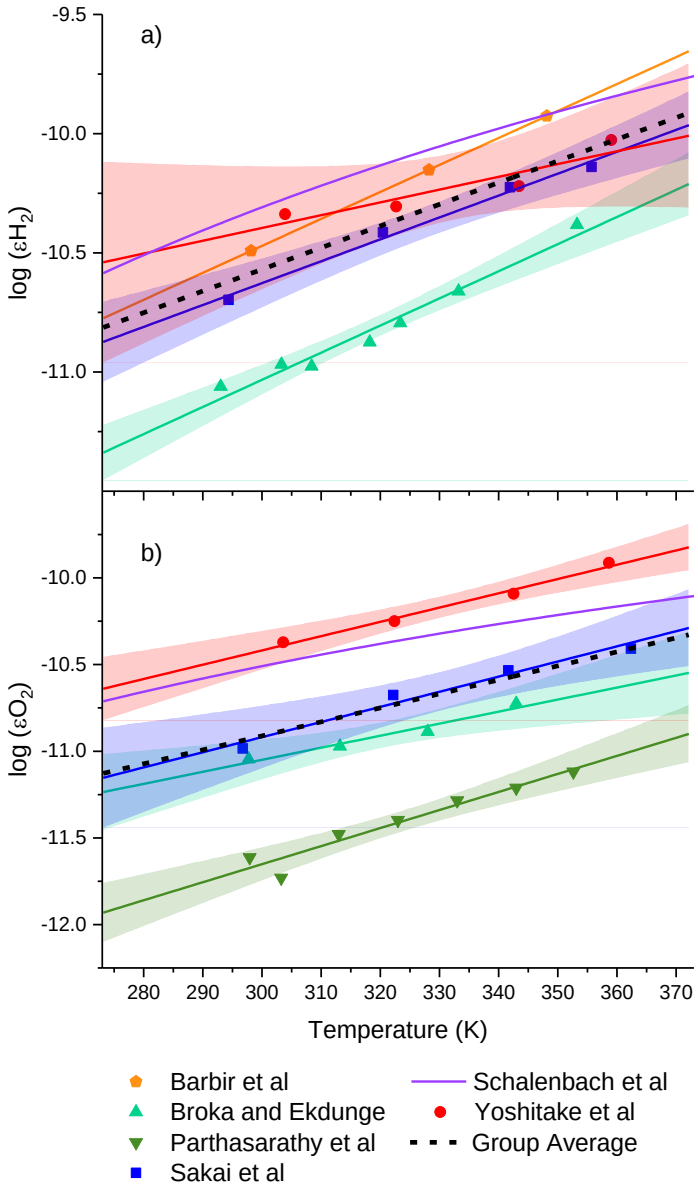

Figure 57. Experimentally derived values for the permeability of (a) H_2 and (b) O_2 in hydrated Nafion over the PEMWE temperature range. The black dotted line represents the average of each of the measurement groups, and it is this value that was used for the modelling.

The experimentally derived permeability values for oxygen in Nafion and hydrogen are given in Figure 57. From these values an average of log(ε) was taken, and from this a linear fit was applied to produce to the group average trends shown. The fitting result of this is given in Table 10, along with the other parameters and equations used to determine the diffusion of dissolved O_2 and H_2 through the water and Nafion phases. In this work,the calculations of the flux of molar diffusion are calculated in a different manner to the usual method (Bruggemann correlation). This was because the tortuosity of the phase was calculated in the one separate bank of equations, whereas the porosity (p) of each of the phases was incorporated into the overall solubility calculation (as shown in Table 1).

Table 10. The solubility and diffusional parameters used in the OCV model

Parameter	Phase	Gas	Fitting	Source
Permeability (ε) (mol cm^{-1} s^{-1} atm^{-1})	Nafion	H_2	$\varepsilon_{H_2/Nafion} = 10^{0.00909T-13.297}$	Figure 57a
		O_2	$\varepsilon_{O_2/Nafion} = 10^{0.00807T-13.333}$	Figure 57b
Solubility (k) (mol cm^{-3} atm^{-1})	Water / Nafion	H_2	$k_{H_2} = \rho k_{0/H_2} \exp\left[\frac{H_{sol/H_2}}{R}\left(\frac{1}{T}-\frac{1}{T_0}\right)\right]$	
		O_2	$k_{O_2} = \rho k_{0/O_2} \exp\left[\frac{H_{sol/O_2}}{R}\left(\frac{1}{T}-\frac{1}{T_0}\right)\right]$	
Enthalpy of solution (J mol^{-1})		H_2	$H_{sol/H_2} = 1000(0.140T - 45.97)$	
		O_2	$H_{sol/O_2} = -12060$	
Equilibrium dissolved gas concentration (C) (mol cm^{-3})	Water / Nafion	H_2	$C_{H_2=} k_{H_2} pH_2$	
		O_2	$C_{O_2=} k_{O_2} pO_2$	
Diffusion (ϕ) (mol cm^{-3})	Water	H_2	$\Phi_{H_2/H_2O} = -D_{H_2/H_2O} \frac{(C_{\varphi H_2O/start} - C_{\varphi H_2O/end})}{\tau l_{\varphi H_2O}}$	
		O_2	$\Phi_{O_2/H_2O} = -D_{O_2/H_2O} \frac{(C_{\varphi H_2O/start} - C_{\varphi H_2O/end})}{\tau l_{\varphi H_2O}}$	
	Nafion	H_2	$\Phi_{H_2/Nafion} = -D_{H_2/Nafion} \frac{(C_{\varphi Nafion/start} - C_{\varphi/Nafion/end})}{l_{\varphi/Nafion}}$	
		O_2	$\Phi_{O_2/Nafion} = -D_{O_2/Nafion} \frac{(C_{\varphi Nafion/start} - C_{\varphi/Nafion/end})}{l_{\varphi/Nafion}}$	
Diffusion coefficient (D) (cm^2 s^{-1})	Water	H_2	$D_{H_2/H_2O} = 10^{(2.816\times10^{-5}T^2 - 8.184\times10^{-3}T - 4.289)}$	[152]
		O_2	$D_{O_2/H_2O} = 10^{\left(-4.410 - \frac{773.8}{T} - \left(\frac{506.4}{T}\right)^2\right)}$	[152]
	Nafion	H_2	$D_{H_2/Nafion} = \frac{\varepsilon_{H_2/Nafion}}{k_{H_2}}$	
		O_2	$D_{O_2/Nafion} = \frac{\varepsilon_{O_2/Nafion}}{k_{O_2}}$	

7.2.2 Electrochemical Considerations

The electrochemical model of both PEMWE electrodes during OCV was an expansion of the theoretical model used in Chapter 1 (Section 6.3.1). The model assumed that the OCV period begins directly after operation, with no reduction in current density before the OCV period. Hence OER and HER occurs, as demonstrated in Figure 47. All tests in this OCV model, at the onset of OCV, had potentials fixed, at 1.6 V NHE for the anode, and -0.1 V NHE for the cathode. The rate of ORR and HOR that occurs on the electrode is directly correlated to the diffusional flux of the O_2 and H_2 gas. The rate of ORR and HOR on the electrodes thus becomes diffusion limited, and so the rate of potential change that occurs is related both to diffusion and the capacitance of the electrode in question. To complete this model, it must be considered that the oxidative charging of the double layer is, in essence, an electrochemical reaction. This oxidation is the association of the proton from the SO_3^- group of the Nafion ionomer side chain. SO_3^- upon the application of potential associates, but does not fully react via electron transfer, onto the positive electrode. This, in effect, represents an oxidised species. This double layer remains during OER, but at the onset of OCV, with an electrode potential still above 1.6 V, there is a thermodynamic preference for OER to continue. This occurs via the reduction of the SO_3 on the double layer surface, becoming SO_3^- and thus allowing an electron to re-enter the double layer and thus drop the potential. This potential drop continues until there is no thermodynamic preference for OER to continue, and so the potential comes to rest at E_{rev}. This is of course equally applicable for HER, and can thus explain the behaviour during OCV also.

In such a system, where potential change on an electrode is limited by both diffusion of the reactants, a variation in reactant flux with time, and the high capacitance of the electrode itself, mixed-potential theory does not provide a complete picture of electrode potential change with time. In a mixed-potential system, wherein a single electrode experiences both an oxidation and reduction reaction (HOR and ORR respectively in this case), the potential of the electrode (E_{corr}) becomes the point at which the currents associated with oxidation and reduction balance out, so there is no net current on the electrode. An example of this system is shown in the Evans diagram in Figure 58a. In this case, the electrode potential is balanced between E_{rev} (H^+/H_2) and E_{rev} (O_2/ H_2O) at approximately 0.4 V NHE, and there are no diffusional limitations on the rates of ORR and HOR. Figure 58b is the same reaction but augmented with diffusional limitations (ϕH_2 and ϕO_2) on the rate of HOR and ORR that may occur. There are two cases of diffusion shown in this figure, the first of which is with a diffusionally limited current of HOR substantially higher than a diffusionally limited current of ORR ($\phi H_2(1)$). In this case, $E_{corr}(1)$ is closer to E_{rev} (H^+/H_2) at 0.28 V NHE. However, in the case where the diffusionally limited current of ORR is higher than HOR ($\phi H_2(2)$), the potential of the electrode $E_{corr}(2)$ is closer to E_{rev} (O_2/ H_2O) at 0.71 V NHE [11]. By following this Evans diagram, it would be concluded that, at the point where the diffusionally limited current

[11] Note that these values are taken as examples from an illustrative Evans diagram. Please see the Figure caption for details.

of HOR becomes less than ORR, there would be a corresponding immediate shift in potential.

Assumptions are made in the creation of this model. Firstly, it is assumed that the double layer capacitance of this system remains constant throughout the test and does not vary dependent on the formation of intermediates. This is an assumption that may be assumed to impact the exact rates of potential change occurring at the electrodes but not the overall effect. It is also assumed that there is no self-discharge of the double layer capacitance. It must also be noted here that this model assumes that the electrodes have zero thickness, which will eliminate any effect that a concentration gradient of reactants in the electrode may have on the overall electrode potential.

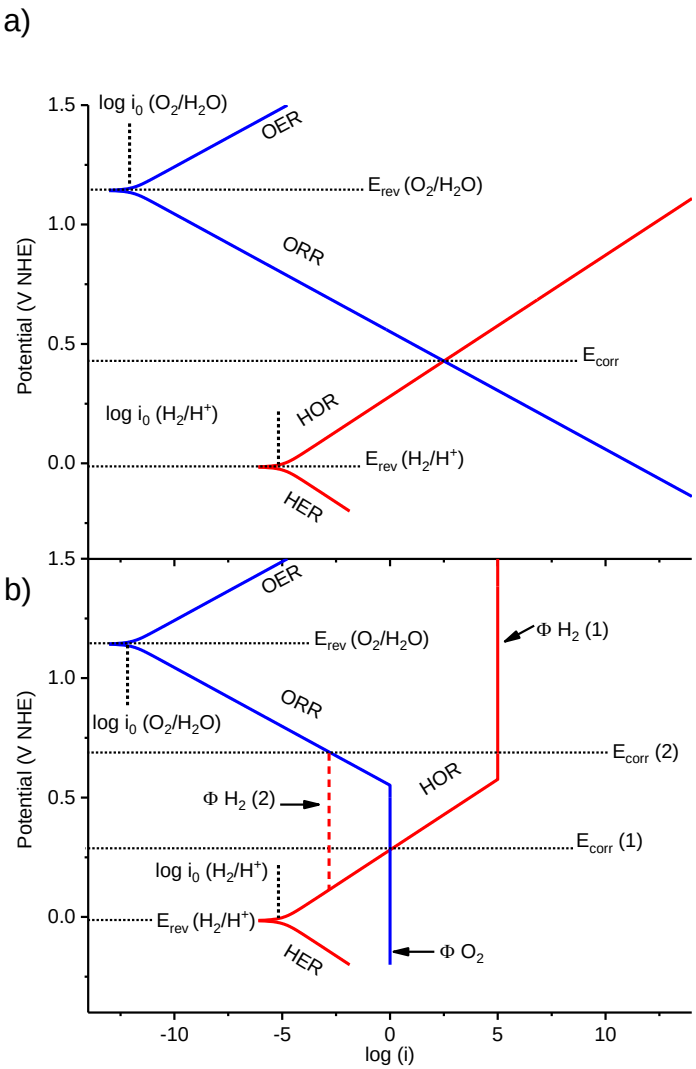

Figure 58. Example Evans (mixed-potential) diagrams of ORR and HOR occurring on an electrode. Shown in (a) is the balance of reaction with no diffusional limitations. Shown in (b) is the same reaction but is diffusion limited by the flux of H_2 or O_2 onto the electrode. Note that these Evans diagrams are illustrative only and are not true representations of the mixed-potential conditions in a PEMWE – The rates of diffusion have been exaggerated for the sake of clarity.

Interpretation of the Evans diagram in this manner would be possible in a system that has negligible associated double layer capacitance. In PEMWE however, the electrodes are high capacitance. Therefore, a high rate of electrode potential change is only possible with a high net current. As the maximum current on the electrode is dictated by diffusion and is hence very limited, it is therefore impossible for the potential of the

electrodes to change rapidly with the changing dissolved gas conditions. Application of the Evans diagram in Figure 58b may therefore only inform on the potential at which an electrode potential is trending towards, rather than on the potential it would be expected to be at any given moment. Factoring in the capacitance and the rate of the diffusion of the reactants provides a graph from which the rate of potential change on the electrode, and the E_{corr} may be predicted (Figure 59).

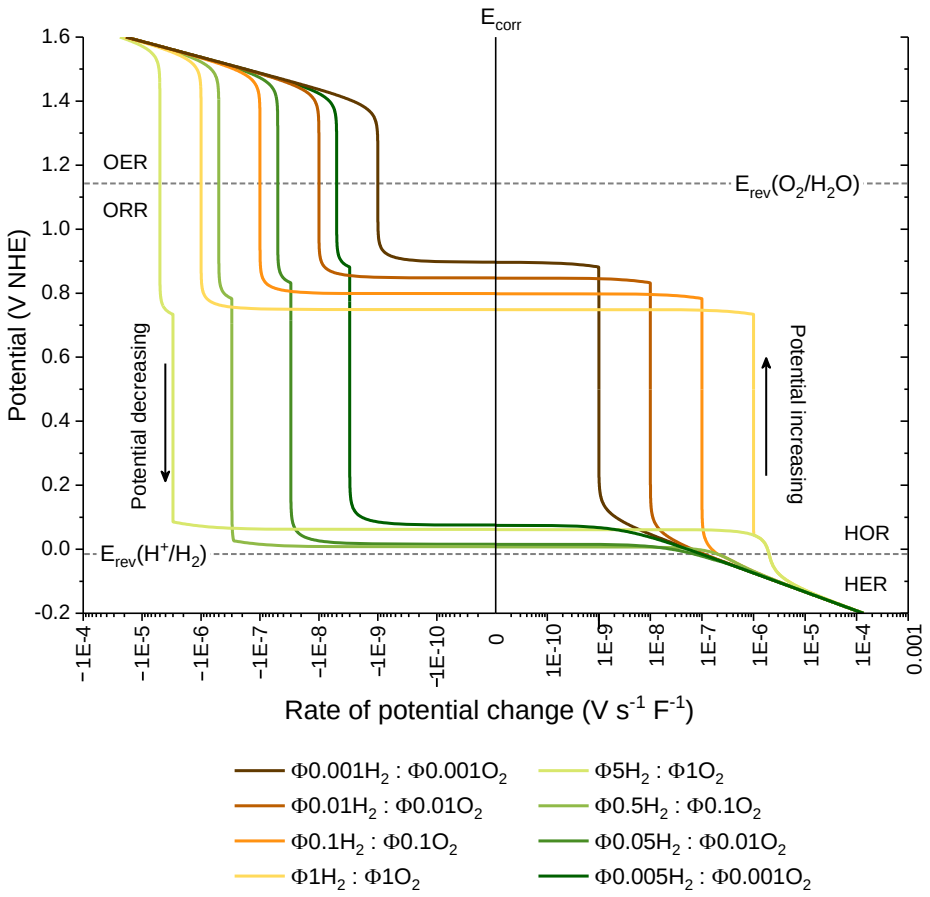

Figure 59. The rate and direction of potential change of a capacitive mixed-potential electrode under different fluxes of gaseous H_2 and O_2. The point at no potential change is the E_{corr} for the respective system. Shown on the x-axis is the expected rate of potential change of the catalyst. A value greater than 0 will cause the potential of the electrode to rise dependent on the capacitance of the electrode. A value

less then zero will correspondingly cause a reduction in potential. This graph is illustrative only and uses arbitrary datasets for aid of visualization.

This graph shows the rate at which the potential of an electrode will change, given different fluxes of O_2 and H_2 gas, and per Farad of electrode capacitance. On the x-axis, the zero point on the graph represents E_{corr}. At E_{corr} there is no rate of potential change as the rate of ORR and HOR is balanced on the electrode. When the electrode potential is not at E_{corr}, the electrode potential will trend back to E_{corr} at a rate shown by the position on the x-axis. For example, at potentials higher than E_{corr}, a greater rate of HOR occurs on the electrode than ORR, and so the potential reduces. When lower than E_{corr}, the potential will increase. The rate at which this occurs is dependent on the gas flux, and so with a higher flux the rate of potential change is greater. The reaction stoichiometry of the reactants is also a key determiner in how the potential changes. As can be seen, with a H_2 stoichiometry less than O_2, the general trend is for the E_{corr} to rest around 0.7 – 0.9 V, whereas with a H_2 stoichiometry greater than O_2, E_{corr} lies close to E_{rev} (H^+/H_2). Figure 59, although using arbitrary data, may itself provide the explanation for why the OCV profiles in Chapter 1 migrate in the somewhat binary manner observed; the electrode potentials either stay at, or migrate to, E_{corr} close to the E_{rev} (H^+/H_2), or to E_{corr} close to the E_{rev} (O_2/H_2O).

With the considerations of diffusion and capacitance, the equations governing the electrochemical model of OCV are here discussed. As several of the equations used have already been covered in Chapter 1, they are only briefly mentioned here, but are included in Table 11 for completeness. In the development of this model, several accommodations have had to be made regarding incomplete information, particularly regarding IrO_x. As IrO_x is not a practical catalyst for ORR, then the parameters of the

charge transfer coefficient have not been experimentally determined here. The dataset on Pt is more complete however; and so this electrochemical model of OCV will instead be based around a 2-electrode system both consisting of Pt electrodes.

In this electrochemical model, the modified Evans diagram in Figure 59 was solved at every time increment. Firstly, the potentials of E_{rev} (H^+/ H_2) and E_{rev} (O_2/H_2O) were calculated on both the anode and cathode. The Butler-Volmer equation was then solved for OER / ORR and HER / HOR on each electrode. At electrode potentials where the current becomes diffusion limited, the maximum current (i_{max}) was calculated. The sum of these reactions provides the total current (i_{total}) on the electrode, and from this value the rate of potential change on the electrode was calculated. Finally, where required, the conversion of partial pressure to concentration was made. The equations for these calculations are given in Table 11.

Table 11. Electrochemical parameters used for the development of the OCV model

Parameter	Equation	
(O_2/H_2O) reversible potential	$\mathrm{E}_{(\mathrm{O_2/H_2O})} = \mathrm{E}^{0}_{(\mathrm{O_2/H_2O})} + \frac{\mathrm{RT}}{4\mathrm{F}} \times \ln\left([\mathrm{H^+}]^4 \mathrm{pO_2}\right)$	(28)
(H^+/H_2) reversible potential	$\mathrm{E}_{(\mathrm{H^+/H_2})} = \mathrm{E}^{0}_{(\mathrm{H^+/H_2})} + \frac{\mathrm{RT}}{2\mathrm{F}} \times \ln\left(\frac{[\mathrm{H^+}]^2}{\mathrm{pH_2}}\right)$	(33)
(O_2/H_2O) current	$\mathrm{i_a} = \mathrm{i}_{\mathrm{o(O_2/H_2O)}} \mathrm{pO_2} \exp\left(\frac{\alpha_\mathrm{O} 4\mathrm{F}}{\mathrm{RT}}\left(\mathrm{E} - \mathrm{E}_{(\mathrm{O_2/H_2O})}\right) - \frac{\alpha_\mathrm{O} 4\mathrm{F}}{\mathrm{RT}}\left(\mathrm{E} - \mathrm{E}_{(\mathrm{O_2/H_2O})}\right)\right)$	(40)
(H^+/H_2) current	$\mathrm{i_c} = \mathrm{i}_{\mathrm{o}(\mathrm{H^+/H_2})} \mathrm{pH_2} \exp\left(\frac{\alpha_\mathrm{H} 2\mathrm{F}}{\mathrm{RT}}\left(\mathrm{E} - \mathrm{E}_{(\mathrm{H^+/H_2})}\right) - \frac{\alpha_\mathrm{H} 2\mathrm{F}}{\mathrm{RT}}\left(\mathrm{E} - \mathrm{E}_{(\mathrm{H^+/H_2})}\right)\right)$	(40)
(O_2/H_2O) max current	$\mathrm{i}_{\mathrm{max/O}} = -4\mathrm{F}\Phi_{\mathrm{O_2}}$	(51)
(H^+/H_2) max current	$\mathrm{i}_{\mathrm{max/H}} = 2\mathrm{F}\Phi_{\mathrm{H_2}}$	(52)
Total current on electrode	$\mathrm{i_{total}} = \left(\mathrm{i_O} \middle| \mathrm{i_{max/O}}\right) + \left(\mathrm{i_H} \middle| \mathrm{i_{max/H}}\right)$	(53)

Rate of potential change	$\frac{dV}{dt} = \frac{i_{total}}{C}$	(47)
Partial pressure to concentration (mol cm^{-3})	$[O_2] = \frac{pO_2 RT}{Pa \times 1 \times 10^{-6}}$	(54)

Overall, although there are numerous variables that may be tested, for the testing to complete within a reasonable timeframe the number of variables was reduced. Factors including the porosity and tortuosity of the GDL, the thickness of the Nafion membrane, the capacitance of the electrodes, and the potentials of the electrodes immediately before OCV were kept constant. Finally, as real PEMWE systems operate at ambient pressures of O_2, the O_2 pressure was kept constant also. In this model the effects of temperature, H_2 pressure, and the position of the gas-water boundary (the length of the water phases) were investigated. The constants and variables chosen are given in Table 12.

Table 12. Constants and variables used for the model of OCV

Constants		**Source**
Porosity (ρ)	0.287	[102]
Tortuosity (τ)	3.3	[102]
Membrane thickness (μm)	200 (approximating the increase in thickness due to swelling)	[246]
Anode capacitance (F cm^{-2})	0.292	Chapter 1
Cathode capacitance (F cm^{-2})	0.043	Chapter 1
OCV duration (h)	2	
Variables		
Temperature (°C)	20, 40, 60, 80	
H_2 pressure (atm)	1, 2, 5, 10	

Anode water phase length (mm)	0.01, 0.1, 1, 2, 3
Cathode water phase length (mm)	0.01, 0.1, 1, 2, 3

7.3 Results and Discussion

To cover the full range of variables, 400 separate OCV tests were modelled. Data on the voltage, anode and cathode potential and the rate of potential change over time were produced for each test. The general trends observed from these tests match the practical results in Chapter 1 - The OCV profile is dominated by either the change in anode or cathode potential, or by neither to any great extent. A large potential change on both electrodes simultaneously was not observed on any test. In order to model this and to aid comparison between the variables the results are either presented as their full OCV profiles, the values for the anode or cathode potential reached at the end of the 2-hour OCV period, or as a comparison of the magnitude of change of both electrodes. The latter was calculated in the following manner.

$$\mathrm{A} = \frac{\left|\mathrm{V}_{\mathrm{anode/start}} - \mathrm{V}_{\mathrm{Anode/end}}\right|}{\left|\mathrm{V}_{\mathrm{cathode/start}} - \mathrm{V}_{\mathrm{Cathode/end}}\right|} \tag{55}$$

$$\mathrm{A} = \begin{cases} \mathrm{A} - 1 \text{ if } \mathrm{A} \geq 1 \\ -1/\mathrm{A} + 1 \text{ if } \mathrm{A} < 1 \end{cases} \tag{56}$$

Where A is the magnitude of change. Therefore, if A is positive, this denotes an OCV in which the greatest potential change occurs on the anode. In these cases, H_2 dominates the overall OCV system, and so these OCV plots were denoted as 'H_2 dominant'. Conversely, a negative A denotes an OCV in which the greatest potential change occurs

on the cathode. In these cases, O_2 dominates the overall OCV system, and so these OCV plots were denoted as 'O_2 dominant'. Respecting the aforementioned OCV trends, a low A value generally denotes an OCV in which neither the anode nor cathode potential changes to any great extent.

7.3.1 Comparison of Model and Real OCVs

To validate the OCV model, some of the modelled data plots were compared to the real OCV profiles. Real OCV Tests 6, 7 and 8 from Chapter 1 were chosen as a comparison, as the conditions of these cells were the most easily controlled and so could be most easily assigned to a particular OCV model. The variables of the chosen modelled OCV plots are given in Table 13, with the OCV plots given in Figure 60.

Table 13. Comparison of real and modelled OCV tests. All real OCV tests took place at 1 atm hydrogen pressure at 20^0C

	Real OCV	Model OCV					
	Test	**Anode condition**	**Cathode condition**	**Hydrogen pressure (atm)**	**Temperature (^{o}C)**	**l H_2O/A (mm)**	**l H_2O/C (mm)**
Figure 60a	6	$O_{2(g)}$ / No flow	$H_{2(dis)}$ / No flow	1	20	0.01/0.1	3
Figure 60b	7	$O_{2(g)}$ / No flow	$H_{2(g)}$ / No flow	1	20	0.01/0.1	0.01/0.1
Figure 60c	8	$O_{2(dis)}$ / No flow	$H_{2(g)}$ + EOD H_2O / No flow	1	20	3	0.01/0.1

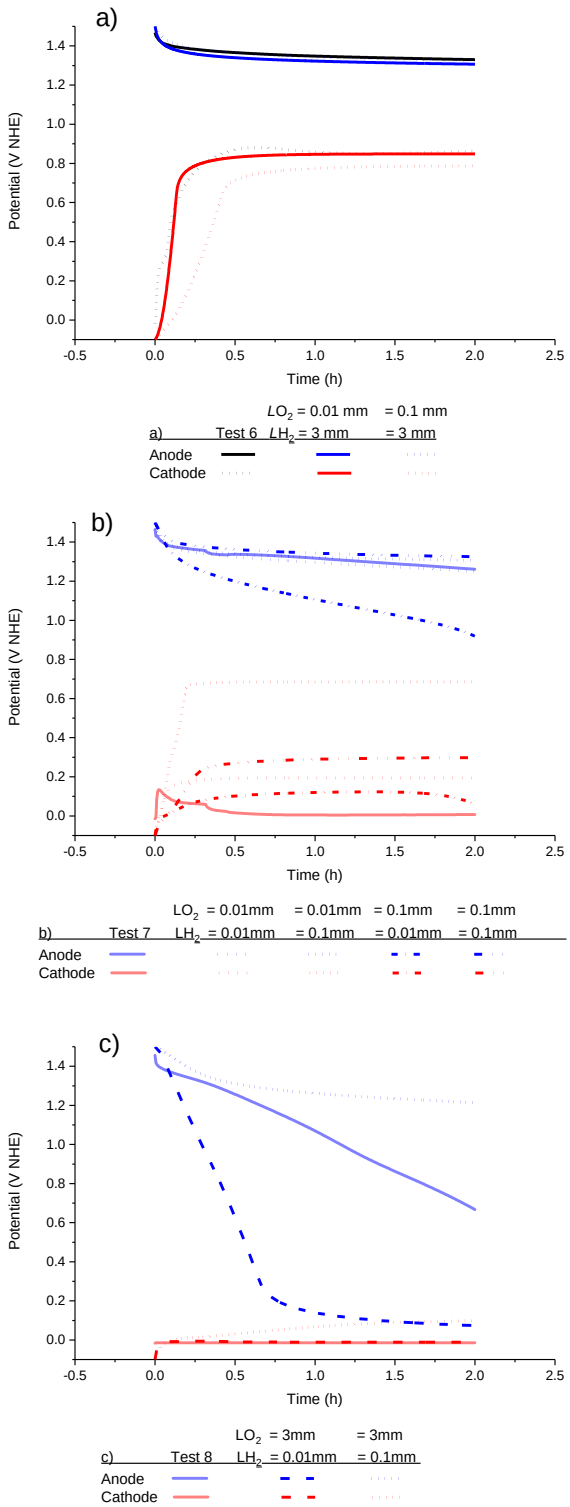

Figure 60. Comparison of real OCV data to the modelled OCV data with the closest conditions. LO_2 and LH_2 denote the phase length of the anode and water phases respectively in each test. These comparisons between the real data and modelled data are based on the closest estimation of the real conditions to the modelled conditions. Therefore, an exact match of theoretical to real data should not be expected.

By comparison of the real and modelled OCV data it can be seen that, in cases where the difference in the phase length of the anode water length versus the cathode water length is very high (i.e. Figure 60a and c), there is a relatively close fit of the real and modelled OCV. The best fit appears in Figure 60a, with a small anode water phase length and large cathode water phase length. Here, the anode potential models especially are a very good fit with real data. The reason for this is that H_2 permeation in these tests is very limited, due both to the length of the cathode water phase and the high rate of HOR occurring on the cathode at high potential. The anode potential is therefore determined predominantly by the rate of OER occurring on the electrode. Furthermore, the high capacitance of the anode (relative to the cathode) means that any differences in the reaction rate between real and modelled systems will only cause smaller changes in potential relative to the cathode. This can be seen in Figure 60c, where the cathode clearly has more sensitivity to slight changes in the OCV conditions. In this case, the modelled cathode water phase length varied from 0.01 mm to 0.1 mm, with the difference being a 100 mV increase in cathode potential by the end of the 2 h OCV period. This test also highlights the very high sensitivity of the OCV plots on the water phase lengths, as the different cathode phase lengths in this test have imparted very different anode potential trends. Although the same overall effect is observed (i.e. the anode potential reduces whilst the cathode potential remains relatively constant), the rates at which the anode potential decays are clearly very different, thus showing that the rate of hydrogen permeation is substantially different. This may be explained by the fact that the Nafion phase length is very short, any changes in the cathode phase length proportionally change the overall phase length, and so the rate of hydrogen permeation is highly affected. Hence, at the very short phase lengths it may be difficult to accurately

match the real and model OCV data, as even very slight differences in the water layer thickness may produce substantially different rates of potential change at the anode or cathode. The sensitivity of the overall OCV profiles is clear in Figure 60b also. Here, the anode potential remains little changed other than the case where the anode phase length is 0.1 mm compared to the cathode phase of 0.01 mm. The cathode, however, varies with each test, which is caused by the lower capacitance of this electrode.

Overall, the real OCV profiles are relatively consistent with the closest matching condition OCV models, showing the same general trends over time, although not matching precisely due to the very high sensitivity of the system to even slight variations in the length of the water phases. This is something that cannot be properly controlled in a real PEMWE system, especially as the water phase length is unlikely to be homogeneous over the entire electrode surface. The OCV model is therefore a good one-dimensional model from which the effect of the water phase lengths, pressure and temperature may be discussed and compared to other modelled data in a quantitative manner. When translating this data to what may be expected in a real PEMWE system however, only a qualitative discussion (i.e. whether the particular system is expected to experience anode potential change, cathode potential change, or neither) is feasible.

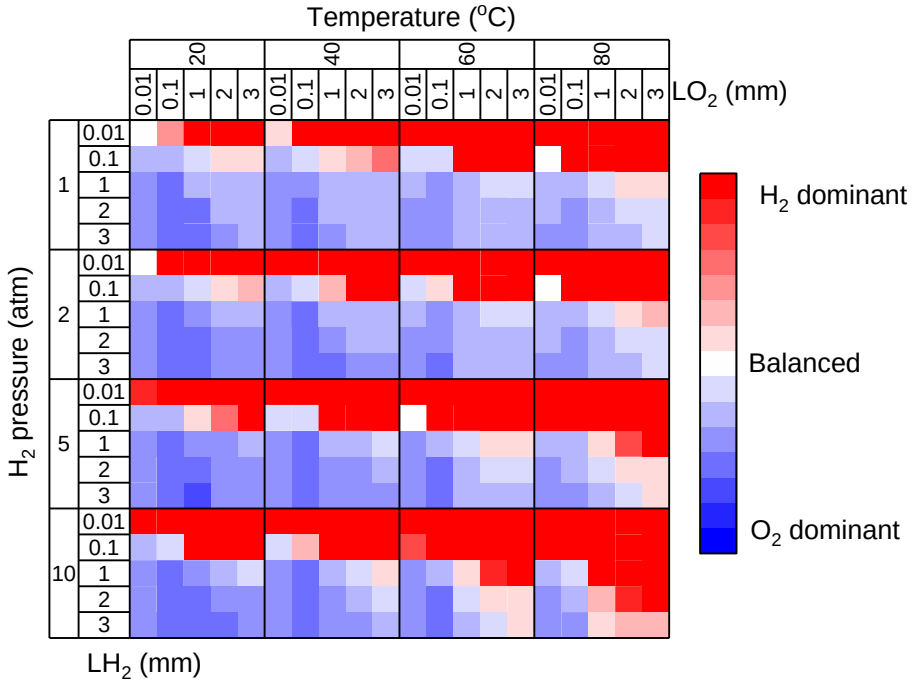

Figure 61. The OCV potential balance over the range of anode phase lengths (LO_2), cathode phase lengths (LH_2), temperatures (top column) and H_2 pressures (right column). Red colours denote an OCV plot in which H_2 is dominant. In these tests the OCV is characterized by a decreasing anode potential. In blue are denoted OCV plots in which O_2 is dominant. In these tests the OCV is characterized by an increasing cathode potential.

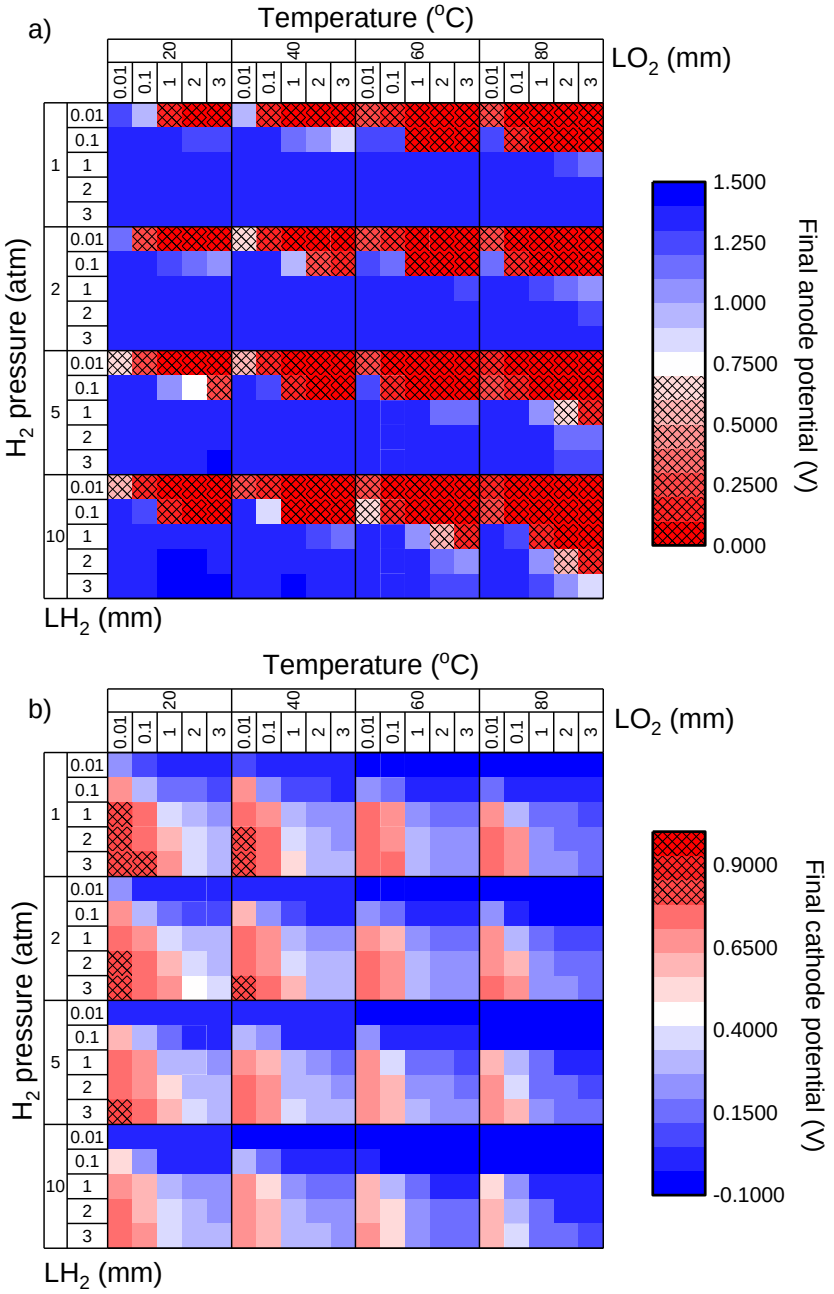

Figure 62. The potential of a) the anode and b) the cathode after 2 h at OCV under each OCV condition. The hatched cells represent potentials in which degradation of the electrocatalyst by a) the reduction of IrO_x or b) oxidation of Pt may be expected. Note that in several cases, particularly at the cathode, the potential reached after 2 h OCV is not steady state.

7.3.2 The Effect of Water Phase Length on the OCV Profile

The permeation rate of the dissolved gases is proportional to the sum of the water and Nafion phase lengths. As the Nafion phase length is relatively short in comparison to the water phase lengths tested, then the relative water phase lengths have a substantial impact on whether the OCV will be H_2 (HOR) or O_2 (ORR) dominated. With equal anode and cathode phase lengths, and up to 2 atm of H_2, the general trend is that the OCV profile is O_2 dominant. Here, the H_2 permeation rate is less than twice that of the O_2 permeation rate. At low pressures, OCV is only H_2 dominant at the extremes of phase length difference. This extreme does, however, represent a common state that is expected of PEM electrolysers (i.e. with a 'dry' cathode and a large head of water at the anode), and so a H_2 dominant OCV is expected, except for cases where O_2 bubbles are close to the CCM. Even with relatively large differences between the phase lengths (e.g. a 1 mm cathode phase depth versus 3 mm anode phase depth (Figure 63), the OCV is O_2 dominant, albeit with a relatively slow rate of cathode potential change trending towards oxidising potentials. Particularly with low pressures, there is a substantial range of water phase lengths tested where there is very little overall change in the potentials of the anode and cathode over 2 h. Examples of these are given in Figure 63, which generally show little potential change in OCV systems with large associated phase lengths, although the cathode potentials are still generally increasing after 2 h. So, whilst these OCV profiles do not show substantial potential change over the course of the experiment, it is unlikely that these represent a true steady state, and the potentials are still likely to migrate further.

Over the course of a 2 hour OCV however, there are still several conditions that result in large potential changes for the anode or cathode. Of particular importance are those

that transition past the potentials of either IrO_x reduction (≈ 0.6 V) or Pt oxidation (≈ 0.85 V). At these potentials therefore, the dissolution of the electrocatalysts may be possible in the manner discussed in section 4.4. These regions have been highlighted in Figure 62a and b, and show that the general trend for these particular profiles are lengthy water phases with a short water phase in the counter compartment. In the case of anode potential change therefore, this is associated with a long water phase at the anode (thereby reducing the permeation rate of O_2 to the anode) and a short water phase length at the cathode, so the combined phase length of the cathode water phase plus the Nafion phase is short. This increases the H_2 permeation rate enough that it becomes greater than twice that of the O_2 permeation rate, and so the anode potential reduces. The converse case also applies for potential change at the cathode; however it can be clearly seen that, at 1 atm of H_2 pressure, there are fewer conditions that cause a substantial potential change of the cathode. The reason for this is the reduced permeability of O_2 in Nafion compared to H_2 (Figure 57).

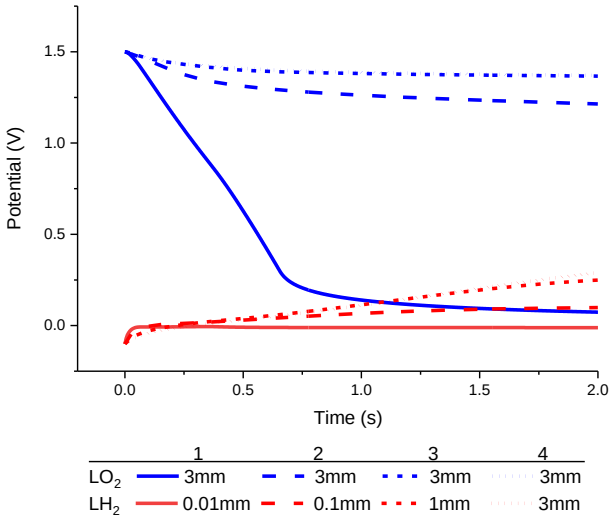

Figure 63. Example of the impact of the variation of phase length on the anode and cathode potentials during an OCV at 293 K and 1 atm H_2 pressure. Shown in red is the cathode potential and shown in blue is the anode potential.

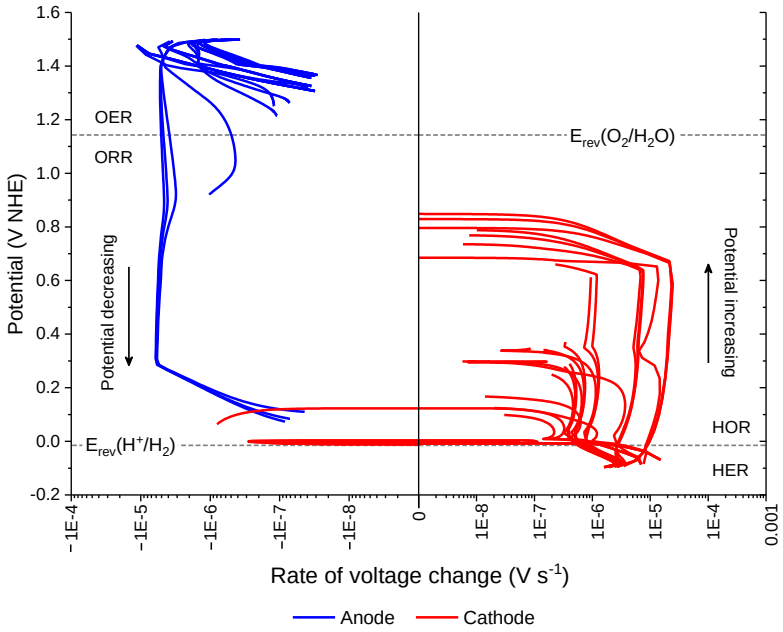

Figure 64. The rate and direction of potential change of the anode and cathode of the modelled one-dimensional PEM electrolyser at 293 K and 1 atm H_2 pressure. This data is modelled in the same manner as the profiles shown in Figure 59.

As the OCV model consists of two electrodes, both participating in simultaneous electrochemical reactions, then the rate of HOR or ORR occurring on one electrode impacts the rate of H_2 or O_2 diffusion onto the other electrode. There is therefore a connection between the two electrodes based on the diffusion of gas through the Nafion. This 2-electrode system is why, in some OCV plots (e.g. the 5 and 10 atm H_2 plots shown in Figure 66) the potentials have been shown to deviate from a steady state. The change from steady state potential occurs when the potential of the other electrode stops completely consuming either the O_2 or H_2, and thus allowing the gas to permeate through the membrane. This coupling between the two electrodes explains why the rate of potential change versus potential, as shown in Figure 64, is substantially more

complicated than that given in Figure 59. This is effectively the difference between a 2-electrode system and a 1-electrode system.

7.3.3 The Effect of Temperature and Pressure

Increasing temperature increases the permeation rate of O_2 and H_2 through Nafion and water. In OCV however, as pressure and temperature are factors in several equations used to produce the model, and as the potential of the anode and cathode is the sum of the rates of both ORR and HOR occurring, then there is no direct correlation between temperature and the rate of potential change at the anode or cathode (Figure 65). Overall, as can be seen in Figure 61 and Figure 62, the general trend is that increasing temperature favours the H_2 dominance of the overall OCV profiles, with a diminishing range of conditions favouring cathode potential change. Additionally, under conditions that are still O_2 dominant, the rate of potential change of the cathode is somewhat suppressed. This is represented by the fact that fewer of the conditions resulted in a cathode potential greater than 0.85 V after 2 h. Additionally, at higher temperature, fewer OCV conditions resulted in a balanced potential profile. Therefore, as higher temperature OCV tends to favour the potential change of the anode, degradation of the anode electrocatalyst over cathode electrocatalyst would be expected under most OCV conditions.

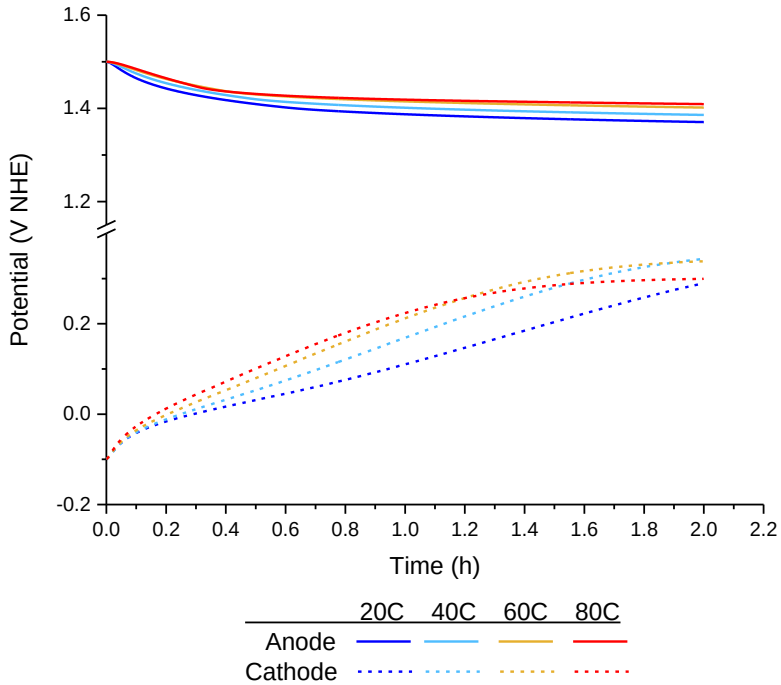

Figure 65. OCV models at 3mm phase depth for the anode and cathode water phases, with 1 atm pressure and over a range of temperatures. OCV at 20°C shown in blue, 40°C shown in green, 60°C shown in orange and 80°C shown in red.

As the increase in H_2 pressure only affects the rate at which HOR occurs, then there is a clear trend that higher pressures result in a greater range of H_2 dominant OCV profiles. The increased pressure furthermore increases the rate at which the potential changes (Figure 66). As such, the anode potential can decrease very rapidly, and this rate is particularly high with a very short anode water phase length. This rapid drop in anode potential matches that observed practically by Weiß et al [119], who determined OCV at 10 atm of H_2 pressure.

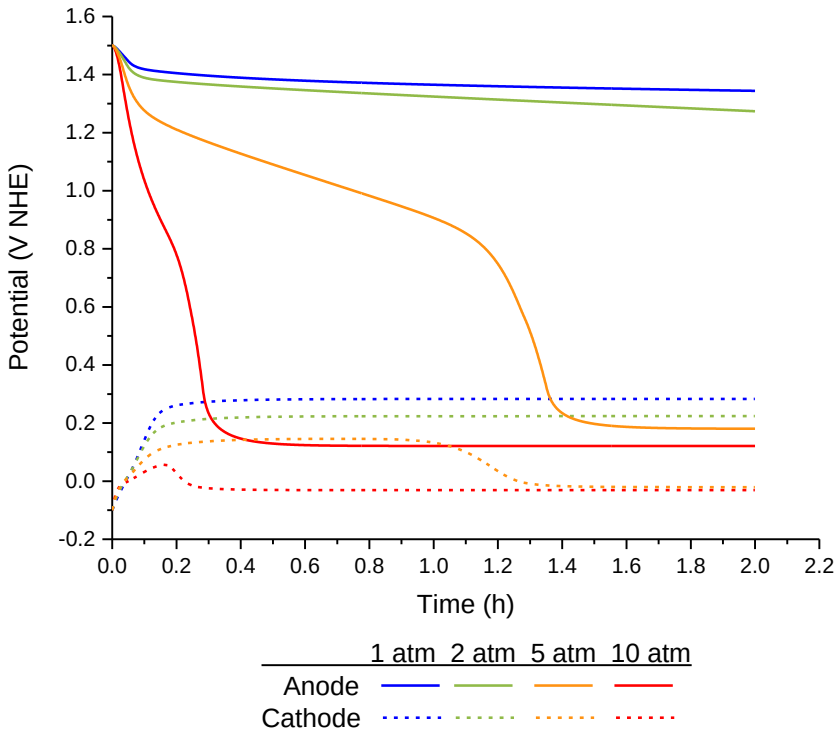

Figure 66. OCV models at 0.1mm phase depth of anode and cathode at 60C at a range of hydrogen pressures. Shown in blue is H_2 pressure at 1 atm, green at 2 atm, orange at 5 atm and red at 10 atm.

7.3.4 Limitations of the Mathematical OCV Model

Some of the limitations of the OCV model can be observed by comparison of the model OCV data to real OCV data. The most salient discrepancy regards the steady state potentials reached by the anode and cathode. In Figure 66, for example, the steady state potential of the cathode reaches a range of potentials dependent on the pressure. This is again observed in Figure 63. These results are in contrast to the real OCV data, where the steady state potentials have been observed to either be very close to E_{rev} (O_2 / H_2O) or E_{rev}(H^+/H_2). The model OCV data therefore seems to be following a mixed-potential model, whereas real potentials seem to be dominated by one redox reaction only. There are two possible explanations for this discrepancy. Firstly, it may be possible that the calculation of the exchange current density of OER/ORR and HOR/HER provides values

that are less than that observed experimentally. With higher exchange current density, the Nernst equation is applicable in a smaller potential range before the reaction becomes diffusion-limited, and so the mixed-potential estimates become closer to E_{rev} (O_2 / H_2O) or $E_{rev}(H^+/H_2)$. However, in order for this to be the case, the exchange current density underestimate must be several orders of magnitude, and this is unlikely. Secondly, the effect of sparging may offer the explanation for the discrepancy. Sparging is the process by which dissolved gases in a solvent are replaced by another dissolved gas through bubbling. In the deaeration of water for example, a gas with a low solubility (N_2 usually) is bubbled through water to remove dissolved oxygen. With bubbling, the partial pressure of dissolved oxygen is greater than the partial pressure of gaseous oxygen (as there is none), and so the system falls out of equilibrium. In order to re-establish equilibrium, the dissolved O_2 exchanges out of the solvent and into the gas phase. Likewise, as the low solubility gas has a higher partial pressure in the gaseous form than as dissolved gas, this gas exchanges into the solvent. In the OCV model there would be no mixing of O_2 or H_2 in the potential ranges in which the electrodes are diffusion-limited, as diffusion limitation means that one dissolved gas is completely consumed by the electrode. The potential ranges that are not diffusion-limited are close to the E_{rev}, and so at close to these potentials some dissolved gas will begin to migrate through the electrode. At this point there may be some interaction between the different dissolved gases. It must also be considered here that the this model is a zero-dimensional model of the PEMWE system, containing electrodes that have no thickness. This ignores concentration gradients that may occur within the electrodes, and so represents another limitation of this model.

7.4 Chapter 2 Conclusions

The discussed limitations aside, the model of OCV has been found to be an acceptable descriptor of a real OCV within specified ranges. Under conditions in which there is an extremely large difference in partial pressure and permeation rate of H_2 to O_2, the anode potential has been found to decrease to reducing potentials. The rate at which this occurs is extremely sensitive to the cathode water phase length, and so it is not possible to perfectly mimic real OCVs. The model OCV does, however, show a number of close similarities to the real OCV plots in section 6. The most important correlation is that there are clearly a large range of conditions that may result in either anode potential change dominated, or cathode potential change dominated OCV plots. Additionally, the OCV plots, although often not matching in time to real OCVs, are very similar in shape. This indicates that the overall model of OCV is probably a good overall descriptor of what actually occurs, and instead there is a difference in magnitude of some of the variables. The OCV model is, however, very sensitive to these variables, and as this may mean that, under some conditions tested, H_2 permeation rate to the electrodes becomes greater than twice that of O_2. Under identical conditions therefore, the model of OCV may not match a real OCV. This model may therefore not be used to predict the exact OCV under every condition, but it does clearly show that OCV's may progress with anode, cathode or no overall potential change, with the most crucial determiner of potential change being the length of the water phases (or the proximity of gas to the electrode). Even under extremes of H_2 differential pressure and temperature, where H_2 dominated OCVs would be expected, the OCV may become O_2 dominated if $O_{2(g)}$ is close to the electrode and $H_{2(g)}$ is far removed.

Whether the OCV conditions tested in this section would match those of real PEMWE systems is dependent on several factors of PEMWE stack design and operation. As a range of PEMWE operational regimes have been determined (as discussed in section 4.1), this section has shown that the resulting OCV profile is highly dependent on those conditions.

8 Chapter 3 - The Application of Voltammetry to Electrocatalyst Dissolution, and the Dissolution of PtB in PEMWE

8.1 Chapter Introduction

Both the experimental OCV profiles and the mathematical model of OCV have shown that potential change may occur on both the anode and the cathode. This therefore means that both the Pt and IrO_2 electrocatalyst may undergo degradation relating to redox changes, as outlined in Section 4.4. Briefly, these degradation mechanisms include electrochemical Ostwald ripening, particle coalescence and agglomeration, dissolution of the electrocatalyst, and, in the case of Pt/C, the detachment of Pt from its carbon support [164,207,220,253]. Of particular interest is the dissolution mechanism, as this has clearly been demonstrated by SFC-ICP-MS techniques to be a mechanism of irreversible catalyst material loss [219,221]. Unlike some of the other mechanisms however, an analysis of *in situ* dissolution has not been made in PEMWE to date; dissolution has only been measured *in vitro*. As *in vitro* systems do not perfectly represent *in situ* systems [254], the use of the 3-electrode cell to quantify dissolution represented an excellent opportinuty to investigate this mechanism in a real PEMWE in which the electrode potentials may be measured.

ICP-MS through the use of the scanning flow cell has clearly demonstrated that it is a powerful method for measuring electrocatalyst dissolution; providing near real-time measurements with extremely low limits of detection of dissolution from electrodes

under electrochemical control [160,215,222]. Because of complexity and high cost however, in-line ICP-MS is not a readily available technique. In replacement of ICP-MS the following sections apply voltammetry as the method of quantifying the dissolution of the electrocatalysts [230,255–257].

This section reports several important findings for the field of electrocatalysts in PEM electrolysers. To the best of the authors knowledge, this is the first time that voltammetry has been used to quantify electrocatalyst dissolution from an electrochemical device. This is also the first reported case of quantified electrocatalyst dissolution from an operating PEMWE cell. In this section, firstly the details of the voltammetric techniques are provided. These techniques are then applied to standard solutions of Pt, Ir and Ru and compared to ICP-MS. Finally, before application to PEMWE systems, the voltammetry techniques are tested for possible interference effects from other elements that may be present in the water.

8.2 Voltammetry as a Method of Determining Electrocatalyst Dissolution

8.2.1 Voltammetry of Pt

The voltammetric technique used to quantify Pt in this report follows the method developed by Zhao and Freiser [255]. Voltammetry by this method was adopted by Metrohm additionally as a standard technique, and this is outlined in detail in the Metrohm Application Bulletin 220/4 e [258]. This method is overall one that utilises the excellent electrocatalytic properties of Pt for facilitating HER. In brief, Pt from the solution under test is adsorbed onto the surface of a hanging mercury drop electrode (HMDE). In contrast to Pt, mercury is an extremely poor catalyst for HER, and so when

the HMDE is swept through a reducing potential, HER will only occur if Pt is present, and will occur at a rate proportional to concentration of Pt adsorbed on the HMDE surface. As HER is a redox process, the rate at which it occurs can be measured by a potentiostat. This voltammetry technique is known as 'Catalytic wave voltammetry'.

There are several steps involved in this voltammetry process to achieve the quantification of Pt. Firstly, the method may only quantify dissolved Pt species (Pt(II) and Pt(IV)). It is not sensitive to Pt(0) as adsorption of a solid is not possible, and the corrosion of Pt(0) to Pt(II) or Pt(IV) in the electrolyte used is not possible also. The acidic electrolyte used in this technique also contains a complexing agent, formaldehyde hydrazone, formed by the reaction of formaldehyde with hydrazine. This molecule complexes with Pt (II) species, forming the complex shown in Figure 67. Additionally, the electrolyte contains an excess of hydrazine for the reaction. This therefore becomes a reducing solution that reduces the Pt(IV) species to Pt(II), thereby allowing it to be complexed with the formaldehyde hydrazone molecule. This complex is then adsorbed onto the surface of the HMDE when it is held at low potentials. One of the primary steps in the voltammetric technique is therefore to 'pre-concentrate' the Pt(II) on the HMDE surface.

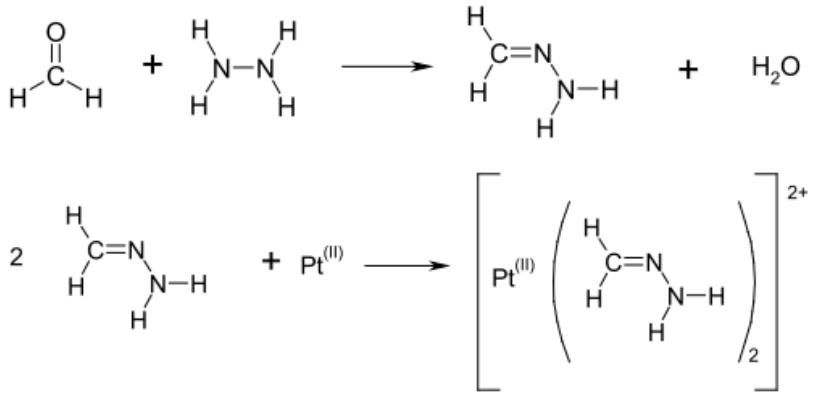

Figure 67. The reaction of formaldehyde and hydrazine to form a formaldehyde-hydrazone complex that may coordinate with Pt(II) species in water. The excess hydrazine in the electrolyte also acts as a reducing agent, reducing Pt (IV) to Pt(II). Reprinted from [258]. Once the HMDE has been pre-concentrated, the HMDE then undergoes a differential pulse voltammetry (DPV) sweep in the reducing direction.

DPV describes a method by which the electrode potential is varied with time. DPV is a technique by which a square wave potential signal is overlaid on a linear sweep profile, with the result being a decreasing or increasing potential DPV profile, as shown in Figure 68a. The essential function of DPV is to measure the difference in the currents at the upper and lower potentials of the pulse profiles (E_{high} and E_{low} respectively). This profile therefore provides the first derivative of an LSV profile of the same potential range and sweep rate. Shown in Figure 68b and c are illustrative examples of how the current – potential profile would manifest in this system with LSV and under DPV. There are three regions of interest here. First is the exponential increase in current signalling the onset of Pt-catalysed HER. By design of the technique, the amount of Pt adsorbed onto the Hg surface is limited, and as the potential decreases further the rate of reaction becomes limited by the limited amount of Pt available for HER. At this point the reaction becomes rate limited (Pt-HER rate limitation). Whilst in LSV this region manifests as a levelling-off

of current, in DPV this manifests as a reduction in the current difference. Finally, is the exponential rise in current associated with HER on Hg. Although Hg is a poor catalyst for HER, the far higher surface in comparison to Pt means that a rate limitation is not observed within the potential range of the test, and as such it appears as an exponential growth both in LSV and DPV.

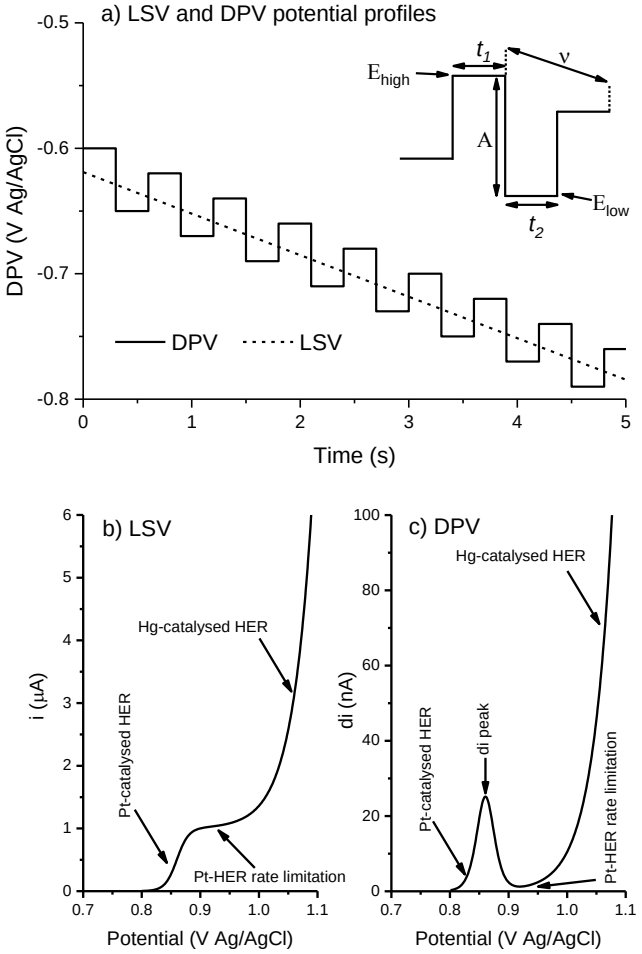

Figure 68a) Potential profile of DPV and LSV techniques with time. The DPV profile parameters correspond to the peak profile as follows: t_1 and t_2 are the step times of the upper and lower potential hold of the pulse, A is the amplitude of the pulse and v is the sweep rate. Shown in b) and c) are illustrative examples of the current-potential profiles obtained by performing b) a linear sweep and c) a DPV in the HER region.

The region in which the quantification of Pt takes place is the di peak shown in Figure 68c, as the magnitude of this peak is proportional to the amount of Pt adsorbed. For a quantification of the Pt to take place, the solution under test then has a 'standard addition' of Pt added to it. This is a known concentration of Pt that will thus increase the concentration by a known amount. On this solution the pre-concentration and DPV step is performed, and as the increase in Pt concentration on the HMDE is proportional to the solution concentration, the magnitude of the 'di' peak measured is proportionally greater (Figure 69a). With the increase in concentration corresponding with the current peaks, the initial concentration of the sample can therefore be determined by following the trendline of the concentration – current graph (Figure 69b) to the value at which the current peak is zero. The corresponding concentration at this point is the negative of the sample concentration.

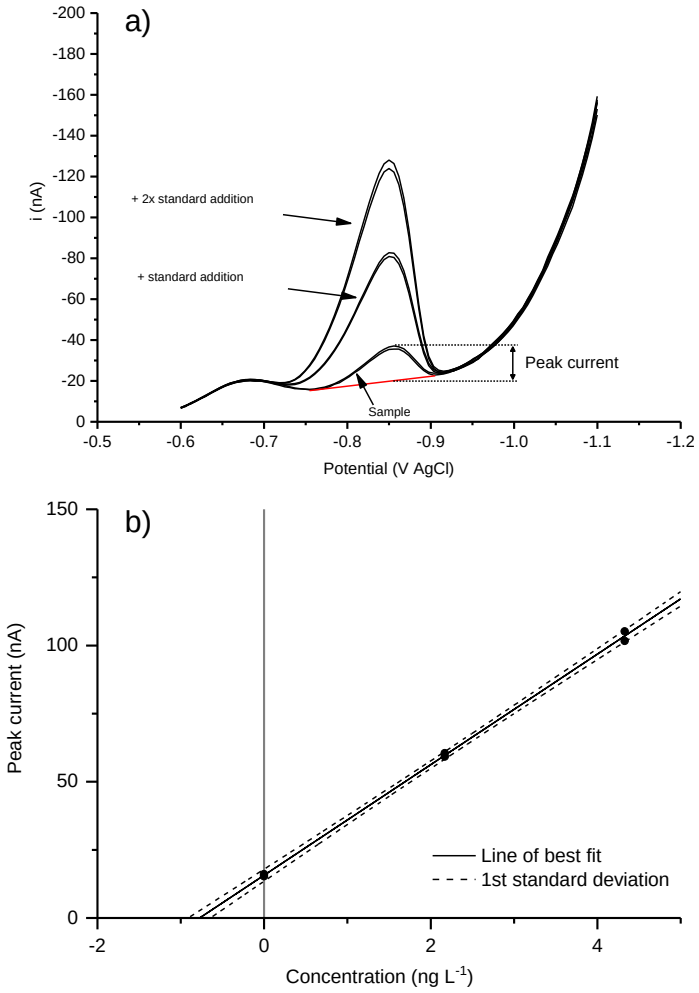

Figure 69a) Typical Pt DPV profiles of the sample and sample with the 1st and 2nd standard additions. The peak current is measured from the baseline shown in red. The peak currents for each DPV profile are calculated and are used in (b), where the initial concentration is fixed at 0 ng L^{-1} (not the actual oncentration) . The standard additions add known concentrations of Pt(II) to the sample. The point at which the trendline passes the y-axis is the concentration of the initial sample. Shown also is the standard deviation for the measurement. Note here that concentration of 0 ng L^{-1} is not the true concentration of the solution, this is the concentration of the solution plus the initial concentration of the solution. This is convention in voltammetry, as the initial concentration of the solution is not known, but the standard additions of known concentrations provides a linear trendline of peak value against concentration increase that can then be extrapolated in the negative direction. The value at which the trendline crosses the x-axis is the negative of the initial concentration, and thus the initial concentration is known.

Technical details on this method is given in Section 5.5.1.

8.2.2 Voltammetry of Ir and Ru

A method for the voltammetry of Ir and Ru was provided in a paper by C. Locatelli [230]. This voltammetric analysis follows a sequential method using the same overall solution, but using differing working electrodes and adding to the supporting electrolyte between analyses. The reference electrode ($Ag/AgCl/KCl_{sat}$) and counter electrode (Pt wire) were constant through the test. For the determination of Ru(III) a HMDE was used. A supporting electrolyte consisting of an acetate buffer (mixture of sodium hydroxide (NaOH) and ethanoic acid) and sodium bromate ($NaBrO_3$) was used as a supporting electrolyte. Ru is electrodeposited on the HMDE by an electrodeposition step in which the HMDE is held at a potential of 0.15 V $Ag/AgCl/KCl_{sat}$. Following from this, DPV is applied to the HMDE proceeding to a negative potential in a similar manner as that shown in Figure 68a. At approximately -0.23 V $Ag/AgCl/KCl_{sat}$ the adsorbed Ru species undergo a reduction process on the electrode. In the presence of $NaBrO_3$ however, which is strong oxidising agent, the reduced elements undergo oxidation again. The oxidized Ru then may the undergo reduction again. The concept behind this is that $NaBrO_3$ acts as an agent that amplifies this reaction – Reduction occurs on the electrode and so it detectable, but the solution itself performs the oxidation reaction without occurring on the electrode, so the signal becomes amplified as the same element may undergo reduction on the electrode several times.

For the detection of Ir(III), the HMDE was replaced with a GCE. For the analysis, 1 mL of cetrimonium bromide (CTAB) and 1 mL of KCl was added. CTAB was here used as a

complexing agent that allows the Ir to be adsorbed on the surface of the GCE, and KCl suppresses the background current and increases the signal: noise ratio. The process overall is otherwise similar to the method for detecting Ru – A negatively progressing DPV profile is applied, and the reduction of the Ir complex is then followed by reoxidation by $NaBrO_3$, and so the signal is enhanced.

Technical details on this method can again be found in Section 5.5.2.

8.2.3 Testing against Standard Solutions and Comparison to ICP-MS

To determine the applicability of the voltammetric techniques for the detection of Pt, Ru and Ir, the methods were used to quantify both the concentration of Pt, Ru and Ir from standard solution and from water samples from the PEMWE. These solutions were additionally analysed by ICP-MS as a comparison. To produce water samples from the PEMWE for the ICP-MS and voltammetry testing, the cell was held at potentials ranging from -0.07 V NHE (the potential of the cathode during operation at 1 A cm^{-2}) to 1 V NHE (the maximum potential that the cathode reaches during OCV). Technical details of this method are given in 5.4.1. Samples of outlet water were taken, and their elemental concentrations were measured by both ICP-MS and voltammetry.

Here it must be disclosed that attempts to detect concentrations of Ru and Ir by the voltammetry method described in section 8.2.2, both with the standard solutions and the PEMWE water samples, were unfortunately unsuccessful. Several separate attempts were made to elucidate the issue, including using more concentrated standard solutions of Ir and Ru, refreshing the electrolyte solutions, repeatedly recalibrating the potentiostat, intensively cleaning the system and varying the voltammetry method to substantially increase the pre-concentration durations. Unfortunately, no signal beyond

background noise was present in any of these tests. In particular, there was no signal at the characteristic potentials during either of the voltammetry techniques. With a negative result for Ru and Ir concentration detection, this study here pivoted to be a study of Pt dissolution from the cathode only, as opposed to a study of dissolution from both the anode and cathode. The following chapters in this work therefore concern the dissolution of Pt species from the cathode of a PEMWE.

Regarding Pt only for the potential hold tests, samples of outlet water were taken, and their Pt concentration was measured by both ICP-MS and DPV, as shown in Figure 70. It is clear from the size of the error bars that the typical concentration of Pt arising from cathode dissolution was too low for meaningful quantification by the available ICP-MS. In contrast, DPV was able to quantify Pt dissolution at this level, making this technique well-suited for quantification of dissolved Pt in PEMWEs. A limit of detection test, shown in Figure 71, similarly demonstrates that DPV was sensitive to Pt(IV) species at concentrations as low as 2 ng L^{-1}, but ICP-MS was only sensitive from 50 ng L^{-1} upwards. Unlike ICP-MS, the DPV technique is not sensitive to Pt(0) however, and cannot therefore detect Pt lost by erosion, or corrosion of the electrode support (if one were to be used, i.e. Pt/C). Although there are high associated standard deviations with ICP-MS results in Figure 70, and so any difference between ICP-MS and DPV values cannot be determined with any statistical significance here, the generally higher recorded dissolution values may be an indication of the contribution of Pt(0) to the ICP-MS recorded dissolution value. It should be noted here that this comparison concerns only the two specific instruments used in this work, and should not be taken as a general comparison between ICP-MS and DPV for Pt sensitivity. The ICP-MS device used here

has higher limits of detection in comparison to state-of-the-art ICP-MS instruments, which may be in the range of 0.001 - 0.1 ng L^{-1} [259]. Likewise, the sensitivity of the DPV measurements may be improved upon, and the limits quoted here do not represent absolute detection limits. A similar comparison study on biological samples was performed by Zimmerman et al., who reported limits of detection for Pt of 1 ng L^{-1} using ICP-MS and 0.13 ng L^{-1} for DPV [260].

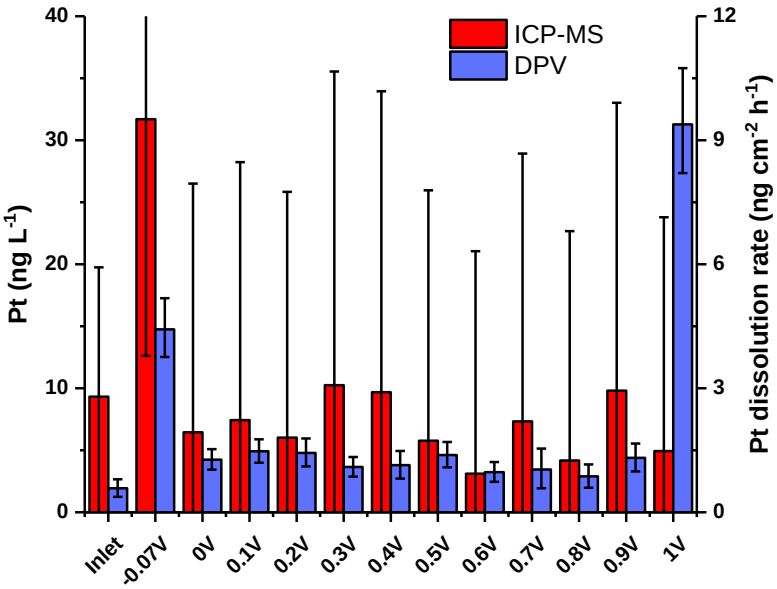

Figure 70 Dissolved Pt concentration in PEMWE cathode water as a function of cathode potential, measured by ICP-MS and DPV. Note that for the cathode outlet measurements from -0.07 V to 1 V (NHE – removed from the graph for the sake of clarity), the background Pt concentration at the cathode inlet has been subtracted. The error bars represent the first standard deviation. With the ICP-MS results, the standard deviation is based on the average of 5 separate measurements. With the DPV results, the standard deviation is the standard deviation of the line of best fit, which was measured from 6 points. Note the samples were taken immediately after potential change, and so for -0.07V NHE the high dissolution value can be explained to be a transient effect. It is clear here that, based on the standard deviations, it is not possible to resolve quantifiable data from the ICP-MS results.

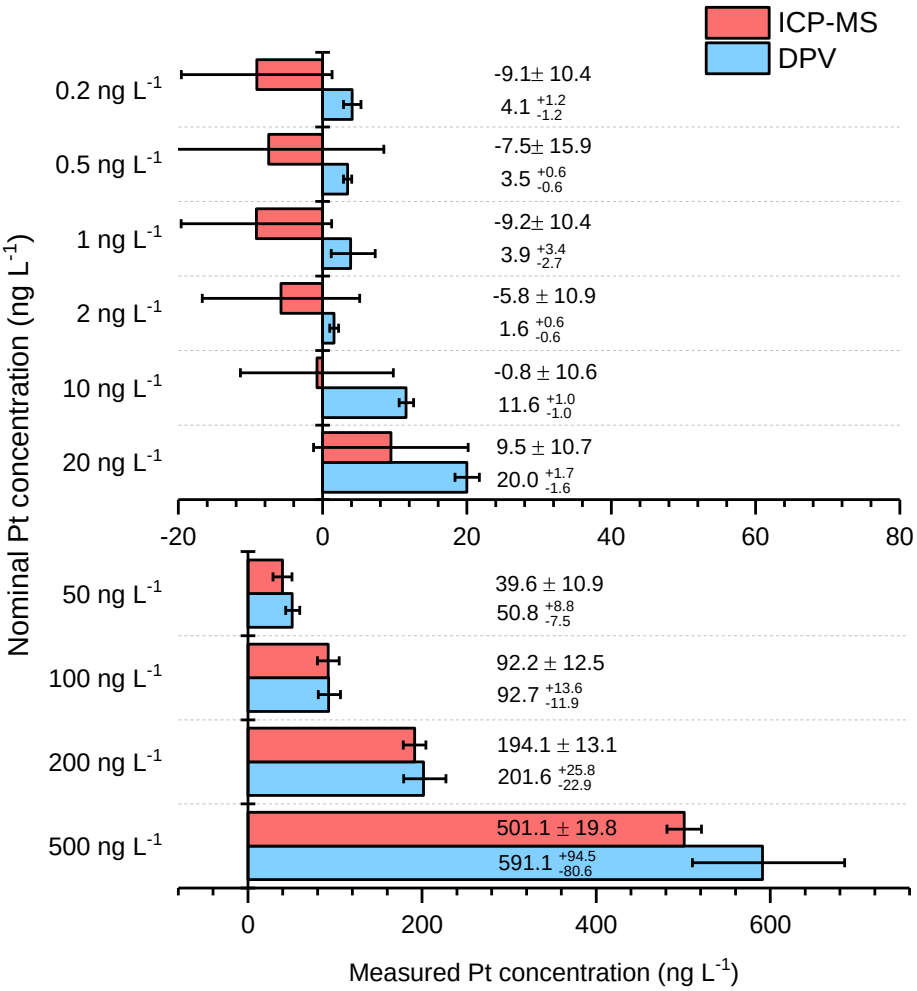

Figure 71. Limit of detection tests of Pt standard solutions with DPV (in blue) and ICP-MS (in red). This is a range of Pt concentrations over the expected concentration range. The limit of detection, regarded as being at least 3 x the background noise, is approximately 2 ng L^{-1} for DPV and between 20 – 50 ng L^{-1} for ICP-MS. At very high concentrations, the DPV measurement is shown to become less precise (see 500 ng L^{-1}). This can be attributed to both the concentrations of the supporting electrolyte. The supporting electrolyte in this system is optimised for solutions in the range of 1 – 100 ng L^{-1} , and at concentrations above this the ratio of electrolyte to Pt is lower and so the system becomes less sensitive to concentration.

Figure 70 also shows that the Pt concentration of the outlet water at a cathode potential of -0.07 V NHE is significantly higher than samples taken at the other potentials. The cause of this is the same as that shown in Figure 78; a high but rapidly diminishing

concentration of Pt is measured from the onset of operation. The -0.07 V NHE sample was taken after only 1 minute of operation, and so is high for the same reasons. The underlying cause of this high initial Pt concentration is discussed in Sections 8.3.2 and 9.4

8.2.4 Interference Testing

A further step in validating the voltammetry method for Pt detection was to determine whether the other PGM electrocatalysts used in the PEMWE, Ir and Ru, interfered with the catalytic wave profile for Pt. To test this a series of standard solutions were analysed. All the solutions nominally has a Pt(IV) concentration of 1 ng L^{-1} with Ru (III) or Ir (III) concentrations of between 0 ng L^{-1} and 1 µg L^{-1}. All tests followed the method of standard Pt additions to provide a quantification of Pt. The first DPV profiles for each test are given in Figure 72.

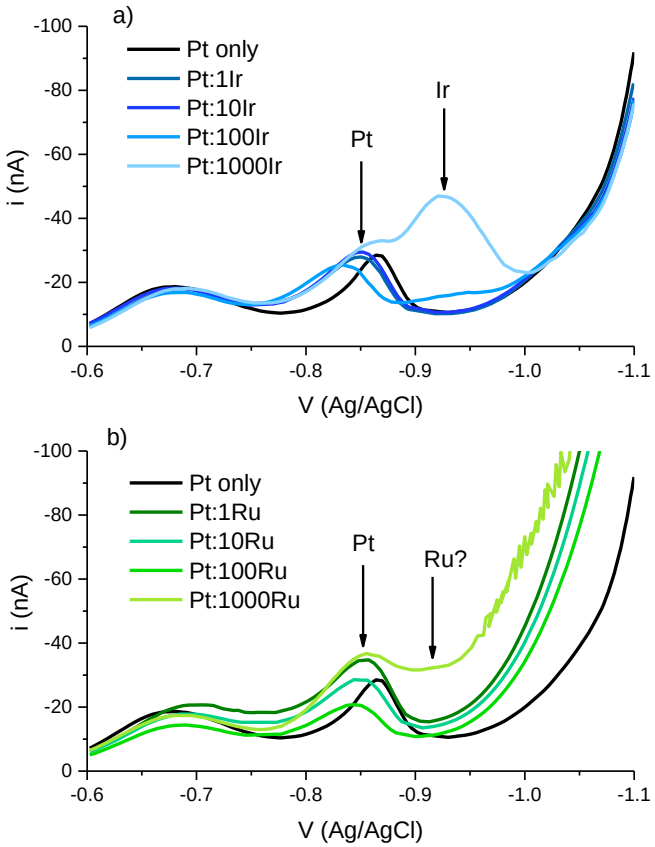

Figure 72. DPV profiles of Pt catalytic wave voltammetry with a) the addition of Ir and b) the addition of Ru. Denoted are the characteristic peaks for the Pt catalytic wave and the possible characteristic peaks of Ir and Ru. A lighter colour denotes an increasing concentration of the contaminant against Pt.

In both these interference tests, the influence of Ir and Ru on the DPV profile doesn't become apparent until the concentration differences are extremely high (Figure 73). Note that it is common for the peak potential to fluctuate somewhat through separate measurement, and the baseline values do also change from test to test (Figure 72).

At a ratio of 100:1 Ir to Pt a possible characteristic peak for HER on Ir appears, and this becomes more defined at 1000:1. For Ru however, no characteristic peak is evident, although there is the possibility of its' occurrence in the same region as the Ir peak. Important for this study is that the possible interferences from Ru (III) and Ir (III) on the

DPV profile itself are very slight – A very high relative concentration is required so that Ru and Ir signals interfere with the quantification of Pt– and the possible Ir (III) and Ru (III) peaks are located at a lower potential than Pt. Therefore, even at very high concentration ratios, the quantification of Pt concentration is still possible. This is shown in Figure 73, wherein the DPV profiles shown in Figure 72 underwent the method of standard additions. In comparison to the measurement of 1 ng L^{-1} Pt alone, not until ratios of 100:1 and above are reached does the quantification of Pt become less precise. Even at these concentrations is it possible to detect, if not quantify the presence of Pt.

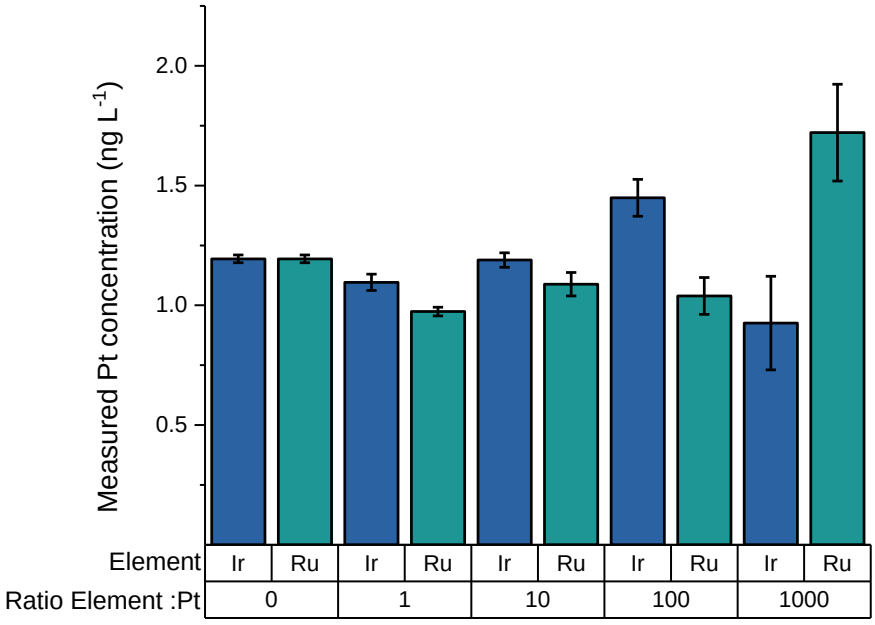

Figure 73. Measurement of 1 ngL^{-1} Pt (IV) solution with various concentrations of Ir (III) and Ru (III). The ratio here is the concentration of the contaminant against the Pt concentration. For example, 1000:1 ratio is a Ru and Ir concentration of 1 ug L^{-1}. Note that the Ir and Ru measurements at a ratio element of 0 are reporting the same measurement and the values are hence the same.

Overall, it can be stated with confidence that the interference of Pt by Ir (III) and Ru (III) is minimal at relative concentration ratios of 100:1 and below. Below this Pt is easily quantifiable, and above this Pt is certainly detectable. In PEMWE, such a concentration ratio would not be expected because the electrocatalysts exist on different sides of the Nafion membrane. For Ir to interfere with the Pt concentration determination it must dissolve at a rate so that the concentration that migrates through the membrane is 1000 times greater than the Pt dissolving at the cathode. Additionally, if this were the case, then by the different characteristic peaks potentials it would be possible to identify the species detected as Ir or Pt. The voltammetric analysis of Pt by DPV is therefore a suitable technique for the determination of Pt from a PEMWE.

8.3 The Dissolution of Pt from a PtB Cathode Electrocatalyst during OCV and Operation

8.3.1 Cell and Test Setup for PtB Dissolution

In this section is reported the dissolution of Pt from a PEMWE during periods of operation at 1 A cm^{-2} and during OCV. In these tests, the cell used an IrO_2 CCM with a PtB cathode. Although PtB is not a state-of-the-art electrocatalyst for HER, it was chosen in this section of the study as it is not a carbon-supported catalyst, and so reduces the number of possible degradation pathways that may occur. Gold-coated GDL components were additionally used to avoid doubt about the origin of the Pt dissolution. Due to the recirculation of the cathode water, all samples taken at the inlet contained a background concentration of Pt of order ≈ 7 ng L^{-1}. There are two possible causes for this background concentration. First, it is possible that this is the natural concentration

of Pt in pure water provided by the laboratory, or that caused by Pt contained in the glassware or HMDE. Note that this voltammetric technique is regularly used to measure urban water Pt concentration. A major source of Pt contamination also comes from water released from catalytic converters, and it is possible that this is being measured in these tests. Alternatively, the inlet water may be expected to carry a certain concentration of Pt in it as water is recirculated from the electrolyser. The water is passed through ion exchange resins, but it would be expected that it would not capture all of the dissolved Pt and so a certain background concentration would remain.

To determine the concentration arising from Pt dissolution from the catalyst layer, the values measured at the cathode outlet were corrected by subtracting the concentration measured at the cathode inlet immediately prior to the cathode outlet measurement. This corrected value was then converted into a Pt dissolution rate (ng cm^{-2} h^{-1}) with respect to the geometric surface area of the CCM.

8.3.2 Dissolution of Pt from PtB during OCV and Operation at 1 A cm^{-2}

The evolution of cathode potential with time during the OCV test is shown in Figure 74 (red line), with the anode potential and cell voltage also included for reference. In this setup water was flowed at the cathode, and there was no bubbling of gas into the anode or cathode reservoir during the OCV period. The cathode potential during operation at 1 A cm^{-2} was -0.07 V NHE. Upon commencement of the OCV period, the potential increased from -0.002 V NHE to 1.02 V NHE in about 5 h and remained steady at this high potential for the remainder of the 72 h period. This was found to be repeatable for the three OCV tests performed, as shown in Figure 75.

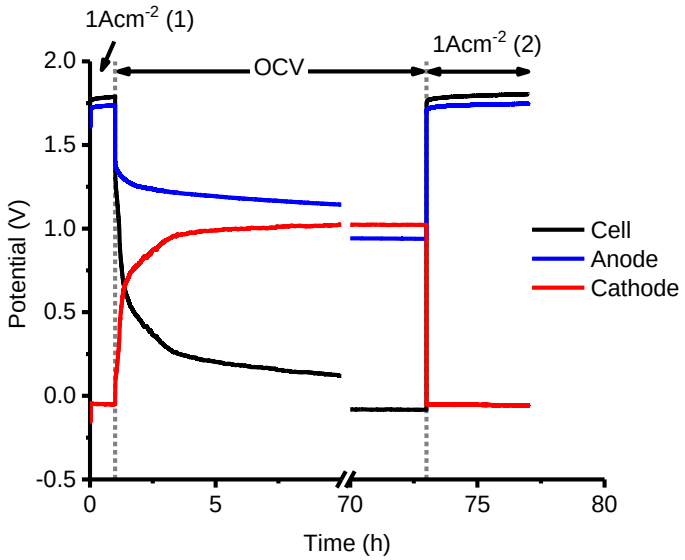

Figure 74. Evolution of cathode potential (red), anode potential (blue) and cell voltage (black) with time, during the OCV test on a CCM with a PtB cathode. The electrolyser was operated at 1 A cm^{-2} for 1 h, followed by a 72 h OCV period, followed by operation at 1 A cm^{-2} again.

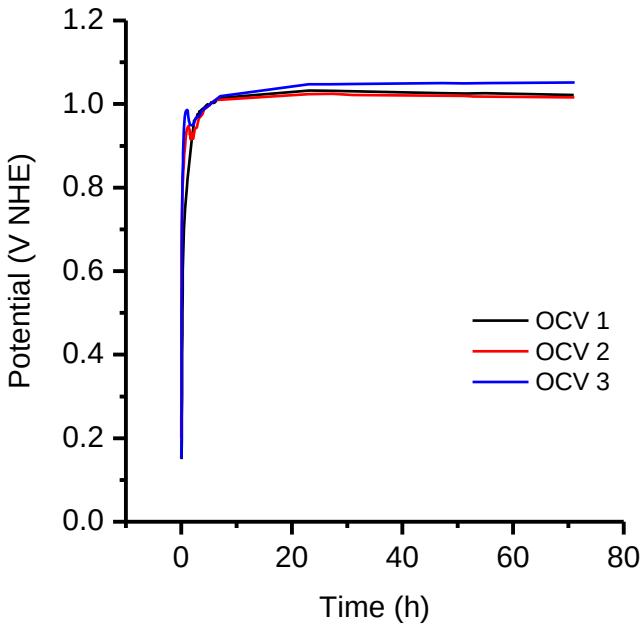

Figure 75. Cathode potential of the three OCV tests during the OCV period

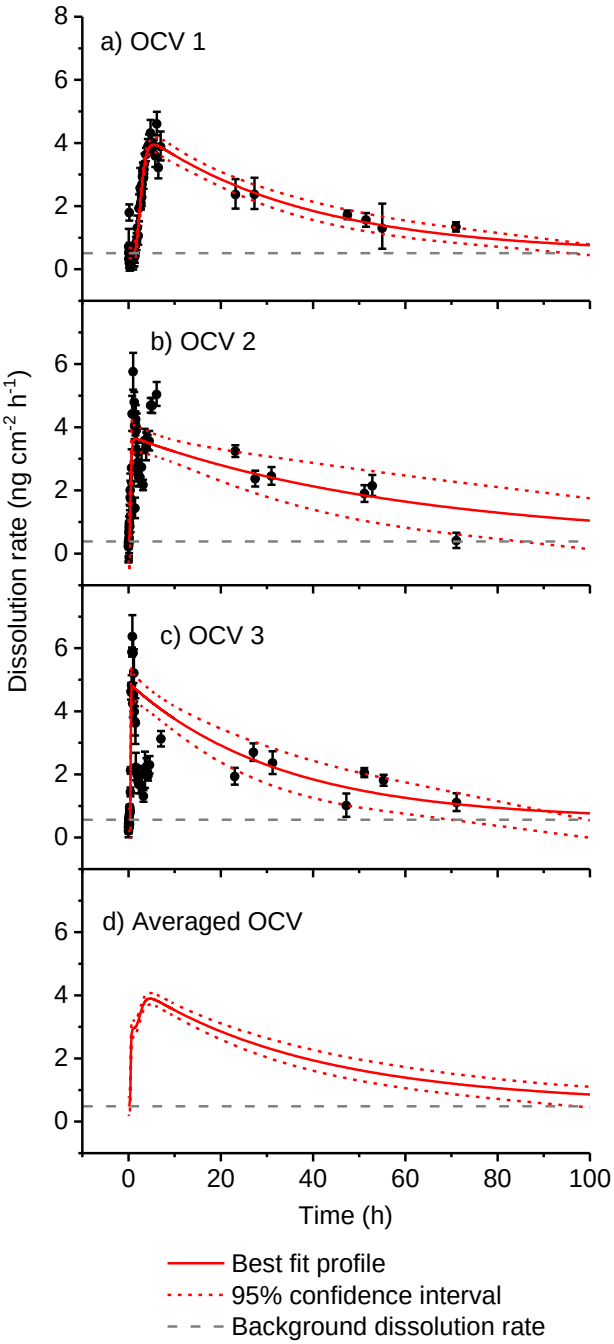

Figure 76. Pt dissolution rate from the PEMWE PtB cathode over the full duration of the three OCV tests (a,b,c). Shown in (d) is the line of best fit of the fits of a,b and c. In red is the best fit profile of each of the tests, with the dotted red lines representing the upper and lower 95% confidence intervals of the fits.

The rate of Pt dissolution from the cathode during the OCV portion of the three OCV tests is shown in Figure 76. From the onset of the OCV period every measurement showed net Pt dissolution (i.e. the outlet concentration of Pt was always higher than the inlet concentration). During the first 1.5 h of OCV, the dissolution rate was measurable, but the standard deviations of the individual measurements were too large for it to be stated with confidence that the dissolution rate was positive. However, it can be assumed that the dissolution rate is constant during this period (i.e. no other dissolution mechanism is occurring), and so the dissolution values in this period may be averaged. In the case of OCV test 1 the dissolution rate was 0.51 ng cm^{-2} h^{-1}, with a lower confidence interval of 0.34 ng cm^{-2} h^{-1} and upper confidence interval of 0.68 ng cm^{-2} h^{-1}. Following on from this constant rate, dissolution increased to a maximum after approximately 5 h and then decayed slowly over the remainder of the 72 h OCV period. This maximum in dissolution rate coincides with the attainment of a steady-state cathode potential due to diffusion of oxygen from the anode. Plotting the dissolution rate as a function of cathode potential, in Figure 77, indicates that the onset of dissolution occurred between 0.85 - 0.90 V NHE, which is in good agreement with SFC-ICP-MS literature [221].

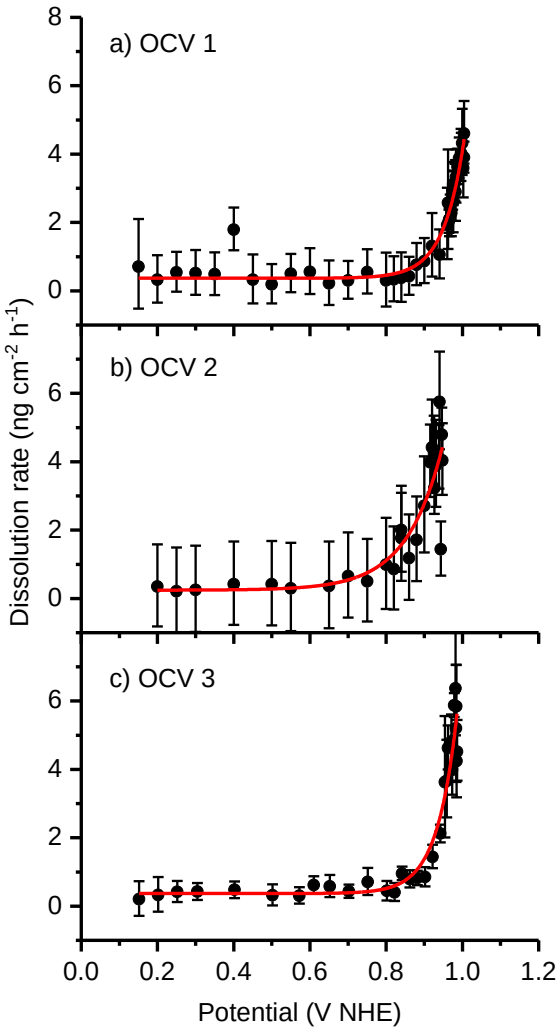

Figure 77. Pt dissolution as a function of increasing cathode potential in a PEMWE. The red line shows an exponential function fitted to the individual measurements.

The Pt dissolution rate was also measured during operation at 1 A cm^{-2} immediately following the OCV period (Figure 78). At the onset of operation, the rate of Pt dissolution was an order of magnitude higher than the maximum rate at OCV, but then decayed rapidly within approximately 30 minutes. There are two potential explanations for this additional dissolution phenomenon. Firstly, as the cathode has built up a surface Pt-oxide layer during the OCV period, the switch to the cathodic potential of operation could invoke dissolution due to reduction of the oxidized Pt surface and the competition

between this and surface dissolution [221]. However, this effect is only significant at low sweep rates and in PEMWEs, with the extremely rapid potential step in cathode potential from OCV to operation, a large dissolution rate caused by this mechanism would not be expected. A second, and more likely explanation is that this instantaneous increase in apparent dissolution rate is an artefact caused by the displacement of the higher Pt concentration solution in the GDL by the evolution of hydrogen gas produced at the start of operation. It must be considered here that the cathode catalyst is a highly tortuous material, and the flow of water across the electrode may not necessarily displace the water that is deeply embedded within the cathode. The water deeply embedded here can be assumed to be stagnant, and hence platinum may dissolve into this water and may concentrate here. Once the cathode has started to undergo HER these voids will fill up with hydrogen gas and then will displace the water that has collected. This will then force the Pt- concentrated water out of the cathode. This could also explain the higher apparent dissolution rate during the brief operation period at a constant potential of -0.07 V NHE (Figure 70).

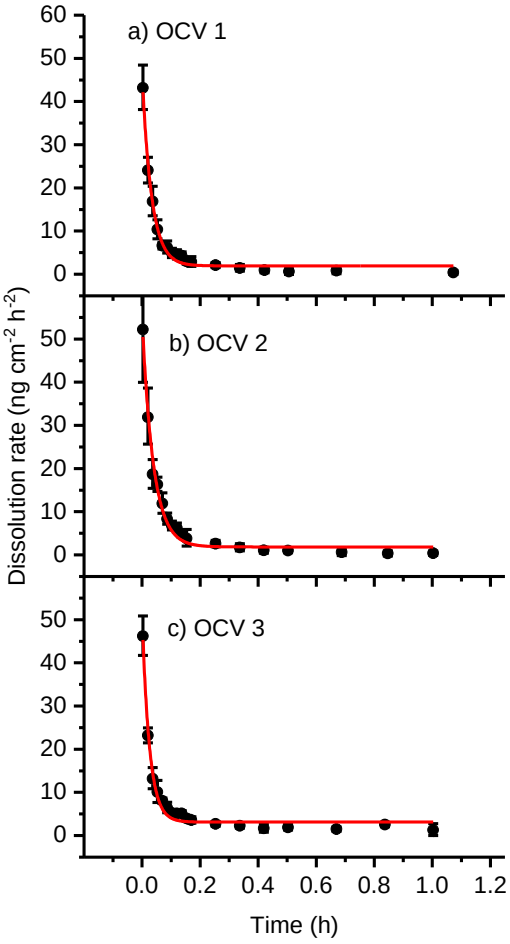

Figure 78. The Pt dissolution rate measured at the transition of OCV to 1 A cm^{-2} operation. The red lines are exponential decay functions fitted to the data.

8.3.3 Effect of Pt Dissolution on Electrode Lifetime

The Pt dissolution data, as shown in Figure 76, make it possible to estimate the lifetime of the PtB electrode under the given test conditions. The dotted lines in these Figures show a best-fit estimate of the OCV Pt dissolution fitted to a pulse profile, and an exponential decay function fitted to the dissolution at the onset of operation. From these an estimation of electrode lifetime was made. This estimation was made with two considerations. Firstly, it was assumed that the background dissolution rate was

constant throughout the OCV and operation period and was unaffected by cathode potential or the increase in the concentration of dissolved Pt close to the electrode surface. Secondly, as the Pt averaged dissolution rate at OCV was still statistically significant after 72 h, the best-fit profile and confidence ranges were extended to the point at which the lower confidence interval reached the averaged background dissolution rate of 0.49 ng cm^{-2} h^{-1}. This is the point at which it can no longer be stated with confidence that potential-induced Pt dissolution is still occurring. In the case of the averaged profile in Figure 76, this was determined to be 90 h.

The Pt dissolution data during OCV were fitted against a pulse profile (Equation (57).

$$y = y_0 + A\left(1 - e^{\frac{-x}{t_1}}\right)^P e^{\frac{-x}{t_2}} \quad (57)$$

The profiles were fitted using the Levenburg-Marquadt algorithm to reach a chi-squared tolerance of 1×10^{-15}. The obtained values for each OCV plot are given in Table 14.

Table 14. Fitted values for Pt dissolution from PtB during OCV against a pulse profile. Results of this fitting are shown in Figure 76.

	OCV 1			**OCV 2**			**OCV 3**		
	Value	Error	Dependency	Value	Error	Dependency	Value	Error	Dependency
y_0	0.5902	0.0827	0.7081	0.3874	0.3584	0.8727	0.5624	0.1543	0.5505
A	4.110	1.162	0.9934	3.457	359575	1	4.3821	15413	1
t_1	0.8038	0.2761	0.9972	0.1828	0.1285	0.9996	0.05609	0.05280	0.9994
P	25.00	368.1	0.9999	7.590×10^6	1.5×10^{12}	1	1.184×10^6	2.433×10^{12}	1
t_2	35.82	4.778	0.6131	61.45	24.57	0.4996	32.77	6.858	0.2864
R^2	0.952			0.722			0.913		

Pt dissolution values at the onset of operation after OCV were fitted against an exponential decay profile with Equation (58. The profiles were fitted using the Levenburg-Marquadt algorithm to reach a chi-squared tolerance of 1×10^{-15}. The obtained values for each plot are given in Table 15. The fitted data is shown in Figure 78.

$$y = y_0 + A\, e^{\frac{-x}{t_1}} \tag{58}$$

Table 15. Fitted values for Pt dissolution during operation after the OCV period.

	OCV 1			**OCV 2**			**OCV 3**		
	Value	Error	Dependency	Value	Error	Dependency	Value	Error	Dependency
y_0	1.9375	0.3986	0.4501	1.849	0.567	0.4864	3.128	0.4294	0.3465
A	44.34	1.39	0.4004	52.76	1.809	0.4166	47.77	1.82	0.3873
t_1	0.03267	0.001950	0.5676	0.03868	1.678	0.5805	0.0254	0.0018	0.5107
R^2	0.988			0.987			0.984		

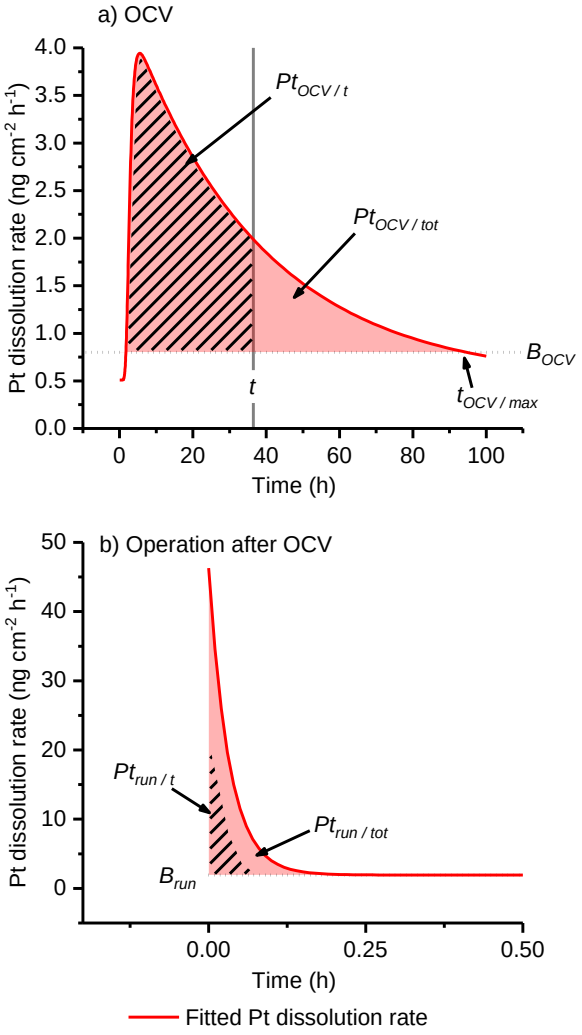

Figure 79. The method used to forecast dissolution through OCV and operation after the OCV period. The background Pt dissolution rates during OCV (B_{OCV}) and during operation (B_{run}) were established, and these values were assumed to be continuous throughout the duration of each test. The amount of total Pt dissolved during the OCV period in question ($Pt_{OCV\,/\,t}$) was integrated from the dissolution profile up to *t* h. The amount Pt dissolved during operation after OCV ($Pt_{run\,/\,tot}$) was obtained by integrating the operation dissolution profile. As it has been assumed that this dissolution rate is a product of OCV dissolution, for an OCV duration of t, the amount of Pt dissolved in this period ($Pt_{run\,/\,t}$) was calculated in the manner shown in Equation 58 and 59. The total amount of Pt dissolved in each test was calculated using Equation 60.

The average of the Pt dissolution rates for each OCV plot, as shown in Figure 78, were calculated in the following manner, with Figure 79 included here as a guide: (1) The background Pt dissolution rates during OCV (B_{OCV}) and during operation (B_{run}) were established, and these values were assumed to be continuous throughout the duration of each test. (2) The fitted Pt dissolution rate data were subtracted from the respective background dissolution rates. The time at which it could no longer be stated with confidence that the fitted Pt dissolution rate was greater than the background dissolution rate was determined to be the time at which OCV dissolution ended ($t_{OCV\,/\,max}$). (3) The amount of total Pt dissolved during the OCV period in question ($Pt_{OCV\,/\,t}$) was integrated from the dissolution profile up to *t* h. (4) The amount Pt dissolved during operation after OCV ($Pt_{run\,/\,tot}$) was obtained by integrating the operation dissolution profile. As it has been assumed that this dissolution rate is a product of OCV dissolution, for an OCV duration of t, the amount of Pt dissolved in this period ($Pt_{run\,/\,t}$) was calculated in the following manner:

$$\theta = \frac{Pt_{OCV/t}}{Pt_{OCV/tot}} \tag{59}$$

$$Pt_{run/t} = \theta\, Pt_{run/tot} \tag{60}$$

Furthermore, for the same reasons as mentioned above, it has been assumed that $Pt_{run\,/\,t}$ is not affected by the duration of operation. Therefore, for a complete OCV cycle of duration of t and operation period of t_{run}, the amount of Pt dissolved per cycle is calculated as follows:

$$\mathrm{Pt_{cycle}} = \mathrm{Pt_{OCV/t}} + \mathrm{B_{OCV}t} + \theta\mathrm{Pt_{run/tot}} + \mathrm{B_{run}t_{run}} \quad (61)$$

Table 16. Pt dissolution amounts and estimations of the cathode electrode lifetimes at 3 mg cm^{-2} PtB

	OCV 1	**OCV 2**	**OCV 3**	**Average**
B_{OCV} (ng cm^{-2} h^{-1})	0.509 ± 0.167	0.388 ± 0.713	0.562 ± 0.315	0.486 ± 0.266
B_{run} (ng cm^{-2} h^{-1})	$1.937^{+0.855}_{-0.855}$	$1.849^{+1.216}_{-1.216}$	$3.128^{+0.915}_{-1.053}$	$2.305^{+0.582}_{-0.607}$
$t_{OCV\ /\ max}$ (h)	91.5	68.5	65	90
Pt_{cycle} (ng cm^{-2})	$123.8^{+27.2}_{-28.0}$	$136.2^{+66.4}_{-66.4}$	$120.1^{+39.4}_{-39.1}$	$152.44^{+61.9}_{-72.4}$
Pt dissolved during operation peak (ng cm^{-2})	$1.423^{+0.179}_{-0.181}$	$1.981^{+0.264}_{-0.666}$	$1.194^{+0.169}_{-0.1794}$	$1.533^{+0.323}_{-0.233}$
Max average OCV dissolution rate (ng cm^{-2} h^{-1})	$3.19^{+0.15}_{-0.26}$	$3.91^{+1.1}_{-0.66}$	$4.41^{+0.49}_{-0.46}$	$3.60^{+2.28}_{-1.84}$
Min average OCV dissolution rate (ng cm^{-2} h^{-1})	$0.52^{+0.51}_{-0.17}$	$0.50^{+0.76}_{-0.07}$	$0.63^{+0.34}_{-0.34}$	$0.59^{+0.74}_{-0.14}$
Most damaging cycle profile (h)	15.1	1.1	4.1	7.9
Minimum electrode lifetime (y)	$108^{+9.0}_{-6.0}$	$87.5^{+17.5}_{-19.1}$	$77.6^{+9.1}_{-7.7}$	$95.2^{+98.8}_{-36.9}$
Maximum electrode lifetime (y)	653^{+316}_{-383}	686^{+117}_{-413}	542^{+542}_{-190}	579^{+178}_{-321}

The dissolution rates observed in Figure 76, and the ensuing calculations, should not be used as an absolute reference for the predicted Pt electrode lifetime, but they do serve a useful purpose in highlighting the substantial effect that different intermittent operational regimes may have on the Pt electrode.

Integration of the averaged OCV dissolution profile gives the total amount of Pt dissolved per cm^2 for each OCV test. This gave a mean value of 152 ng cm^{-2}, with lower and upper confidence intervals of 80 ng cm^{-2} and 214 ng cm^{-2} respectively. For this

particular CCM / PtB combination, the percentage of Pt lost from the electrode during an OCV period lasting 90 h was around 0.005 %. This corresponds to about 20,000 on-off cycles until complete Pt dissolution, although the performance loss of the electrode would be likely to precede this as a certain amount of Pt is of course needed for adequate HER kinetics. It should be noted that this value does not take into account Pt lost by mechanical means and cannot be correlated to catalyst layer performance losses by Ostwald ripening or particle agglomeration [261].

The amount of Pt dissolved during on-off cycling will naturally depend on the duration of the OCV period, with less Pt dissolved per cycle with a shorter OCV period. However, with the OCV period being shorter, the time taken for a complete on-off cycle is reduced accordingly. In principle, the duration of operation is also a factor that can influence lifetime due to the operational background dissolution rate, measured at 2.31 ng cm^{-2} h^{-1} for these particular conditions. However, the total amount of dissolved Pt measured under the peak during operation (Figure 78) is relatively small at only 1.5 ng cm^{-2}, and so does not contribute significantly to the overall dissolution. As the Pt dissolution rate at OCV is not constant, the duration of the OCV period has an impact upon how rapidly over time Pt dissolves, which has implications for the overall lifetime of the cathode. An estimation of the time averaged dissolution rate from the PtB electrode under a range of on-off operational regimes is given in Figure 80. From extrapolation of the average dissolution and operation dissolution data, the most damaging intermittent operation mode is a cycle of operation for 0.01 h (the shortest duration calculated), followed by an OCV period of 7.9 h. This provides an average dissolution rate of 3.60 ng cm^{-2} h^{-1} with lower and upper confidence intervals of 1.76 and 5.88 ng cm^{-2} h^{-1} respectively. Conversely, the mode of operation which will reduce

the degradation the most, and hence extend lifetime by the greatest extent, is an operation period of 0.01 h followed by an OCV period of 0.2 h. In this case the average dissolution rate is 0.59 ng cm^{-2} h^{-1} with lower and upper confidence intervals of 0.45 and 1.33 ng cm^{-2} h^{-1} respectively. Such short operational periods are not reflective of realistic operational conditions, however the dissolution rate is found to be relatively insensitive to the operational duration and is much more dependent on the OCV duration. With an operation period of 1 hour, the maximum dissolution rate is on average 3.48 ng cm^{-2} h^{-1} with lower and upper limits of 1.73 and 5.62 ng cm^{-2} h^{-1} respectively. Only at much longer operation times (>10 h) does the operation time substantially alter the average dissolution rate.

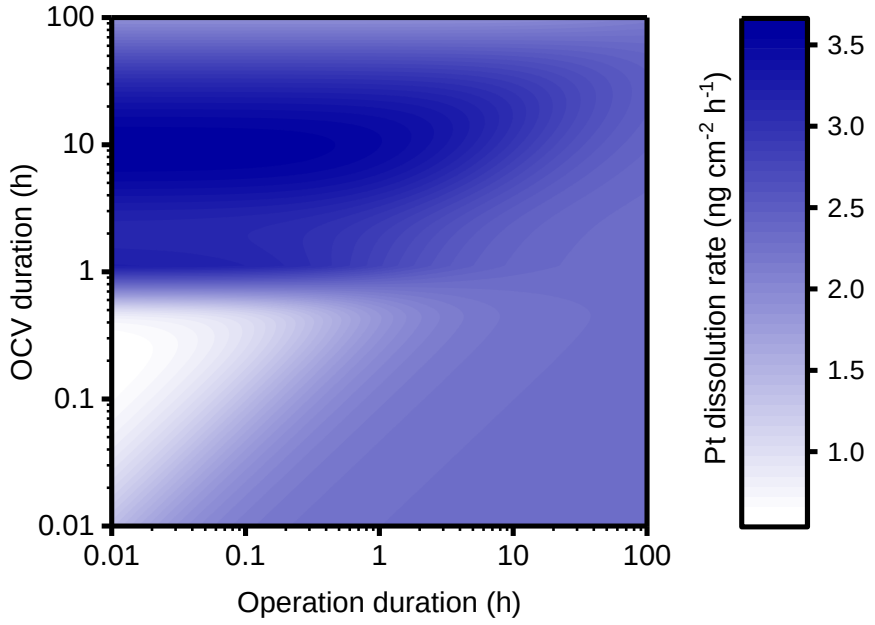

Figure 80. Average Pt dissolution rate as a function of the duration of operation versus the duration of the OCV period. The dissolution rate during operation is constant, but dissolution at OCV is dependent on the potential and duration of OCV. In the case of the PtB OCV test the most damaging on-off regime was found to be a short operation (<0.01h) followed by a 17.9 h OCV period. The average dissolution rate at this point is 3.60 ng cm^{-2} h^{-1}. Performing the same analysis against the lower and upper confidence intervals of the plot (Figure S.I.9d) gives 1.76 ng cm^{-2} h^{-1} and 5.88 ng cm^{-2} h^{-1} respectively.

If it is assumed that Pt dissolution is the only degradation mechanism occuring on the CCM, and that performance loss would only occur once the Pt has completely dissolved from the cathode, then the lifetime of the CCM tested in this report (3 mg cm^{-2} PtB) is estimated to be 95 years, with a lower and upper confidence limit of 58.3 and 194 years, respectively. With reduction of the Pt to a more commercially relevant loading (0.5 mg cm^{-2} Pt for example [44]) dissolution may become a more significant degradation mechanism, with the estimated time for complete dissolution at 16 years instead. This estimation however does not take into account the minimum required Pt loadings for adequate performance, and does not account for the other degradation

mechanisms which may also reduce ECSA. 95 years of lifetime may therefore stand as an upper limit of lifetime for the 3 mg cm^{-2} Pt cathode in this report and 16 years for a cathode at 0.5 mg cm^{-2}. These results are of importance when developing accelerated stress tests (ASTs) which mimic long-term degradation of the PEMWE within short timeframes. As can be seen here, a short duration of OCV seems to cause the least Pt loss by dissolution and therefore gives the longest lifetime estimate. Under the conditions studied in this work, the most damaging AST would be one that operates the cell for a very short time period and then holds the cell at OCV for 7.9 h. In comparison to an OCV period of 10 min, the degradation by Pt dissolution during a 7.9 h OCV period is accelerated by a factor of 5.

A further complication when considering AST development is the method by which the cathode potential is controlled during the off period of the cycle. There are two possible ways to manipulate the cathode potential during this period: through OCV, where the cathode potential is free to adjust depending on the balance of hydrogen and oxygen concentrations at the electrode surface; or potential control, where the cathode potential is held constant by an external source, such as a potentiostat. At OCV, the

cathode potential rises to more oxidising potentials due to diffusion of oxygen from the anode (Figure 74), while under potential control it is often fixed [123].

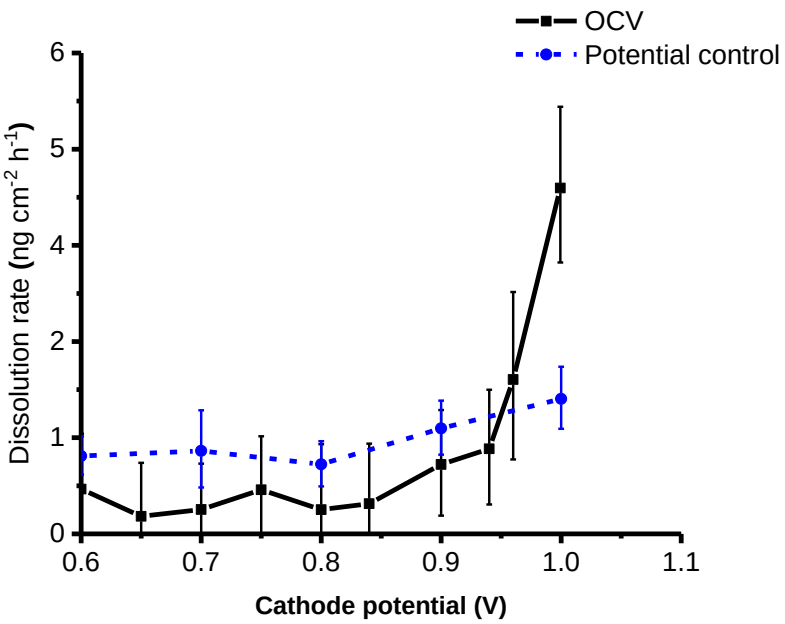

Figure 81. Comparison of Pt dissolution rates for the cathode at OCV (black) and under direct potential control (blue dotted line). The data in this graph is a combination of the potential control data in Figure 70and OCV data in Figure 77.

Comparison of Pt dissolution rate at OCV versus dissolution under potential control is given in Figure 81. Under potential control, the dissolution rate does not show the same marked increase above 0.9 V that is evident in the OCV plot. This therefore shows that, despite being at similar potentials, the early stages of OCV where the cathode potential rises induces a greater rate of dissolution than the equivalent potential under potential control. This does not mean that no transient dissolution process occurs under potential control, as the resolution of the sampling (one sample at each potential after holding for 1 minute) will have precluded observation of such a peak. However, the lack of onset of increased dissolution with increasing potential under potential control is in agreement

with SFC-ICP-MS reports [218,221]. The cause of the greater dissolution during OCV is expanded on in Section 8.3.5.

8.3.4 PtB Surface Changes

CV measurements of the PtB electrode reveal interesting structural changes occurring as a result of the OCV test. Shown in Figure 82 are CV measurements taken before the OCV test 1 (BoT) and after (EoT). Measurement of the electrochemical surface area (ECSA) from the integration of the hydrogen underpotential deposition (H_{upd}) peaks shows that the OCV period had an impact upon the ECSA, which decreased from 319 cm^2_{Pt} cm^{-2} to 261 cm^2_{Pt} cm^{-2}, approximating an 18 % loss of the active surface area. It can furthermore be seen that the magnitudes of the H_{upd} peaks corresponding to hydrogen adsorption at the Pt(100) step sites were proportionally more reduced in comparison to Pt(110), indicating that the Pt dissolution rate may be higher with the more active, and therefore more labile, active sites [262]. This 18 % loss of ECSA does not correspond with the total Pt lost from the cathode during the OCV test however. From the dissolution analysis, approximately only 0.005 % of the catalyst was dissolved, and so the large loss of ECSA clearly represents the loss of surface atoms only.

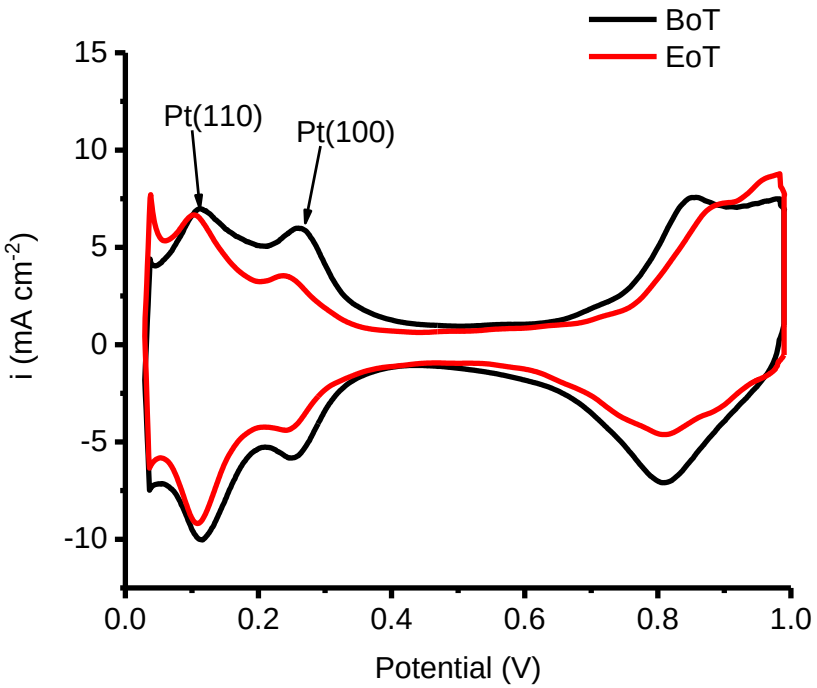

Figure 82. Cyclic voltammetry of PtB cathode before OCV test (BoT, shown in black) and after the 72 h OCV period (EoT, shown in red) of OCV test 1. Highlighted are the peaks associated with the Pt(100) and Pt(110) H_{upd} step sites.

8.3.5 Mechanisms of Pt Dissolution in PEMWE Cathodes

The mechanisms of Pt dissolution in PEMWE cathodes are likely to be similar in nature to those in PEM fuel cells [263]. These include electrochemical dissolution of Pt (Table 1,Reaction 7), and the formation of an oxide film (Table 1, Reaction 8) followed by chemical reduction to Pt^{2+} (41) [264]. For simplicity these are numerically denoted in the following paragraphs.

(1) $$Pt \rightarrow Pt^{2+} + 2e^- \qquad E_0\,(Pt/Pt^{2+}) = 1.188\ V + 0.0295 \log (Pt^{2+})$$ Table 1,7

(2) $$Pt + H_2O \rightarrow PtO + 2H^+ + 2e^- \qquad E_0(Pt/PtO) = 0.98\ V - 0.59pH$$ Table 1,8

(3) $$PtO + 2H^+ \rightarrow Pt^{2+} + H_2O \quad (41)$$

Reaction (1) was reported by Cherevko et al. [162] as occurring at potentials as low as 0.85 V on Pt, correlating well with the onset of dissolution observed in this study. It has been noted that, since the equilibrium potential of this reaction is dependent on the surface concentration of Pt^{2+} species, the equilibrium potential becomes more positive as dissolution proceeds, and thus the reaction should be self-limiting at the surface of a fuel cell electrocatalyst [218]. However, in a PEMWE the presence of water flowing through the cathode may prevent the surface concentration of Pt^{2+} on the electrode from increasing to the point where the equilibrium potential is significantly changed. This reaction may therefore be more significant in PEMWEs than in PEM fuel cells, and could contribute to the dissolution observed. Even with this dissolution reaction, the place exchange of Pt and OH species would occur, eventually forming an oxide layer and thus decreasing the dissolution rate over time. This would provide a rationale for the observed decrease in dissolution rate over the OCV period, and is consistent with the explanation of transient dissolution of Pt given by Topalov et al. [221]. The production of protons through reactions (2) and (3) may, however, contribute to the observed Pt dissolution. Yadav et al. [265] reported on this matter on high surface area Pt electrodes, and determined that reaction (2) is suppressed at lower pH due to the elevated equilibrium potential, therefore favouring reaction (1). The lower pH may also promote reaction (3), again resulting in an overall increase in Pt dissolution. However, the pH shift due to the reaction may be relatively small for the same reasons given to explain the increased Pt dissolution in PEMWEs compared to PEMFC; due to the presence of water

at the cathode, the volume into which the protons are migrating is large and therefore the change in concentration may not shift the equilibrium potential substantially. Furthermore, as evidence suggests that Nafion has a pH of between -0.08 and 1.4 [167–169] the effect of a slight increase in proton concentration may not significantly alter the equilibria of reactions (2) and (3). As it has been shown here that one of the factors which may impact the rate of Pt dissolution is the volume of water at the cathode, the dissolution rate may differ in PEMWEs where the cathode is operated 'dry' (without an active water flow through the cathode). The volume of water present at the cathode in 'dry' systems is variable, and is a function of the amount of water collecting in the cell due to electroosmosis, the length of time the cell is operated, and is even dependent on the cell design and orientation.

The rate at which dissolution occurs is likely to be due to the relative availability of oxygen at the cathode. Unlike PEM fuel cell cathodes, PEMWE cathodes are not oxygen-rich, and as such, Pt dissolution is likely to be correlated to the kinetics of oxygen diffusion through the membrane. [147,148,266–269].

8.4 Chapter 3 Conclusions

For the first time, Pt dissolution from the cathode during intermittent operation of a PEMWE has been observed. Dissolution was analysed using DPV, a technique which shows promise as a cost-effective and highly sensitive method to detect dissolved Pt species in PEMWE cathode water, giving comparable limits of detection to ICP-MS. Pt dissolution has been shown to occur over a long timeframe with approximately 152 ng cm^{-2} of a 3 mg cm^{-2} PtB catalyst predicted to be lost during a 90 h OCV period,

equivalent to 0.005 % of the total catalyst loading. This places the estimate of the lifetime of the studied catalyst layer at approximately 95.2 years, far in excess of the majority of other components in the PEMWE. This lifetime estimate is, however, only relevant for the PtB catalyst tested, and is likely to be substantially reduced for state-of-the-art Pt/C catalysts with loadings in the range 0.2 mg cm^{-2} - 0.5 mg cm^{-2} [44] due to the lower initial loadings involved. Method development for the DPV technique may allow for the separate speciation of Pt(0) from Pt(II) and Pt(IV), which would also provide information pertaining to the rate of Pt loss due to carbon support corrosion. The mechanism of this dissolution process is likely to be similar to that of the cathode catalyst in PEM fuel cells, in which the dissolution of Pt gradually becomes hindered by surface passivation. However, in PEMWEs it is anticipated that the Pt dissolution rate would be amplified due to the increased volume and flow rate of liquid water at the cathode. In addition, the kinetics of these reactions will be complicated by oxygen crossover from the anode, which is dependent on several factors including the thickness of the Nafion membrane, the distribution of vapour phase and dissolved gases, and their respective partial pressures. Finally, this work may highlight the need for consideration about how PEWME systems are managed when non-operational. Unlike AWE, where it is common practice to apply a 'protecting current' that protects the cell components against the damaging potential swings of OCV [52], there is no information regarding performing the same in PEMWE. As one of the simple solutions to mitigate Pt dissolution would be to maintain a low cathode potential, then the application of a protecting current should be considered in this case. This does however have to be balanced against other considerations, such as the need to continuously draw power, and the

possible promotion of other degradation mechanisms, such as peroxide formation [269].

9 Chapter 4 - The Dissolution of Pt/C in PEMWE

9.1 Chapter Introduction

The work of the previous section has established that the dissolution of Pt on wet PEMWE cathodes is an important degradation mechanism, but was unlikely to be one of the major lifetime limiting factors of the PEMWE system itself. In part, one of the reasons for this was the high loading of PtB used in the study. Although an ideal catalyst for the study of the dissolution phenomenon as it reduced the number of possible degradation pathways, PtB is not a widely commercially used PEMWE electrocatalyst. Like PEMFC, Pt/C in a range of Pt: carbon ratios are more typical for PEMWE HER electrocatalysts as the loadings of Pt can be substantially reduced compared to PtB. Typical Pt/C loadings in PEMWE range from 0.2 – 0.5 mg cm^{-2} [44]. Assuming that the kinetics of O_2 crossover are unchanged by the difference in HER electrocatalyst formulation, it would be expected that the process of Pt dissolution would be the same and would be of comparable rates. This would naturally mean that the dissolution process on lower loaded Pt/C would have a more severe impact on lifetime. Equally, the thicker layer of the Pt/C electrode means that, closest to the membrane and in the area where oxygen permeation is highest, the degradation of the Pt may be even further accelerated, resulting in even more rapid degradation and performance loss. Conversely, as the degradation mechanism is clearly affected by the presence of oxygen and the lack of a hydrogen atmosphere, then a thicker membrane could hold on better to the hydrogen and thus become less prone to degradation. Pt lost by carbon corrosion must be factored into the overall loss of Pt in the case of Pt/C also. With the lower

loadings and the extra degradation mechanism possible, the lifetime of Pt/C under the OCV regime used in Chapter 3 was expected to be substantially reduced. For the most accurate estimation of lifetime to be made therefore, Pt(0) lost from the PEMWE cathode was also measured.

Although voltammetry has proved to be an ideal technique to quantify Pt (II) and Pt (IV), it does have a limitation in that it cannot measure Pt(0), meaning that Pt lost by carbon corrosion or mechanical erosion is not directly measurable. Although ICP-MS provides a measure of the total Pt in a solution, the poor sensitivity of the available ICP-MS at the ng L^{-1} range (Figure 71) precluded its use for the study of Pt(0). Voltammetry was therefore used in this section also, and the sample solutions instead were processed so that Pt(0) was oxidized to Pt(II) or Pt(IV), therefore allowing for its' detection in addition to Pt(II) and Pt(IV).

In this section, the dissolution of Pt from a Pt/C catalyst during OCV and operation at 1 A cm^{-2} is reported. Efforts to determine the total amount of Pt loss during these periods is also reported.

9.2 The Dissolution of Pt from Pt/C during OCV

9.2.1 Cell and Test Setup

The PEMWE cell used in this and the following sections used a CCM containing an IrO_2 anode at 3 mg cm^{-2}, a Pt/C cathode at 0.5 mg cm^{-2} Pt loading, and a Nafion 117 membrane. Gold-coated GDL components were used. The balance of plant setup is that shown in section 5.2, and was operated in the same manner as given in section 8.3 – With no purging of the anode or cathode water reservoir, water flowed at both anode

and cathode at 5 mL cm^{-2} min^{-1}, and a temperature maintained at 60 ^{o}C. In this test however, the duration of the OCV period was increased to reflect the significant rates of Pt dissolution still observed at the end of the OCV period with the PtB OCV dissolution profiles (Figure 76). Note that in this section, the dissolution of Pt during the transition from OCV to operation was not analysed as it was decided that its' contribution to the overall amount of Pt lost during the OCV-operation test was insignificant. Instead of this, the amount of Pt dissolved during operation at 1 A cm^{-2} was determined from water samples taken during the operational period before the OCV period.

Voltammetry was performed on regularly taken water samples from the cathode outlet and inlet, with the reported values given as outlet concentration minus inlet concentration. These values were then converted from ng L^{-1} to ng cm^{-2} h^{-1}.

9.2.2 The Dissolution of Pt from Pt/C during OCV and Operation at 1 A cm^{-2}

In the same manner as that shown by the OCV on the PtB-based CCM (Figure 74), the cathode potential of the Pt/C CCM demonstrated similar dynamic behaviour, with the cathode potential transitioning from an operational potential of -0.07 V NHE to a maximum potential of 1.02 V NHE (Figure 83). The time taken to each this maximum potential is shorter than that observed by PtB, taking ≈ 3 h to reach as opposed to ≈ 5 h for PtB, although this difference may be accounted for by possible differences in the capacitance of the anode or cathode rather than differences in the rates of gas diffusion through the CCM. Showing similar behaviour also, the anode potential reduces only steadily during this OCV period. The attainment of the same electrode potentials once the cathode is at a steady high potential shows that the electrochemical conditions present in the OCV test of PtB and Pt/C are the same.

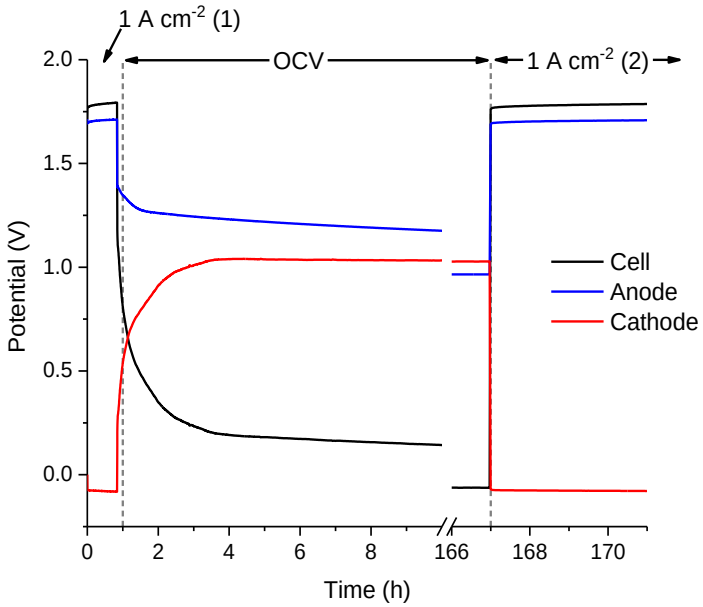

Figure 83. Evolution of cathode potential, anode potential and cell voltage with time, during the OCV test on a CCM with a Pt/C cathode. The electrolyser was operated at 1 A cm-2, followed by a 166 h OCV period, followed by operation at 1 A cm-2 again.

The dissolution profile of Pt from Pt/C was found to follow the same profile as that of the three PtB tests – a constant dissolution rate was observed below potentials of 0.85 V NHE, after which the dissolution rate rises to a maximum when the maximum cathode potential is reached, followed by a slow decay in dissolution rate over time (Figure 84). The line of best fit was produced following the same method provided in section 8.3.3 and fitted against the pulse profile (Equation (57) with the results of this fitting provided in Table 17.

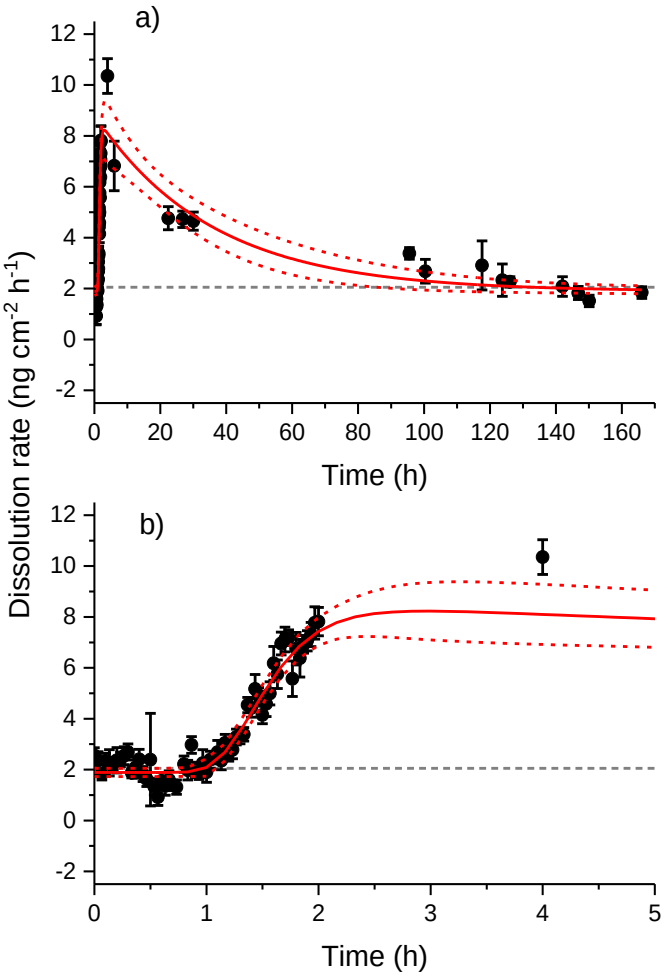

Figure 84. Pt dissolution rate from the PEMWE Pt/C cathode over a) the full duration of the OCV and b) during the first 5 h. Shown in red are the lines of best fit for a pulse profile. The solid red line shows the line of best fit with the dotted line showing the upper and lower 95% confidence intervals. Shown in grey is the average background dissolution rate.

s

Table 17. Fitted values for Pt dissolution from Pt/C during OCV against a pulse profile (Equation (57). The result of this fitting is shown in Figure 84.

	Pt/C OCV		
	Value	Error	Dependency
$\mathbf{y_0}$	1.889	0.082	0.4656
A	7.557	1.896×10^4	1
$\mathbf{t_1}$	0.3305	0.1221	0.9998
P	525668	1.415×10^{11}	1
$\mathbf{t_2}$	35.47	6.905	0.6845
$\mathbf{R^2}$	0.899		

This dissolution profile was again curtailed at the time at which it could no longer be stated with confidence that dissolution above the background rate was occurring. This was determined to be 85 h, roughly corresponding with the PtB OCV profiles. The total amount of Pt dissolved from the 85 h OCV period (subtracting the background dissolution rate) was calculated at 176.7 ng cm^{-2} with lower and upper confidence intervals of 149.3 ng cm^{-2} and 204.1 ng cm^{-2} respectively. This corresponds to an average of 0.035% of the total Pt lost per 85 h cycle, with lower and upper confidence intervals of 0.030 % and 0.041 % respectively. This corresponds to between 2400 and 3300 cycles for the complete loss of the Pt catalyst by dissolution, although like the PtB lifetime analysis, this does not take into account Pt lost by other means and the minimum Pt required for adequate HER performance. In the extreme OCV profile case (Figure 85), the electrode lifetime is estimated to be 7.28 years with a lower and upper confidence interval of 6.68 and 7.78 years respectively. To maximise the lifetime of the electrocatalyst, the operation mode that limits Pt dissolution to the greatest extent is

either continuous operation, or by holding the PEMWE cell at OCV for less than an hour (Figure 85).

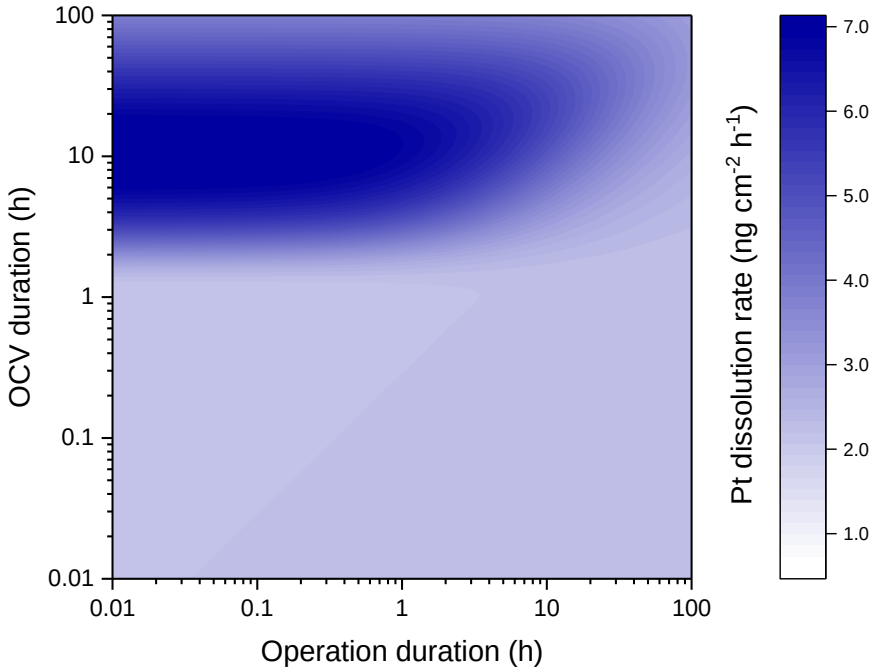

Figure 85. Average Pt dissolution rate from Pt/C electrocatalyst as a function of the duration of operation versus the duration of the OCV period. The dissolution rate during operation is constant, but dissolution at OCV is dependent on the potential and duration of OCV. In the case of the Pt/C OCV test the most damaging on-off regime was found to be a short operation (<0.01h) followed by a 10.5h OCV period.

Table 18.Pt dissolution amounts and estimations of the cathode electrode lifetimes at 0.5 mg cm-2 Pt on Pt/C

	Pt/C OCV
B_{OCV} (ng cm^{-2} h^{-1})	2.07 ± 0.19
B_{run} (ng cm^{-2} h^{-1})	$2.24^{+0.33}_{-0.34}$
$t_{OCV\ /\ max}$ (h)	85
Pt_{cycle} (ng cm^{-2})	176.7 ± 27.4
Max average OCV dissolution rate (ng cm^{-2} h^{-1})	7.28 ± 0.60
Min average OCV dissolution rate (ng cm^{-2} h^{-1})	2.07 ± 0.19
Most damaging cycle profile (h)	10.5
Minimum electrode lifetime (y)	$7.84^{+0.71}_{-0.60}$
Maximum electrode lifetime (y)	$27.56^{+2.76}_{-2.30}$

In comparison to PtB dissolution, the Pt/C dissolution profile occurs over the same timeframe but to a generally greater extent than PtB. The maximum rate of dissolution predicted is ≈ 8 ng cm^{-2} h^{-1}, compared to the ≈ 4 ng cm^{-2} h^{-1} of PtB. The total amount of Pt dissolved during each full OCV profile is slightly higher than PtB, at 176 ng cm^{-2} compared to the 152 ng cm^{-2} for PtB. For these reasons, the forecast lifetime of the Pt/C electrode at 0.5 mg cm^{-2} are less than that predicted in Section 8.3.3. The exact cause of the difference in dissolution rate is unclear, as the CCM utilized the same cell, demonstrated similar electrochemical profiles during OCV, and the measured ECSA of the Pt/C electrode (Figure 86) was lower than that of PtB, measured at 210 cm^2_{Pt} cm^{-2} as opposed to 319 cm^2_{Pt} cm^{-2} of PtB at BoT. Therefore, the mechanisms that may have affected dissolution, the Pt/C surface area and the rate of oxygen diffusion, should have either resulted in a lower overall rate of dissolution or resulted in the same overall dissolution rate. Even by estimating the total, rather than electrochemical, surface area

of the catalyst layer (calculated from the supplier provided catalytic surface area measurements), the PtB surface area is still higher, at 750 $cm^2_{Pt}\,cm^{-2}$ compared to Pt/C at 319 $cm^2_{Pt}\,cm^{-2}$. Therefore, even if Pt dissolution may occur on Pt catalyst that it not electrochemically active, then the dissolution would be expected to be lower. This finding supports the notion that reducing the surface area does not reduce the dissolution rate, and so it is likely that these dissolution profiles may be consistent as the ECSA reduces due to further Pt dissolution. It should be noted here that the higher surface area per mass of Pt on the Pt/C catalyst makes it more susceptible to agglomeration, oxidation and dissolution.

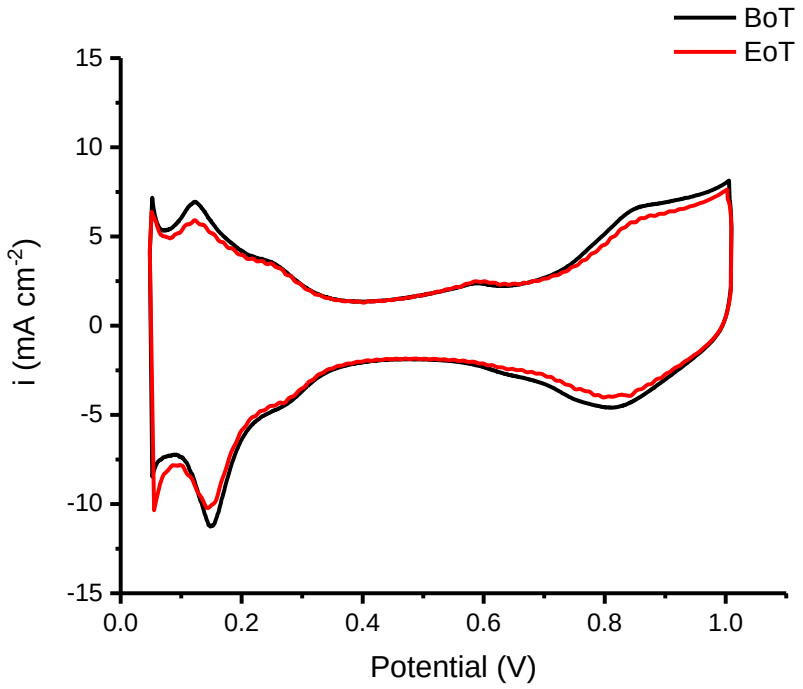

Figure 86. Cyclic voltammetry of Pt/C cathode before OCV test (BoT, shown in black) and after the OCV period (EoT, shown in red) of OCV test 1.

Interestingly, the loss of ECSA through the OCV dissolution test in Pt/C was found to be slightly less than PtB, with a reduction of 210 – 189 $cm^2_{Pt}\,cm^{-2}$ or approximately 10 %, in

comparison to the 18 % loss of PtB. These values are still high in comparison to the loss of Pt estimated during the OCV cycle, and so whilst there is a difference in the percentage of ECSA loss, these results still seem compatible with the hypothesis provided in section 8.3.4.

9.3 Measurement of Total Pt Loss from Pt/C

Pt dissolution has proved to be an important degradation mechanism in Pt/C-cathode based PEMWE systems; however, it has not been determined thus far whether it is the predominant degradation pathway. Mechanisms, such as Ostwald ripening or the coalescence of Pt nanoparticles (Figure 31), whilst contributing to performance loss, would not themselves result in the loss of Pt mass from the PEMWE cathode in the manner that Pt dissolution does. The mechanisms of erosion and carbon corrosion (in the case of Pt/C) would however result in additional Pt(0) mass loss from the PEMWE system. The rate at which these two mechanisms occur in a PEMWE system is not known, although studies have shown that carbon corrosion has less of an impact on ECSA loss than coalescence does. Nevertheless, with electrodes of substantially higher loadings than that used *in vitro*, a quantification of the total Pt lost is important for both performance, lifetime and cost reasons.

Although the voltammetry technique for determining dissolved Pt cannot itself be adjusted to detect Pt(0) species in water, a treatment method for oxidising the Pt(0) species to Pt(II) or Pt(IV) was developed so that a measurement of the total amount of Pt lost from the PEMWE cathode could be attempted. This method is covered in detail in 5.5.4. Briefly, this method involved the removal of water from each of the samples, followed by the addition of aqua regia (a 3:1 molar mix of HCl and NHO_3) to each of the

dried sample vials. These aqua regia samples were then diluted before analysis by the voltammetry technique.

9.3.1 Voltammetry of Samples Treated with Aqua Regia

The quantification of the aqua regia-based samples by voltammetry was complicated by two factors. Firstly, the presence of nitrates in the test solution was found to alter the DPV profiles by improving the HER kinetics on the mercury. At the characteristic peak of Pt there was a substantial current already participating in HER on the mercury electrode (Figure 87). The aqua regia samples were therefore diluted by 10-fold to minimise this interference as much as practically possible, whilst still obtaining a quantifiable Pt catalytic wave. With a reduced Pt peak and a higher background signal, the characteristic peaks were generally reduced in magnitude, and so the quantification became less precise generally. The second factor affecting the measurement precision and accuracy were the several additional preparation steps required for the aqua regia samples compared to the typical water samples. The additional steps were calculated to add approximately an additional 5 % error compared to the normal water samples.

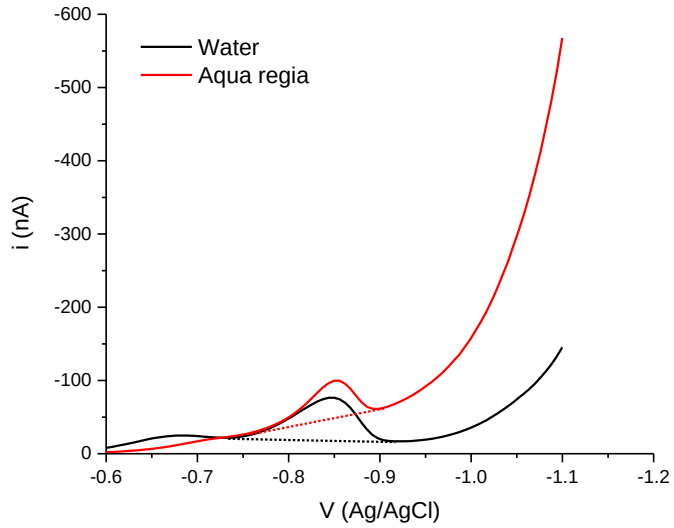

Figure 87. Impact of the presence of nitrates in the aqua regia sample on the DPV profile, in pure water (black) versus in diluted aqua regia (red). The more rapid exponential increase in current (shown in red) is caused by an increased rate of HER facilitated by an increased presence of nitrates in the solution. As can be seen, however, a Pt attributable peak is still present and quantifiable.

9.3.2 Measurement of Dissolved Pt and Pt(0) from a PEMWE

The water samples taken from the PEMWE were tested both for dissolved Pt and for Pt(0). The OCV test was performed in the same manner as the previous OCV test in section 9.2. There are therefore two datasets produced in this study- dissolved Pt and total Pt.

With regards to the quantification of dissolved Pt in this test, the results (shown in Figure 88) unfortunately did not provide an adequate profile against which a pulse profile could be fitted. The profile was instead fitted against an exponential decay profile from the value of maximum dissolution, and the dissolution rates below 0.85 V NHE were averaged together to produce the constant background dissolution rate. The dissolution

decay region was fitted against an exponential decay function shown in Equation (58, using the Levenburg-Marquadt algorithm to reach a chi-squared tolerance of 1×10^{-15}.

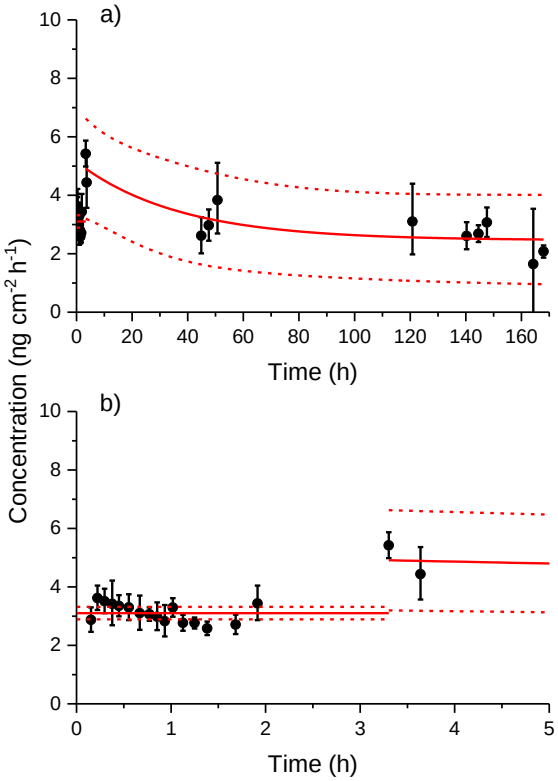

Figure 88. Dissolution rate of Pt from the PEMWE Pt/C cathode over a) the full duration of the OCV and b) during the first 5 h. The solid red line shows the line of best fit with the dotted line showing the upper and lower 95% confidence intervals. It was not possible to model this data in the same manner as the PtB curves, hence the approach to model the background dissolution rate and then an exponential decay function after the onset of dissolution.

Table 19. Fitting profiles for the Pt(II) and Pt(IV) dissolution profiles shown in Figure 88.

Pt(II) and Pt(IV) OCV			
	Value	Error	Dependency
y_0	2.458	0.315	0.664
A	2.683	0.556	0.374
t	36.759	20.197	0.606
R^2	0.367		

The background dissolution rate was calculated from the dissolution values before 0.85 V NHE, giving an average dissolution rate of 3.10 ng cm^{-2} h^{-1}, with upper and lower confidence intervals of 3.31 and 2.89 ng cm^{-2} h^{-1} respectively.

The measurement of the total Pt lost over time is given in Figure 89. There is a clear distinction between the dissolved Pt and total Pt profiles here. Dissolved Pt rate has been found to increase at 0.85 V NHE and above, whereas it cannot be determined that the amount of total Pt lost follows any similar profile. Although the determined amounts of Pt have a high variability, a general trend is observed of total Pt loss rate decreasing steadily over time. Hence the rate of total Pt loss was fitted against the same exponential decay profile given in Equation (58, with the results of the fitting provided in Table 20. In this fitting the circled data points shown in Figure 89b were treated as outliers and ignored.

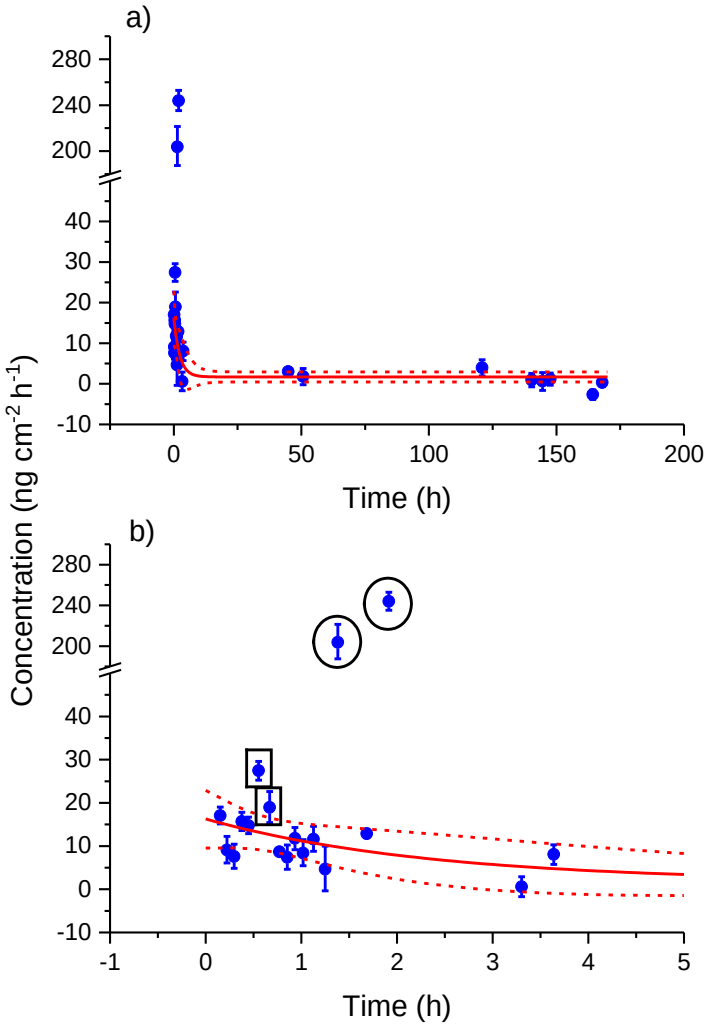

Figure 89. Measurement of total Pt lost from a PEMWE during period of OCV. The dotted lines represent the confidence intervals. Highlighted in circles are data points omitted from the fitting. The data highlighted in the squares are the data points indicating a peak in Figure 90. The solid red line shows the line of best fit with the dotted line showing the upper and lower 95% confidence intervals

Table 20. Fitting profiles for the total Pt loss profiles shown in Figure 89.

Total Pt during OCV			
	Value	Error	Dependency
y_0	1.701	0.647	-
A	14.570	2.719	0.627
t	2.339	1.264	0.627
R^2	0.573		

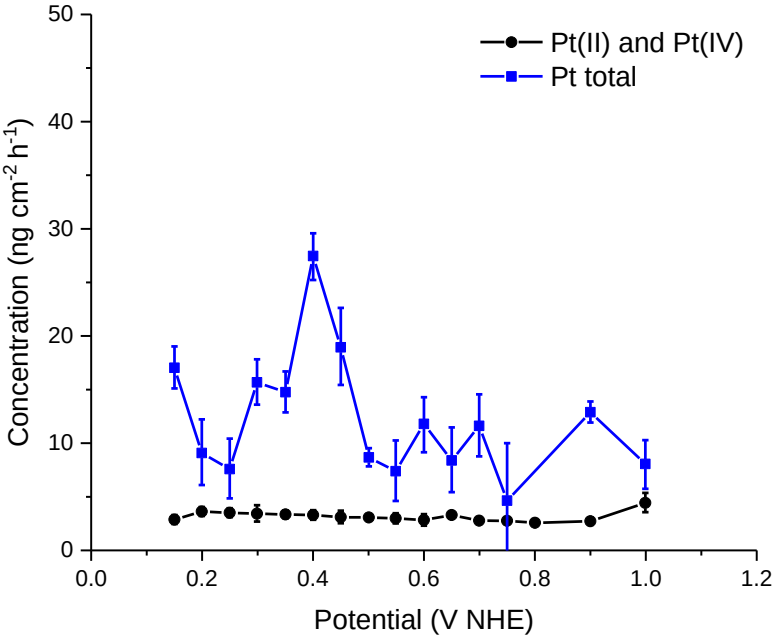

Figure 90. Measurement of dissolved Pt concentration and measurement of total Pt lost as a function of potential. Shown in black are the Pt(II) and Pt(IV) species alone and in blue is the total Pt lost (Pt (0), Pt(II) and Pt(IV)).

Over the duration of the OCV period, a general decay in total Pt loss was likely observed; however, the signal was highly variable during the period of time in which the potential of the cathode rose. This is shown in Figure 90, along with the dissolved Pt rates that show the same characteristic rise in dissolution above 0.85 V NHE that is seen in Figure

77. Regarding the total Pt loss within this potential range, the apparent peak at 0.3 – 0.5 V NHE is a clear feature. This would appear to roughly coincide with the potential at which the Pt-induced corrosion of the carbon support has been reported [270]. In this case, the Pt detected is that liberated due to the loss of the underlying carbon support. Whilst considering only the dataset given in Figure 90 it would appear that a peak here is detectable if not quantifiable, when considering the whole Pt loss dataset (Figure 89) the presence of a meaningful peak here becomes less likely. Highlighted by squares in Figure 89 are the two main data points (0.4 V NHE and 0.45 V NHE) that form the peak in Figure 90. The presence of the circled data points at 204 and 243 ng cm^{-2} h^{-1} have been treated as outliers in the fitting process; however, when trying to identify peaks within the whole profile their presence must be considered. Against these, it is clear that the relatively subtle changes in loss rates that form the peak are not sufficiently meaningful to say with any confidence that a transient Pt loss process is occurring.

The high loss rates of the circled data points in Figure 89 are not mirrored by the respective data points for Pt dissolution in Figure 88, and so these high total Pt loss rates originate from Pt(0). Contamination here is the likeliest explanation as no extra transient process causing the loss of Pt(0) is expected in this region.

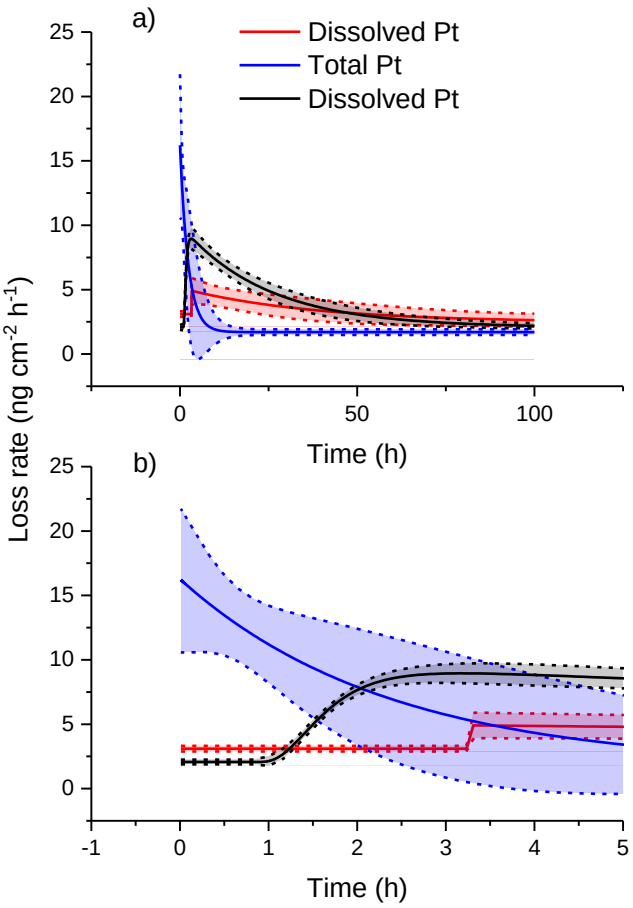

Figure 91. Comparison of the estimated Pt dissolution rate profiles (from this section, in red) with total Pt loss profiles (blue). Included is black is the Pt dissolution profile from the Section 9.2. Plots given are a) over the course of the whole OCV and b) during the first 5 h. The solid lines show the line of best fit with the dotted lines showing the upper and lower 95% confidence intervals.

The fitted profiles of Pt dissolution against total Pt loss during the OCV period are compared in Figure 91. In this figure, the dissolution profile from the previous Pt/C study is included also (in black). As the total Pt loss is the combination of both the dissolved Pt plus Pt(0), the total Pt signal should be equal to or higher than dissolved Pt throughout the OCV duration. Comparing the Pt dissolution and total Pt loss profiles of this particular study, this is clearly the case only during the first 2 h of OCV. As this should

not be the case, this error suggests a poor choice of fitting profile, poor data, or a systematic error in the total Pt loss samples. As the total Pt loss rate is also lower than the dissolved rate profile produced in the previous study, this would suggest that a systematic error is indeed the cause. By comparison of this data, both in Figure 90 and Figure 91, it may therefore only be stated with confidence that an additional loss of Pt(0) occurs during the first 2.05 h of OCV (when comparing to the Pt dissolution profile produced in this section) or 1.54 h of OCV (when comparing to the dissolution profile produced in the Section 9.2).

The initial difference in total Pt loss versus Pt dissolution during the initial hours of OCV matches that observed during operation also (Figure 92). During operation before the OCV period, three water samples were taken, with dissolution and total Pt loss measured. In comparison to the initial OCV dissolution rate, it can be stated with confidence that there is a difference when compared to operation. This is in agreement with the results of the previous Pt/C study and the PtB study. However, it cannot be stated with confidence here that a difference between the total Pt loss rates at OCV and operation exists. In comparison to Pt dissolution however, total Pt loss during operation is clearly far higher, and so the presence of Pt(0) in the water samples is very likely.

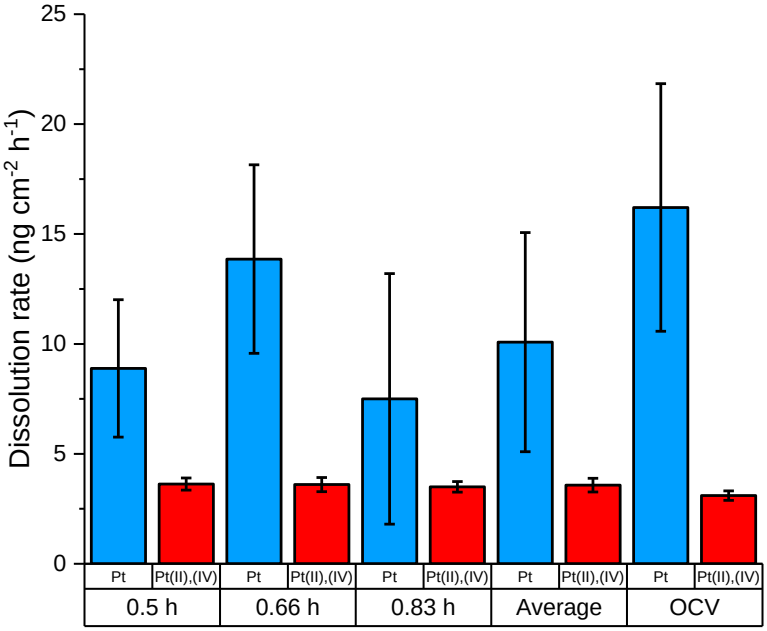

Figure 92. Measurements of Pt dissolution and total Pt loss during operation at 1A cm^{-2} and at the start of the OCV period. In blue is the total measurement (Pt(0), Pt(II) and Pt(IV) species) with red representing the Pt(II) and Pt(IV) species only.

9.3.3 The Mechanism of Pt(0) Loss

Pt loss by dissolution during OCV and operation has now been well established, and is present in all the OCV studies performed. Figure 91 makes it is clear that Pt dissolution is the major contributor to total Pt loss after the initial 2 h of OCV. Therefore, the loss of Pt(0) from the electrode only seems to be a degradation mechanism relevant to these first few hours. Pt(0) loss is also clearly present during operation. There is no strong evidence of an accelerated loss of Pt(0) caused by Pt-induced carbon corrosion. Even at high potential there is no evidence of carbon corrosion causing the loss of Pt. It therefore seems likely that the cause of this Pt(0) loss is not induced by potential change on the cathode. The likeliest source of Pt(0) loss is therefore from operation, and by the erosion

of the cathode layer by gas evolution. Although Pt(0) loss would therefore be expected to occur during operation only, the loss of Pt(0) may still be detected in the same manner that dissolved Pt was detected during the onset of operation after OCV in Figure 78. Due to the high porosity of the cathode and GDL, it takes time for the species to diffuse through and be removed from the cell. In this case however, no gas evolution takes place to force the removal of these species, and so Pt(0) is present in the outlet water over a long period of time. This erosion process is likely to have occurred on PtB also as this process may not be dependent on the carbon support.

9.3.4 Estimation of Pt/C Lifetime Based on Total Pt Loss

In the same manner as PtB and the previous Pt/C test, an estimate of the lifetime of the PEMWE cell based on the total Pt loss during operation and OCV was made. As the quality of the Pt/C profile in Section 9.2 (Figure 84) is better than that produced in this section, the former profile was used for the lifetime estimation in conjunction with the total Pt loss profile. As is shown in Figure 91, total Pt loss in only greater than Pt dissolution within the first 1.54 h of OCV. The overall Pt loss profile therefore follows whichever profile has a greater value at the given time. It was additionally assumed that the rate of Pt total loss during OCV was independent of the operational runtime. As it could not be stated with confidence that the Pt total loss rate at the start of OCV was different to the loss rate during operation, then it was assumed that the loss rate during operation was equal to the loss rate at the beginning of the OCV period.

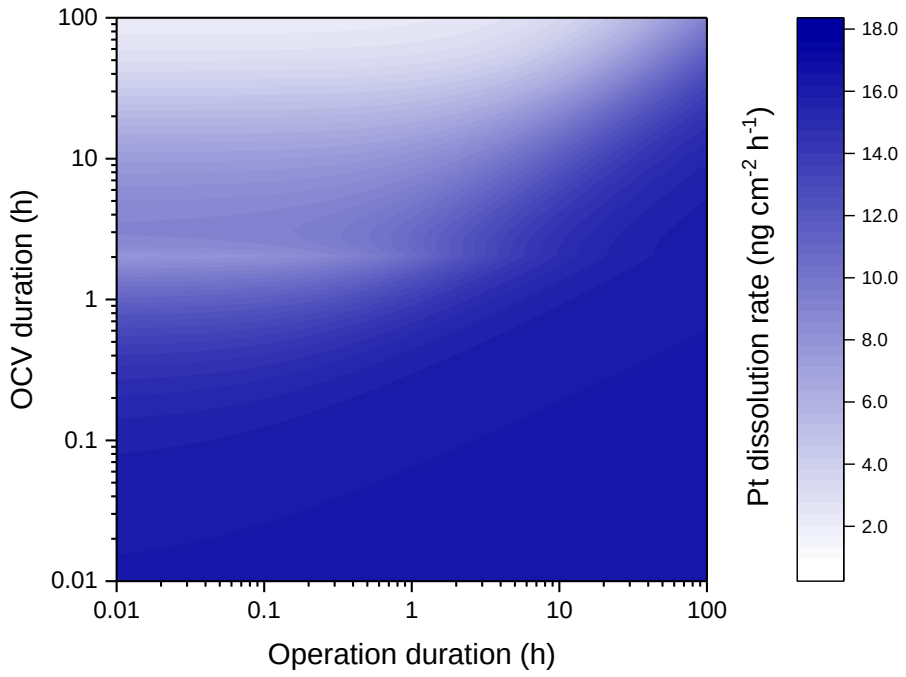

Figure 93. Average total Pt loss rate from Pt/C electrocatalyst as a function of the duration of operation versus the duration of the OCV period. Lighter blue regions represent the on-off regimes that do less damage to the cathode catalyst and darker blue regions represent the more damaging regimes.

Figure 93 gives the estimated dissolution rates from operational regimes of different lengths. In contrast to the estimations of Figure 80 and Figure 85, the additional factor of total Pt loss at the start of the OCV period and operation result in generally higher rates of loss in comparison to Pt dissolution alone. As the additional factor of total Pt loss is present during operation and early during OCV, then it is clear here that continuous operation and short period OCVs impart the most damage onto the cathode. In the most severe case, the average Pt loss rate is 16.21 ng cm^{-2} h^{-1}, which is present during continuous operation. The lifetime estimate at this dissolution rate is 3.52 years, which is short of the required lifetime estimates for PEMWE systems.

Table 21. Fitted values for total Pt loss from Pt/C cathode during OCV and operation.

Pt/C OCV	
B_{run} (ng cm^{-2} h^{-1})	$16.21^{+5.52}_{-5.61}$
Pt_{cycle} (ng cm^{-2})	$399.5^{+55.5}_{-52.0}$
Max average OCV dissolution rate (ng cm^{-2} h^{-1})	$16.21^{+5.52}_{-5.61}$
Min average OCV dissolution rate (ng cm^{-2} h^{-1})	$2.20^{+0.20}_{-0.21}$
Most damaging cycle profile (h)	Continuous operation
Minimum electrode lifetime (y)	$3.52^{+1.86}_{-0.89}$
Maximum electrode lifetime (y)	$25.97^{+2.67}_{-2.21}$

The result that continuous operation imparts the greatest Pt loss from the cathode is a concern for PEMWE systems, as it is predicted here that the cathode will be the lifetime limiting factor of the overall system. This would indicate that there is a need to either increase the loading of the cathode catalyst, or to improve the cathode electrode to make it less susceptible to erosion (possibly by increasing the ratio of Nafion ionomer). This prediction has not been backed up by evidence from the post-mortem of long-running PEMWE systems however [146], which typically show membrane thinning to be the lifetime limiting factor. It does have to be considered that the PEMWE system used in this section may not completely reflect the OCV conditions of the commercial units, however. The PEMWE cell used in this section used a flow of water at the cathode, which both imparts the potential change and allows for water samples to be taken. There may not always be the presence of water at the cathode in commercial units, however. As has been shown in section 6 and 7, a dry hydrogen atmosphere at the cathode will prevent potential variation on the cathode, and so Pt dissolution will be prevented. Pt dissolution may therefore not be a relevant mechanism during some OCV periods. Pt(0)

erosion, however, as it is mechanical in nature and does not rely on potential, would foreseeably still occur. By extrapolating the loss rate by Pt(0) erosion, this mechanism would itself still limit the lifetime of the cathode system to < 5 years if continuously operated. As this erosion process seem to be substantial, but has not been reported as a pertinent issue in other literature regarding electrocatalyst degradation, then it therefore seems unlikely that the process of Pt(0) erosion is one that is continuous. It is more likely that this erosion process is an artefact of the CCM being relatively fresh (less than 10 h of operation), with the erosion process occurring on catalyst particles that are less well adhered to the overall electrode. Over time, these particles will be removed and so the process of erosion will diminish. The process of erosion may not necessarily just diminish however, as it may occur as the result of another degradation mechanism occurring, such as the process of membrane thinning itself. Pt(0) erosion is therefore not likely to be one of the major lifetime limiting factors of PEMWE systems, but it should certainly be considered, especially during the early life of the CCM.

9.4 Investigation of Pt Dissolution Signal during the OCV-Operation Transition

One of the remaining unclear phenomenon in this Pt dissolution study remains the high Pt dissolution rate observed at the transition from OCV to operation (as has been shown in Figure 78). The high Pt signal here was attributed to the removal of high Pt concentration water by the evolution of H_2; however this does not preclude any other reactions occurring here that may additionally contribute to Pt loss. Principally, the possible reduction of Pt-oxides and the associated dissolution [215] could not be detected due to the expulsion of the dissolved Pt concentration. To investigate this

phenomenon, and to attempt to detect an additional contribution of dissolved Pt from oxide reduction, three tests using modified OCV transition profiles were performed. All the tests followed an operational period at 1 A cm^{-2} for 10 minutes, followed by an OCV period of 30 minutes. However, the transition after OCV varied for each test. Firstly, the transition from OCV to operation at 1 A cm^{-2} was investigated (OCV – 1 A cm^{-2}) to establish the normal dissolution peak expected of an OCV - operation transition from an OCV of 30 minutes duration. Secondly a transition from OCV to a cell voltage of 1.2 V was performed. The cathode potential in this test reduced to 0.24 V NHE. This test was performed to investigate the dissolution profile when the cathode potential transitioned from an oxidising potential to a potential that would have caused Pt-oxide reduction but would not have also caused HER. Thirdly, a transition from OCV to a cell voltage of 0.45 V was performed, with the cathode potential reaching 0.92 V NHE. In this case, as the cathode potential remained high, then Pt surface oxide reduction would not occur, and so this test provides a measure of Pt dissolution decay without either Pt oxide reduction of HER. By comparison of the dissolution profiles from each of these tests, the effect of Pt oxide reduction on the dissolution rate during reduction was analysed.

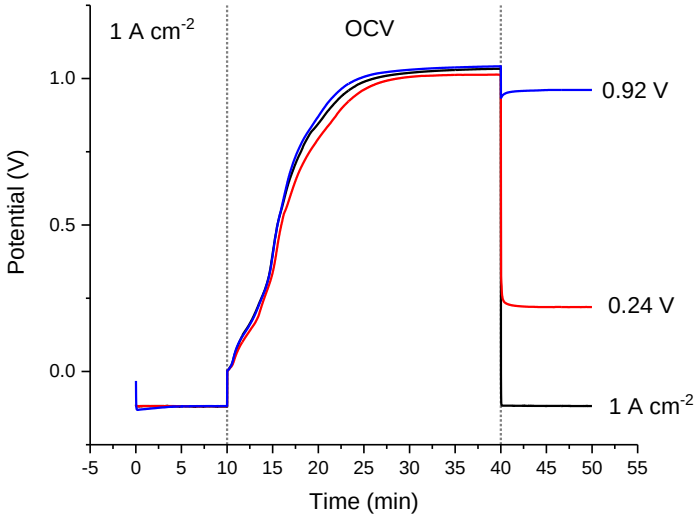

Figure 94. Cathode potential of the 1 A cm^{-2}, 0.24 V NHE and 0.92 V NHE OCV transition tests. In blue is the transition from OCV to a cathode potential hold of 0.92 V, in red is the transition from OCV to a cathode potential hold of 0.24 V, and black is the transition from OCV to 1 A cm^{-2}.

In each of the tests the cathode potentials during OCV were found to be relatively consistent, with the potentials progressing above 0.85 V NHE at similar times (Figure 94). In total, the 1 A cm^{-2} test was above 0.85 V NHE for 19 minutes, the 0.24 V NHE test for 18.2 minutes and the 0.92 V NHE test for 20 minutes. Water samples were taken 1 minute before the transition, and then at 2 minute intervals from the onset of the current or potential hold. These solutions were tested for dissolved Pt only.

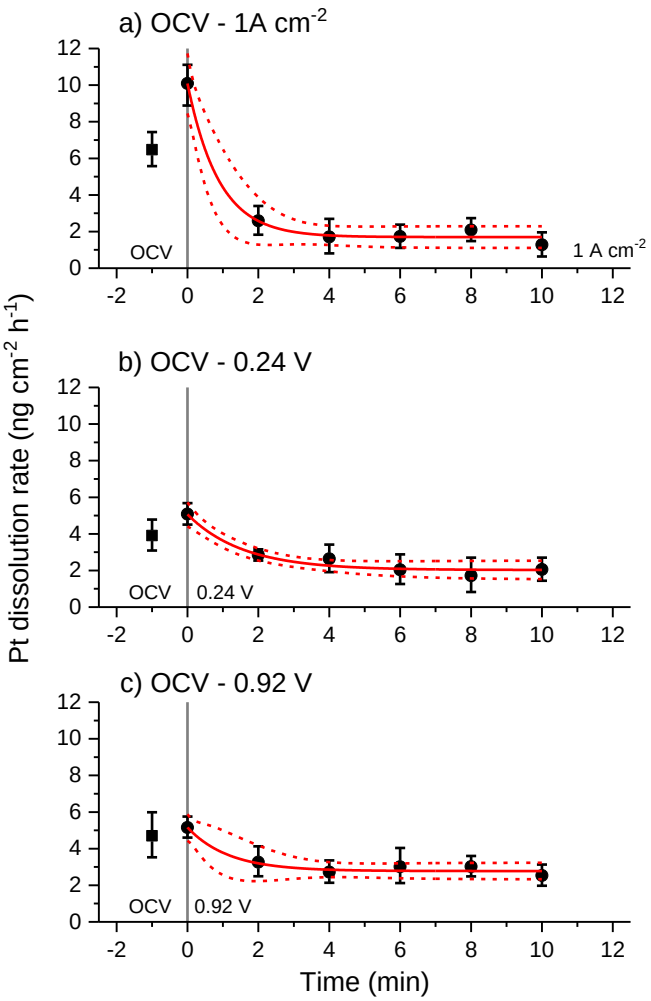

Figure 95. Pt dissolution rates during OCV and after the transition from OCV to a) 1A cm^{-2} b) a cathode potential of 0.24 V NHE and c) a cathode potential of 0.92 V NHE. Shown in red is the fitted exponential decay function with the upper and lower 95% confidence intervals represented as the red dotted lines.

The dissolution profiles were fitted against an exponential decay profile (Equation (58), with the results of the fittings given in Table 22.

Table 22. Fitting parameters of the exponential decay function against the dissolution profiles in Figure 95.

	OCV – 1A cm^{-2}			**OCV – 0.24 V**			**OCV – 0.92 V**		
	Value	Error	Dependency	Value	Error	Dependency	Value	Error	Dependency
y_0	1.699	0.186	0.292	2.026	0.162	0.723	2.777	0.142	0.457
A	8.394	0.546	0.127	3.039	0.257	0.504	2.382	0.27	0.282
t	0.886	0.203	0.204	1.568	0.257	0.659	1.153	0.556	0.279
R^2	0.987			0.979			0.968		

A first indication of whether there is a difference in the dissolved Pt loss mechanism at the OCV – current / potential transition is the comparison of the dissolution rate at OCV versus rate at the start of the current or potential hold (Table 23). This occurred in the case of OCV – 1 A cm^{-2}, where the p-value (a value that states the probability of the null hypothesis being correct – i.e. there is no difference between dissolution rates at OCV and current / potential hold) is below 0.05, thus indicating that there is a statistical significance (to 95 % confidence) in there being a difference in the mechanism of Pt loss from the cathode. This is, however, not the case for the OCV – potential holds, as the p-values produced here do not meet the criteria for statistical significance. Whilst there was a 74 – 78 % probability that the OCV – 0.24 V NHE transition induced in Pt loss mechanism that resulted in greater Pt loss, there is only a 24 – 25 % probability that this was the case for the OCV – 0.92 V NHE transition.

Table 23. Dissolution rates at OCV, the start of current / potential hold from the fitted profile and from the data point, and the p-values of the OCV minus fitted or data point.

Test	OCV (ng $cm^{-2}h^{-1}$)	Fitted current/potential hold (ng $cm^{-2}h^{-1}$)	p-value (OCV – fitted)	Data point current/potential hold (ng $cm^{-2}h^{-1}$)	p-value (OCV – data point)
OCV – 1A cm^{-2}	$6.47^{+0.96}_{-0.9}$	10.09 ± 1.64	0.00028	$10.09^{+2.32}_{-1.96}$	0.0015
OCV – 0.24 V	$3.91^{+1.68}_{-1.56}$	5.06 ± 0.66	0.22	$5.09^{1.15}_{-1.1}$	0.26
OCV – 0.92 V	$4.7^{+2.46}_{-2.26}$	5.16 ± 0.73	0.74	$5.16^{+1.15}_{-1.06}$	0.75

From this comparison alone, it can be stated that H_2 evolution causes a rate of Pt dissolution greater than that observed during OCV. The lack of this difference in the potential hold tests therefore shows that gas evolution displaces the high concentration Pt from the cathode and GDL. Although the balance of probability suggests that a Pt dissolution rate difference exists at the OCV - 0.24 V NHE transition, this cannot be stated with confidence. Instrumental error is the more likely cause of this difference.

If Pt oxide reduction and dissolution were to occur, it would not be an immediately detectable signal due to the tortuosity of the GDL and the cathode electrocatalyst. There would instead be a difference in the longer-term profile during the hold instead, with a greater amount of total Pt dissolution occurring with the 0.24 V NHE and 1 A cm^{-2} hold compared to 0.92 V NHE. The integration of the profiles therefore indicates whether this occurs. The results of the integration are given in Table 24. The p-values given in the table were calculated from the difference between the integration results. None of the integration results match the criteria for statistical significance to 95 % confidence, and so the null hypothesis applied in this case, that there is no difference in the amount of

total Pt dissolved between tests, cannot be refuted. There is a high probability of similarity between operation at 1 A cm^{-2} and the potential hold at 0.24 V NHE, and although there is a higher probability of a difference between the 0.24 V NHE and 0.92 V NHE tests, the 0.92 V NHE test had a greater total amount of Pt dissolution occurring on it. If oxide reduction and dissolution were to contribute to the total dissolution a greater amount of dissolution on the 0.24 V NHE test would have been expected. These datasets therefore do not indicate the presence of an additional dissolution caused by the reduction of a possible Pt-oxide at the cathode.

Table 24. Integration results of total Pt dissolved during the current / potential hold periods and the p-values of the difference between the integration results

Test	**Total Pt dissolved (ng cm^{-2})**	**p-values of difference between total Pt dissolved**		
		1 A cm^{-2}	0.24 V	0.92 V
1A cm^{-2}	$24.43^{+7.57}_{-9.57}$	-	0.939	0.353
0.24 V	$25.02^{+4.03}_{-4.04}$	-	-	0.140
0.92 V	$30.52^{+5.9}_{-5.9}$	-	-	-

This study cannot therefore associate the OCV – operation transition to any mechanism other than the expulsion of the high concentration Pt from the GDL and cathode. There are several possible explanations for this result. Firstly, the transition from high potential to low potential has been shown to be dependent on the rate of potential change. Topalov et al [221] reported a strong correlation between the rate of reducing scan rate and dissolution on a Pt electrode. When sweeping the potential from a highly oxidins potential to reducing potential with scan rates varying from 500 mV s^{-1} to 5 mV s^{-1} a six-fold increase in dissolution was observed with the slowing rates. In the case of the

PEMWE cathode the electrodes undergo near-instantaneous potential changes (Figure 94), and so there may have been very little associated dissolution. A further possibility is that the short duration of OCV may not have allowed for a sufficient oxide layer to have developed before the transition from OCV took place. Finally, if dissolution due to reduction did occur, it may have been at a small enough rate that it could not be detected.

9.5 Chapter 4 Conclusions

The dissolution of Pt and erosion of Pt(0) from a Pt/C electrocatalyst *in situ* has been demonstrated. It has been shown to occur on the PEMWE cathode during both periods of OCV and operation. Under certain on-off cycling regimes it has been shown that, in combination, these two phenomena are mechanisms that may become lifetime limiting factors for the cathode electrode and the PEMWE system. These findings are relevant to the PEMWE cell tested, which operated using a 'wet' cathode. In systems such as these, the lifetimes of the Pt/C electrode are estimated to be between 3.5 and 26 years. The upper estimate of lifetime though is unrealistic, as this would require the PEMWE system to be held continuously at OCV and never operated. The dissolution process itself may not occur on nominally 'dry' cathodes that do not experience potential change during OCV. The process of Pt(0) erosion however, as the evidence suggests that it is driven by gas generation, would likely occur regardless of whether the electrode is 'wet' or 'dry'. The erosion process itself, whilst measured to be high in magnitude in this study, may only be relevant to this CCM, particularly when it is considered that the CCM used was relatively new. Whether erosion remains a pertinent degradation long-term is uncertain. Although, if erosion were a continuous process that occurred at the rates

calculated in this study, then it would certainly be evident, and would have been reported prior to this study in the post-mortem of PEMWE systems. The likelihood therefore is that the rate of erosion will diminish with the length of time that the CCM is operated.

10 Overall Conclusions

In this thesis are presented a number of evolutions in the understanding of PEMWE systems, and of *in situ* electrocatalyst degradation of the Pt HER electrocatalyst. The major focus of this study in particular was to understand the conditions of OCV and how this may be related to degradation. Prior literature has shown that OCV may cause electrocatalyst degradation at the anode or cathode; however the nature and reaction mechanism underpinning OCV had not been explored. This was the subject of study in sections 6 and 7. In these sections both a range of OCV conditions were explored using a 3-electrode PEMWE cell, and a limited but sufficient mathematical model of OCV was developed. In both studies it was shown that OCV would normally be expected to progress with anode potential change, although a range of conditions existed in which cathode potential change would instead be expected. By drawing parallels between the potential change and the established SFC-ICP-MS literature [215,221,271], it was evident that degradation could occur as a result of this potential change through redox reactions occurring on the electrocatalyst. In the case of the anode, the reduction of the surface oxide would be expected. For the cathode, the oxidation of Pt would expected.

Although the state-of-the-art technique for measuring electrocatalyst degradation by dissolution is ICP-MS, it was unfortunately not readily available, especially at the ng L^{-1} concentrations that were found to be necessary. Instead, lost-cost voltammetric techniques were identified to allow this quantification. Two distinct techniques were identified. Firstly was a method for determining Pt concentration by DPV on a HMDE. This method used the excellent catalytic properties of Pt to determine concentration as a function of the rate of HER occurring. Secondly, a method to sequentially determine Ir

and Ru concentration by DPV was found. Unfortunately, however, the results given in the source literature could not be replicated.

By using both the 3-electrode PEMWE cell and the Pt DPV technique, a low cost, *in situ* method of determining Pt electrocatalyst dissolution was thus developed. The dissolution of Pt from both PtB and Pt/C during periods of operation and OCV was quantified, and it was demonstrated that the dissolution of Pt occurred during OCV when the cathode potential rose above 0.85 V NHE. It was also found that, during OCV, this dissolution continued for up to 100 h, thus drawing a link between the length of OCV duration and the lifetime of the Pt electrocatalyst. From the study of PtB an estimate of PEMWE lifetime (assuming that the only degradation mechanism was Pt dissolution), was approximately 95 years in the worst-case scenario. The further study of Pt/C also incorporated an estimation of the Pt lost by erosive mechanisms also, and this placed a worst-case estimate of lifetime at less than 4 years. Although this estimate is clearly worrying, under normal modes of electrolyser operation this estimate can be seen as an extreme case. The cathode potential during OCV only rises substantially when the cathode is immersed in bulk water and oxygen bubbles are present at the anode. For commercial systems therefore, this would be a rare but not unforeseen circumstance, as the accumulation of EOD water at the cathode is easily possible, as demonstrated in this thesis.

Therefore, this work is not complete enough that it can be stated with any confidence that Pt dissolution is the major PEMWE degradation mechanism, or even whether it is the major degradation mechanism occurring on the electrode itself. However, this thesis has uncovered this mechanism occurring in PEMWE for the first time, and it has

demonstrated that it may occur under a range of OCV conditions. The dissolution of Pt from PEMWE must therefore be considered an important degradation mechanism that must be considered, and ideally, mitigated.

11 Further Work

There is an extensive range of investigations that should be followed up from the work in this thesis. Firstly, the OCV model developed should be expanded upon, ideally incorporating O_2 and H_2 diffusion in the 2nd and 3rd dimensions over time. An improved model such as this will hopefully shed a greater light on how inhomogeneities in the diffusion rates over the electrodes will balance, and how the overall electrode potential will look. A model such as this will be able to inform PEMWE system designers on the ideal porosity and tortuosity of GDL materials also, and so there may be a direct commercial impact of this work. Furthermore, an improved model may help describe whether electrocatalyst degradation would occur across the whole electrode or in localised areas instead.

In regards to the *in situ* electrocatalyst degradation, although this thesis presents a detailed account of the dissolution of Pt, there is further work needed here also. It is important that the lifetime estimates from dissolution be more accurately established. To do this, the minimum required loadings for adequate HER and OER kinetics should be found. Furthermore, more detailed investigations of the HER electrocatalyst should be performed to inform on whether degradation by dissolution is the major degradation mechanism, or whether another degradation mechanism is predominant. The dissolution and degradation of the anode electrocatalyst has not been studied in this investigation. Like the cathode electrocatalyst, there is no prior literature on the *in situ* dissolution of Ir or Ru from the anode, and this represents a very good opportunity for research. It will not only inform on the degradation mechanisms occurring, but it will also be a useful aid in the development of MMO $IrRuO_2$ catalysts. The author believes

that this work will be of high impact and will have a high commercial relevance, particularly regarding reducing Ir loadings.

Finally, although the Pt DPV technique determined in this thesis was extremely useful, and allowed for the speciation of Pt(0) from Pt(II) and (IV), state-of-the-art ICP-MS should be able to determine concentration of Pt, Ir and Ru at sufficiently low concentrations. If possible, the author recommends using ICP-MS for further studies, especially if it may be coupled to ICP-MS in a method akin to SFC-ICP-MS. This setup would provide high sensitivity and high throughput measurements, and such a setup could prove to be extremely versatile as well as being a relatively simple arrangement. For example, a SFC would not be required as the electrolyser also naturally acts as an electrochemical cell with a flowing electrolyte.

12 Bibliography

[1] J.E. Overland, M. Wang, When will the summer Arctic be nearly sea ice free?, Geophys. Res. Lett. 40 (2013) 2097–2101. https://doi.org/10.1002/grl.50316.

[2] G.R. Van Der Werf, J.T. Randerson, L. Giglio, T.T. Van Leeuwen, Y. Chen, B.M. Rogers, M. Mu, M.J.E. Van Marle, D.C. Morton, G.J. Collatz, R.J. Yokelson, P.S. Kasibhatla, Global fire emissions estimates during 1997-2016, Earth Syst. Sci. Data. 9 (2017) 697–720. https://doi.org/10.5194/essd-9-697-2017.

[3] N.J.L. Lenssen, G.A. Schmidt, J.E. Hansen, M.J. Menne, A. Persin, R. Ruedy, D. Zyss, Improvements in the GISTEMP Uncertainty Model, J. Geophys. Res. Atmos. 124 (2019) 6307–6326. https://doi.org/10.1029/2018JD029522.

[4] J. Tollefson, How hot will Earth get by 2100?, Nature. 580 (2020) 443–445. https://doi.org/10.1038/d41586-020-01125-x.

[5] G.A. Schmidt, NASA GISS Surface Temperature Analysis (v4), (2021). https://data.giss.nasa.gov/gistemp/maps/index_v4.html (accessed May 28, 2021).

[6] United Nations, United Nations Framework Convention on Climate Change, 1992. https://doi.org/10.4337/9781785363924.00012.

[7] United Nations, The Kyoto Protocol - Status of Ratification, United Nations. (2020). https://unfccc.int/process/the-kyoto-protocol/status-of-ratification (accessed March 5, 2021).

[8] Kyoto Protocol To the United Nations Framework Convention on Climate Change, 1998. https://doi.org/10.1111/1467-9388.00150.

[9] Paris Agreement, Eur. Comm. (2018). https://ec.europa.eu/clima/policies/international/negotiations/paris_en (accessed October 21, 2020).

[10] I. Shishlov, R. Morel, V. Bellassen, Compliance of the Parties to the Kyoto Protocol in the first commitment period, Clim. Policy. 16 (2016) 768–782. https://doi.org/10.1080/14693062.2016.1164658.

[11] S. Fleming, Chart of the day: These countries create most of the world's CO2 emissions, World Econ. Forum. (2019). https://www.weforum.org/agenda/2019/06/chart-of-the-day-these-countries-create-most-of-the-world-s-co2-emissions/ (accessed October 3, 2020).

[12] C. Dreyfus, A Conversation with: Jerry Mahlman; Listening to the Climate Models, And Trying to Wake Up the World, NY Times. (2003). https://www.nytimes.com/2003/12/16/science/conversation-with-jerry-mahlman-listening-climate-models-trying-wake-up-world.html (accessed October 21, 2020).

[13] H. Sælen, J. Hovi, D. Sprinz, A. Underdal, How US withdrawal might influence

cooperation under the Paris climate agreement, Environ. Sci. Policy. 108 (2020) 121–132. https://doi.org/10.1016/j.envsci.2020.03.011.

[14] C.D. Keeling, R.B. Bacastow, A.E. Bainbridge, C.A. Ekdahl Jr, G.R. Peter, L.S. Waterman, Atmospheric carbon dioxide variations at Mauna Loa Observatory, Hawaii, Tellus. 28 (1976) 538–551. https://doi.org/10.3402/tellusa.v28i6.11322.

[15] C.D. Keeling, S.C. Piper, R.B. Bacastow, M. Wahlen, T.P. Whorf, M. Heimann, H.A. Meijer, Atmospheric CO2 and 13CO2 Exchange with the Terrestrial Biosphere and Oceans from 1978 to 2000: Observations and Carbon Cycle Implications, in: I.T. Baldwin, M.M. Caldwell, G. Heldmaier, R.B. Jackson, O.L. Lange, H.A. Mooney, E.-D. Schulze, U. Sommer, J.R. Ehleringer, M. Denise Dearing, T.E. Cerling (Eds.), A Hist. Atmos. CO2 Its Eff. Plants, Anim. Ecosyst., Springer New York, New York, NY, 2005: pp. 83–113. https://doi.org/10.1007/0-387-27048-5_5.

[16] G.P. Peters, J.C. Minx, C.L. Weber, O. Edenhofer, Growth in emission transfers via international trade from 1990 to 2008, Proc. Natl. Acad. Sci. U. S. A. 108 (2011) 8903–8908. https://doi.org/10.1073/pnas.1006388108.

[17] United Nations Environment Programme, Emissions Gap Report 2019, Nairobi, 2019. http://www.unenvironment.org/emissionsgap.

[18] H. Ritchie, How long before we run out of fossil fuels, Our World Data. (2017). https://ourworldindata.org/how-long-before-we-run-out-of-fossil-fuels (accessed October 22, 2020).

[19] IRENA, Renewable Power Generation Costs in 2019, Abu Dhabi, 2020. https://www.irena.org/-/media/Files/IRENA/Agency/Publication/2018/Jan/IRENA_2017_Power_Costs_2018.pdf.

[20] W. Spry, B. Lucking, Section 6 – UK Renewables April to June 2019, 2019. https://assets.publishing.service.gov.uk/government/uploads/system/uploads/attachment_data/file/835114/Renewables_September_2019.pdf.

[21] H. Ritchie, M. Roser, Emissions by sector, Our World Data. (2016). https://ourworldindata.org/emissions-by-sector (accessed October 10, 2020).

[22] J.O.M. Bockris, The hydrogen economy: Its history, Int. J. Hydrogen Energy. 38 (2013) 2579–2588. https://doi.org/10.1016/j.ijhydene.2012.12.026.

[23] J.O.M. Bockris, The origin of ideas on a Hydrogen Economy and its solution to the decay of the environment, Int. J. Hydrogen Energy. 27 (2002) 731–740. https://doi.org/10.1016/S0360-3199(01)00154-9.

[24] IEA, The Future of Hydrogen for G20. Seizing today's opportunities, Japan, 2019.

[25] G.J. Stiegel, M. Ramezan, Hydrogen from coal gasification: An economical pathway to a sustainable energy future, Int. J. Coal Geol. 65 (2006) 173–190. https://doi.org/10.1016/j.coal.2005.05.002.

[26] Environmental Protection Agency U.S, Technical Support Document for Hydrogen Production : Proposed Rule for Mandatory Reporting of Greenhouse Gases, 2008.

[27] D.R. Simbeck, Hydrogen costs with CO2 capture, Greenh. Gas Control Technol. 2 (2005) 1059–1066. https://doi.org/10.1016/B978-008044704-9/50108-7.

[28] IEA, Global average levelised cost of hydrogen production by energy source and technology, 2019 and 2050, IEA. (2020). https://www.iea.org/data-and-statistics/charts/global-average-levelised-cost-of-hydrogen-production-by-energy-source-and-technology-2019-and-2050 (accessed November 10, 2020).

[29] A. Al-Qahtani, B. Parkinson, K. Hellgardt, N. Shah, G. Guillen-Gosalbez, Uncovering the true cost of hydrogen production routes using life cycle monetisation, Appl. Energy. 281 (2021) 115958. https://doi.org/10.1016/j.apenergy.2020.115958.

[30] Royal Society, Options for producing low-carbon hydrogen at scale, 2018. https://royalsociety.org/-/media/policy/projects/hydrogen-production/energy-briefing-green-hydrogen.pdf.

[31] IEA, Low-carbon hydrogen production, 2010-2030, historical, announced and in the Sustainable Development Scenario, 2030, (2020). https://www.iea.org/data-and-statistics/charts/low-carbon-hydrogen-production-2010-2030-historical-announced-and-in-the-sustainable-development-scenario-2030 (accessed December 1, 2020).

[32] Global CCS Institute, Global Status of CCS 2020, 2020.

[33] T. Lepage, M. Kammoun, Q. Schmetz, A. Richel, Biomass-to-hydrogen: A review of main routes production, processes evaluation and techno-economical assessment, Biomass and Bioenergy. 144 (2021) 105920. https://doi.org/10.1016/j.biombioe.2020.105920.

[34] N. Fajrina, M. Tahir, A critical review in strategies to improve photocatalytic water splitting towards hydrogen production, Int. J. Hydrogen Energy. 44 (2019) 540–577. https://doi.org/10.1016/j.ijhydene.2018.10.200.

[35] S. Wainaina, Lukitawesa, M. Kumar Awasthi, M.J. Taherzadeh, Bioengineering of anaerobic digestion for volatile fatty acids, hydrogen or methane production: A critical review, Bioengineered. 10 (2019) 437–458. https://doi.org/10.1080/21655979.2019.1673937.

[36] IRENA, Green Hydrogen: A guide to policy making, Abu Dhabi, 2020.

[37] A. van Wijk, J. Chatzimarkakis, Green Hydrogen for a European Green Deal: A 2x40 GW Initiative, 2020. www.hydrogeneurope.eu.

[38] O. Schmidt, A. Gambhir, I. Staffell, A. Hawkes, J. Nelson, S. Few, Future cost and performance of water electrolysis: An expert elicitation study, Int. J. Hydrogen Energy. 42 (2017) 30470–30492. https://doi.org/10.1016/j.ijhydene.2017.10.045.

[39] F. Mueller-Langer, E. Tzimas, M. Kaltschmitt, S. Peteves, Techno-economic assessment of hydrogen production processes for the hydrogen economy for the short and medium term, Int. J. Hydrogen Energy. 32 (2007) 3797–3810. https://doi.org/10.1016/j.ijhydene.2007.05.027.

[40] E. Commission, Questions and answers: A Hydrogen Strategy for a climate neutral Europe, Eur. Comm. (2020). https://ec.europa.eu/commission/presscorner/detail/en/QANDA_20_1257.

[41] I. Staffell, D. Scamman, A. Velazquez Abad, P. Balcombe, P.E. Dodds, P. Ekins, N. Shah, K.R. Ward, The role of hydrogen and fuel cells in the global energy system, Energy Environ. Sci. 12 (2019) 463–491. https://doi.org/10.1039/c8ee01157e.

[42] S. Trasatti, Water electrolysis: Who first?, J. Electroanal. Chem. 476 (1999) 90–91. https://doi.org/10.1016/S0022-0728(99)00364-2.

[43] G. Pearson, Experiments and Observations made with the View of ascertaining the Nature of the Gaz produced by passing Electric Discharges through Water, Philisophical Trans. R. Socierty London. 87 (1797) 142–158.

[44] M. Carmo, D.L. Fritz, J. Mergel, D. Stolten, A comprehensive review on PEM water electrolysis, Int. J. Hydrogen Energy. 38 (2013) 4901–4934. https://doi.org/10.1016/j.ijhydene.2013.01.151.

[45] E. Montoneri, Inorganic separators for water electrolysis: Chemical stability and wettability of hydrophilic asbestos composites, Int. J. Hydrogen Energy. 14 (1989) 29–33. https://doi.org/10.1016/0360-3199(89)90153-5.

[46] P. Vermeiren, W. Adriansens, R. Leysen, Zirfon: A new separator for Ni-H2 batteries and alkaline fuel cells, Int. J. Hydrogen Energy. 21 (1996) 679–684.

[47] J. Brauns, T. Turek, Alkaline water electrolysis powered by renewable energy: A review, Processes. 8 (2020). https://doi.org/10.3390/pr8020248.

[48] Y. Yan, B.Y. Xia, B. Zhao, X. Wang, A review on noble-metal-free bifunctional heterogeneous catalysts for overall electrochemical water splitting, J. Mater. Chem. A. 4 (2016) 17587–17603. https://doi.org/10.1039/C6TA08075H.

[49] J. Chi, H. Yu, Water electrolysis based on renewable energy for hydrogen production, Chinese J. Catal. 39 (2018) 390–394. https://doi.org/10.1016/S1872-2067(17)62949-8.

[50] M. David, C. Ocampo-Martínez, R. Sánchez-Peña, Advances in alkaline water electrolyzers: A review, J. Energy Storage. 23 (2019) 392–403. https://doi.org/10.1016/j.est.2019.03.001.

[51] S. Shiva Kumar, V. Himabindu, Hydrogen production by PEM water electrolysis – A review, Mater. Sci. Energy Technol. 2 (2019) 442–454. https://doi.org/10.1016/j.mset.2019.03.002.

[52] A. Buttler, H. Spliethoff, Current status of water electrolysis for energy storage, grid balancing and sector coupling via power-to-gas and power-to-liquids: A review, Renew. Sustain. Energy Rev. 82 (2018) 2440–2454. https://doi.org/10.1016/j.rser.2017.09.003.

[53] S. Marini, P. Salvi, P. Nelli, R. Pesenti, M. Villa, M. Berrettoni, G. Zangari, Y. Kiros, Advanced alkaline water electrolysis, Electrochim. Acta. 82 (2012) 384–391. https://doi.org/10.1016/j.electacta.2012.05.011.

[54] R. Phillips, C.W. Dunnill, Zero gap alkaline electrolysis cell design for renewable energy storage as hydrogen gas, RSC Adv. 6 (2016) 100643–100651. https://doi.org/10.1039/C6RA22242K.

[55] P. Fortin, T. Khoza, X. Cao, S.Y. Martinsen, A. Oyarce Barnett, S. Holdcroft, High-performance alkaline water electrolysis using Aemion™ anion exchange membranes, J. Power Sources. 451 (2020) 227814. https://doi.org/10.1016/j.jpowsour.2020.227814.

[56] M.R. Kraglund, D. Aili, K. Jankova, E. Christensen, Q. Li, J.O. Jensen, Zero-Gap Alkaline Water Electrolysis Using Ion-Solvating Polymer Electrolyte Membranes at Reduced KOH Concentrations, J. Electrochem. Soc. 163 (2016) F3125–F3131. https://doi.org/10.1149/2.0161611jes.

[57] Y. Leng, G. Chen, A.J. Mendoza, T.B. Tighe, M.A. Hickner, C.Y. Wang, Solid-state water electrolysis with an alkaline membrane, J. Am. Chem. Soc. 134 (2012) 9054–9057. https://doi.org/10.1021/ja302439z.

[58] G. Merle, M. Wessling, K. Nijmeijer, Anion exchange membranes for alkaline fuel cells: A review, J. Memb. Sci. 377 (2011) 1–35. https://doi.org/10.1016/j.memsci.2011.04.043.

[59] J. Mougin, A. Chatroux, K. Couturier, M. Petitjean, M. Reytier, G. Gousseau, F. Lefebvre-Joud, High temperature steam electrolysis stack with enhanced performance and durability, Energy Procedia. 29 (2012) 445–454. https://doi.org/10.1016/j.egypro.2012.09.052.

[60] A. Scipioni, A. Manzardo, J. Ren, Hydrogen Economy: Supply Chain, Life Cycle Analysis and Energy Transition for Sustainability, Academic Press, 2017.

[61] M. Ni, M.K.H. Leung, D.Y.C. Leung, Technological development of hydrogen production by solid oxide electrolyzer cell (SOEC), Int. J. Hydrogen Energy. 33 (2008) 2337–2354. https://doi.org/10.1016/j.ijhydene.2008.02.048.

[62] M.A. Laguna-Bercero, Recent advances in high temperature electrolysis using solid oxide fuel cells: A review, J. Power Sources. 203 (2012) 4–16. https://doi.org/10.1016/j.jpowsour.2011.12.019.

[63] F.M. Sapountzi, J.M. Gracia, C.J. Weststrate, H.O.A. Fredriksson, J.W. Niemantsverdriet, Electrocatalysts for the generation of hydrogen, oxygen and synthesis gas, Prog. Energy Combust. Sci. 58 (2017) 1–35. https://doi.org/10.1016/j.pecs.2016.09.001.

[64] J. Aicart, F. Usseglio-Viretta, J. Laurencin, M. Petitjean, G. Delette, L. Dessemond, Operating maps of high temperature H2O electrolysis and H2O+CO2 co-electrolysis in solid oxide cells, Int. J. Hydrogen Energy. 41 (2016) 17233–17246. https://doi.org/10.1016/j.ijhydene.2016.07.269.

[65] A. Mahmood, S. Bano, J.H. Yu, K.H. Lee, Performance evaluation of SOEC for CO2/H2O co-electrolysis: Considering the effect of cathode thickness, J. CO2 Util. 33 (2019) 114–120. https://doi.org/10.1016/j.jcou.2019.05.014.

[66] V.I. Sharma, B. Yildiz, Degradation Mechanism in La0.8Sr0.2CoO3 as Contact Layer

on the Solid Oxide Electrolysis Cell Anode, J. Electrochem. Soc. 157 (2010) B441. https://doi.org/10.1149/1.3288835.

[67] X. Zhang, J.E. O'Brien, R.C. O'Brien, J.J. Hartvigsen, G. Tao, G.K. Housley, Improved durability of SOEC stacks for high temperature electrolysis, Int. J. Hydrogen Energy. 38 (2013) 20–28. https://doi.org/10.1016/j.ijhydene.2012.09.176.

[68] F. Tietz, D. Sebold, A. Brisse, J. Schefold, Degradation phenomena in a solid oxide electrolysis cell after 9000 h of operation, J. Power Sources. 223 (2013) 129–135. https://doi.org/10.1016/j.jpowsour.2012.09.061.

[69] P. Moçoteguy, A. Brisse, A review and comprehensive analysis of degradation mechanisms of solid oxide electrolysis cells, Int. J. Hydrogen Energy. 38 (2013) 15887–15902. https://doi.org/10.1016/j.ijhydene.2013.09.045.

[70] A. V. Virkar, Mechanism of oxygen electrode delamination in solid oxide electrolyzer cells, Int. J. Hydrogen Energy. 35 (2010) 9527–9543. https://doi.org/10.1016/j.ijhydene.2010.06.058.

[71] A. Hauch, S.D. Ebbesen, S.H. Jensen, M. Mogensen, Solid Oxide Electrolysis Cells: Microstructure and Degradation of the Ni/Yttria-Stabilized Zirconia Electrode, J. Electrochem. Soc. 155 (2008) B1184. https://doi.org/10.1149/1.2967331.

[72] J. Wei, T. Osipova, J. Malzbender, M. Krüger, Mechanical characterization of SOFC/SOEC cells, Ceram. Int. 44 (2018) 11094–11100. https://doi.org/10.1016/j.ceramint.2018.03.103.

[73] W.T. Grubb, L.W. Niedrach, Batteries with Solid Ion-Exchange Membrane Electrolytes: II. Low-Temperature Hydrogen-Oxygen Fuel Cells, Batter. with Solid Ion-Exchange Membr. Electrolytes II. Low-Temperature Hydrog. Fuel Cells. 107 (1960) 131–135. https://doi.org/10.1149/1.2427622.

[74] J. Eichman, K. Harrison, M. Peters, Novel Electrolyzer Applications : Providing More Than Just Hydrogen Novel Electrolyzer Applications : Providing More Than Just Hydrogen, 2014. http://www.nrel.gov/docs/fy14osti/61758.pdf.

[75] L. Allidières, A. Brisse, P. Millet, S. Valentin, M. Zeller, On the ability of pem water electrolysers to provide power grid services, Int. J. Hydrogen Energy. 44 (2019) 9690–9700. https://doi.org/10.1016/j.ijhydene.2018.11.186.

[76] G. Matute, J.M. Yusta, L.C. Correas, Techno-economic modelling of water electrolysers in the range of several MW to provide grid services while generating hydrogen for different applications: A case study in Spain applied to mobility with FCEVs, Int. J. Hydrogen Energy. 44 (2019) 17431–17442. https://doi.org/10.1016/j.ijhydene.2019.05.092.

[77] L.E. Owe, M. Tsypkin, K.S. Wallwork, R.G. Haverkamp, S. Sunde, Iridium-ruthenium single phase mixed oxides for oxygen evolution: Composition dependence of electrocatalytic activity, Electrochim. Acta. 70 (2012) 158–164. https://doi.org/10.1016/j.electacta.2012.03.041.

[78] S. Siracusano, N. Van Dijk, E. Payne-Johnson, V. Baglio, A.S. Aricò, Nanosized IrOx and IrRuOx electrocatalysts for the O2evolution reaction in PEM water

electrolysers, Appl. Catal. B Environ. 164 (2015) 488–495. https://doi.org/10.1016/j.apcatb.2014.09.005.

[79] H. Kim, S. Choe, H. Park, J.H. Jang, S.H. Ahn, S.K. Kim, An extremely low Pt loading cathode for a highly efficient proton exchange membrane water electrolyzer, Nanoscale. 9 (2017) 19045–19049. https://doi.org/10.1039/c7nr07224d.

[80] S. Siracusano, N. Van Dijk, R. Backhouse, L. Merlo, V. Baglio, A.S. Aricò, Degradation issues of PEM electrolysis MEAs, Renew. Energy. 123 (2018) 52–57. https://doi.org/10.1016/j.renene.2018.02.024.

[81] S. Thiele, B. Mayerhöfer, D. McLaughlin, T. Böhm, M. Hegelheimer, D. Seeberger, Bipolar membrane electrode assemblies for water electrolysis, ACS Appl. Energy Mater. 3 (2020) 9635–9644. https://doi.org/10.1021/acsaem.0c01127.

[82] L. Lei, J. Zhang, Z. Yuan, J. Liu, M. Ni, F. Chen, Progress Report on Proton Conducting Solid Oxide Electrolysis Cells, Adv. Funct. Mater. 29 (2019) 1–17. https://doi.org/10.1002/adfm.201903805.

[83] T. Jafary, W.R. Wan Daud, M. Ghasemi, M.H. Abu Bakar, M. Sedighi, B.H. Kim, A.A. Carmona-Martínez, J.M. Jahim, M. Ismail, Clean hydrogen production in a full biological microbial electrolysis cell, Int. J. Hydrogen Energy. 44 (2019) 30524–30531. https://doi.org/10.1016/j.ijhydene.2018.01.010.

[84] M. Chase, NIST-JANAF Thermochemical Tables, 4th Edition, 1998. https://doi.org/citeulike-article-id:12140840.

[85] M. Pourbaix, Atlas d'équilibres électrochimiques à 25°C, Gauthier-Villars & Cie, Paris, 1963.

[86] Y. Abe, H. Yanagisawa, K. Sasaki, Preparation of oxygen-containing Pt and Pt oxide thin films by reactive sputtering and their characterization, Japanese J. Appl. Physics, Part 1 Regul. Pap. Short Notes Rev. Pap. 37 (1998) 4482–4486. https://doi.org/10.1143/jjap.37.4482.

[87] S. Shibata, Conductance measurement of thin oxide films on a platinum anode, Electrochem. Commun. 22 (1977) 175–179.

[88] A.J. Bard, L.R. Faulkner, Electrochemical Methods, in: Electrochem. Methods, 2nd ed., John Wiley & Sons, Ltd, 2001: p. 108.

[89] D. Bessarabov, P. Millet, Fundamentals of Water Electrolysis, in: A. Godula-Jopek (Ed.), Academic Press, 2015: pp. 43–3. https://doi.org/https://doi.org/10.1002/9783527676507.ch2.

[90] W. Sheng, H.A. Gasteiger, Y. Shao-Horn, Hydrogen Oxidation and Evolution Reaction Kinetics on Platinum: Acid vs Alkaline Electrolytes, J. Electrochem. Soc. 157 (2010) B1529. https://doi.org/10.1149/1.3483106.

[91] J.O.M. Bockris, Parameters of Electrode Kinetics, in: Electrochem. Constants, Department of Commerce, Washington, DC, 1953: pp. 243–262. papers2://publication/uuid/4E51C08C-DFE0-4FB4-A86D-72966FDBFE81.

[92] J.O.M. Bockris, R. Parsons, The kinetics of the hydrogen evolution reaction at mercury cathodes, Trans. Faraday Soc. 45 (1949) 917–928.

[93] P. Quaino, F. Juarez, E. Santos, W. Schmickler, Volcano plots in hydrogen electrocatalysis-uses and abuses, Beilstein J. Nanotechnol. 5 (2014) 846–854. https://doi.org/10.3762/bjnano.5.96.

[94] S. Trasatti, Work function, electronegativity, and electrochemical behaviour of metals. III. Electrolytic hydrogen evolution in acid solutions, J. Electroanal. Chem. 39 (1972) 163–184. https://doi.org/10.1016/S0022-0728(72)80485-6.

[95] T. Reier, H.N. Nong, D. Teschner, R. Schlögl, P. Strasser, Electrocatalytic Oxygen Evolution Reaction in Acidic Environments – Reaction Mechanisms and Catalysts, Adv. Energy Mater. 7 (2017). https://doi.org/10.1002/aenm.201601275.

[96] S. Siracusano, V. Baglio, N. Van Dijk, L. Merlo, A.S. Aricò, Enhanced performance and durability of low catalyst loading PEM water electrolyser based on a short-side chain perfluorosulfonic ionomer, Appl. Energy. 192 (2017) 477–489. https://doi.org/10.1016/j.apenergy.2016.09.011.

[97] P. Shirvanian, F. van Berkel, Novel components in Proton Exchange Membrane Water Electrolyzers (PEMWE): Status, challenges and future needs, Electrochem. Commun. 114 (2020) 106704. https://doi.org/10.1016/j.elecom.2020.106704.

[98] J.K. Lee, C. Lee, K.F. Fahy, B. Zhao, J.M. LaManna, E. Baltic, D.L. Jacobson, D.S. Hussey, A. Bazylak, Critical Current Density as a Performance Indicator for Gas-Evolving Electrochemical Devices, Cell Reports Phys. Sci. 1 (2020) 100147. https://doi.org/10.1016/j.xcrp.2020.100147.

[99] Y. Yang, X. Zhou, B. Li, C. Zhang, Recent progress of the gas diffusion layer in proton exchange membrane fuel cells: Material and structure designs of microporous layer, Int. J. Hydrogen Energy. 46 (2021) 4259–4282. https://doi.org/10.1016/j.ijhydene.2020.10.185.

[100] M. Chen, C. Zhao, F. Sun, J. Fan, H. Li, H. Wang, Research progress of catalyst layer and interlayer interface structures in membrane electrode assembly (MEA) for proton exchange membrane fuel cell (PEMFC) system, ETransportation. 5 (2020) 100075. https://doi.org/10.1016/j.etran.2020.100075.

[101] J.O. Majasan, J.I.S. Cho, I. Dedigama, D. Tsaoulidis, P. Shearing, D.J.L. Brett, Two-phase flow behaviour and performance of polymer electrolyte membrane electrolysers: Electrochemical and optical characterisation, Int. J. Hydrogen Energy. 43 (2018) 15659–15672. https://doi.org/10.1016/j.ijhydene.2018.07.003.

[102] M. Maier, J. Dodwell, R. Ziesche, C. Tan, T. Heenan, J. Majasan, N. Kardjilov, H. Markötter, I. Manke, L. Castanheira, G. Hinds, P.R. Shearing, D.J.L. Brett, Mass transport in polymer electrolyte membrane water electrolyser liquid-gas diffusion layers: A combined neutron imaging and X-ray computed tomography study, J. Power Sources. 455 (2020). https://doi.org/10.1016/j.jpowsour.2020.227968.

[103] J.W. Haverkort, H. Rajaei, Electro-osmotic flow and the limiting current in alkaline water electrolysis, J. Power Sources Adv. 6 (2020) 100034. https://doi.org/10.1016/j.powera.2020.100034.

[104] G. Schmidt, M. Suermann, B. Bensmann, R. Hanke-Rauschenbach, I. Neuweiler, Modeling Overpotentials Related to Mass Transport Through Porous Transport Layers of PEM Water Electrolysis Cells, J. Electrochem. Soc. 167 (2020) 114511. https://doi.org/10.1149/1945-7111/aba5d4.

[105] IRENA, Green Hydrogen Cost Reduction: Scaling up Electrolysers to Meet the 1.5^0C Climate Goal, Abu Dhabi, 2020. https://www.irena.org/-/media/Files/IRENA/Agency/Publication/2020/Dec/IRENA_Green_hydrogen_cost_2020.pdf.

[106] G. Kakoulaki, I. Kougias, N. Taylor, F. Dolci, J. Moya, A. Jäger-Waldau, Green hydrogen in Europe – A regional assessment: Substituting existing production with electrolysis powered by renewables, Energy Convers. Manag. 228 (2021). https://doi.org/10.1016/j.enconman.2020.113649.

[107] European Commission, A hydrogen strategy for a climate-neutral Europe, 2020.

[108] L. Bertuccioli, A. Chan, D. Hart, F. Lehner, B. Madden, E. Standen, Development of Water Electrolysis in the European Union, 2014.

[109] K.E. Ayers, E.B. Anderson, C.B. Capuano, B.D. Carter, L.T. Dalton, G. Hanlon, J. Manco, M. Niedzwiecki, Research Advances Towards Low Cost, High Efficiency PEM Electrolysis, ECS Trans. 33 (2010) 3–15.

[110] F. Fouda-Onana, M. Chandesris, V. Médeau, S. Chelghoum, D. Thoby, N. Guillet, Investigation on the degradation of MEAs for PEM water electrolysers part I: Effects of testing conditions on MEA performances and membrane properties, Int. J. Hydrogen Energy. 41 (2016) 16627–16636. https://doi.org/10.1016/j.ijhydene.2016.07.125.

[111] P. Frühwirt, A. Kregar, J.T. Törring, T. Katrašnik, G. Gescheidt, Holistic approach to chemical degradation of Nafion membranes in fuel cells: Modelling and predictions, Phys. Chem. Chem. Phys. 22 (2020) 5647–5666. https://doi.org/10.1039/c9cp04986j.

[112] H. Kim, E. Hwang, H. Park, B.-S. Lee, J.H. Jang, H.J. Kim, S.H. Ahn, S.-K. Kim, Non-precious metal electrocatalysts for hydrogen production in proton exchange membrane water electrolyzer, Appl. Catal. B Environ. 206 (2017) 608–616. https://doi.org/10.1016/j.apcatb.2017.01.074.

[113] S.A. Grigoriev, V.N. Fateev, D.G. Bessarabov, P. Millet, Current status, research trends, and challenges in water electrolysis science and technology, Int. J. Hydrogen Energy. 45 (2020) 26036–26058. https://doi.org/10.1016/j.ijhydene.2020.03.109.

[114] A.E. Samani, A. D'Amicis, J.D.M. de Kooning, P. Silva, L. Vandevelde, Grid balancing with a large-scale electrolyser providing primary reserve, in: IET Conf. Publ., 2019: pp. 1–7. https://doi.org/10.1049/cp.2019.0542.

[115] R. Reissner, A. Soreng, N. Van Dijk, L. Abadia, C. Bourasseau, S. You, C. Traeholt, F. de Jong, M. Pablo, C. Imboden, M. Sprig, QualyGridS - Standardized qualifying tests of electrolysers for grid services, in: Conf. Proc. 6th Eur. PEFC Electrolyser Forum, 2017.

[116] R. Reißner, QualyGridS - Publishable Final report, 2020.

[117] C. Mittelsteadt, T. Norman, M. Rich, J. Willey, PEM Electrolyzers and PEM Regenerative Fuel Cells Industrial View, in: Electrochem. Energy Storage Renew. Sources Grid Balanc., Elsevier B.V., Newton, 2014: pp. 159–181. https://doi.org/10.1016/B978-0-444-62616-5.00011-5.

[118] S.M. Alia, J.E. Soc, S.M. Alia, M. Ha, G.C. Anderson, C. Ngo, S. Pylypenko, R.E. Larsen, The Roles of Oxide Growth and Sub-Surface Facets in Oxygen Evolution Activity of Iridium and Its Impact on Electrolysis, J. Electrochem. Soc. 166 (2019) F1243–F1252. https://doi.org/10.1149/2.0771915jes.

[119] A. Weiß, A. Siebel, M. Bernt, T.-H. Shen, V. Tileli, H.A. Gasteiger, Impact of Intermittent Operation on Lifetime and Performance of a PEM Water Electrolyzer, J. Electrochem. Soc. 166 (2019) F487–F497. https://doi.org/10.1149/2.0421908jes.

[120] P. Pei, Z. Wu, Y. Li, X. Jia, D. Chen, S. Huang, Improved methods to measure hydrogen crossover current in proton exchange membrane fuel cell, Appl. Energy. 215 (2018) 338–347. https://doi.org/10.1016/j.apenergy.2018.02.002.

[121] J. Zhang, Y. Tang, C. Song, J. Zhang, H. Wang, PEM fuel cell open circuit voltage (OCV) in the temperature range of 23 °C to 120 °C, J. Power Sources. 163 (2006) 532–537. https://doi.org/10.1016/j.jpowsour.2006.09.026.

[122] C.Y. Jung, W.J. Kim, S.C. Yi, Computational analysis of mixed potential effect in proton exchange membrane fuel cells, Int. J. Hydrogen Energy. 37 (2012) 7654–7668. https://doi.org/10.1016/j.ijhydene.2012.01.102.

[123] E. Brightman, J. Dodwell, N. Van Dijk, G. Hinds, In situ characterisation of PEM water electrolysers using a novel reference electrode, Electrochem. Commun. 52 (2015) 1–4. https://doi.org/10.1016/j.elecom.2015.01.005.

[124] C. Rakousky, U. Reimer, K. Wippermann, S. Kuhri, M. Carmo, W. Lueke, D. Stolten, Polymer electrolyte membrane water electrolysis : Restraining degradation in the presence of fluctuating power, J. Power Sources. 342 (2017) 38–47. https://doi.org/10.1016/j.jpowsour.2016.11.118.

[125] G. Tsotridis, A. Pilenga, EU Harmonised Terminology for Low Temperature Water Electrolysis for Energy Storage Applications, 2018.

[126] J.J. Caparrós Mancera, F. Segura Manzano, J. Manuel Andújar, F. José Vivas, A. José Calderón, An Optimized Balance of Plant for a Medium-Size PEM Electrolyzer: Design, Control and Physical Implementation, Electronics. 9 (2020). https://doi.org/10.3390/electronics9050871.

[127] K. Bareiß, C. de la Rua, M. Möckl, T. Hamacher, Life cycle assessment of hydrogen from proton exchange membrane water electrolysis in future energy systems,

Appl. Energy. 237 (2019) 862–872. https://doi.org/10.1016/j.apenergy.2019.01.001.

[128] S.A. Grigoriev, P. Millet, S. V. Korobtsev, V.I. Porembskiy, M. Pepic, C. Etievant, C. Puyenchet, V.N. Fateev, Hydrogen safety aspects related to high-pressure polymer electrolyte membrane water electrolysis, Int. J. Hydrogen Energy. 34 (2009) 5986–5991. https://doi.org/10.1016/j.ijhydene.2009.01.047.

[129] B. Lee, K. Park, H.M. Kim, Dynamic simulation of PEM water electrolysis and comparison with experiments, Int. J. Electrochem. Sci. 8 (2013) 235–248.

[130] H.S. Shin, B.S. Oh, Water transport according to temperature and current in PEM water electrolyzer, Int. J. Hydrogen Energy. 45 (2020) 56–63. https://doi.org/10.1016/j.ijhydene.2019.10.209.

[131] T.A. Zawodzinski, C. Derouin, S. Radzinski, R.J. Sherman, V.T. Smith, T.E. Springer, S. Gottesfeld, Water Uptake by and Transport Through Nafion® 117 Membranes, J. Electrochem. Soc. 140 (1993) 1041–1047. https://doi.org/10.1149/1.2056194.

[132] M. Schalenbach, M. Carmo, D.L. Fritz, J. Mergel, D. Stolten, Pressurized PEM water electrolysis: Efficiency and gas crossover, Int. J. Hydrogen Energy. (2013). https://doi.org/10.1016/j.ijhydene.2013.09.013.

[133] S. Sun, Z. Shao, H. Yu, G. Li, B. Yi, Investigations on degradation of the long-term proton exchange membrane water electrolysis stack, J. Power Sources. 267 (2014) 515–520. https://doi.org/10.1016/j.jpowsour.2014.05.117.

[134] M.N. Silberstein, M.C. Boyce, Hygro-thermal mechanical behavior of Nafion during constrained swelling, J. Power Sources. 196 (2011) 3452–3460. https://doi.org/10.1016/j.jpowsour.2010.11.116.

[135] H. Tang, S. Peikang, S.P. Jiang, F. Wang, M. Pan, A degradation study of Nafion proton exchange membrane of PEM fuel cells, J. Power Sources. 170 (2007) 85–92. https://doi.org/10.1016/j.jpowsour.2007.03.061.

[136] B. Kienitz, Optimizing polymer electrolyte membrane thickness to maximize fuel cell vehicle range, Int. J. Hydrogen Energy. 46 (2021) 11176–11182. https://doi.org/10.1016/j.ijhydene.2020.03.126.

[137] X. Yuan, S. Zhang, S. Ban, C. Huang, H. Wang, V. Singara, M. Fowler, M. Schulze, A. Haug, K.A. Friedrich, R. Hiesgen, Degradation of a PEM fuel cell stack with Nafion ® membranes of different thicknesses . Part II : Ex situ diagnosis, J. Power Sources. 205 (2012) 324–334. https://doi.org/10.1016/j.jpowsour.2012.01.074.

[138] M. Inaba, T. Kinumoto, M. Kiriake, R. Umebayashi, A. Tasaka, Z. Ogumi, Gas crossover and membrane degradation in polymer electrolyte fuel cells, 51 (2006) 5746–5753. https://doi.org/10.1016/j.electacta.2006.03.008.

[139] V.A. Sethuraman, J.W. Weidner, A.T. Haug, S. Motupally, L. V. Protsailo, Hydrogen peroxide formation rates in a PEMFC anode and cathode: Effect of humidity and temperature, J. Electrochem. Soc. 155 (2020) B50. https://doi.org/10.1149/1.2801980.

[140] M. Inaba, H. Yamada, J. Tokunaga, A. Tasaka, Effect of Agglomeration of Pt / C Catalyst on Hydrogen Peroxide Formation, Electrochem. Solid-State Lett. 7 (2004) A474–A477. https://doi.org/10.1149/1.1814595.

[141] R. Serra-maia, M. Bellier, S. Chastka, K. Tranhuu, A. Subowo, J.D. Rimstidt, P.M. Usov, A.J. Morris, F.M. Michel, Mechanism and Kinetics of Hydrogen Peroxide Decomposition on Platinum Nanocatalysts, ACS Appl. Mater. Interfaces. 10 (2018) 21224–21234. https://doi.org/10.1021/acsami.8b02345.

[142] V.A. Sethuraman, J.W. Weidner, A.T. Haug, S. Motupally, L. V. Protsailo, Hydrogen Peroxide Formation Rates in a PEMFC Anode and Cathode, J. Electrochem. Soc. 155 (2008) B50. https://doi.org/10.1149/1.2801980.

[143] M. Chandesris, V. Médeau, N. Guillet, S. Chelghoum, D. Thoby, F. Fouda-Onana, Membrane degradation in PEM water electrolyzer: Numerical modeling and experimental evidence of the influence of temperature and current density, Int. J. Hydrogen Energy. 40 (2015) 1353–1366. https://doi.org/10.1016/j.ijhydene.2014.11.111.

[144] S.A. Grigoriev, K.A. Dzhus, D.G. Bessarabov, P. Millet, Failure of PEM water electrolysis cells: Case study involving anode dissolution and membrane thinning, Int. J. Hydrogen Energy. 39 (2014) 20440–20446. https://doi.org/10.1016/j.ijhydene.2014.05.043.

[145] P. Chandran, A. Ghosh, S. Ramaprabhu, High-performance Platinum-free oxygen reduction reaction and hydrogen oxidation reaction catalyst in polymer electrolyte membrane fuel cell, Sci. Rep. 8 (2018) 1–11. https://doi.org/10.1038/s41598-018-22001-9.

[146] S. Stucki, G.G. Scherer, S. Schlagowski, E. Fischer, PEM water electrolysers: Evidence for membrane failure in 100 kW demonstration plants, J. Appl. Electrochem. 28 (1998) 1041–1049. https://doi.org/10.1023/A:1003477305336.

[147] M. Schalenbach, T. Hoefner, P. Paciok, M. Carmo, W. Lueke, D. Stolten, Gas Permeation through Nafion. Part 1: Measurements, J. Phys. Chem. C. 119 (2015) 25145–25155. https://doi.org/10.1021/acs.jpcc.5b04155.

[148] M. Schalenbach, M.A. Hoeh, J.T. Gostick, W. Lueke, D. Stolten, Gas Permeation through Nafion. Part 2: Resistor Network Model, J. Phys. Chem. C. 119 (2015) 25156–25169. https://doi.org/10.1021/acs.jpcc.5b04157.

[149] W.Y. Hsu, T.D. Gierke, Ion transport and clustering in nafion perfluorinated membranes, J. Memb. Sci. 13 (1983) 307–326. https://doi.org/10.1016/S0376-7388(00)81563-X.

[150] K.A. Mauritz, R.B. Moore, State of understanding of Nafion, Chem. Rev. 104 (2004) 4535–4585. https://doi.org/10.1021/cr0207123.

[151] D. Seeliger, C. Hartnig, E. Spohr, Aqueous pore structure and proton dynamics in solvated Nafion membranes, Electrochim. Acta. 50 (2005) 4234–4240. https://doi.org/10.1016/j.electacta.2005.03.071.

[152] D.L. Wise, G. Houghton, The diffusion coefficients of ten slightly soluble gases in

water at 10-60°C, Chem. Eng. Sci. 21 (1966) 999–1010. https://doi.org/10.1016/0009-2509(66)85096-0.

[153] S.A. Vilekar, R. Datta, The effect of hydrogen crossover on open-circuit voltage in polymer electrolyte membrane fuel cells, J. Power Sources. (2010). https://doi.org/10.1016/j.jpowsour.2009.10.023.

[154] T. Nakagawa, C.A. Beasley, R.W. Murray, Efficient electro-oxidation of water near its Reversible potential by a mesoporous IrO x nanoparticle film, J. Phys. Chem. C. 113 (2009) 12958–12961. https://doi.org/10.1021/jp9060076.

[155] T. Reier, M. Oezaslan, P. Strasser, Electrocatalytic oxygen evolution reaction (OER) on Ru, Ir, and pt catalysts: A comparative study of nanoparticles and bulk materials, ACS Catal. 2 (2012) 1765–1772. https://doi.org/10.1021/cs3003098.

[156] N. Yoshinaga, W. Sugimoto, Y. Takasu, Oxygen reduction behavior of rutile-type iridium oxide in sulfuric acid solution, Electrochim. Acta. 54 (2008) 566–573. https://doi.org/10.1016/j.electacta.2008.07.020.

[157] A.M. Gómez-Marín, J.M. Feliu, E. Ticianelli, Oxygen Reduction on Platinum Surfaces in Acid Media: Experimental Evidence of a CECE/DISP Initial Reaction Path, ACS Catal. 9 (2019) 2238–2251. https://doi.org/10.1021/acscatal.8b03351.

[158] J.C.F. Boodts, S. Trasatti, Hydrogen evolution on iridium oxide cathodes, J. Appl. Electrochem. 19 (1989) 255–262. https://doi.org/10.1007/BF01062309.

[159] J.X. Wang, T.E. Springer, P. Liu, M. Shao, R.R. Adzic, Hydrogen oxidation reaction on Pt in acidic media: Adsorption isotherm and activation free energies, J. Phys. Chem. C. 111 (2007) 12425–12433. https://doi.org/10.1021/jp073400i.

[160] P. Jovanovič, N. Hodnik, F. Ruiz-Zepeda, I. Arčon, B. Jozinović, M. Zorko, M. Bele, M. Šala, V.S. Šelih, S. Hočevar, M. Gaberšček, Electrochemical Dissolution of Iridium and Iridium Oxide Particles in Acidic Media: Transmission Electron Microscopy, Electrochemical Flow Cell Coupled to Inductively Coupled Plasma Mass Spectrometry, and X-ray Absorption Spectroscopy Study, J. Am. Chem. Soc. 139 (2017) 12837–12846. https://doi.org/10.1021/jacs.7b08071.

[161] S. Ardizzone, A. Carugati, S. Trasatti, Properties of thermally prepared iridium dioxide, J. Electroanal. Chem. 126 (1981) 287–292.

[162] S. Cherevko, G.P. Keeley, S. Geiger, A.R. Zeradjanin, N. Hodnik, N. Kulyk, K.J.J. Mayrhofer, Dissolution of Platinum in the Operational Range of Fuel Cells, ChemElectroChem. 2 (2015) 1471–1478. https://doi.org/10.1002/celc.201500098.

[163] S. Cherevko, S. Geiger, O. Kasian, A. Mingers, K.J.J. Mayrhofer, Oxygen evolution activity and stability of iridium in acidic media. Part 2. - Electrochemically grown hydrous iridium oxide, J. Electroanal. Chem. 774 (2016) 102–110. https://doi.org/10.1016/j.jelechem.2016.05.015.

[164] L. Castanheira, W.O. Silva, F.H.B. Lima, A. Crisci, L. Dubau, F. Maillard, Carbon Corrosion in Proton-Exchange Membrane Fuel Cells: Effect of the Carbon Structure, the Degradation Protocol, and the Gas Atmosphere, ACS Catal. 5 (2015)

2184–2194. https://doi.org/10.1021/cs501973j.

[165] A. Marcu, G. Toth, P. Pietrasz, J. Waldecker, Cathode catalysts degradation mechanism from liquid electrolyte to membrane electrode assembly, Comptes Rendus Chim. 17 (2014) 752–759. https://doi.org/10.1016/j.crci.2013.09.008.

[166] S. Maass, F. Finsterwalder, G. Frank, R. Hartmann, C. Merten, Carbon support oxidation in PEM fuel cell cathodes, J. Power Sources. 176 (2008) 444–451. https://doi.org/10.1016/j.jpowsour.2007.08.053.

[167] B. Seger, K. Vinodgopal, P. V. Kamat, Proton activity in Nafion films: Probing exchangeable protons with methylene blue, Langmuir. 23 (2007) 5471–5476. https://doi.org/10.1021/la0636816.

[168] M. Umeda, K. Sayama, T. Maruta, M. Inoue, Proton activity of Nafion 117 membrane measured from potential difference of hydrogen electrodes, Ionics (Kiel). 19 (2013) 623–627. https://doi.org/10.1007/s11581-012-0791-z.

[169] E. Brightman, D. Pasquier, Measurement and adjustment of proton activity in solid polymer electrolytes, Electrochem. Commun. 82 (2017) 145–149. https://doi.org/10.1016/j.elecom.2017.08.005.

[170] R.G. González-Huerta, G. Ramos-Sánchez, P.B. Balbuena, Oxygen evolution in Co-doped RuO2and IrO2: Experimental and theoretical insights to diminish electrolysis overpotential, J. Power Sources. 268 (2014) 69–76. https://doi.org/10.1016/j.jpowsour.2014.06.029.

[171] O.T. Holton, J.W. Stevenson, The Role of Platinum in Proton Exchange Membrane Fuel Cells, Platin. Met. Rev. 57 (2013) 259–271. https://doi.org/10.1595/147106713X671222.

[172] U. Babic, M. Suermann, F.N. Büchi, L. Gubler, T.J. Schmidt, Review—Identifying Critical Gaps for Polymer Electrolyte Water Electrolysis Development, J. Electrochem. Soc. 164 (2017) F387–F399. https://doi.org/10.1149/2.1441704jes.

[173] N. Mamaca, E. Mayousse, S. Arrii-Clacens, T.W. Napporn, K. Servat, N. Guillet, K.B. Kokoh, Electrochemical activity of ruthenium and iridium based catalysts for oxygen evolution reaction, Appl. Catal. B Environ. 111–112 (2012) 376–380. https://doi.org/10.1016/j.apcatb.2011.10.020.

[174] R. Patel, J.T. Park, M. Patel, J.K. Dash, E.B. Gowd, R. Karpoormath, A. Mishra, J. Kwak, J.H. Kim, Transition-metal-based layered double hydroxides tailored for energy conversion and storage, J. Mater. Chem. A. 6 (2017) 12–29. https://doi.org/10.1039/c7ta09370e.

[175] S. Cherevko, S. Geiger, O. Kasian, N. Kulyk, J.P. Grote, A. Savan, B.R. Shrestha, S. Merzlikin, B. Breitbach, A. Ludwig, K.J.J. Mayrhofer, Oxygen and hydrogen evolution reactions on Ru, RuO2, Ir, and IrO2 thin film electrodes in acidic and alkaline electrolytes: A comparative study on activity and stability, Catal. Today. 262 (2016) 170–180. https://doi.org/10.1016/j.cattod.2015.08.014.

[176] V.A. Saveleva, L. Wang, W. Luo, S. Zafeiratos, C. Ulhaq-Bouillet, A.S. Gago, K.A. Friedrich, E.R. Savinova, Uncovering the Stabilization Mechanism in Bimetallic

Ruthenium-Iridium Anodes for Proton Exchange Membrane Electrolyzers, J. Phys. Chem. Lett. 7 (2016) 3240–3245. https://doi.org/10.1021/acs.jpclett.6b01500.

[177] R. Kötz, S. Stucki, D. Scherson, D.M. Kolb, In-situ identification of RuO4 as the corrosion product during oxygen evolution on ruthenium in acid media, J. Electroanal. Chem. 172 (1984) 211–219. https://doi.org/10.1016/0022-0728(84)80187-4.

[178] A. Reksten, F. Moradi, F. Seland, S. Sunde, Iridium-Ruthenium Mixed Oxides for Oxygen Evolution Reaction Prepared by Pechini Synthesis, ECS Trans. 58 (2014) 39–50. https://doi.org/10.1149/05825.0039ecst.

[179] T. Audichon, E. Mayousse, S. Morisset, C. Morais, C. Comminges, T.W. Napporn, K.B. Kokoh, Electroactivity of RuO2-IrO2 mixed nanocatalysts toward the oxygen evolution reaction in a water electrolyzer supplied by a solar profile, Int. J. Hydrogen Energy. 39 (2014) 16785–16796. https://doi.org/10.1016/j.ijhydene.2014.07.170.

[180] O. Kasian, S. Geiger, P. Stock, G. Polymeros, B. Breitbach, A. Savan, A. Ludwig, S. Cherevko, K.J.J. Mayrhofer, On the Origin of the Improved Ruthenium Stability in RuO2 –IrO2 Mixed Oxides, J. Electrochem. Soc. 163 (2016) F3099–F3104. https://doi.org/10.1149/2.0131611jes.

[181] L. Wang, V.A. Saveleva, S. Zafeiratos, E.R. Savinova, P. Lettenmeier, P. Gazdzicki, A.S. Gago, K.A. Friedrich, Highly active anode electrocatalysts derived from electrochemical leaching of Ru from metallic Ir0.7Ru0.3for proton exchange membrane electrolyzers, Nano Energy. 34 (2017) 385–391. https://doi.org/10.1016/j.nanoen.2017.02.045.

[182] S. Geiger, O. Kasian, B.R. Shrestha, A.M. Mingers, K.J.J. Mayrhofer, S. Cherevko, Activity and Stability of Electrochemically and Thermally Treated Iridium for the Oxygen Evolution Reaction, J. Electrochem. Soc. 163 (2016) F3132–F3138. https://doi.org/10.1149/2.0181611jes.

[183] K. Kadakia, M.K. Datta, O.I. Velikokhatnyi, P. Jampani, S.K. Park, P. Saha, J.A. Poston, A. Manivannan, P.N. Kumta, Novel (Ir,Sn,Nb)O2anode electrocatalysts with reduced noble metal content for PEM based water electrolysis, Int. J. Hydrogen Energy. 37 (2012) 3001–3013. https://doi.org/10.1016/j.ijhydene.2011.11.055.

[184] M.K. Datta, K. Kadakia, O.I. Velikokhatnyi, P.H. Jampani, S.J. Chung, J.A. Poston, A. Manivannan, P.N. Kumta, High performance robust F-doped tin oxide based oxygen evolution electro-catalysts for PEM based water electrolysis, J. Mater. Chem. A. 1 (2013) 4026–4037. https://doi.org/10.1039/c3ta01458d.

[185] K.S. Kadakia, P.H. Jampani, O.I. Velikokhatnyi, M.K. Datta, P. Patel, S.J. Chung, S.K. Park, J.A. Poston, A. Manivannan, P.N. Kumta, Study of fluorine doped (Nb,Ir)O2solid solution electro-catalyst powders for proton exchange membrane based oxygen evolution reaction, Mater. Sci. Eng. B Solid-State Mater. Adv. Technol. 212 (2016) 101–108. https://doi.org/10.1016/j.mseb.2016.06.015.

[186] K. Kadakia, M.K. Datta, O.I. Velikokhatnyi, P.H. Jampani, P.N. Kumta, Fluorine

doped (Ir,Sn,Nb)O2anode electro-catalyst for oxygen evolution via PEM based water electrolysis, Int. J. Hydrogen Energy. 39 (2014) 664–674. https://doi.org/10.1016/j.ijhydene.2013.10.123.

[187] J. Polonsky, M. Paidar, K. Bouzek, P. Mazu, P. Mazúr, J. Polonský, M. Paidar, K. Bouzek, Non-conductive TiO2 as the anode catalyst support for PEM water electrolysis, Int. J. Hydrogen Energy. 37 (2012) 12081–12088. https://doi.org/10.1016/j.ijhydene.2012.05.129.

[188] C. Rozain, E. Mayousse, N. Guillet, P. Millet, Influence of iridium oxide loadings on the performance of PEM water electrolysis cells: Part I-Pure IrO2-based anodes, Appl. Catal. B Environ. 182 (2016) 153–160. https://doi.org/10.1016/j.apcatb.2015.09.013.

[189] C. Rozain, E. Mayousse, N. Guillet, P. Millet, Influence of iridium oxide loadings on the performance of PEM water electrolysis cells: Part II - Advanced oxygen electrodes, Appl. Catal. B Environ. 182 (2016) 123–131. https://doi.org/10.1016/j.apcatb.2015.09.011.

[190] K.B. Kokoh, E. Mayousse, T.W. Napporn, K. Servat, N. Guillet, E. Soyez, A. Grosjean, A. Rakotondrainibé, J. Paul-Joseph, Efficient multi-metallic anode catalysts in a PEM water electrolyzer, Int. J. Hydrogen Energy. 39 (2014) 1924–1931. https://doi.org/10.1016/j.ijhydene.2013.11.076.

[191] A. Minguzzi, O. Lugaresi, E. Achilli, C. Locatelli, A. Vertova, P. Ghigna, S. Rondinini, Observing the oxidation state turnover in heterogeneous iridium-based water oxidation catalysts, Chem. Sci. 5 (2014) 3591–3597. https://doi.org/10.1039/c4sc00975d.

[192] Z. Ma, Y. Zhang, S. Liu, W. Xu, L. Wu, Y.C. Hsieh, P. Liu, Y. Zhu, K. Sasaki, J.N. Renner, K.E. Ayers, R.R. Adzic, J.X. Wang, Reaction mechanism for oxygen evolution on RuO2, IrO2, and RuO2@IrO2core-shell nanocatalysts, J. Electroanal. Chem. 819 (2018) 296–305. https://doi.org/10.1016/j.jelechem.2017.10.062.

[193] C.C.L. McCrory, S. Jung, I.M. Ferrer, S.M. Chatman, J.C. Peters, T.F. Jaramillo, Benchmarking Hydrogen Evolving Reaction and Oxygen Evolving Reaction Electrocatalysts for Solar Water Splitting Devices, J. Am. Chem. Soc. 137 (2015) 4347–4357. https://doi.org/10.1021/ja510442p.

[194] J.H. Kim, J. Kim, H. Kim, J. Kim, S.H. Ahn, Facile fabrication of nanostructured NiMo cathode for high-performance proton exchange membrane water electrolyzer, J. Ind. Eng. Chem. (2019). https://doi.org/10.1016/j.jiec.2019.06.049.

[195] G.H. Han, H. Kim, J. Kim, J. Kim, S.Y. Kim, S.H. Ahn, Micro-nanoporous MoO2@CoMo heterostructure catalyst for hydrogen evolution reaction, Appl. Catal. B Environ. 270 (2020) 118895. https://doi.org/10.1016/j.apcatb.2020.118895.

[196] D. Wang, H. Li, N. Du, W. Hou, Amorphous molybdenum sulfide monolayer nanosheets for highly efficient electrocatalytic hydrogen evolution, Chem. Eng. J. 398 (2020). https://doi.org/10.1016/j.cej.2020.125685.

[197] T. Corrales-Sánchez, J. Ampurdanés, A. Urakawa, MoS2-based materials as alternative cathode catalyst for PEM electrolysis, Int. J. Hydrogen Energy. 39 (2014) 20837–20843. https://doi.org/10.1016/j.ijhydene.2014.08.078.

[198] P.K.R. Holzapfel, M. Bühler, D. Escalera-López, M. Bierling, F.D. Speck, K.J.J. Mayrhofer, S. Cherevko, C. V. Pham, S. Thiele, Fabrication of a Robust PEM Water Electrolyzer Based on Non-Noble Metal Cathode Catalyst: [Mo3S13]2− Clusters Anchored to N-Doped Carbon Nanotubes, Small. 16 (2020) 1–10. https://doi.org/10.1002/smll.202003161.

[199] J.W.D. Ng, T.R. Hellstern, J. Kibsgaard, A.C. Hinckley, J.D. Benck, T.F. Jaramillo, Polymer Electrolyte Membrane Electrolyzers Utilizing Non-precious Mo-based Hydrogen Evolution Catalysts, ChemSusChem. 8 (2015) 3512–3519. https://doi.org/10.1002/cssc.201500334.

[200] S.U.B. Ramakrishna, D. Srinivasulu Reddy, S. Shiva Kumar, V. Himabindu, Nitrogen doped CNTs supported Palladium electrocatalyst for hydrogen evolution reaction in PEM water electrolyser, Int. J. Hydrogen Energy. 41 (2016) 20447–20454. https://doi.org/10.1016/j.ijhydene.2016.08.195.

[201] J.H. Koh, R. Abbaraju, P. Parthasarathy, A. V. Virkar, Design and synthesis of degradation-resistant core-shell catalysts for proton exchange membrane fuel cells, J. Power Sources. 261 (2014) 271–277. https://doi.org/10.1016/j.jpowsour.2014.03.102.

[202] N.V. Long, M. Ohtaki, T.D. Hien, J. Randy, M. Nogami, A comparative study of Pt and Pt-Pd core-shell nanocatalysts, Electrochim. Acta. 56 (2011) 9133–9143. https://doi.org/10.1016/j.electacta.2011.07.090.

[203] B.G. Pollet, S.S. Kocha, I. Staffell, Current status of automotive fuel cells for sustainable transport, Curr. Opin. Electrochem. 16 (2019) 90–95. https://doi.org/10.1016/j.coelec.2019.04.021.

[204] K. Videm, S. Lamolle, M. Monjo, J.E. Ellingsen, S.P. Lyngstadaas, H.J. Haugen, Hydride formation on titanium surfaces by cathodic polarization, Appl. Surf. Sci. 255 (2008) 3011–3015. https://doi.org/10.1016/j.apsusc.2008.08.090.

[205] Y. Shao-Horn, W.C. Sheng, S. Chen, P.J. Ferreira, E.F. Holby, D. Morgan, Instability of supported platinum nanoparticles in low-temperature fuel cells, Top. Catal. 46 (2007) 285–305. https://doi.org/10.1007/s11244-007-9000-0.

[206] P. Parthasarathy, A. V. Virkar, Electrochemical Ostwald ripening of Pt and Ag catalysts supported on carbon, J. Power Sources. 234 (2013) 82–90. https://doi.org/10.1016/j.jpowsour.2013.01.115.

[207] R. Sharma, S. Gyergyek, Q. Li, S.M. Andersen, Evolution of the degradation mechanisms with the number of stress cycles during an accelerated stress test of carbon supported platinum nanoparticles, J. Electroanal. Chem. 838 (2019) 82–88. https://doi.org/10.1016/j.jelechem.2019.02.052.

[208] A. Zana, J. Speder, M. Roefzaad, L. Altmann, M. Bäumer, M. Arenz, Probing Degradation by IL-TEM: The Influence of Stress Test Conditions on the

Degradation Mechanism, J. Electrochem. Soc. 160 (2013) F608–F615. https://doi.org/10.1149/2.078306jes.

[209] Z. Siroma, K. Ishii, K. Yasuda, M. Inaba, A. Tasaka, Stability of platinum particles on a carbon substrate investigated by atomic force microscopy and scanning electron microscopy, J. Power Sources. 171 (2007) 524–529. https://doi.org/10.1016/j.jpowsour.2007.06.016.

[210] L. Castanheira, L. Dubau, M. Mermoux, G. Berthomé, N. Caqué, E. Rossinot, M. Chatenet, F. Maillard, Carbon corrosion in proton-exchange membrane fuel cells: From model experiments to real-life operation in membrane electrode assemblies, ACS Catal. 4 (2014) 2258–2267. https://doi.org/10.1021/cs500449q.

[211] L.M. Roen, C.H. Paik, T.D. Jarvi, Electrocatalytic Corrosion of Carbon Support in PEMFC Cathodes, Electrochem. Solid-State Lett. 7 (2004) A19–A22. https://doi.org/10.1149/1.1630412.

[212] K. Yasuda, A. Taniguchi, T. Akita, T. Ioroi, Z. Siroma, Platinum dissolution and deposition in the polymer electrolyte membrane of a PEM fuel cell as studied by potential cycling, Phys. Chem. Chem. Phys. 8 (2006) 746–752. https://doi.org/10.1039/b514342j.

[213] S.O. Klemm, A.A. Topalov, C.A. Laska, K.J.J. Mayrhofer, Coupling of a high throughput microelectrochemical cell with online multielemental trace analysis by ICP-MS, Electrochem. Commun. 13 (2011) 1533–1535. https://doi.org/10.1016/j.elecom.2011.10.017.

[214] O. Kasian, S. Geiger, K.J.J. Mayrhofer, S. Cherevko, Electrochemical On-line ICP-MS in Electrocatalysis Research, Chem. Rec. 19 (2019) 2130–2142. https://doi.org/10.1002/tcr.201800162.

[215] S. Cherevko, A.R. Zeradjanin, A.A. Topalov, N. Kulyk, I. Katsounaros, K.J.J. Mayrhofer, Dissolution of noble metals during oxygen evolution in acidic media, ChemCatChem. 6 (2014) 2219–2223. https://doi.org/10.1002/cctc.201402194.

[216] S. Cherevko, Stability and dissolution of electrocatalysts : Building the bridge between model and " real world " systems, Curr. Opin. Electrochem. (2018) 1–8. https://doi.org/10.1016/j.coelec.2018.03.034.

[217] D. Göhl, A.M. Mingers, S. Geiger, M. Schalenbach, S. Cherevko, J. Knossalla, D. Jalalpoor, F. Schüth, K.J.J. Mayrhofer, M. Ledendecker, Electrochemical stability of hexagonal tungsten carbide in the potential window of fuel cells and water electrolyzers investigated in a half-cell configuration, Electrochim. Acta. 270 (2018) 70–76. https://doi.org/10.1016/j.electacta.2018.02.129.

[218] S. Cherevko, N. Kulyk, K.J.J. Mayrhofer, Durability of platinum-based fuel cell electrocatalysts: Dissolution of bulk and nanoscale platinum, Nano Energy. 29 (2016) 275–298. https://doi.org/10.1016/j.nanoen.2016.03.005.

[219] A.A. Topalov, I. Katsounaros, M. Auinger, S. Cherevko, J.C. Meier, S.O. Klemm, K.J.J.J. Mayrhofer, Dissolution of Platinum: Limits for the Deployment of Electrochemical Energy Conversion ? Angewandte, Angew. Chemie - Int. Ed. 51

(2012) 12613–12615. https://doi.org/10.1002/anie.201207256.

[220] A. Pavlišič, P. Jovanovič, V.S. Šelih, M. Šala, N. Hodnik, M. Gaberšček, Platinum Dissolution and Redeposition from Pt/C Fuel Cell Electrocatalyst at Potential Cycling, J. Electrochem. Soc. 165 (2018) F3161–F3165. https://doi.org/10.1149/2.0191806jes.

[221] A.A. Topalov, S. Cherevko, A.R. Zeradjanin, J.C. Meier, I. Katsounaros, K.J.J. Mayrhofer, Towards a comprehensive understanding of platinum dissolution in acidic media, Chem. Sci. 5 (2014) 631–638. https://doi.org/10.1039/C3SC52411F.

[222] S. Cherevko, T. Reier, A.R. Zeradjanin, Z. Pawolek, P. Strasser, K.J.J. Mayrhofer, Stability of nanostructured iridium oxide electrocatalysts during oxygen evolution reaction in acidic environment, Electrochem. Commun. 48 (2014) 81–85. https://doi.org/10.1016/j.elecom.2014.08.027.

[223] S. Geiger, S. Cherevko, K.J.J. Mayrhofer, Dissolution of Platinum in Presence of Chloride Traces, Electrochim. Acta. 179 (2015) 24–31. https://doi.org/10.1016/j.electacta.2015.03.059.

[224] O. Kasian, S. Geiger, T. Li, J.P. Grote, K. Schweinar, S. Zhang, C. Scheu, D. Raabe, S. Cherevko, B. Gault, K.J.J. Mayrhofer, Degradation of iridium oxides via oxygen evolution from the lattice: Correlating atomic scale structure with reaction mechanisms, Energy Environ. Sci. 12 (2019) 3548–3555. https://doi.org/10.1039/c9ee01872g.

[225] S. Cherevko, S. Geiger, O. Kasian, A. Mingers, K.J.J. Mayrhofer, Oxygen evolution activity and stability of iridium in acidic media. Part 1. - Metallic iridium, J. Electroanal. Chem. 773 (2016) 69–78. https://doi.org/10.1016/j.jelechem.2016.04.033.

[226] O. Kasian, J.P. Grote, S. Geiger, S. Cherevko, K.J.J. Mayrhofer, The Common Intermediates of Oxygen Evolution and Dissolution Reactions during Water Electrolysis on Iridium, Angew. Chemie - Int. Ed. 57 (2018) 2488–2491. https://doi.org/10.1002/anie.201709652.

[227] W. Xu, K. Scott, The effects of ionomer content on PEM water electrolyser membrane electrode assembly performance, Int. J. Hydrogen Energy. 35 (2010) 12029–12037. https://doi.org/10.1016/j.ijhydene.2010.08.055.

[228] A. Papaderakis, D. Tsiplakides, S. Balomenou, S. Sotiropoulos, Electrochemical impedance studies of IrO2 catalysts for oxygen evolution, J. Electroanal. Chem. 757 (2015) 216–224. https://doi.org/10.1016/j.jelechem.2015.09.033.

[229] B.Y. Chang, Conversion of a constant phase element to an equivalent capacitor, J. Electrochem. Sci. Technol. 11 (2020) 318–321. https://doi.org/10.33961/jecst.2020.00815.

[230] C. Locatelli, Sequential Voltammetric Determination of Ultratrace Osmium, Ruthenium and Iridium. Application to Superficial Water, Electroanalysis. 23 (2011) 1329–1336. https://doi.org/10.1002/elan.201100043.

[231] D. Bessarabov, G. Human, A.J. Kruger, S. Chiuta, P.M. Modisha, S.P. du Preez, S.P.

Oelofse, I. Vincent, J. Van Der Merwe, H.W. Langmi, J. Ren, N.M. Musyoka, South African hydrogen infrastructure (HySA infrastructure) for fuel cells and energy storage: Overview of a projects portfolio, Int. J. Hydrogen Energy. 42 (2017) 13568–13588. https://doi.org/10.1016/j.ijhydene.2016.12.140.

[232] I. Dedigama, P. Angeli, N. Van Dijk, J. Millichamp, D. Tsaoulidis, P.R. Shearing, D.J.L. Brett, Current density mapping and optical flow visualisation of a polymer electrolyte membrane water electrolyser, J. Power Sources. 265 (2014) 97–103. https://doi.org/10.1016/j.jpowsour.2014.04.120.

[233] S. Sun, Y. Xiao, D. Liang, Z. Shao, H. Yu, M. Hou, B. Yi, Behaviors of a proton exchange membrane electrolyzer under water starvation, RSC Adv. 5 (2015) 14506–14513. https://doi.org/10.1039/c4ra14104k.

[234] S. Al Shakhshir, F. Zhou, S.K. Kær, On the Effect of Bipolar Plate Mechanical Properties on the Current Distribution of Proton Exchange Membrane Water Electrolysis, ECS Trans. 86 (2018) 683–693. https://doi.org/10.1149/08613.0683ecst.

[235] G. Hinds, E. Brightman, In situ mapping of electrode potential in a PEM fuel cell, Electrochem. Commun. 17 (2012) 26–29. https://doi.org/10.1016/j.elecom.2012.01.007.

[236] G. Liu, X. Li, H. Wang, X. Liu, M. Chen, J.Y. Woo, J.Y. Kim, X. Wang, J.K. Lee, Design of 3-electrode system for in situ monitoring direct methanol fuel cells during long-time running test at high temperature, Appl. Energy. 197 (2017) 163–168. https://doi.org/10.1016/j.apenergy.2017.04.016.

[237] H. Finklea, X. Chen, K. Gerdes, S. Pakalapati, I. Celik, Analysis of SOFCs Using Reference Electrodes, J. Electrochem. Soc. 160 (2013) F1055–F1066. https://doi.org/10.1149/2.093309jes.

[238] G.J. Offer, P. Shearing, J.I. Golbert, D.J.L. Brett, A. Atkinson, N.P. Brandon, Using electrochemical impedance spectroscopy to compensate for errors when measuring polarisation curves during three-electrode measurements of solid oxide fuel cell electrodes, Electrochim. Acta. 53 (2008) 7614–7621. https://doi.org/10.1016/j.electacta.2008.04.001.

[239] J. Rossmeisl, Z.W. Qu, H. Zhu, G.J. Kroes, J.K. Nørskov, Electrolysis of water on oxide surfaces, J. Electroanal. Chem. 607 (2007) 83–89. https://doi.org/10.1016/j.jelechem.2006.11.008.

[240] L. Böhm, J. Näther, M. Underberg, N. Kazamer, L. Holtkotte, U. Rost, G. Marginean, F. Wirkert, M. Brodmann, T. Hülser, F. Köster, Pulsed electrodeposition of iridium catalyst nanoparticles on titanium suboxide supports for application in PEM electrolysis, Mater. Today Proc. 45 (2021) 4254–4259. https://doi.org/10.1016/j.matpr.2020.12.507.

[241] R.F. Savinell, R.L. Zeller, J.A. Adams, Electrochemically Active Surface Area : Voltammetric Charge Correlations for Ruthenium and Iridium Dioxide Electrodes, J. Electrochem. Soc. 137 (1990) 489–494. https://doi.org/10.1149/1.2086468.

[242] T. Pajkossy, D.M. Kolb, Double layer capacitance of the platinum group metals in the double layer region, Electrochem. Commun. 9 (2007) 1171–1174. https://doi.org/10.1016/j.elecom.2007.01.002.

[243] E. Fabbri, A. Habereder, K. Waltar, R. Kötz, T.J. Schmidt, Developments and perspectives of oxide-based catalysts for the oxygen evolution reaction, Catal. Sci. Technol. 4 (2014) 3800–3821. https://doi.org/10.1039/c4cy00669k.

[244] H. Dau, C. Limberg, T. Reier, M. Risch, S. Roggan, P. Strasser, The Mechanism of Water Oxidation: From Electrolysis via Homogeneous to Biological Catalysis, ChemCatChem. 2 (2010) 724–761. https://doi.org/10.1002/cctc.201000126.

[245] M. Busch, Water oxidation: From mechanisms to limitations, Curr. Opin. Electrochem. 9 (2018) 278–284. https://doi.org/10.1016/j.coelec.2018.06.007.

[246] H. Ito, T. Maeda, A. Nakano, H. Takenaka, Properties of Nafion membranes under PEM water electrolysis conditions, Int. J. Hydrogen Energy. 36 (2011) 10527–10540. https://doi.org/10.1016/j.ijhydene.2011.05.127.

[247] G. Karimi, X. Li, Electroosmotic flow through polymer electrolyte membranes in PEM fuel cells, J. Power Sources. 140 (2005) 1–11. https://doi.org/10.1016/j.jpowsour.2004.08.018.

[248] K. Onda, T. Murakami, T. Hikosaka, M. Kobayashi, R. Notu, K. Ito, Performance Analysis of Polymer-Electrolyte Water Electrolysis Cell at a Small-Unit Test Cell and Performance Prediction of Large Stacked Cell, J. Electrochem. Soc. 149 (2002) A1069. https://doi.org/10.1149/1.1492287.

[249] S. Ge, B. Yi, P. Ming, Experimental Determination of Electro-Osmotic Drag Coefficient in Nafion Membrane for Fuel Cells, J. Electrochem. Soc. 153 (2006) A1443. https://doi.org/10.1149/1.2203934.

[250] G. Xie, T. Okada, Water Transport Behavior in Nafion 117 Membranes, J. Electrochem. Soc. 142 (1995) 3057–3062. https://doi.org/10.1149/1.2048686.

[251] R. Hanke-Rauschenbach, B. Bensmann, P. Millet, Hydrogen production using high-pressure electrolyzers, Elsevier Ltd, 2015. https://doi.org/10.1016/B978-1-78242-361-4.00007-8.

[252] R. Sander, Compilation of Henry's law constants (version 4.0) for water as solvent, Atmos. Chem. Phys. 15 (2015) 4399–4981. https://doi.org/10.5194/acp-15-4399-2015.

[253] Z. Zhao, L. Castanheira, L. Dubau, G. Berthomé, A. Crisci, F. Maillard, Carbon corrosion and platinum nanoparticles ripening under open circuit potential conditions, J. Power Sources. 230 (2013) 236–243. https://doi.org/10.1016/j.jpowsour.2012.12.053.

[254] J. Knöppel, M. Möckl, Z. Bayern, D. Escalera-López, K. Stojanovski, M. Bierling, T. Böhm, S. Thiele, M. Rzepka, On the limitations in assessing stability of oxygen evolution catalysts using aqueous model electrochemical cells, Nat. Commun. (2020) 1–18. https://doi.org/10.1038/s41467-021-22296-9.

[255] Z. Zhao, H. Freiser, Differential Pulse Polarographic Determination of Trace Levels of Platinum, Anal. Chem. 58 (1986) 1498–1501. https://doi.org/10.1021/ac00298a050.

[256] K. Hoppstock, F. Alt, K. Cammann, G. Weber, Determination of platinum in biotic and environmental materials part II: A sensitive voltammetric method, Fresenius Z Anal. Chemie. 335 (1989) 813–816. https://doi.org/10.1007/BF01204094.

[257] C.M.G. Van Den Berg, G.S. Jacinto, The determination of platinum in sea water by adsorptive cathodic stripping voltammetry, Anal. Chim. Acta. 211 (1988) 129–139. https://doi.org/10.1016/S0003-2670(00)83675-2.

[258] Metrohm, Application Bulletin 220/4 e- Determination of platinum and rhodium in the ultratrace range by adsorptive stripping voltammetry, 2000.

[259] R. Komendova, Recent advances in the preconcentration and determination of platinum group metals in environmental and biological samples, Trends Anal. Chem. 122 (2020) 115708. https://doi.org/10.1016/j.trac.2019.115708.

[260] S. Zimmermann, C.M. Menzel, Z. Berner, J.D. Eckhardt, D. Stüben, F. Alt, J. Messerschmidt, H. Taraschewski, B. Sures, Trace analysis of platinum in biological samples: A comparison between sector field ICP-MS and adsorptive cathodic stripping voltammetry following different digestion procedures, Anal. Chim. Acta. 439 (2001) 203–209. https://doi.org/10.1016/S0003-2670(01)01041-8.

[261] Q. Feng, X.-Z. Yuan, G. Liu, B. Wei, Z. Zhang, H. Li, H. Wang, A review of proton exchange membrane water electrolysis on degradation mechanisms and mitigation strategies, J. Power Sources. 366 (2017) 33–55. https://doi.org/10.1016/j.jpowsour.2017.09.006.

[262] O. Diaz-Morales, T.J.P. Hersbach, C. Badan, A.C. Garcia, M.T.M. Koper, Hydrogen adsorption on nano-structured platinum electrodes, Faraday Discuss. 210 (2018) 301–315. https://doi.org/10.1039/c8fd00062j.

[263] R.M. Darling, J.P. Meyers, Kinetic Model of Platinum Dissolution in PEMFCs, J. Electrochem. Soc. 150 (2003) A1523–A1527. https://doi.org/10.1149/1.1613669.

[264] K. Sasaki, M. Shao, R. Adzic, Dissolution and stabilization of platinum in oxygen cathodes, in: Polym. Electrolyte Fuel Cell Durab., Springer, 2009: pp. 7–27. https://doi.org/10.1007/978-0-387-85536-3_2.

[265] A.P. Yadav, T. Okayasu, Y. Sugawara, A. Nishikata, T. Tsuru, Effects of pH on Dissolution and Surface Area Loss of Platinum Due to Potential Cycling, J. Electrochem. Soc. 159 (2012) C190–C194. https://doi.org/10.1149/2.065204jes.

[266] J. Zhang, B.A. Litteer, W. Gu, H. Liu, H.A. Gasteiger, Effect of Hydrogen and Oxygen Partial Pressure on Pt Precipitation within the Membrane of PEMFCs, J. Electrochem. Soc. 154 (2007) B1006. https://doi.org/10.1149/1.2764240.

[267] A. Kongkanand, J.M. Ziegelbauer, Surface platinum electrooxidation in the presence of oxygen, J. Phys. Chem. C. 116 (2012) 3684–3693. https://doi.org/10.1021/jp211490a.

[268] S. Mitsushima, Y. Koizumi, S. Uzuka, K.I. Ota, Dissolution of platinum in acidic media, Electrochim. Acta. 54 (2008) 455–460. https://doi.org/10.1016/j.electacta.2008.07.052.

[269] F.N. Khatib, T. Wilberforce, O. Ijaodola, E. Ogungbemi, Z. El-Hassan, A. Durrant, J. Thompson, A.G. Olabi, Material degradation of components in polymer electrolyte membrane (PEM) electrolytic cell and mitigation mechanisms: A review, Renew. Sustain. Energy Rev. 111 (2019) 1–14. https://doi.org/10.1016/j.rser.2019.05.007.

[270] N. Macauley, D.D. Papadias, J. Fairweather, D. Spernjak, D. Langlois, R. Ahluwalia, K.L. More, R. Mukundan, R.L. Borup, Carbon Corrosion in PEM Fuel Cells and the Development of Accelerated Stress Tests, J. Electrochem. Soc. 165 (2018) F3148–F3160. https://doi.org/10.1149/2.0061806jes.

[271] S. Cherevko, Electrochemical dissolution of noble metals native oxides, in: J. Electroanal. Chem., Elsevier Inc., 2017: pp. 11–13. https://doi.org/10.1016/j.jelechem.2017.01.029.

[272] J. Shen, Xu. Liang, H. Chang, Z. Tu, S.W. Chan, Partial flooding and its effect on the performance of a proton exchange membrane fuel cell. Energy Conversion and Management 207 (2020) 112537. https://doi.org/10.1016/j.enconman.2020.112537

[273] T. Mittermeier, PEM Fuel Cell Start-Up/Shut-Down Losses vs Relative Humidity: The Impact of Water in the Electrode Layer on Carbon Corrosion2018 J. Electrochem. Soc. 165 F1349

[274] C. Minke, M. Suermann, B. Bensmann, R. Hanke-Rauschenbach, Is iridium demand a potential bottleneck in the realization of large-scale PEM water electrolysis? , Int. J. Hydrogen Energy 46 (2021) 23581 - 23590